ASME
SETTING THE STANDARD

Transactions of the ASME, Journal of Fluids Engineering
(ISSN 0098-2202) is published monthly by
The American Society of Mechanical Engineers,
Three Park Avenue, New York, NY 10016.
Periodicals postage paid at New York, NY
and additional mailing offices.
POSTMASTER: Send address changes to Transactions of the
ASME, Journal of Fluids Engineering, c/o THE AMERICAN
SOCIETY OF MECHANICAL ENGINEERS,
22 Law Drive, Box 2300, Fairfield, NJ 07007-2300.
CHANGES OF ADDRESS must be received at Society
headquarters seven weeks before they are to be effective.
Please send old label and new address.
STATEMENT from By-Laws. The Society shall not be
responsible for statements or opinions advanced in papers
or ... printed in its publications (B7.1, Par. 3).

Journal of Fluids Engineering

Published Monthly by ASME

VOLUME 132 • NUMBER 3 • MARCH 2010

RESEARCH PAPERS

Flows in Complex Systems

Fundamental Issues and Canonical Flows

Multiphase Flows

Techniques and Procedures

(Contents continued on inside back cover)

This journal is printed on acid-free paper, which exceeds the ANSI Z39.48-1992 specification for permanence of paper and library materials. ♾™
♻ 85% recycled content, including 10% post-consumer fibers.

(**Contents continued**)

Journal of Fluids Engineering **Volume 132, Number 3** **MARCH 2010**

TECHNICAL BRIEFS

The ASME Journal of Fluids Engineering is abstracted and indexed in the following:

Applied Science & Technology Index, Chemical Abstracts, Chemical Engineering and Biotechnology Abstracts (Electronic equivalent of Process and Chemical Engineering), Civil Engineering Abstracts, Computer & Information Systems Abstracts, Corrosion Abstracts, Current Contents, Ei EncompassLit, Electronics & Communications Abstracts, Engineered Materials Abstracts, Engineering Index, Environmental Engineering Abstracts, Environmental Science and Pollution Management, Excerpta Medica, Fluidex, Index to Scientific Reviews, INSPEC, International Building Services Abstracts, Mechanical & Transportation Engineering Abstracts, Mechanical Engineering Abstracts, METADEX (The electronic equivalent of Metals Abstracts and Alloys Index), Petroleum Abstracts, Process and Chemical Engineering, Referativnyi Zhurnal, Science Citation Index, SciSearch (The electronic equivalent of Science Citation Index), Shock and Vibration Digest, Solid State and Superconductivity Abstracts, Theoretical Chemical Engineering

Hayder Schneider[1]
e-mail: hayder.schneider@kit.edu

Dominic von Terzi

Hans-Jörg Bauer

Institut für Thermische Strömungsmaschinen,
Karlsruher Institut für Technologie (KIT),
Kaiserstr. 12,
76131 Karlsruhe, Germany

Wolfgang Rodi
Institut für Hydromechanik,
Karlsruher Institut für Technologie (KIT),
Kaiserstr. 12,
76131 Karlsruhe, Germany

Reliable and Accurate Prediction of Three-Dimensional Separation in Asymmetric Diffusers Using Large-Eddy Simulation

Large-eddy simulations (LES) and Reynolds-averaged Navier–Stokes (RANS) calculations of the flow in two asymmetric three-dimensional diffusers were performed. The setup was chosen to match an existing experiment with separation. Both diffusers possess the same expansion ratio but differ in performance. The aim of the present study is to find the least expensive method to reliably and with reasonable accuracy account for the impact of the change in geometry. RANS calculations failed to predict both the extent and location of the separation. In contrast, LES with wall-functions delivered results within the accuracy of the experimental data. [DOI: 10.1115/1.4001009]

1 Introduction

One major requirement in the design process of jet engines is the reliable operation of the combustion system. As a prerequisite, the axial flow velocity entering the combustion chamber is to be significantly decreased. This can be conceptually realized via two-dimensional (2D) asymmetric dump diffusers that link the last stage of the compressor to the combustion chamber. More advanced realizations use three-dimensional (3D) asymmetric diffusers that allow for higher area expansion ratios per unit length. Shorter diffuser lengths promote compact engine designs and reduce skin friction losses but imply strong flow deceleration. This deceleration together with the associated adverse pressure gradient may cause the flow to separate. The separation then initiates the formation of unsteady large-scale vortical structures. Typically, slight changes in geometry or operating conditions can lead to a drastic alteration of the flow-field. The reverse flow downstream of separation, as well as the large-scale unsteadiness, reduces the pressure recovery and the flow rate. As a consequence, the overall device performance is reduced. Reliable and accurate prediction of the complex 3D separation and reattachment is therefore crucial in the design process.

Computational fluid dynamics (CFD) with a Reynolds-averaged Navier–Stokes (RANS) turbulence closure has become the main design tool used in the aerospace industry today. RANS models are generally used for preliminary design studies due to their relatively low computational cost compared with more advanced methods, e.g., large-eddy simulation (LES). This cost advantage stems from the incorporation of a high level of empiricism through the modeling of all turbulent scales, which often allows for either steady-state and/or 2D simulations. However, the accuracy and reliability of RANS computations for predicting the flow in asymmetric 2D diffusers is in question once the flow separates. This can be seen by scrutinizing the results of a workshop held at Helsinki University of Technology, Finland, in 1999 [1]. At this workshop, prototypical experiments were simulated with various RANS models and LES. It was found that standard two-equation RANS models are not appropriate and that even full Reynolds stress closures do not guarantee success while their use is naturally more demanding for the user. LES on the other hand gave fairly reasonable results [2]. In the case of 3D asymmetric diffusers, in addition, the cost advantage of RANS compared with LES is cast in doubt. The reason is that both simulations must be 3D and the reduction in computational time due to a steady-state solution is at least partly canceled by the additional transport equations needed for suitable RANS models. The loss in accuracy due to the RANS models is therefore often not justifiable. This is particularly true if for the LES wall-functions (WF) can be used instead of the no-slip boundary condition (BC), leading to further cost savings due to coarser grids and larger time-steps. However, whether LES with WF can predict this flow reliably, accurately, and at reasonable cost is still unclear.

Recently, experiments of incompressible flow in two 3D diffusers were performed at Stanford University [3,4] aiming at providing a new test case for complex 3D separated flows. One of the two diffusers served as a test case for different CFD methods at a workshop held at Graz University of Technology, Austria, in 2008 [5]. The two diffusers have the same rectangular inlet section with fully developed turbulent channel-flow and the same expansion ratio but different aspect ratios at the outlet. The observed resulting flow fields are vastly different and challenge turbulence models in two ways. First, a simulation should be able to predict the size and the location of the 3D separation zone. Second, it should capture the effect of the change in geometry. How well LES with WF performs is scrutinized in the following by applying the method to the two diffuser test cases. First, the results will be presented confirming the findings in Ref. [5] that simulations with today's most prominent RANS models fail in determining the extent and location of the 3D separation bubble. Therefore, they cannot be used to assess the impact of the geometric changes. Then results will be shown demonstrating that, in contrast, LES with wall-functions is able to compute this flow within the accuracy of experimental data. While for the workshop discussed above and in Ref. [6], wall-resolving LES were performed, these were all for one diffuser only and delivered results comparable to the considerably more economical simulations presented here. Moreover, in this paper, computations for the other diffuser are shown for the first time. In our study, the focus is on simplicity of the grid generation and low computational cost in order to verify if, in the near future, LES can replace or at least complement RANS calculations in the design process of industrial diffusers.

2 Computational Setup

2.1 Experiments Simulated. The measurements [3,4] were performed in a recirculating water channel with magnetic reso-

[1]Corresponding author.

Contributed by the Fluids Engineering Division of ASME for publication in the JOURNAL OF FLUIDS ENGINEERING. Manuscript received August 20, 2009; final manuscript received December 23, 2009; published online March 4, 2010. Assoc. Editor: Paul Durbin.

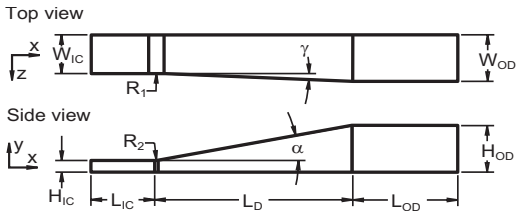

Fig. 1 Diffuser design; flow in positive *x*-direction (from left to right)

nance velocimetry. Figure 1 shows a schematic view of the simulated flow region that consists of an inlet channel (IC), a diffuser (D1 or D2), and an outlet duct (OD). The Reynolds number based on the inlet channel height and the bulk velocity was 10,000 for both diffusers. Both the geometry and Reynolds number for the simulations are in accordance with the experiments mentioned above. The origin of the Cartesian coordinate system was placed at the intersection of the two nonexpanding walls and the beginning of the expansion. All values reported are made dimensionless using the bulk velocity $U_b=1$ m/s and inlet channel height $H=H_{IC}=1$ cm, inlet channel width $B=W_{IC}=3.33$ cm, or diffuser length $L=L_D=15$ cm as reference values. Table 1 summarizes the geometric features of the two diffusers studied.

Unlike in the experiment, the two constant radii at the intersection of the two expanding walls at the diffuser inlet were replaced by sharp ones. This measure facilitated easier grid generation. A sensitivity analysis was conducted to assess the effect of replacing rounded corners by sharp ones using a simpler 2D diffuser geometry with only one deflected wall. The same computational parameters and the same expansion ratio as in the 3D case were applied. In this study, the effect of sharpening the corner was limited locally to the entrance area of the diffuser and had an insignificant impact on the pressure recovery and the flow farther downstream. Therefore, it seems reasonable to apply this simplification. The agreement with the experimental data will show that this is indeed justified.

It should be noted that the experimental data reported herein exhibit a variation in mass flux along the diffuser. This deviation can be of the order of 10% from the mass flux measured upstream where the Reynolds number is defined, see Fig. 3c of Ref. [3]. As a consequence, the experimental streamwise velocities display systematically lower values than the simulation data in the figures shown in the following. Furthermore, an asymmetry of the experimental U/U_b velocity profiles at $x/H=0$ is visible whose origin remains unclear.

2.2 Numerical Method. All simulations were performed with the finite volume flow solver large-eddy simulation on curvilinear coordinates (LESOCC2) developed at the University of Karlsruhe [7]. This FORTRAN 95 program solves the incompressible, three-dimensional, time-dependent, filtered or Reynolds-averaged Navier–Stokes equations on body-fitted, collocated, curvilinear, and block-structured grids. The viscous fluxes are always discretized with second-order accurate central differences whereas the convective fluxes are approximated either with the same method for LES or a monotonic second-order upwind scheme for RANS calculations. Time advancement is accomplished by an explicit, three-step low-storage Runge–Kutta method for LES. For RANS calculations, a second-order implicit multistep method was used. Conservation of mass is achieved by the SIMPLE algorithm with the pressure-correction equation being solved by the strongly implicit procedure of Stone. Pressure-velocity decoupling is prevented by a momentum interpolation technique. Parallelization is achieved via domain decomposition with the use of ghost cells and MPI for the data transfer.

Table 1 Dimensions of diffusers D1 and D2 based on inlet height

	Dimensions	D1	D2
Inlet channel	Height (H_{IC})	1	
	Width (W_{IC})	3.33	
Diffuser	Length (L_D)	15	
	Top angle of expansion (α) [deg]	11.3	9
	Side angle of expansion (γ) [deg]	2.56	4
	Radius ($R1=R2$)	6	2.8
Outlet duct	Height (H_{OD})	4	3.37
	Width (W_{OD})	4	4.51

2.3 Computational Domain and Resolution. The various parameters of the computational grids used are compiled in Table 2. Simulations were carried out on five different grids (G1–G5) employing between 1.6×10^6 and 7.4×10^6 grid cells and covering different domain lengths. All grids feature equidistant grid spacing with 16 cells per channel height unit H in the streamwise direction. Four grids (G1–G4) consist of 60 cells and one grid (G5) of 120 cells in both the vertical and lateral directions. While one grid (G1) is stretched in the two wall-normal directions in order to allow for wall-resolving simulations, the other grids (G2–G5) are equidistant for use with wall-functions. Adaptive time-stepping ensured a CFL limit of less than 0.65 (with $\Delta t\approx0.006-0.01$). In total, 600,000 time-steps were computed. Averaging started after roughly 150 H/U, resulting in an averaging time of more than 5000 H/U and 2500 H/U or 200 and 100 domain flow-through times for the simulations on grids G2–G4 and G5, respectively. The data presented were obtained using between 112 and 144 processors on an HP Linux cluster of the Karlsruhe Institute of Technology.

2.4 Turbulence Models and Boundary Conditions. LES was performed for both diffusers (D1 and D2) using grids G2–G5. The standard Smagorinsky [8] model with $C_s=0.065$ and van Driest damping served as a subgrid-scale model. At walls, an adaptive wall-function developed by Hinterberger [7] is used. In this approach, the wall-function is based on direct numerical simulation data of turbulent channel-flow and switches itself off if the wall is well resolved and near separation and reattachment; more details are given in the appendix of Ref. [9]. For comparison, one simulation was repeated with the alternative wall-function of Werner and Wengle [10]. At the outlet a convective BC is enforced. In grid G4, a buffer zone was placed before the outlet ($x/H\in[27;28]$). In the buffer zone, the viscosity is increased by a factor of 100 in order to damp flow structures before they arrive

Table 2 Details on computational grids employed; domain length includes inflow generator

Grid	G1	G2	G3	G4	G5
Domain size $x/H\in$	[−5;23]		[−5;28]	[−8;28]	[−5;28]
$N_x\times N_y\times N_z$	$448\times60\times60$		$528\times60\times60$	$576\times60\times60$	$528\times120\times120$
	$\approx1.6\times10^6$		$\approx1.9\times10^6$	$\approx2.1\times10^6$	$\approx7.4\times10^6$
Inflow at $x/H=$		−2		−5	−2
Grid spacing	Stretched			Equidistant	

Table 3 Overview, purpose, and costs of simulations discussed

Simulation	Diffuser	Model	Grid	Inflow BC	CPU hours	Purpose
Ia	D1	RANS	G1	Uniform	1.5×10^3	Inlet sensitivity
Ib	D1	RANS	G1	Turbulent	2.2×10^3	RANS-reference
IIa	D1	LES	G2	Turbulent	15×10^3	LES-reference
IIb	D1	LES	G3	Turbulent	18×10^3	Outlet position sensitivity
IIc	D1	LES	G4	Turbulent	20×10^3	Inlet position sensitivity
IId	D1	LES	G5	Turbulent	120×10^3	Grid resolution study
IIIa	D2	LES	G2	Turbulent	15×10^3	LES-reference
IIIb	D2	LES	G3	Turbulent	18×10^3	Outlet position sensitivity
IIIc	D2	LES	G4	Turbulent	20×10^3	Inlet position sensitivity
IIId	D2	LES	G3	Turbulent	18×10^3	Wall-function sensitivity

at the outflow boundary. Unsteady turbulent inflow data were generated in a synchronized computation running in parallel. To this end, in the front part of the domain, periodicity was enforced in the streamwise direction within a section of length $l/H=3$ and a controller was used to enforce the nominal experimental mass flux. This is essentially a fully developed channel-flow simulation providing time-dependent realistic flow structures for the diffuser inlet (at $x/H=-2$ or $x/H=-5$).

For RANS simulations, the standard two-equation $k-\omega$ model of Wilcox [11] was used as turbulence closure. The simulations were wall-resolving on the stretched grid (G1) and were restricted to diffuser D1. Two inlet BC were tested: a uniform inlet velocity profile as well as a fully developed channel-flow profile. The no-slip condition was enforced at the wall and a homogeneous Neumann BC at the outlet. Using the implicit time-scheme, the dimensionless time-step was set to 0.01 and the simulations were converged to steady-state. Twenty thousand time-steps were computed for the $k-\omega$ RANS simulations with both the uniform and turbulent inlet velocity BC.

2.5 Simulation Overview. The different geometries, turbulence models and grids used, as well as the CPU hours computed and the purpose of the various simulations are compiled in Table 3. Simulation Ia used a uniform velocity profile as the inlet condition while all other simulations used a fully developed channel profile. Simulations with other RANS models using LESOCC2 and commercial flow solvers were conducted as well but are not reported since they did not yield any better results than those presented here.

3 Results

3.1 Impact of Turbulence Models and Boundary Conditions. The wall-pressure coefficient C_p is a quantity that directly reflects the efficiency of a diffuser, hence its prediction is of prime interest in engineering design. For incompressible flow, C_p is defined as $C_p=2(p-p_{\mathrm{ref}})/(\rho U_{\mathrm{ref}}^2)$, where p is the mean pressure, p_{ref} is the pressure at the reference point $(x/H,y/H,z/B)=(0,0,0.5)$, $\rho=1$ is the nondimensional density of the fluid and $U_{\mathrm{ref}}=U_b$.

Figure 2 shows C_p for RANS simulations Ia and Ib and LES IIa and IIb together with the experimental data for diffuser D1. The experimental data yield a continuous rise in C_p along the diffuser. The RANS simulation Ia yields a qualitatively good picture, whereas the RANS simulation Ib delivers a too low pressure recovery. The pressure increase is best captured by the LES. Both simulations are in fairly good agreement with the experimental data until the influence of the outflow BC becomes noticeable inside the outlet duct. For LES IIa, this occurs at $x/L>1.3$. LES IIb revealed that an extended domain length delays this effect (until $x/L=1.6$) but no impact of the outflow BC is visible upstream of $x/L=1.3$.

Figure 3 shows the profiles of the mean velocity U/U_b at various streamwise locations at the centerplane $z/B=0.5$ again for diffuser D1. The $k-\omega$ model, i.e., simulations Ia and Ib, does not predict any reverse flow close to the upper wall and underpredicts the velocity magnitude close to the lower wall along the streamwise direction. In contrast, the LES used in simulation IIa is in reasonably good agreement with the experimental data, being able to match both the shape and magnitude of the velocity profile. The good qualitative performance of simulation Ia regarding C_p is therefore the result of a fortuitous prediction of the velocity magnitude and gradient close to the lower wall along the centerplane. This becomes clearer when considering Fig. 4. In this figure the mean streamwise velocity contours are shown at $x/H=12$. This location is the most critical location in diffuser D1. The experimental data show that the recirculation bubble is horizontally aligned at the upper wall and simulation IIa yields reasonable agreement for both the extent of the recirculation bubble and the location of maximum forward velocity. However, RANS Ia and Ib shift the separation bubble to the right wall and attest that the $k-\omega$ model fails to correctly predict 3D separation.

The failure of the $k-\omega$ model to accurately replicate the flowfield can be partly explained by the presence of secondary (mean) flow structures in the rectangular inlet channel. Contrary to the LES, RANS simulations Ia and Ib do not resolve these structures because of the inherent assumptions in the model. This conjecture is corroborated by results reported in Ref. [5]. These results show that advanced RANS closures such as Reynolds stress models, that can resolve secondary flows in the inlet channel, yield some qualitative improvement compared with those obtained by the $k-\omega$ model. However, these improvements vanish in regions of strong separation, especially in the vicinity of the two expanding walls. From the above observations, it is unlikely that the change in separation lines in such diffusers due to geometric variations can be captured reliably by RANS calculations.

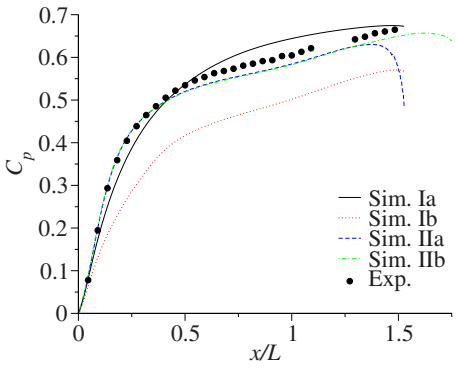

Fig. 2 Mean wall-pressure coefficient C_p at $z/B=0.5$ along the lower wall of diffuser D1: x is normalized with the diffuser length L, p_{ref} is taken at $x=y=0$, and the experimental data are shifted accordingly

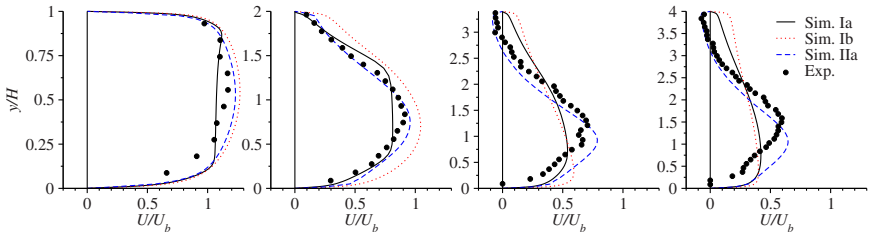

Fig. 3 Mean streamwise velocity U/U_b profiles at $z/B=0.5$ for diffuser D1; from left to right: $x/H=0$, 5, 12, and 16

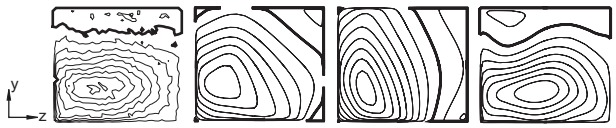

Fig. 4 Mean streamwise velocity U/U_b contours of experiments and simulations Ia, Ib, and IIa (left to right) in a cross section at $x/H=12$ for diffuser D1; same velocity contours with interval 0.1 shown for all plots: thicker line indicates zero-velocity contour

3.2 Impact of Domain Length and Resolution. In order to estimate the influence of the domain length on the LES results, additional simulations IIb and IIc were conducted. Figure 5 shows mean velocity U/U_b profiles of LES IIa–IIc at different streamwise locations at the centerplane $z/B=0.5$ for diffuser D1. The profiles show little deviation and indicate that the position of both the inlet and the outlet BC exhibit a negligible effect on the numerical results.

The effect of changes in resolution on the LES results can be determined by comparing simulations IIb and IId having the same domain length but a different number of grid points. Figure 6 shows the mean velocity U/U_b and rms velocity u_{rms}/U_b profiles of simulations IIb and IId at various spanwise locations for the streamwise location $x/H=12$, i.e., in the center of the recirculation zone. The coarse grid used in simulation IIb yields better agreement with the experimental data at the upper wall and shows an inverse trend at the lower wall of the diffuser for increasing spanwise location. Simulation IIb tends to overpredict the amount of both reverse flow at the upper wall and forward flow at the lower wall for increasing spanwise location. For all locations, simulation IId is superior in predicting the amount of backward flow as well as the location of the maximum forward velocity, and the overall agreement is good. The same is true for the u_{rms}/U_b values that can additionally be studied at the same positions. All simulations capture the profiles and location of the peak value within measurement uncertainty. Consequently, the additional accuracy gained by the increased computational cost of simulation IId may be regarded as not worthwhile, confirming that the resolution of simulation IIb, and hence also IIa, is sufficient.

3.3 LES of Diffuser D2 and Impact of Wall-Function. The study on the domain length influence on the LES results was repeated for diffuser D2. In Fig. 7 the profiles of mean streamwise velocity U/U_b are shown for diffuser D2 at various streamwise locations at the centerplane $z/B=0.5$. Simulations IIIa–IIIc are in good agreement with the experimental data close to the upper wall and overpredict the velocity magnitude at the lower diffuser wall for increasing streamwise location. All simulations yield very similar results and confirm the negligible influence of both the inlet and outlet BC also for diffuser D2.

The contour plots of U/U_b shown in Fig. 8 reveal the difference in the flow-field characteristics of diffuser D2 compared with diffuser D1 for the same location $x/H=12$. Recall that this location was chosen since here the deviations between the experimental data and the simulations are most obvious. The experimental data show that, due to the change in the outlet geometry, the separation bubble moves from a horizontal alignment at the top wall (see Fig. 4) to a predominantly vertical orientation on the right side. The LES data exhibit the same trend and show good agreement with the region of maximum forward flow. At other locations, even better agreement is obtained. Only simulation IIIa is shown since the other LES IIIb–IIId yielded the same result.

The good agreement of the LES with the experimental data becomes clearer when scrutinizing Fig. 9, where mean streamwise velocity profiles at various spanwise locations at $x/H=12$ are

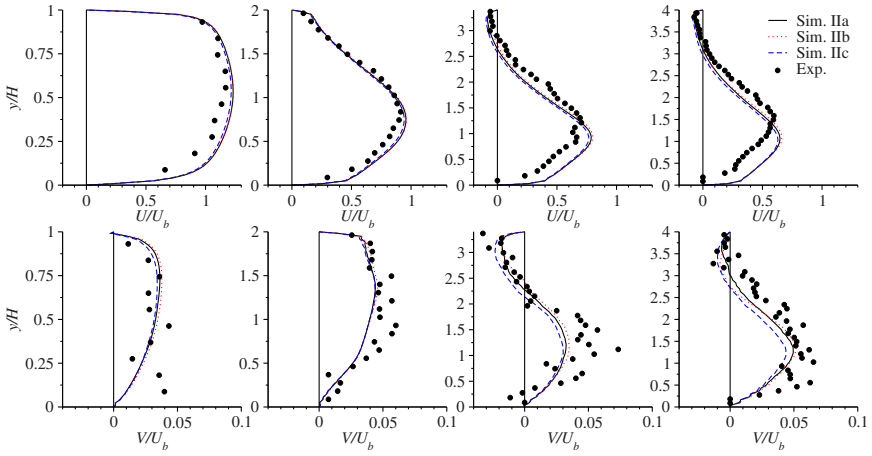

Fig. 5 Mean streamwise velocity U/U_b (top row) and mean vertical velocity V/U_b (bottom row) profiles at $z/B=0.5$ for diffuser D1; from left to right: $x/H=0$, 5, 12, and 16

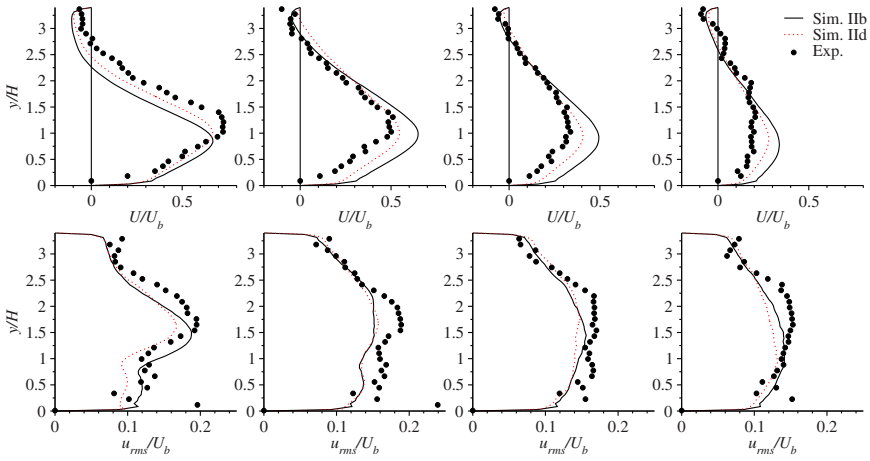

Fig. 6 Mean streamwise velocity U/U_b (top row) and u_{rms}/U_b (bottom row) profiles in diffuser D1 at $x/H=12$; from left to right: $z/B=0.25$, 0.75, 0.875, and 1

shown. It can be seen that the LES first slightly overpredicts and then tends to underpredict the amount of reverse flow at the upper wall for increasing spanwise location but overall deviations are within measurement uncertainty. Recall that, on the other hand, the RANS simulations for diffuser D1 shown above, and in Ref. [5], predicted results resembling those of diffuser D2 while attempting to compute diffuser D1. In contrast, the LES is clearly able to predict the difference in the flow-field due to the change in geometry.

In order to assess the sensitivity of the LES results on the kind of wall-function used, simulation IIId was performed employing the wall-function of Ref. [10]. The data of LES IIId are included in Fig. 9 for comparison. Any differences between the two LES are barely visible demonstrating that the details of the wall-function employed are of no importance here.

3.4 Assessment of the Geometric Sensitivity Using LES. Figure 10 is particularly instructive for assessing the global quality of the LES. In this plot, for both experiments and LES, the fraction of cross-sectional area of reverse flow is shown. The experimental uncertainty is indicated by the dot-dashed lines and was obtained by calculating the same fraction of cross-sectional area using $U/U_b=\pm 0.05$ instead of $U/U_b=0$ as threshold.

The characteristics of diffuser D1 are matched by all LES (simulations IIb and IId shown) and deviations reside within experimental uncertainties beyond the location of the maximum in this plot. Until $x/L=0.4$, the simulations are in agreement with the experimental data. From that point on simulations IIb predicts marginally higher separation until $x/L=1.6$, where the effect of the outflow BC becomes noticeable. On the other hand, simulation IId gives a lower fraction of area with separated flow until $x/L=1.1$. From this location on the predictions are higher and yield fully attached flow at $x/L=1.6$. Exchanging the round corner at the diffuser inlet by a sharp one has clearly no detrimental effects (a tiny separation bubble is formed, which is not visible in Fig. 10). The results of simulations IIa and IIc (not shown in Fig. 10) are in close agreement to those obtained by simulation IIb. The amount of area fraction separated along the diffuser computed by simulation IIa is almost identical to the one obtained by simulation IIb until $x/L=1.3$, where the effect of the outflow BC becomes evident due to the shorter domain length. The same identity is true for simulation IIc, except that from $x/L=1.3$ the amount of separated flow is further diminished until fully attached flow is attained at $x/L=1.6$. This improved behavior may be due to employing a buffer zone for this simulation.

Both the amount and streamwise distribution of reverse flow per cross-sectional area in diffuser D2 (Fig. 10, right) are well matched by the LES IIIa and IIIb and deviations reside again within measurement uncertainty. Again until $x/L=0.4$, the computational results are in agreement with the experimental data.

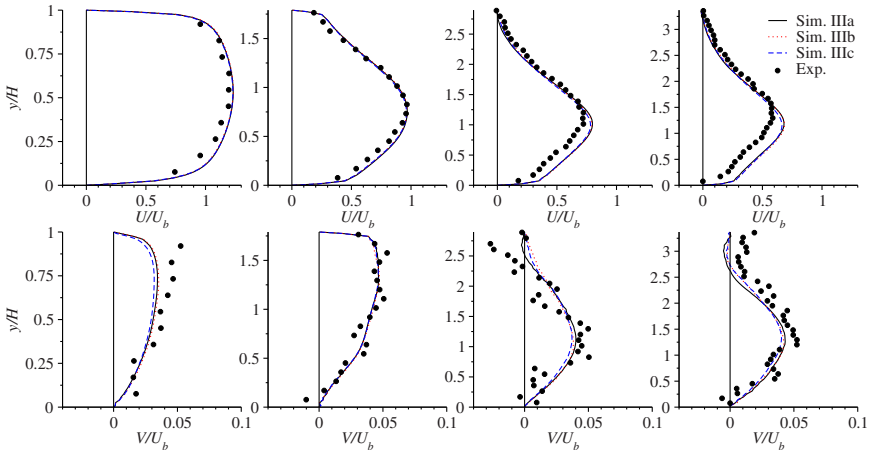

Fig. 7 Mean streamwise velocity U/U_b (top row) and mean vertical velocity V/U_b (bottom row) profiles at $z/B=0.5$ for diffuser D2; from left to right: $x/H=0$, 5, 12, and 16

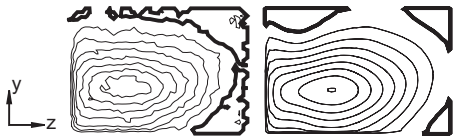

Fig. 8 Mean streamwise velocity U/U_b contours of experiments (left) and simulation IIIa (right) in a cross section at $x/H=12$ for diffuser D2; same velocity contours with interval 0.1 shown for all plots; thicker line indicates zero-velocity contour

Between $x/L=0.4$ and 0.8, the LES results underpredict and then overpredict the backward flow until $x/L=1.3$. Thereafter, again the effect of the outflow BC is visible for simulation IIIa.

Figure 11 shows iso-contours of the mean streamwise velocity $U/U_b=0$ for the two diffusers D1 (left) and D2 (right). The LES data are particularly well suited for 3D visualization of the separated zones highlighted by the white dashed lines. Note the complicated three-dimensionality of these lines. The variation in the top-to-side angle of expansion ratio between the two diffusers determines the differences in the flow-field in which three different separation bubbles (SBs) can be identified. The first one (SB1) is small in size and extent and is located at the beginning of the diffuser at the sharp upper corner and is symmetric and asymmetric in diffusers D1 and D2, respectively. This is an artifact of our setup but apparently had no effect on the downstream results and made the grid generation much easier. The second separation bubble (SB2) close to the upper wall is rather large and ranges from the middle of the diffuser until the beginning of the outlet duct. The third one (SB3) is found at the edge of the lower and expanding side wall in the region of the outlet duct. For both diffusers, SB2 is geometrically triggered at the corner of the two expanding walls and develops as a function of the top-to-side

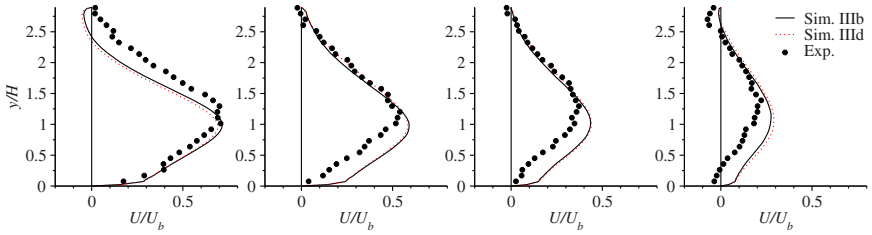

Fig. 9 Mean streamwise velocity U/U_b profiles in diffuser D2 at $x/H=12$; from left to right: $z/B=0.25$, 0.75, 0.875, and 1

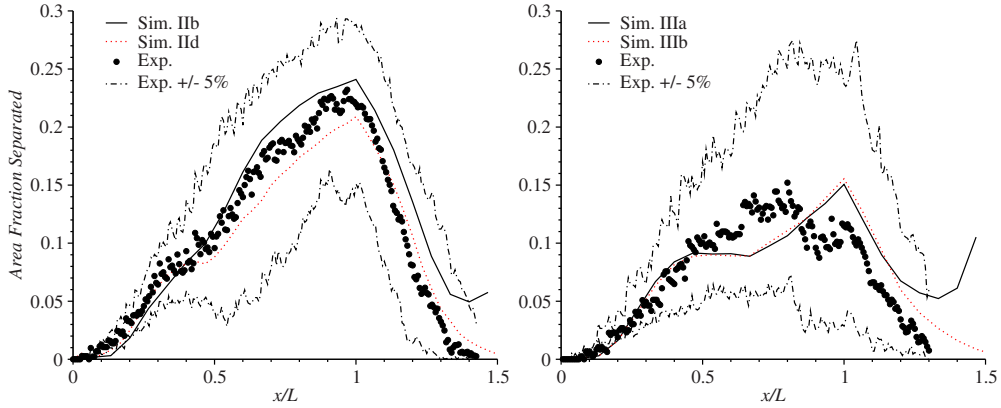

Fig. 10 Mean fraction of cross-sectional area separated in experiments and simulations IIb and IId for diffuser D1 (left) and simulations IIIa and IIIb for diffuser D2 (right); RANS data of diffuser D1 deviate substantially (not shown)

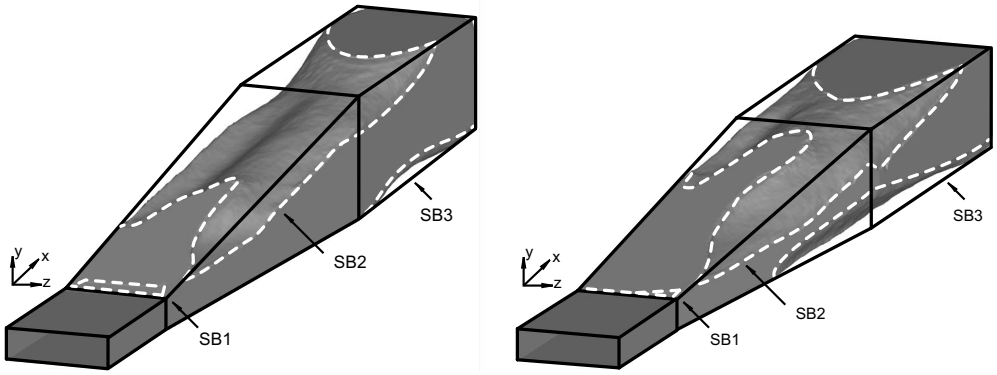

Fig. 11 Mean streamwise velocity iso-contour $U/U_b=0$ for diffuser D1 (simulation IIb, left) and D2 (simulation IIIb, right) until $x/L=1.67$; white dashed lines indicate separation bubbles; no presence of separation in the regions not shown

angle of expansion ratio. In diffuser D1 a higher ratio is realized resulting in a larger separation bubble close to the upper wall, which is nearly horizontally aligned. In contrast for diffuser D2, SB2 is less dominant close to the upper wall but is shifted more to the expanding side wall. SB3 shows to have a much larger upstream effect in diffuser D2 and extends until the middle of the diffuser where it nearly merges with SB2.

3.5 Cost Assessment. An important aspect of the present study is the comparison of computational costs between RANS and LES. This can be carried out with the data of diffuser D1 given in Table 3. Note that simulations IIb–IId served to verify the quality of the chosen setup. The relative cost between the RANS calculation (simulation Ia) and LES with WF (simulation IIa) according to Table 3 is a factor of 1:10. However, the LES was converged extremely well and differences in the final results compared with those obtained after half the computation time were minute. The effective cost between the chosen two-equation RANS model and the LES is therefore at most 1:5. If more complex RANS methods such as Reynolds stress closures are used, the relative cost advantage of RANS decreases by a factor of two [12], finally resulting in a maximum relative cost factor of 1:2.5. Moreover, in an industrial application, depending on the quality of results desired, even less computational time could yield satisfactory LES results.

4 Conclusions

LES on a coarse equidistant grid using the standard Smagorinsky model and wall-functions is able to predict the three-dimensionally separated flow in asymmetric diffusers with fair accuracy at reasonable cost. On the other hand, the $k-\omega$ RANS model falls short, as do other RANS models [5]. They predict a qualitatively different flow-field. In this light, it seems that the additional computer time required for the LES is well spent considering the higher reliability and accuracy of the results, in particular since only the LES was able to correctly predict the impact of the change in geometry on the flow-field. In conclusion, for the design process of asymmetric diffusers that are prone to separation, it is recommended that key configurations should be computed with a simple LES in order to corroborate and supplement any RANS results.

Acknowledgment

The work reported here was carried out within the "Research Group Turbo-DNS" at the Institut für Thermische Strömungsmaschinen. Its financial support by means of the German Excellence Initiative and Rolls-Royce Deutschland is gratefully acknowledged. The authors appreciate the provision of computer time by the Steinbuch Centre for Computing.

References

[1] 1999, *Proceedings of the Eighth ERCOFTAC/IAHR/COST Workshop on Refined Turbulence Modelling*, A. Hellsten and P. Rautaheimo, eds., Helsinki University of Technology, Helsinki, Finland.

[2] Kaltenbach, H.-J., Fatica, M., Mittal, R., Lund, T., and Moin, P., 1999, "Study of Flow in a Planar Asymmetric Diffuser Using Large-Eddy Simulation," J. Fluid Mech., **390**, pp. 151–185.

[3] Cherry, E. M., Elkins, C. J., and Eaton, J. K., 2008, "Geometric Sensitivity of Three-Dimensional Separated Flows," Int. J. Heat Fluid Flow, **29**(3), pp. 803–811.

[4] Cherry, E. M., Elkins, C. J., and Eaton, J. K., 2009, "Pressure Measurements in a Three-Dimensional Separated Diffuser," Int. J. Heat Fluid Flow, **30**(1), pp. 1–2.

[5] 2008, *Proceedings of the 13th SIG15 ERCOFTAC/IAHR Workshop on Refined Turbulence Modelling*, G. Brenn, S. Jakirlić, and H. Steiner, eds., Graz University of Technology, Graz, Austria.

[6] Cherry, E. M., Iaccarino, G., Elkins, C. J., and Eaton, J. K., 2006, "Separated Flow in a Three-Dimensional Diffuser: Preliminary Validation," *Annual Research Briefs*, Center for Turbulence Research, Stanford University, Stanford, CA.

[7] Hinterberger, C., 2004, "Dreidimensionale und tiefengemittelte Large-Eddy-Simulation von Flachwasserströmungen," Ph.D. thesis, Universität Karlsruhe (TH), Karlsruhe, Germany.

[8] Smagorinsky, J., 1963, "General Circulation Experiments With the Primitive Equations. I: The Basic Experiment," Mon. Weather Rev., **91**, pp. 99–165.

[9] Schneider, H., von Terzi, D., Bauer, H.-J., and Rodi, W., 2009, "Reliable and Accurate Prediction of Three-Dimensional Separation in Asymmetric Diffusers Using Large-Eddy Simulation," ASME Paper No. GT2009-60110.

[10] Werner, H., and Wengle, H., 1993, "Large-Eddy Simulation of Turbulent Flow Over and Around a Cube in a Plate Channel," *Eighth Symposium on Turbulent Shear Flows*, F. Durst, R. Friedrich, B. E. Launder, F. W. Schmidt, U. Schumann, and J. H. Whitelaw, eds., Springer-Verlag, Berlin.

[11] Wilcox, D., 1993, *Turbulence Modeling for CFD*, DCW, La Cañada, CA.

[12] Pope, S. B., 2000, *Turbulent Flows*, Cambridge University Press, Cambridge.

The Effects of Fins on the Intermediate Wake of a Submarine Model

Juan M. Jiménez[1]
e-mail: jjimenez@upenn.edu

Ryan T. Reynolds
e-mail: ryan.reynolds@lmco.com

Alexander J. Smits
e-mail: asmits@princeton.edu

Department of Mechanical and Aerospace Engineering,
Princeton University,
Princeton, NJ 08544-5263

Results are presented on the behavior of the turbulent wake behind a submarine model for a range of Reynolds numbers based on the model length between 0.49×10^6 and 1.8×10^6, for test locations between 3 and 9 diameters downstream of the stern. The shape of the model emulates an idealized submarine, and tests were performed with and without stern fins. In the absence of fins, the velocity profile in planes away from the influence of the sail rapidly becomes self-similar and is well described by a function of exponentials. The fins create defects in the velocity profiles in the outer region of the wake, while yielding higher values of turbulence at locations corresponding to the tips of the fins. Measurements conducted in planes away from the midline plane show that the velocity profiles remain self-similar, while the shear stress profiles clearly show the effects of the necklace vortices trailing from the base of the fins. [DOI: 10.1115/1.4001010]

1 Introduction

For axisymmetric and two-dimensional wakes in a uniform stream, Townsend [1] proposed that at locations *sufficiently far* downstream, the wake would become self-similar so that the flow field could be described by one velocity scale u_0 and one length scale l_0, where u_0 is the maximum velocity defect and l_0 is the distance from the centerline to where the streamwise velocity $u=0.5u_0$ (see Fig. 1). In the case of an axisymmetric wake with a small velocity defect, we expect that $u_0\sim(x-x_0)^{-2/3}$ and $l_0\sim(x-x_0)^{1/3}$, where x is the streamwise coordinate and x_0 is the virtual origin of the wake [1].

Experiments show that what is meant by sufficiently far depends on the geometry of the wake generator and the Reynolds number. Experiments also indicate that the mean velocity profiles typically reach a self-preserving state much earlier than the turbulence distributions (see, for example, Ref. [2] for two-dimensional wake generators, and Ref. [3] for an axisymmetric wake generator). Similarly, Chevray [4] found that the mean velocity in the wake of a 6:1 prolate spheroid attains self-similarity for $x\geq3$ diameters, D, while turbulent parameters need much longer distances to become self-similar, a result matched by Sirviente and Patel [5], who found that in the wake of a body of revolution with a blunt stern, the mean velocity distribution becomes self-similar for $x\geq3.63D$, while the turbulent profiles do not.

Here, we examine the wake downstream of a SUBOFF geometry, which is an idealized shape intended for basic studies of submarine flow fields. We are interested in the intermediate wake, where the mean velocity profiles are expected to be self- similar but the turbulence intensities are not. Previous studies have examined the boundary layer development on the SUBOFF body, and some data are available on the characteristics of the near wake [6], but little is known on the evolution of the wake further downstream. Furthermore, the influence of body appendages such as a sail or fins is not well documented. Simpson [7] reported that junction flows can generate trailing vortices that strongly interact with the wake. In addition, Huang et al. [6] showed that in the near wake of a SUBOFF submarine model, these vortices introduce spatial nonuniformities in the mean axial velocity distribution, promote an efflux of low momentum and high turbulence level fluid away from the appendage, redistribute the normal and shear stresses, and cause an influx of high momentum and low turbulence level fluid behind the appendage. To improve our understanding of the intermediate wake and the effects of fins, experiments were conducted for Reynolds number based on the model length Re_L from 4.9×10^5 to 1.8×10^6.

2 Experimental Apparatus and Techniques

The wake is generated by a 1/120 scale DARPA SUBOFF model [8]. The overall length of the model is $L=0.87$ m, with a maximum diameter of $D=0.1016$ m. The model is held in place by a support located on the midbody section where the sail would normally be located (see Fig. 1). The cross section of the support corresponds to that of the sail described in Ref. [8], so that the support resembles a semi-infinite sail. A 1 mm diameter trip wire was placed about $0.25D$ downstream of the nose of the model to promote an early transition to turbulence.

The experiments were conducted in a closed-loop wind tunnel. The flow was conditioned by a honeycomb, a screen, and a rectangular 4.2:1 contraction before entering a rectangular $0.61\times0.91\times2.44$ m^3 (height$\times$width$\times$length) test section. The freestream velocity downstream of the submarine model varied less than 1% with axial position and the freestream turbulence was at most 0.2%. The air temperature varied less than 0.2°C from its 17.8°C mean value.

Mean velocity measurements were made using a Pitot tube at $4.5D$ and $8.5D$ downstream of the model along the vertical midline plane for a Reynolds number range between 4.9×10^5 and 1.8×10^6. The Pitot tube was connected to an electronic manom-

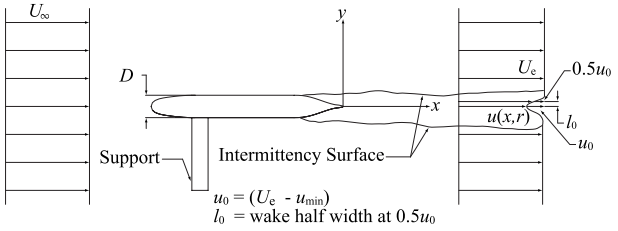

Fig. 1 Wake flow behind an axisymmetric body and defining nomenclature for the flow

[1]Corresponding author. Present address: Institute for Medicine and Engineering, University of Pennsylvania, Philadelphia, PA 19104.

Contributed by the Fluids Engineering Division of ASME for publication in the JOURNAL OF FLUIDS ENGINEERING. Manuscript received September 8, 2009; final manuscript received January 11, 2010; published online March 4, 2010. Assoc. Editor: Pavlos P. Vlachos.

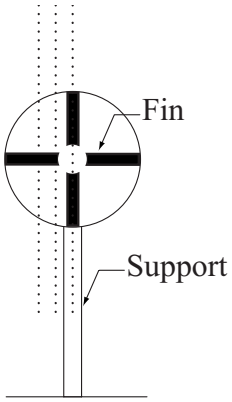

Fig. 2 Three different offset planes $z/D=0$, 0.125, and 0.25; view is looking upstream

eter (Setra Systems Inc., Boxborough, MA) with a 689.5 Pa range. The signal was sampled at 1 kHz for 50 s, and the error in the mean velocity was estimated to be less than 1%.

Hot wire probes were used to obtain the turbulence data and additional mean flow measurements. The probes were made using a 5 μm in diameter silver-coated platinum wires, soldered on to a Dantec 55P501 single wire probe and a Dantec 55P51 crossed hot-wire probe, and operated using constant temperature DANTEC Type 55M01 anemometers equipped with 55M12 symmetrical bridges. The hot-wire signals were sampled for 50 s at 40 kHz and filtered at 20 kHz with an ITHACO 4213 filter. The 12 bit analog to digital signal conversion was conducted with a PCI E Series data acquisition board (National Instruments Corp., Austin, TX) with a minimum resolution of 0.24 mV. The probes were mounted on a two axis traversing system with a NACA 0020 fairing to reduce the aerodynamic interference. The single wire measurements were conducted at axial positions $x/D=3$ and 6 downstream in the vertical midline plane at $\mathrm{Re}_L=1.0\times10^6$. The errors in the mean velocity and axial turbulence intensity measurements for the single normal wire were 1% and 3%, respectively. The crossed-wire measurements were conducted at $x/D=6$ and $\mathrm{Re}_L=1.2\times10^6$ in the midline plane as well as two transversally offset planes (Fig. 2). For the crossed-wire measurements, the error in the mean velocity was $<1\%$, for the streamwise component of the turbulence intensity $\sqrt{\overline{u'^2}}$, it was estimated to be $\leq5\%$, and for the normal component $\sqrt{\overline{v'^2}}$, it was $\leq10\%$.

Additional measurements were conducted using particle image velocimetry (PIV) along the vertical midline plane for $\mathrm{Re}_L=1.1\times10^6$. The PIV algorithm employed is described in Ref. [9]. The PIV measurements yielded about 1100 velocity fields with a resolution of 81×59 vectors calculated from 16×16 pixel windows with an 8 pixel window overlap. Particle displacement error was at most 0.25% without considering the uncertainty arising from particle lagging effects, which was estimated to be at most 1% for these experiments.

The flow was continuously seeded about 4 m downstream from the tail of the submarine model with approximately 1 μm in diameter olive oil particles. The particles were illuminated with a 1 mm thick laser sheet generated by a Spectra Physics PIV-400 double pulse frequency-doubled Nd:YAG laser and captured with a 10 bit, 496×656 pixel resolution Cohu 6612–3000 charge-coupled device (CCD) camera, yielding a 240×240 $\mu\mathrm{m}^2$ area projection onto each pixel. The signal generated by a DG535 Digital Delay/Pulse Generator (Stanford Research Systems Inc., Sunnyvale, CA) with 5 ps resolution was used to trigger the laser and the CCD camera. The images were recorded to random access memory (RAM) using a PIXCI-D PCI digital video capture board. A Hoya 533 nm bandpass filter was installed on the 35 mm focal length lens to reduce background noise.

Further details on these experiments and additional results are presented by Reynolds [10] and Jiménez [9].

3 Results and Discussion

3.1 Flow With No Appendages. The PIV data clearly show the asymmetry introduced by the support. Figure 3 shows the instantaneous nondimensionalized spanwise vorticity $\omega_z^*=(\omega_z D)/U_e$, where U_e is the velocity at the edge of the wake in the midline plane containing the support. The two shear layers observed in the flow field most likely correspond to the boundary layer separating from the rear of the body. As the wake develops, the intensity of the vorticity concentrations decreases faster on the side where the support is located (the lower part in Fig. 3).

The asymmetry introduced by the support is seen more clearly in the mean velocity profiles, as shown in the similarity coordinates in Fig. 4. For the upper half of the wake (away from the support, that is, $y/l_0\geq0$), the defect velocity and half-wake width were found to follow the power law scaling relationships expected from the similarity arguments (see Ref. [9] for details). That is, $u_0/U_e=A(x/D+2)^{-2/3}$ and $l_0/D=B(x/D+2)^{1/3}$, where $A=1.05$ and $B=0.11$. The profiles for $y/l_0\geq0$ collapse very well in this scaling, and are well represented by the function

$$f_1(\eta)=\exp(-0.525\eta^2-0.1375\eta^4-0.03\eta^6-0.002225\eta^8) \tag{1}$$

where $\eta=y/l_0$. Other exponential functions defined by

$$f_2(\eta)=\exp(-0.693\eta^2) \tag{2}$$

and

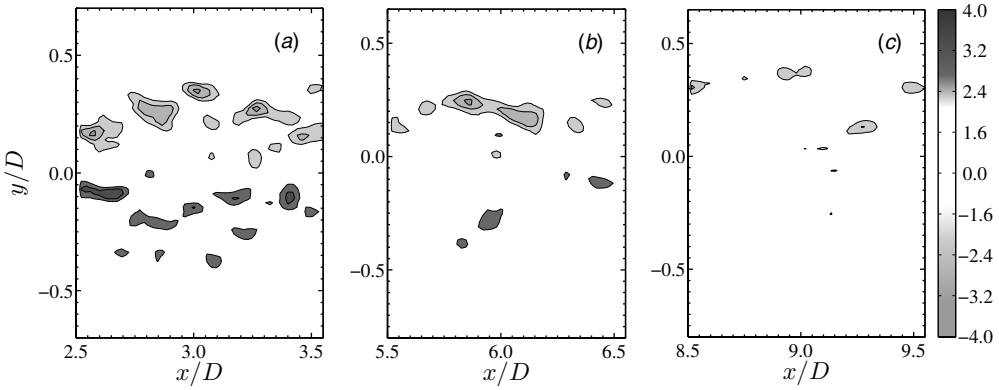

Fig. 3 Instantaneous nondimensional spanwise vorticity fields $\omega^*=\omega_z D/U_e$ centered around $x/D=$ (*a*) 3, (*b*) 6, and (*c*) 9; no fins

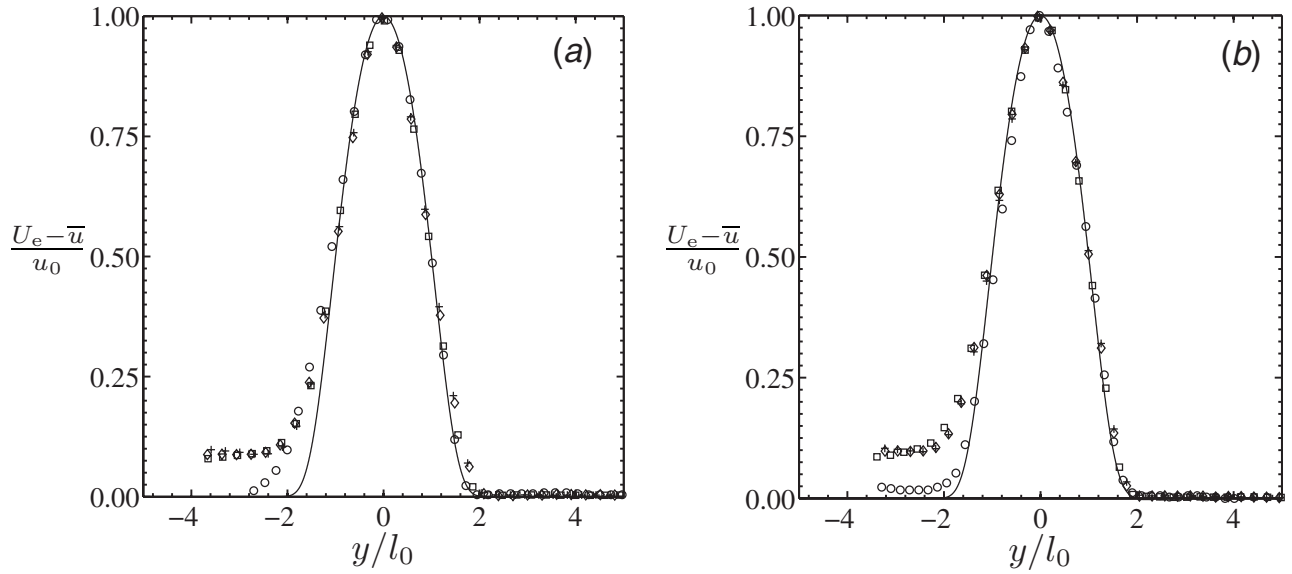

Fig. 4 Mean axial velocity profiles on the midline at x/D= (*a*) 4.5 and (*b*) 8.5 for $Re_L = 4.9\times10^5$, ○; 1.1×10^6, +; 1.4×10^6, ◇; and 1.8×10^6, □. The functions f_1, ——, f_2, - - -, and f_3, ⋯ are defined by Eqs. (1)–(3), respectively.

$$f_3(\eta) = \exp(-0.637\eta^2 - 0.056\eta^4) \tag{3}$$

have been proposed from previous studies. Function f_2 comes from the Gaussian distribution $\exp(-\alpha\eta^2)$, where $\alpha = 0.693$, from Ref. [11]. Function f_2 overestimates the mean velocity near the edge of the SUBOFF wake. Wygnanski et al. [2] made a same observation and proposed function f_3 as a better fit, although it also overestimates the mean velocity distribution near the edge of the SUBOFF wake.

At $x/D = 4.5$, the velocity deficits on the side away from the support ($y/l_0 \geq 0$) at $Re_L = 4.9\times10^5$ are somewhat lower than the values seen at the higher Reynolds numbers. This may be caused by inadequate tripping, although these effects seem to be confined to the near wake (and this Reynolds number) because by $x/D = 8.5$, the data collapse at all Reynolds numbers.

On the side of the support ($y/l_0 < 0$), the velocity profiles show the far-reaching influence of the wake generated by the support. Again, the profile at the lowest Reynolds number deviates from the other profiles, suggesting that the effects of tripping are more important on this side of the wake, but only at this Reynolds number.

Mean flow measurements were also taken in vertical planes transversely away from the midline plane (see Fig. 2). Figure 5(*a*) indicates that, as may be expected, moving away from the midline plane reduces the effect of the support, allowing the velocity to recover closely to the freestream values on the support side, and reduces the profile asymmetry. Figure 5(*b*) shows the normalized axial velocity profiles for three different offset planes. The velocity defect u_0 decreases from 39% to 20%, to 8% with respect to the velocity at the edge of the wake U_e for the offset planes $z/D = 0$, 0.125, and 0.25, correspondingly. The profiles demonstrate that the velocity distribution away from the midline plane maintains self-similarity, and function f_1 accurately describes the

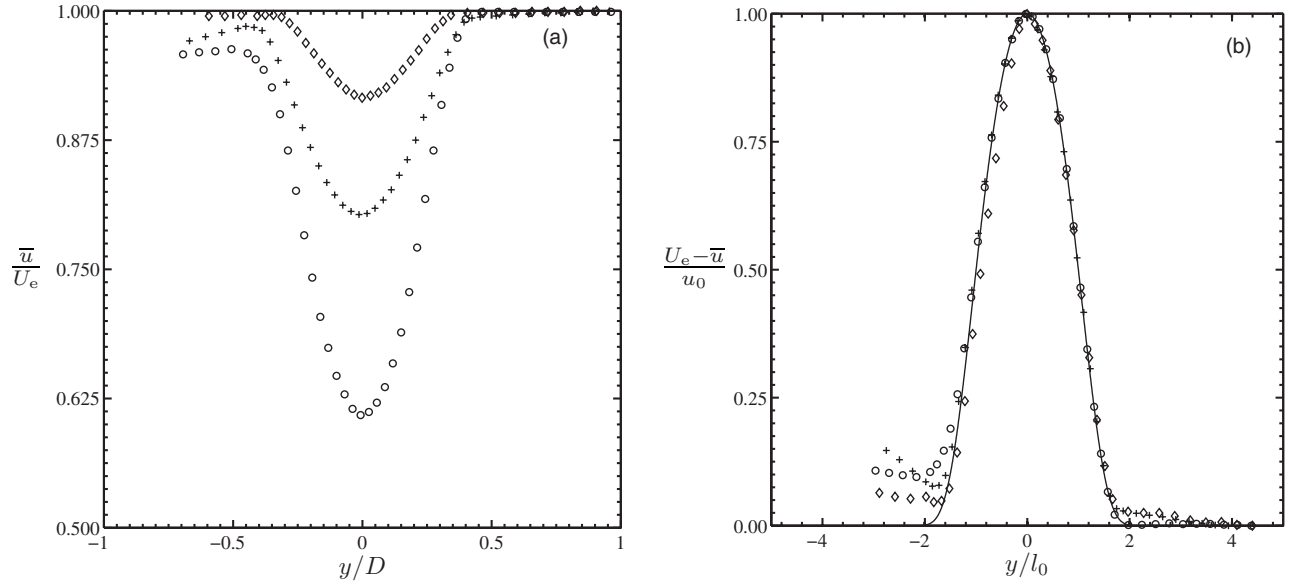

Fig. 5 Mean velocity profiles for the offset planes $z/D = 0$, ○; 0.125, +; 0.25, ◇; and f_1, ——, at $Re_L = 1.2\times10^6$ and $x/D = 6$: (*a*) normalized by U_e and D; (*b*) in similarity form

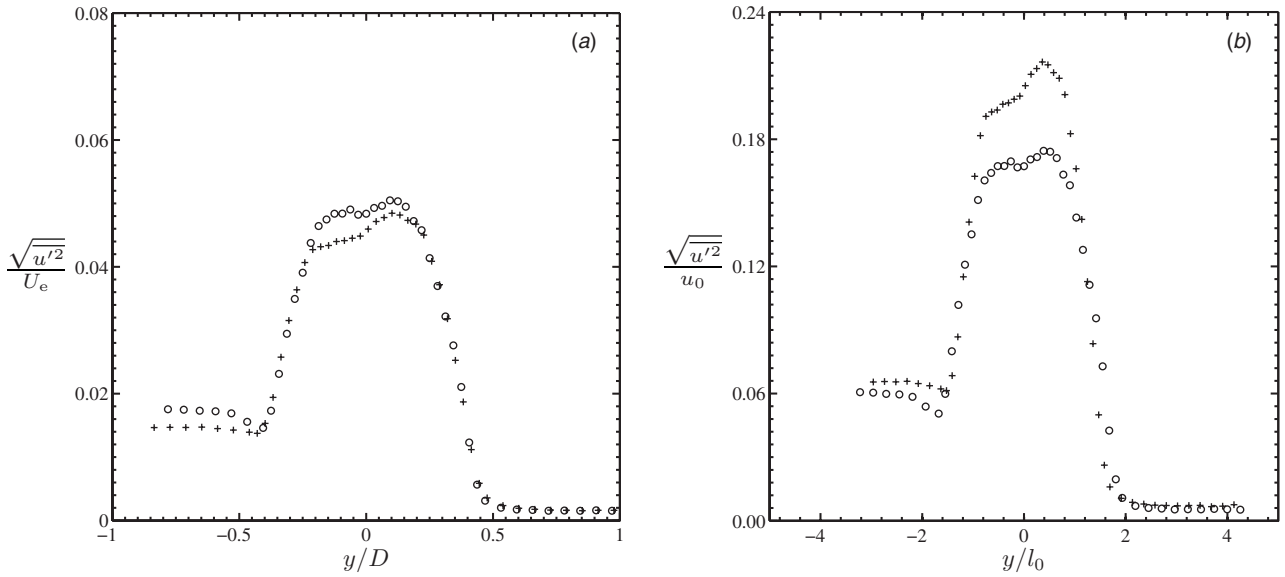

Fig. 6 Axial turbulence intensity on the midline plane at $x/D=3$, ○, and $x/D=6$, +, for $Re_L=1.0\times10^6$; no fins: (*a*) normalized by U_e and D; (*b*) in similarity form

normalized axial mean velocity profiles up to and including the furthest offset position at $z/D=0.25$. The influence of the support is seen to be diminishing but still present even at $z/D=0.25$.

With regard to the turbulence, we find, as expected from earlier studies, that the turbulence intensity is far from attaining self-similarity in the intermediate wake, as seen in Fig. 6 for the axial component. The same is true for all other turbulence distributions presented here. For $y/D<0$, the turbulence generated by the support significantly distorts the turbulence levels generated by the SUBOFF body. The influence of the support is felt even near the centerline, causing the distributions to be asymmetric. These effects are somewhat exaggerated when plotted in similarity coordinates (Fig. 6(*b*)). Despite the asymmetry, a bimodal distribution is evident near the centerline, with peaks located away from the centerline. The peaks relate to formation of the wake from the boundary layers present on the model. As the boundary layer on the model encounters the adverse pressure gradient in the stern region, it thickens, and the maximum in the turbulence intensity values moves away from the wall, as seen by Patel et al. [12] and Merz et al. [13], producing a peak away from the centerline in the wake. This bimodal shape has also been observed for circular cylinders, symmetric airfoils, flat plates, and screens [2,14]. Sato and Kuriki [11] additionally suggested that the local minimum is due to the distribution of large vortices about the centerline of the wake, and it seems likely that the high intensity peaks may be related to some form of vortex shedding.

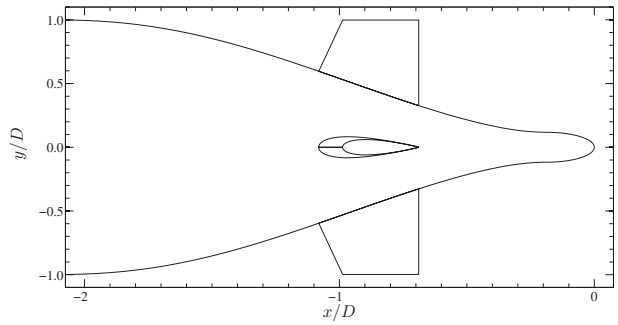

Fig. 7 Fins mounted on the stern of the SUBOFF submarine model

3.2 Flow With Fins. Four fins were installed on the stern of the submarine model to examine their influence on the wake development (Fig. 7). Two fins were aligned along the midline plane that passes through the support plane (vertical) and two fins were aligned with the centerline plane (horizontal) (see Fig. 2). The leading edge of the swept-back fins is located at $x/D=-1.075$ and $r/D=\pm0.6$, and the trailing edge extends up to $x/D=-0.7$ and $r/D=\pm0.33$.

Despite the presence of the fins, hot-wire measurements of the mean velocity show a self-similar behavior except near the outer edge of the wake near $y/l_0=2$ (Fig. 8). The tips of the fins extend physically to $r/l_0=\pm1.96$, so it appears that the source of the downstream disturbance is the tip of the fins.

Mean flow measurements were also taken in the vertical planes away from the midline plane (see Fig. 9). These results should be compared with the data obtained in the absence of the fins, as shown in Fig. 5. We see for $y/l_0>0$ that as we move away from the midline plane, the velocity in the region downstream of the tip of the top fin $y/l_0\approx2$ first undershoots the level seen on the midline, and then overshoots it. This may be caused by the tip vortex reorganizing the momentum in the wake, bringing lower momen-

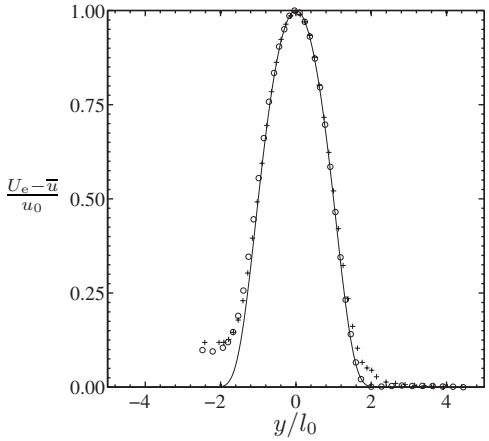

Fig. 8 Effects of fins on the mean velocity profile at $x/D=6$ for $Re_L=1.2\times10^6$: without fins, ○; with fins, +; and f_1, ——

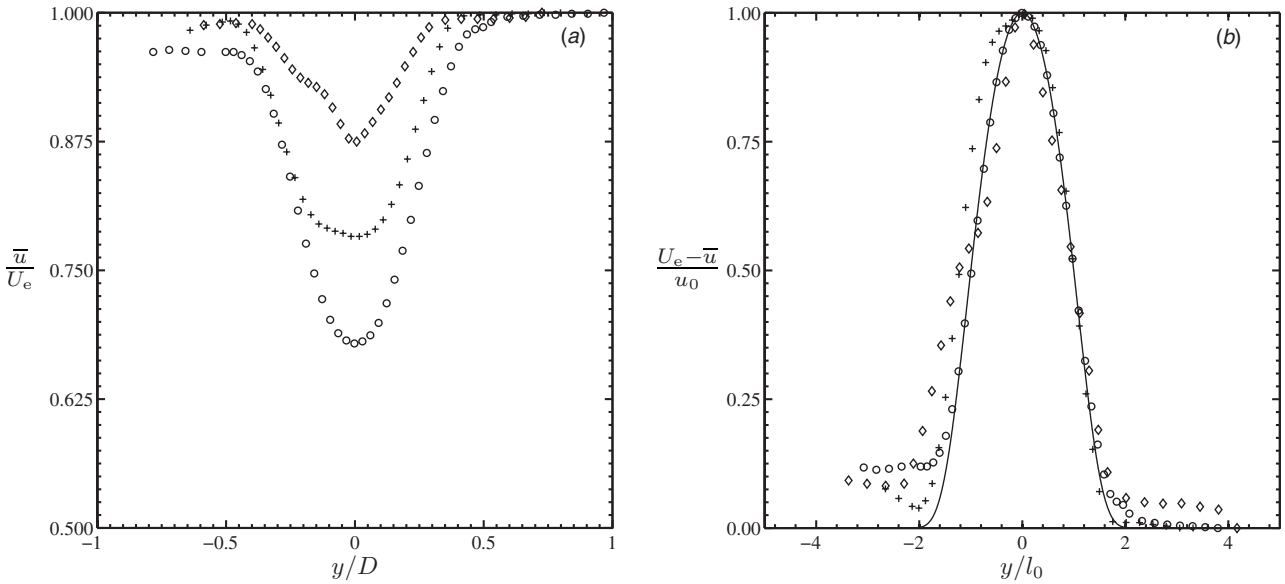

Fig. 9 Effects of fins on the mean velocity profiles at $x/D=6$ and $Re_L=1.2\times10^6$ for offset planes $z/D=0$, ○; 0.125, +; 0.25, ◇; and f_1, ——: (*a*) normalized by U_e and D; (*b*) in similarity form

tum fluid from the central part of the body wake to the edge of the wake, and higher momentum fluid from the edge of the wake closer to the centerline. In addition, it is possible that the mean quantities in the intermediate wake of an axisymmetric body with appendages may become self-similar with different scales than those for an axisymmetric body with no appendages. For the side where the support is located $y/l_0<0$, the flow field produced by the main body, the fins, and the support interact in a very significant way, where the greater the offset from the midline plane, the greater the effect of the fins, but there is no obvious explanation for the mechanism.

As to the axial component of turbulence, in the absence of fins, the influence of the support decreases away from the midline, as seen in Fig. 10(*a*), and the profiles become more symmetric. The addition of fins results in a bimodal distribution persisting for all offset planes, as shown in Fig. 10(*b*). The addition of fins also increases the maximum intensity by about 10%, which is likely the result of streamwise vorticity production in the fin/body junction and at the fin tips. The increase in turbulence intensity is particularly noticeable on the support side.

The normal turbulence intensity distributions are shown in Fig. 11. In the absence of fins, the distributions display similar trends to those seen in the axial intensity profiles, although the peaks are about half of the magnitude of the axial intensities. The normal turbulence intensity for the midline plane shows a mildly asymmetric bimodal distribution, while the other two offset planes are more symmetric, with the exception of higher turbulence levels in the wake of the support. With the addition of fins (Fig. 11(*b*)), the normal intensity distribution on the midline plane becomes strongly bimodal, while the distribution at $z/D=0.125$ becomes significantly more asymmetric, and the peak intensity at $z/D=0.25$ increases by about 30%. For each of the profiles, the addition of fins results in a normal turbulence intensity increase along

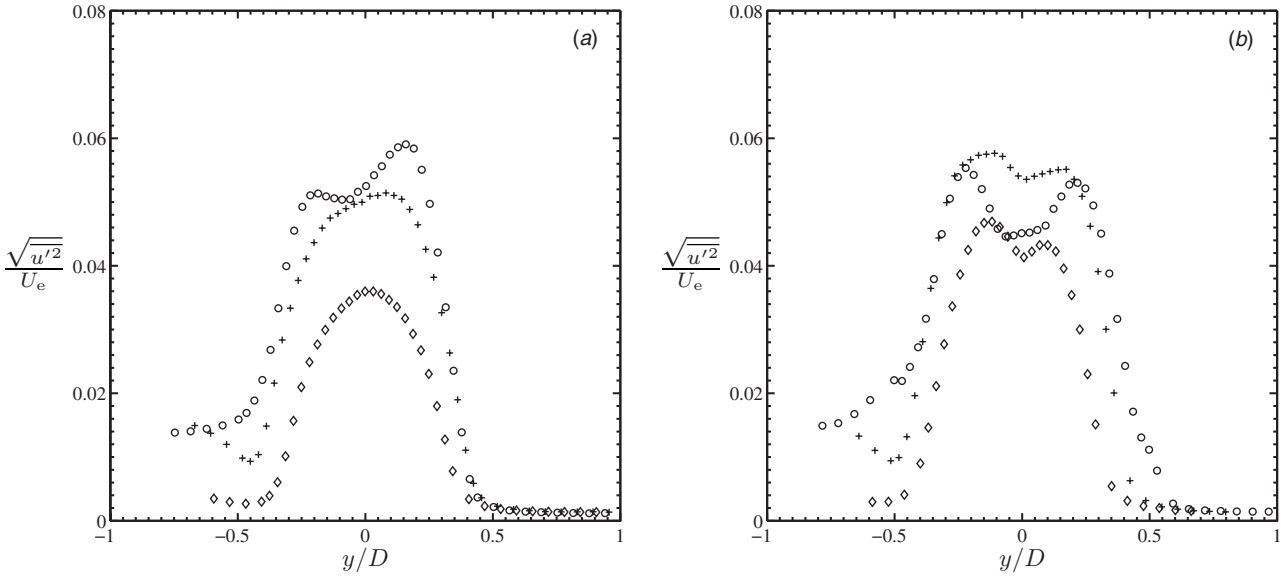

Fig. 10 Axial turbulence intensity at $x/D=6$, for offset planes $z/D=0$, ○; 0.125, +; and 0.25, ◇: (*a*) without fins and (*b*) with fins

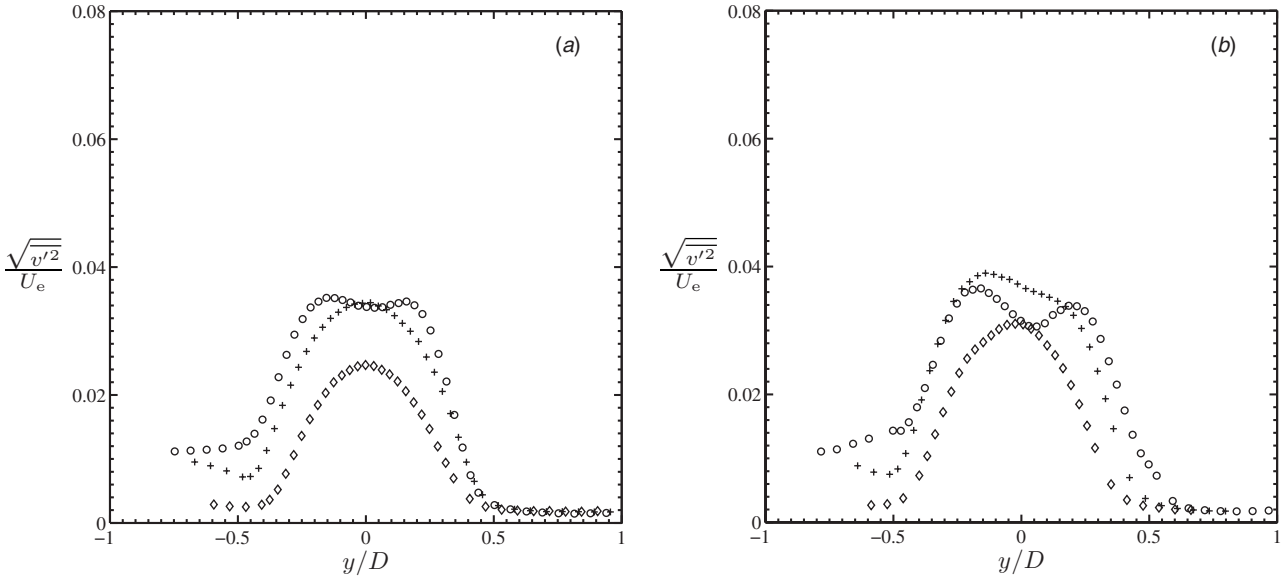

Fig. 11 Normal turbulence intensity at $x/D=6$, for offset planes $z/D=0$, ○; 0.125, +; and 0.25, ◇: (*a*) without fins and (*b*) with fins

the centerline ($y/D=0$) except for the distribution along the midline plane. Similarly, boundary layer measurements have shown that the addition of fins yields lower normal turbulence intensity values along the midline plane and significant increases on the offset planes with the effect being small beyond $r/D=0.25$ [6]. This suggests that the initial conditions persist in the intermediate wake.

The shear stress distributions are shown in Fig. 12. On the midline plane ($z/D=0$), in the absence of fins (Fig. 12(*a*)), the peak stress on the side away from the support is almost 50% higher than on the side with the support, attesting to the destructive interference due to the wake of the support where the dominant shear stress is in a plane normal to the midline plane of the body. When the midline plane shear stress distribution is plotted using similarity coordinates (data not shown), the distributions have not attained self-similarity, although in previous results, it was observed that turbulent shear attains self-preservation more rapidly than the axial turbulent intensity distribution [2].

Along the midline plane, the addition of fins strengthens the shear stress on the support side, while somewhat diminishing it on the other side, resulting in a more symmetric profile (see Fig. 12(*b*)). Away from the midline plane, the profiles without fins show a decreasing level of asymmetry (see Fig. 12(*a*)), while the location of zero shear moves slightly below the body centerline. Adding fins significantly changes the shear stress distributions in the offset planes (compare Figs. 12(*a*) and 12(*b*)), introducing local peaks, as may be expected from the presence of necklace vortices trailing from the base of the fins. Along the midline plane on the side away from the support, the addition of fins yields lower shear stress values with increases for the offset planes. This trend was reported by Huang et al. [6] in the boundary layer at $x/D=-0.19$, where the addition of fins results in shear stress intensity decreases in the midline plane below the values seen in the

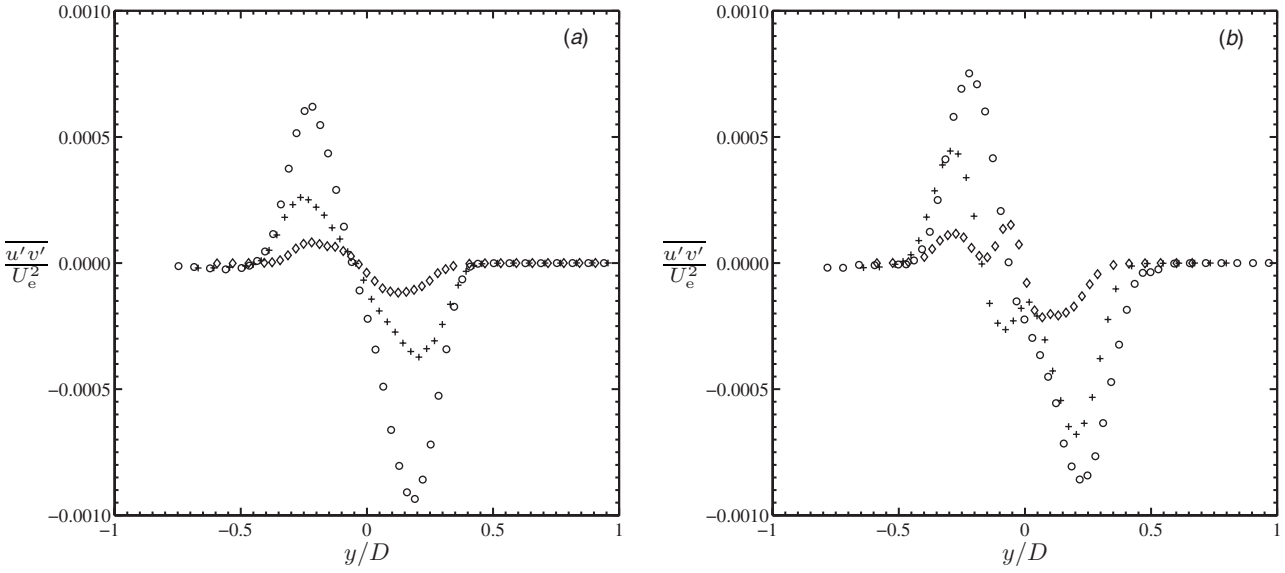

Fig. 12 Turbulent shear stress at $x/D=6$, for offset planes $z/D=0$, ○; 0.125, +; and 0.25, ◇: (*a*) without fins and (*b*) with fins

no-fin case and increases above the no-fin case for the offset planes, emphasizing the importance of initial conditions.

4 Conclusion

Measurements were conducted to gain a better understanding of the evolution of the intermediate wake of a SUBOFF submarine model in the presence of a support formed by a semi-infinite extension of the sail, with and without fins. The mean wake velocity profile for the side without the support attains self-similarity between $x/D \approx 4.5$ and 8.5, and is described accurately by the exponential function f_1 given by Eq. (1). The turbulent intensity distributions do not approach self-similarity within the range of measurements. The presence of the support affects the wake by weakening the shear layer below the centerline, reducing the turbulence intensities and shear stress levels.

The addition of fins increases the turbulence intensity levels and reduces the mean velocity in regions that lie directly downstream of the tips of the fins, indicating the important effects of the fin geometry on the wake evolution. The velocity defect decreased with offset distance from the midline plane, while the mean velocity profiles, when scaled by the similarity variables, were accurately described by the same exponential curve that described the profiles on the midline plane. In addition, the shear stress distributions in the offset planes showed clear evidence of necklace vortices generated near the base of the fins persisting in the intermediate wake.

Acknowledgment

This work was made possible by ONR under Grant Nos. N00014-07-1-0111 and N00014-09-1-0263.

Nomenclature

D = maximum diameter of submarine model
L = overall length of submarine model
l_0 = half-wake width
r = radial coordinate, $r^2 = y^2 + z^2$
Re_L = Reynolds number based on length of model
u = axial (streamwise) velocity component
u' = axial (streamwise) fluctuation velocity
$u'v'$ = turbulent shear stress
U_e = velocity at the edge of the wake
U_∞ = freestream velocity upstream of the model
u_0 = wake velocity deficit
v = normal (vertical) velocity component
v' = normal (vertical) fluctuation velocity
x = axial (streamwise) coordinate
y = normal (vertical) coordinate
z = transverse (spanwise) coordinate
ω_z = spanwise vorticity

References

[1] Townsend, A. A., 1956, *The Structure of Turbulent Shear Flow*, Cambridge University Press, Cambridge, England.
[2] Wygnanski, I., Champagne, F., and Marasli, B., 1986, "On the Large Scale Structures in Two Dimensional, Small Deficit Turbulent Wakes," J. Fluid Mech., **168**, pp. 31–71.
[3] Johansson, P. B. V., and George, W. K., 2006, "The Far Downstream Evolution of the High-Reynolds-Number Axisymmetric Wake Behind a Disk. Part 1. Single-Point Statistics," J. Fluid Mech., **555**, pp. 363–385.
[4] Chevray, R., 1968, "The Turbulent Wake of a Body of Revolution," ASME J. Basic Eng., **90**, pp. 275–284.
[5] Sirviente, A. I., and Patel, V. C., 1999, "Experiments in the Turbulent Near Wake of an Axisymmetric Body," AIAA J., **37**(12), pp. 1670–1673.
[6] Huang, T., Liu, H. L., Groves, N., Forlini, T., Blanton, J., and Gowing, S., 1992, "Measurements of Flows Over an Axisymmetric Body With Various Appendages in a Wind Tunnel: The DARPA Suboff Experimental Program," *Proceedings of the 19th Symposium on Naval Hydrodynamics*, Seoul, Korea.
[7] Simpson, R. L., 2001, "Junction Flows," Annu. Rev. Fluid Mech., **33**, pp. 415–443.
[8] Groves, N. C., Huang, T. T., and Chang, M. S., 1989, "Geometric Characteristics of DARPA SUBOFF Models," David Taylor Research Center, Bethesda, MD, Technical Report No. DTRC/SHD-1298-01.
[9] Jiménez, J. M., 2007, "High Reynolds Number Flows About Bodies of Revolution With Application to Submarines and Torpedoes," Ph.D. thesis, Princeton University, Princeton, NJ.
[10] Reynolds, R., 2003, "An Experimental Study of Axisymmetric Wakes (With Application to Submarines)," MS thesis, Princeton University, Princeton, NJ.
[11] Sato, H., and Kuriki, K., 1961, "The Mechanism of Transition in the Wake of a Thin Flat Plate Placed Parallel to a Uniform Flow," J. Fluid Mech., **11**, pp. 321–352.
[12] Patel, V. C., Nakayama, A., and Damian, R., 1974, "Measurements in the Thick Axisymmetric Turbulent Boundary Layer Near the Tail of a Body of Revolution," J. Fluid Mech., **63**, pp. 345–367.
[13] Merz, R. A., Yi, C. H., and Przirembel, C. E. G., 1986, "Turbulence Intensities in the Near-Wake of a Semielliptical Afterbody," AIAA J., **24**, pp. 2038–2040.
[14] Ramaprian, B. R., and Patel, V. C., 1982, "The Symmetric Turbulent Wake of a Flat Plate," AIAA J., **20**, pp. 1228–1235.

Flow Force Analysis of a Variable Force Solenoid Valve for Automatic Transmissions

Gee Soo Lee

Hyung Jin Sung[1]
e-mail: hjsung@kaist.ac.kr

Department of Mechanical Engineering,
KAIST,
373-1 Guseong-dong, Yuseong-gu,
Daejeon 305-701, Korea

Hyun Chul Kim
KATECH,
74 Yongjung-Ri, Pungse-Myun, Chonan-Si,
Chungnam 330-912, Korea

Hyun Woo Lee
UNICK,
10-1 Jukgok-Ri, Jhinyoung-Eub, Gimhae-Si,
Kyungnam 621-801, Korea

Three-dimensional numerical simulations were carried out to investigate the flow dynamic behavior and pressure characteristics of a variable force solenoid (VFS) valve used in automatic transmissions. To visualize the dynamic movement of the spool, a moving mesh with dynamic layering meshes for varying boundary conditions was employed. Relevant experiment was performed to validate the simulations. The VFS valve was characterized by determining the variation in the equivalent orifice area with the spool displacement. The pressure sensitivity was found to be precisely controlled by the relation between the depth and the area of the notch in the range of the characteristic length of the valve. The results of model C, which takes into account both seal leakage and notches, indicate that there are linear pressure sensitivities in the range of the valve overlap and that there are smooth pressure control characteristics in the range of the two notches. The VFS valve with a spool was shown to have an unavoidable and unique hysteresis, which is caused by the nonlinear electromagnetic forces at the end of strokes of the spool and by the friction forces in the valve overlap. The effects of varying the oil temperature on the pressure sensitivity curves and the seal leakage flow rates were also examined. [DOI: 10.1115/1.4001070]

Keywords: automatic transmission modeling, variable force solenoid valve

1 Introduction

A variable force solenoid (VFS) valve is an electrohydraulic valve that controls pressure in proportion (or inversely proportion) to a signal from the transmission control unit of a power train. The demand in the field of automatic transmissions for variable line-pressure control techniques has recently increased. Since VFS valves with a high carrier frequency (normally 200 Hz) driven by pulse width modulation are free of ripple pressure, they are widely used in automatic transmissions despite their high cost. Moreover, the use of VFS valves can simplify hydraulic control systems because clutches can then be controlled without a pressure control valve [1]. It is thus important to investigate the flow dynamic behaviors and pressure response characteristics of VFS valves. The pressure sensitivity curve does not exactly match the spool motional direction, i.e., "forward (on)" or "backward (off)," as shown in Fig. 1. Since three-dimensional numerical flow analysis can provide insight into fluid dynamic behavior that cannot be obtained experimentally, it is a powerful tool for the design and optimization of hydraulic VFS valves.

Numerous attempts have been made to analyze the flow forces in hydraulic valves and to improve their response characteristics. A theoretical approach was used in an attempt to predict the fluid dynamic behaviors of hydraulic valves [1–3]. Davis and Stewart performed two-dimensional numerical simulations for predicting the globe control valve performance [4] and experiments for verifying the axisymmetric numerical model of the control valve [5]. Krishnaswamy and Li found that unstable valves had faster responses than their stable counterparts when the stroking force was limited [6]. Yuan and Li investigated the effects on the steady flow force of various material properties, such as the fluid viscosity and the momentum flux at the nonmetering surface [7]. However, the numerical studies cited above were limited to hydraulic valves, which have geometries that are relatively axisymmetric and simple. Since the spools of VFS valves have geometrically circumferential notches, their flows are comparatively complicated and fully three dimensional. Amirante et al. performed three-dimensional numerical simulations and experimental analyses of a closed center directional control valve [8,9] and of a proportional control valve [10]. To ensure the reliability of these numerical simulations [8], the variation in the calculated flow rate with the spool stroke was compared with experimental data [9]. Furthermore, the effects of notch shape on the flow force were scrutinized. As a result, they were able to minimize the flow force of the spool for a compensated spool notch [10]. More recently, Valdes et al. [11] developed a reduced-order model for estimating the fluid flow and flow force of a hydraulic proportional valve for use in antilock braking systems. That model can be used to estimate quickly the stationary flow rate and the flow force. Guillermo et al. [12] performed three-dimensional numerical simulations inside a control valve and discussed the effect of the piston shapes on the hydraulic behavior and the cavitation inception. Most previous studies, however, have dealt with hydraulic steady flow forces and overall performance of valves. There have been few studies of the pressure response characteristics that are important to the robust feedback control of VFS valves by using spool dynamic analysis.

The main objectives of the present study were to investigate the flow dynamic behavior of a VFS valve used in automatic transmissions and to analyze its pressure response characteristics and seal leakage flow rates. Three-dimensional numerical simulations were carried out in order to obtain the flow fields in the spool valve; in particular, a commercial computational fluid dynamics (CFD) program, FLUENT 6.3, was used to simulate the dynamic movements of the spool. Moving meshes with dynamic layering meshes for varying boundary conditions were employed. In our physical modeling of the VFS valve, we accounted for the motional direction of the spool, the notch depth in the advance/delay components, and the oil temperature of the working fluid. The pressure response characteristics and seal leakage flow rates were determined from these simulations. The effects of varying the oil

[1]Corresponding author.

Contributed by the Fluids Engineering Division of ASME for publication in the JOURNAL OF FLUIDS ENGINEERING. Manuscript received December 11, 2008; final manuscript revised January 19, 2010; published online March 17, 2010. Assoc. Editor: Paul Durbin.

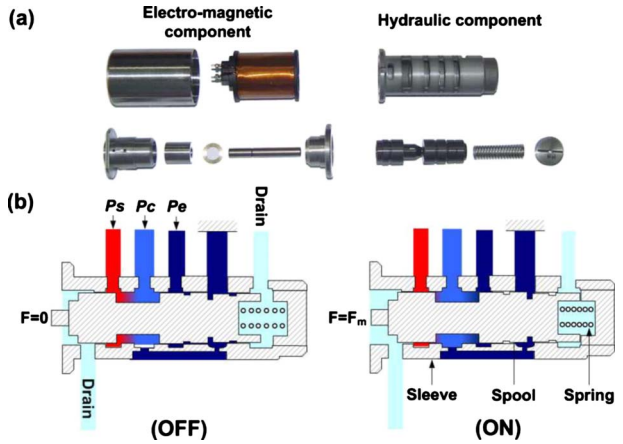

Fig. 1 A variable force solenoid valve of an automatic transmission: (*a*) disassembly and (*b*) hydraulic component

temperature were also examined. Relevant experiments were carried out to validate the simulations.

2 Problem Formulation

2.1 Variable Force Solenoid Valve. Figure 1 shows a cross section of a VFS valve typical of those used in automatic transmissions. The VFS valve is composed of hydraulic and electromagnetic components. The hydraulic components consist of a spool, a sleeve, and a spring. When no electric current is supplied to the VFS valve, the electromagnetic force is zero and the spool is located at the left end (Fig. 1(*a*)). When an electric current is present, the spool moves to the location where the spring and electromagnetic forces are balanced. As shown in Fig. 1(*b*), the VFS valve has a total of six ports, and the controllable pressure change is obtained by moving the spool between the supply port and the exhaust port. Figure 2 shows the computational domain for the VFS valve that was used in our numerical simulations. A numerical simulation of the whole valve would require a very large computational grid system and excessive computing time. In addition, the important dynamic flow behavior occurs near the three supply, control, and exhaust ports relating to spool displacement [8–10]. The computational domain and values of the design parameters are shown in detail in Fig. 2(*b*) and Table 1, respectively.

2.2 Numerical Method. The governing equation for the hydraulic flow inside the VFS valve is the incompressible Navier–Stokes equation. For the dynamic moving meshes, the integral formulation of the conservation equation for a general scalar variable ϕ in an arbitrary control volume V with boundaries that move can be written in the following form:

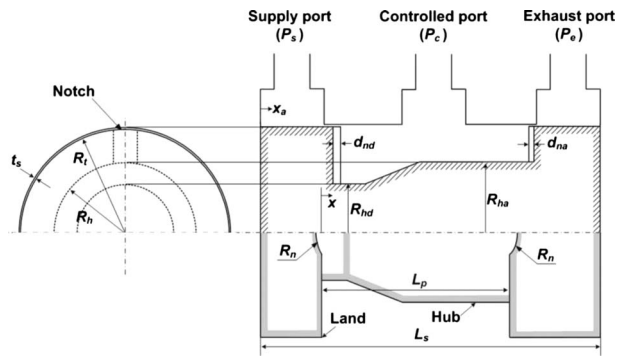

Fig. 2 Computational domain of the VFS valve

Table 1 Values of the design parameters of the VFS valve

No.	Parameter	Unit	Value
1	L_s	mm	19.8
2	L_c	mm	12.0
3	L_c-L_p	mm	0.8
4	R_{ha}	mm	3.85
5	R_{ha}	mm	2.32
6	R_t	mm	6.5
7	R_n	mm	4.0
8	d_{nd}	mm	0.4
9	d_{na}	mm	0.2
10	N_n	ea	2
11	t_s	mm	0.02

$$\frac{d}{dt}\int_V \rho\phi dV + \oint_{\partial V} \rho\phi(\vec{u}-\vec{u}_g)\cdot dA = \oint_{\partial V} \Gamma \nabla \phi \cdot d\vec{A} \tag{1}$$

where ρ, $\vec{u}$, $\vec{u}_g$, and Γ are the density of the working fluid, the velocity of flow, the velocity of the moving mesh, and the diffusion coefficient, respectively. By using the first-order backward difference formula, the time derivative term in Eq. (1) can be expressed as

$$\frac{d}{dV}\int_V \rho\phi dV = \frac{(\rho\phi V)^{n+1}-(\rho\phi V)^n}{\Delta t} \tag{2}$$

where n and $n+1$ denote the values at the current and next time levels, respectively. The control volume V^{n+1} at the next time level can be calculated with

$$V^{n+1} = V^n + \frac{dV}{dt}\Delta t$$
$$\frac{dV}{dt} = \oint_{\partial V} \boldsymbol{u}_g \cdot dA = \sum_j^{n_f} \boldsymbol{u}_{g,j}\cdot \boldsymbol{A}_j \tag{3}$$

where n_f is the number of faces on the control volume and $\boldsymbol{A}_j$ is the area vector at surface j. The dot product of $\boldsymbol{u}_{g,j}\cdot\boldsymbol{A}_j$ for the control volume is given by

$$\boldsymbol{u}_{g,j}\cdot\boldsymbol{A}_j = \frac{\delta V_j}{\Delta t} \tag{4}$$

here, δV_j is the volume swept by the control volume face j during the time step Δt.

Figure 3 shows the computational grid system for the VFS valve. The computational domain consists of two regions, a sta-

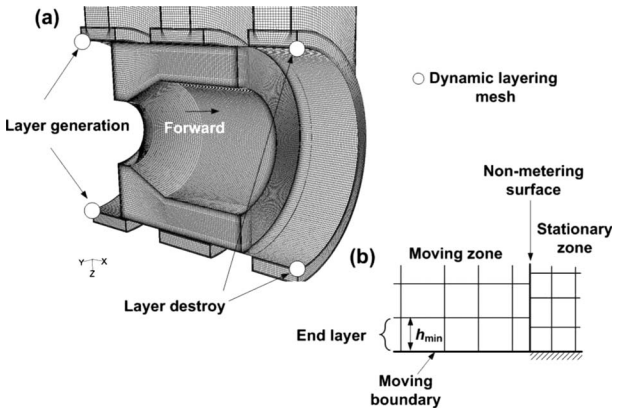

Fig. 3 Computational grids of the VFS valve: (*a*) overall mesh and (*b*) dynamic layering mesh

Table 2 Boundary conditions of simulation at oil temperature 85°C

No.	Parameter	Unit	Value
1	P_s	Pa	2,026,500
2	P_e	Pa	101,325
3	V_s	mm/s	1.8
4	ρ	kg/m^3	826.55
5	μ	kg/m s	0.0082655
6	x_{max}	mm	1.2

tionary zone and a moving zone. These two zones are connected at the nonmetering surface. Dynamic layering that adds or removes cell layers adjacent to moving boundaries is applied at the end layers indicated in Fig. 3(*a*). When the end layers are compressed or expanded according to the spool motional direction, as shown in Fig. 3(*b*), the cells in layer j are also compressed or expanded until the following equations are satisfied:

$$h_{min} > (1 + \alpha_s)h_{ideal} \quad \text{for layer generation for expansion} \tag{5}$$

$$h_{min} > \alpha_c h_{ideal} \quad \text{for layer destroyed for compression} \tag{6}$$

where h_{min}, h_{ideal}, α_c, and α_s are the minimum cell height, the ideal cell height, the layer split factor, and the layer collapse factor, respectively. Further details of the computational algorithm and implementation are provided in Ref. [14].

Table 2 summarizes the boundary conditions and working fluid properties used in the numerical simulations. The supplied and exhaust pressures were 20.0 bars and 1.0 bar, respectively. The initial pressure condition inside the valve was set at the same value as the exhaust pressure (1.0 bar). The spool speeds for "forward" and "backward" were set at 1.8 mm/s. The maximum displacement of the spool was designed by 1.8 mm. The properties of the automatic transmission fluid were set at values for the normal operation temperature in hydraulic systems (T=85°C). The flow inside the VFS valve can be regarded as laminar. The governing equation of Eq. (1) was discretized with the finite volume method and pressure-velocity coupling was implemented by using the SIMPLEC algorithm [13]. A second-order scheme was adopted to calculate the fluxes at the cell interface, and a first-order implicit scheme was employed for the time derivative term [14].

2.3 Experimental Apparatus and Testing Procedure. A schematic diagram of the experimental apparatus are shown in Fig. 4. It is comprised of a VFS valve control driver, a hydraulic power unit, and a data acquisition system. To enhance a control performance of the VFS valve, the control driver with 300 Hz carrier frequency and current feedback algorithm were used. The hydraulic power unit consisting of 1.5 kW positive displacement pump and 50 l reservoir tank can provide 20.0 l/min of oil at 20 bars. The oil temperature was controlled by 10.0 kW electrical heater and 0.2 kW cooling pump with a fan. The commercial transmission oil (AFT SP-II) was used in this test stand. The seal leakage flow rate was measured by a gear type flow meter (Hydrotechnik, GFM-30). The pressure was measured by two pressure sensors (Sensor-technik, A09-30) both inward and outward ports of the VFS valve. The spool displacements were measured by a laser displacement sensor (Mikroelectronik, M7L-20) and a minirod attached to the top of the spool, as shown in Fig. 4. The digital oscilloscope (Yokogawa, DLM-2024) was used for the data acquisition and the sampling rate was set as 2.5 kHz. The Fast Fourier Transform (FFT) filter smoothing was accomplished by removing the Fourier components with frequencies higher than a cutoff frequency:

$$f_{cutoff} = \frac{1}{n\Delta t} \tag{7}$$

where the number of data point considered at a time is n=5 and the time spacing between two adjacent data points is $\Delta t = 4.0 \times 10^{-4}$ s. The test procedures were conducted by both static and dynamic performance tests. The spool sweep frequency was set as 1.0 Hz for the static performance test, i.e., it takes 1.0 s for the spool to move to the end for a one-way direction. The dynamic time response of the VFS valve was measured with stepwise control current duties (1.2 A) during on (from 0 A to 1.2 A) and off (from 1.2 A to 0 A) operations.

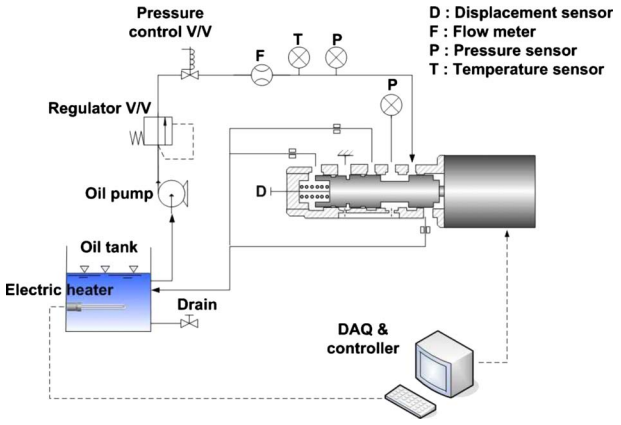

Fig. 4 Schematic diagram of the experimental setup

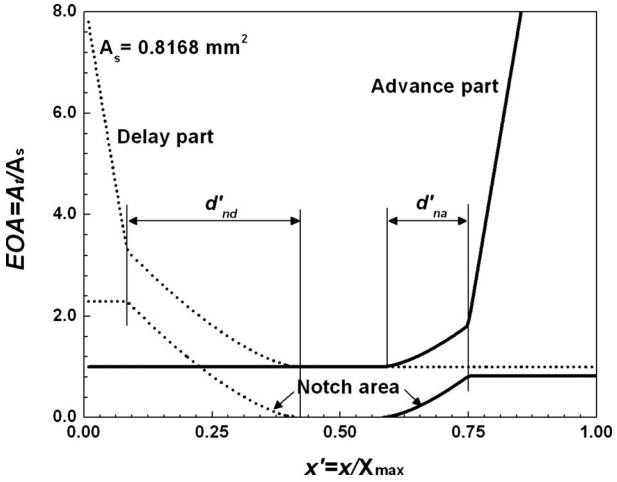

Fig. 5 Variation of the *EOA* with spool displacement

3 Results and Discussion

3.1 Physical Modeling of the VFS Valve. Figure 5 shows the variation in the equivalent orifice area (*EOA*) with the spool displacement. The equivalent orifice area is the ratio of the total area (A_t) to the leakage area (or the radial clearance area) (A_s), i.e., $EOA = A_t/A_s$, and is one of the most important parameters for valve behavior analysis. In general, spool type valves such as VFS valves are characterized by the variation in the *EOA* with the spool displacement. The *EOA* of the delay component of the spool (the dotted line in Fig. 5) falls rapidly as the spool moves from its initial position ($x'=0$). Beyond a certain displacement ($x'=0.083$), the *EOA* decreases slowly to a constant value of the leakage area until the delay component is entirely closed ($x'=0.416$). At the same time, the *EOA* of the advance component of the spool (the thick solid line in Fig. 5) increases gradually once this component starts to open ($x'=0.565$) until the advance com-

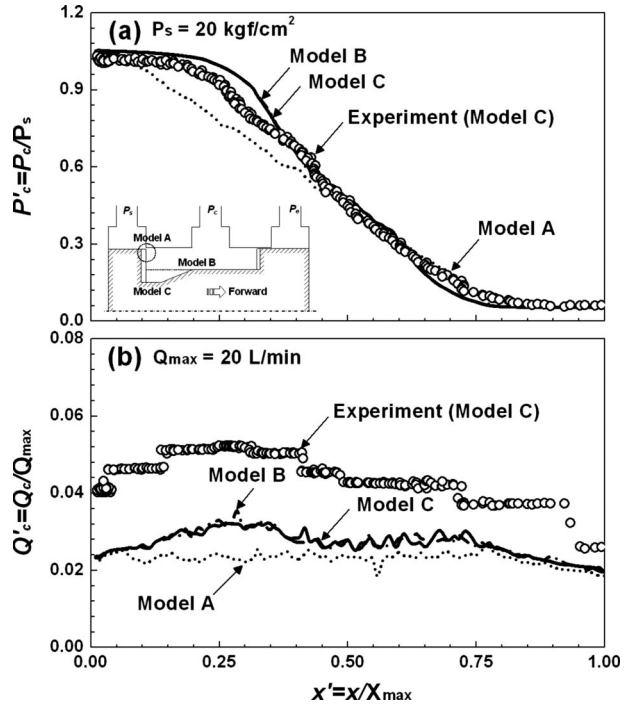

Fig. 6 Effects of varying physical model approach: (*a*) on the pressure sensitivities and (*b*) on the leakage flow rates

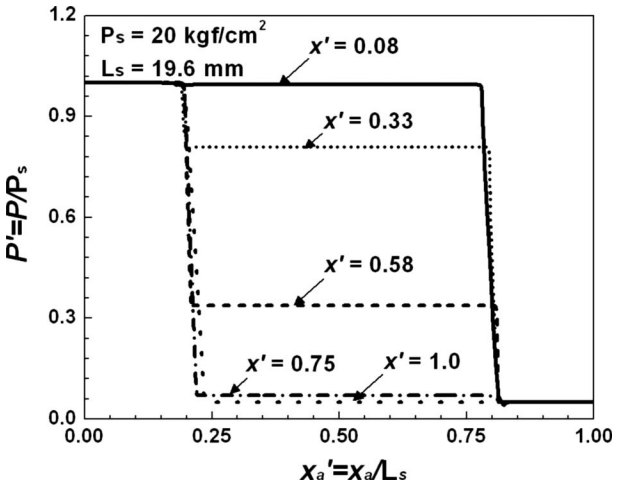

Fig. 7 Static pressure distributions along the seal leakage centerline for model C at 85°C

ponent is completely open ($x'=0.75$). The characteristic length (ΔL) is defined as the difference between the port-to-port and land-to-land distances ($\Delta L=0.8$ mm), which determines the range of controllable spool displacement with respect to the pressure sensitivity. The spool has two kinds of notches with diameters $R_n=4.0$ mm, and the depths of the advance and delay components are 0.2 mm and 0.4 mm, respectively. The *EOA* is constant in the range of valve overlap ($x'=0.416-0.565$), where the effect of viscous force is dominant. The major role of the notches is to enhance the control and durability of the valve, and, in particular, to prevent abrupt changes in the *EOA* and thus reduce the ripple pressure and the settling time in its dynamic performance. In general, the shapes of these notches are circular. As can be seen in Fig. 5, the pressure sensitivity can be precisely controlled according to the relation between the depth and the area of the notch in the range of the characteristic length with regard to the *EOA*.

Figure 6 shows the variation in the pressure sensitivity curves and the seal leakage flow rates with the spool displacement obtained from the physical modeling of the VFS valve. Three physical models were considered in the present study and are summarized in Table 3. Model A is the simplest model, in that it only accounts for a seal leakage. Model B treats case with a notch and leakage. With the increase in the spool stroke in an electrohydraulic valve, the magnetic field and magnetic force inevitably decrease [2]. The final model, model C, has notches and pressure-compensated hub profiles for nonlinear electromagnetic forces with spool strokes. As the spool in model A starts to move in a forward motion, the controlled pressure remains at the supplied pressure ($P_c'=1.0$) because the control port is already open to the supplied port. The controlled pressure decreases at $x'=0.083$, at which the delay component of the spool starts to overlap. The controlled pressure decreases linearly in model A in the range of valve overlap ($x'=0.083-0.75$). The controlled pressure becomes to be the exhaust pressure. The seal leakage flow is the dominant factor affecting spool valve behavior and the associated pressure sensitivity curve [2]. Model B exhibits a linear pressure response that is similar to that of model A. Model B includes notches, which prevent sudden changes in the *EOA*. The notch delays the controlled pressure drop near the delay component and moves the arrival point of the exhaust pressure ($P_c'=0.05$) to near the advance component (forward), as shown in Fig. 6(*a*). Thus the control of pressure in model B is smoother than in model A, which does not contain notches.

Table 3 Physical modeling of the VFS valve

No.	Parameter	Modeling
1	Model A	Model with a seal leakage
2	Model B	Model with a notch and a seal leakage
3	Model C	Model B with pressure-compensated hub profile

The unbalanced hydraulic force by area discrepancy in the spool of model C reacts against the electromagnetic force, which compensates for the nonlinear electromagnetic force characteristics during spool strokes. The spool shape of model C affects the location at which the spring and electromagnetic forces are balanced. Because we did not consider electromagnetic force in the numerical simulations, there is no effect on the pressure sensitivity curves and seal leakage flow rates at the same spool displacement. In the case of model A, the seal leakage flow rate increases slowly and remains almost unchanged in the range of valve overlap, for which the *EOA* is constant. Beyond this range, the leakage flow rate decreases again because the spool lands start to overlap at the delay component of the spool. In particular, in models B and C, the seal leakage flow is maximum at the center of the delay notch ($x'=0.25$). The seal leakage flow rate characteristics of model C are similar to those of model B. Note that in hydraulic control systems the leakage flow critically affects hydraulic power losses and is determined by the design parameters. In the present study, the maximum allowable flow rate (Q_c') was 0.035 at the normal operation temperature. The experimental data such as the pressure, the seal leakage flow rate, and the control current duty based on time were converted to those with the spool displacement to compare with numerical simulations (model C). At the normal operation temperature ($T=85°C$), the seal leakage flow rates of experimental data are higher than those of numerical simulations. This may be attributed to the fact that the seal leakage flow phenomena through the both moving boundaries of the spool were not considered in the present study, as shown in Fig. 3(*b*). Nevertheless, the numerical simulations are in qualitatively good agreement with the experimental results.

Figure 7 shows the variation for model C in the static pressure (P') along the centerline of radial clearance with respect to sleeve

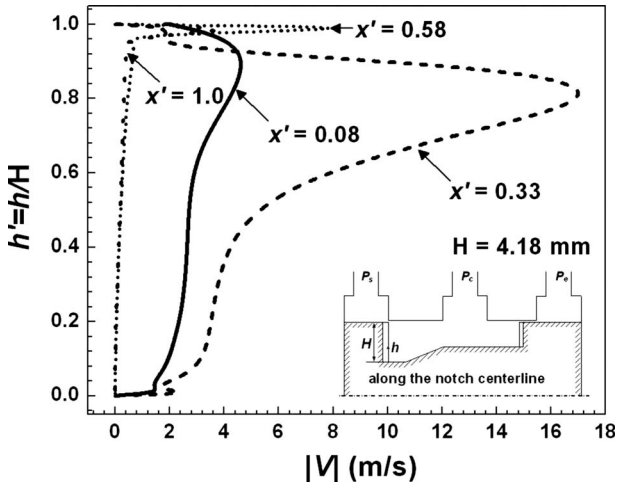

Fig. 8 Velocity profiles along the notch centerline for model C at 85°C

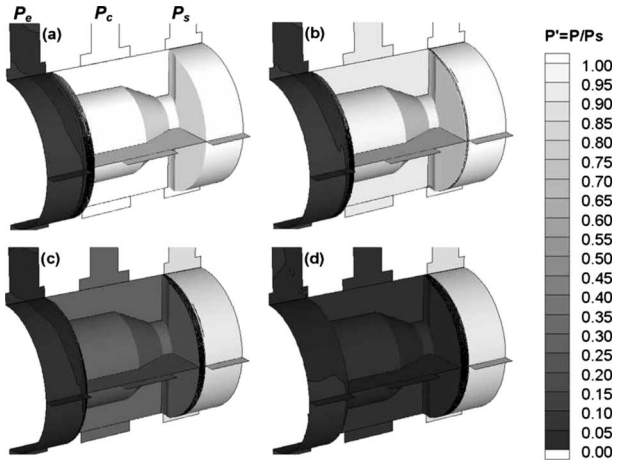

Fig. 10 Static pressure contours on the spool wall and the mid section for Model C at 85°C; (*a*) $x'=0.08$, (*b*) $x'=0.33$, (*c*) $x'=0.58$, and (*d*) $x'=0.75$

location (x'_a). Since pressure drops occur mainly at the valve orifices ($x'_a \approx 0.2$ and 0.8), steep variations of pressure are observed at these two locations. Once the spool moves in a forward direction, the static pressure distributions become step functions and then gradually decrease. At $x'_a=0.82$, the static pressure reaches an equilibrium state ($P'=0.05$), i.e., the exhaust pressure. In Fig. 8, the relative velocity magnitude ($|V|=\sqrt{u^2+v^2+w^2}$) of model C along the notch centerline (h'), which is the line from the hub to the land at the delay component of the spool. Jet flow or leakage flow that is proportional to the pressure difference results from the radial clearance. The velocity magnitude and the flow inclination smoothly increase with the spool displacement (x'), due to the increase in the leakage flow. The velocity magnitude then reaches a peak near the middle of the delay notch ($x'=0.33$), where the seal leakage flow is the largest according to Fig. 6(*b*). Beyond the end of the advance notch, the velocity magnitude gradually decreases since the flow rate is lower in the equilibrium state between the supplied port and controller port.

Figures 9 and 10 show the static pressure variation and the relative velocity magnitude contours, respectively, for model C at two of midsections ($y=0, z=0$) and the spool wall. Once the spool moves in a forward direction, the flow rate increases monotonically and the seal leakage flow appears from the radial clearance of the delay component of the spool. As the spool approaches $x'=0.33$, the strong jet flow from the orifice collides against the pressure-compensated wall and the flow structure covers the whole region of the spool, as shown in Fig. 9(*b*). In the region of valve overlap in Fig. 9(*c*), the seal leakage flow is parallel to the sleeve. It can be clearly seen that the pressure contours vary instantly at two of orifices with changes in the *EOA* for each spool displacement due to the incompressibility of the transmission fluid, as shown in Fig. 10.

Figure 11 displays the variations in the pressure sensitivity and the seal leakage flow rates with the ratio of notch depth ($d'=d_{nd}/d_{na}$), when the notch depth of advance component (d_{na}) is fixed at 0.2 mm. Other parameters of the valve geometry such as the radius and the number of notches were held constant. Numeri-

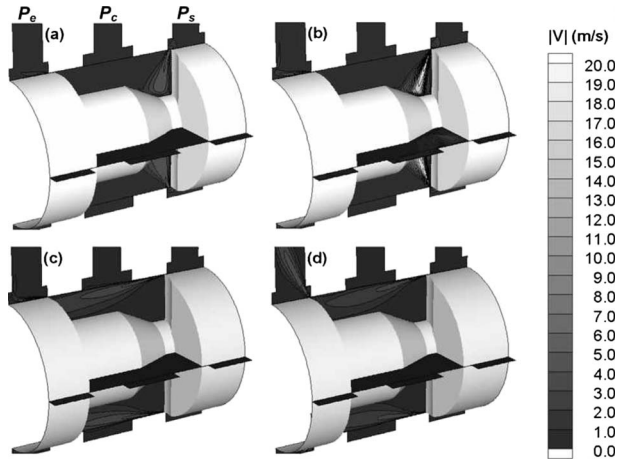

Fig. 9 Relative velocity contours on the spool wall and the mid section for model C at 85°C; (*a*) $x'=0.08$, (*b*) $x'=0.33$, (*c*) $x'=0.58$, and (*d*) $x'=0.75$

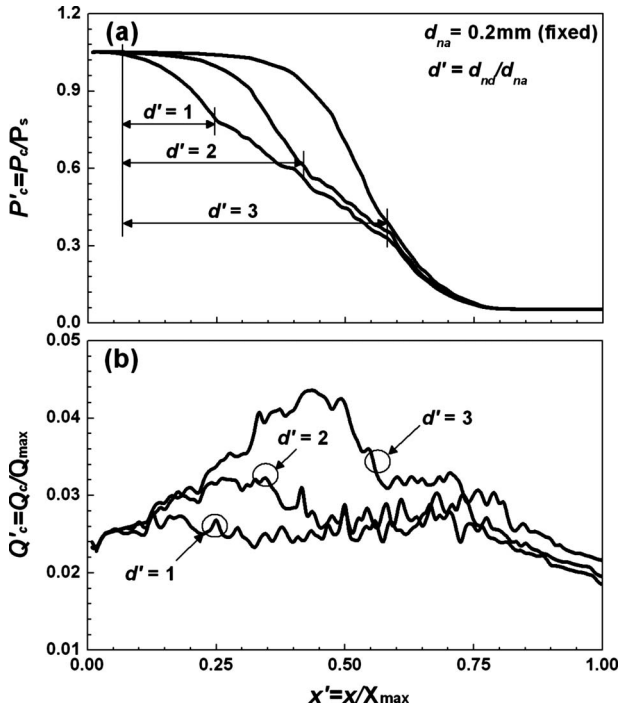

Fig. 11 Effects of varying the notch depth ratio of the delay part: (*a*) on the pressure sensitivities and (*b*) on the leakage flow rates

cal simulations were performed for $d'=1.0, 2.0, 3.0$. The relationship between the characteristic length and the notch depths should satisfy the geometrical condition ($\Delta L \leq d_{na}+d_{nd}$) to prevent immoderate increases in the leakage flow, as shown in Fig. 4. In this regard, we selected $d'=3.0$, that is, the characteristic length is equal to the sum of two notch depths ($\Delta L=d_{na}+d_{nd}$). According to Fig. 11(*a*), the falling positions of the controlled pressure are shifted forward as the ratio of notch depth increases, and the inclination of the pressure sensitivity curves is steeper and proportional to the notch depth of the delay component. The change in the *EOA* due to the increase in the ratio of notch depth results in an increase in the seal leakage flow. The effect of the viscous force in a radial clearance is small at the geometrical condition ($d'=3.0$). Figure 11(*b*) shows the variation in the seal leakage flow rate with respect to the notch depth ratio. As the notch depth of the delay component increases, the seal leakage flow increases due to the reduction in flow resistance. In addition, the location of the maximum in the leakage flow varies with d'. When $d'=3.0$, the maximum leakage flow is near 0.042 at $x'=0.47$.

3.2 Effect of Oil Temperature. The VFS valves installed in automatic transmissions usually operate under severe service conditions such as extensive idling, cold temperature driving, and sustained hot weather driving. Since the viscosity of transmission oil decreases markedly with increases in temperature [2], the oil temperature of the working fluid affects the fluid behavior of the VFS valve. The kinematic viscosity of the transmission oil can be expressed as

$$v^* = 15.77233 \exp\left(-\frac{T}{25.18295}\right) + 10.42578 \exp\left(-\frac{T}{9.47194}\right) + 0.40093 \quad (8)$$

where T is the oil temperature (°C) and ν^* is 1.0 at the normal operation temperature ($T=85$°C). These simulations were carried out for $T=30$, 85, and 100°C. The kinematic viscosities (ν^*) for $T=30$ and 100°C are 5.56 and 0.745, respectively.

The effect of varying the oil temperature on the spool displacement from the static performance test of model C is shown in Fig. 12. The dead zones, where there are no spool motions with regard to i', appear until the control current duty (i') goes up to 15% and then the spool displacements are linearly controlled by the control current duty in the range of characteristic length. Except the dead zones, the spool displacement with regard to i' is divided by three regions. In regions A and C, the spool displacements decided by the balance of electromagnetic force and spring force are different at the same i'. This indicates that a hysteresis made by nonlinear electromagnetic force exists in these regions. Once the control current duty decreases from the maximum duty ($I_{\max}$), the spool does not move to a backward direction due to a residual magnetic force until the control current duty becomes 85%, as shown in Fig. 12(*a*). In region B, the spool displacements for current duty coincide regardless of a spool motional direction. The pressure-viscosity-balanced flow mechanism should be considered in this region and the friction force affects a hysteresis. As a result, the VFS valve with a spool is shown to have an unavoidable and unique hysteresis, which is caused by nonlinear electromagnetic forces at the end of strokes of the spool and by the friction forces in the range of valve overlap, as shown in Fig. 12(*b*). In general, the oil temperature affects the electromagnetic material resistance and the oil viscosity. At high oil temperatures, the average speed of the molecules increases and the average intermolecular forces decrease. More control current duty is needed to maintain or control the spool displacement due to the increase in the coil resistance shown in Fig. 12(*a*). Although the oil temperature increases, the pressure sensitivity curves with respect to i' are shown to be similar due to the decrease in the control current duties, as shown in Fig. 12(*b*).

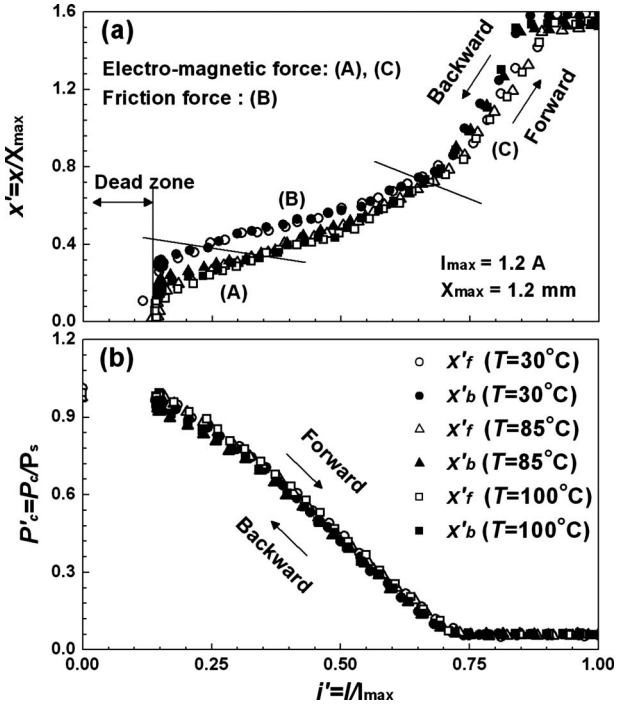

Fig. 12 Effects of varying oil temperature: (*a*) on the spool displacements and (*b*) on the pressure sensitivities

Figure 13 shows the effects of varying the oil temperature on the pressure sensitivities and the leakage flow rates. As the oil temperature increases, the pressure sensitivity curve has a gentle slope, as shown in Fig. 13(*a*). Low kinematic viscosity at high temperatures means that the leakage flow rate increases, as shown in Fig. 13(*b*). The maximum leakage flow rate (Q_c') at $T=85$°C is experimentally approximately 0.053 at the center of the delay

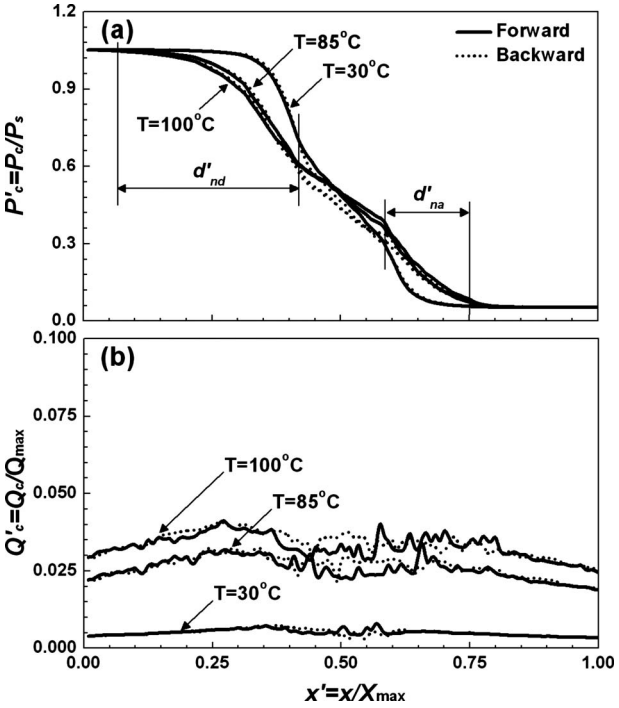

Fig. 13 Effects of varying the oil temperature: (*a*) on the pressure sensitivities and (*b*) on the leakage flow rates

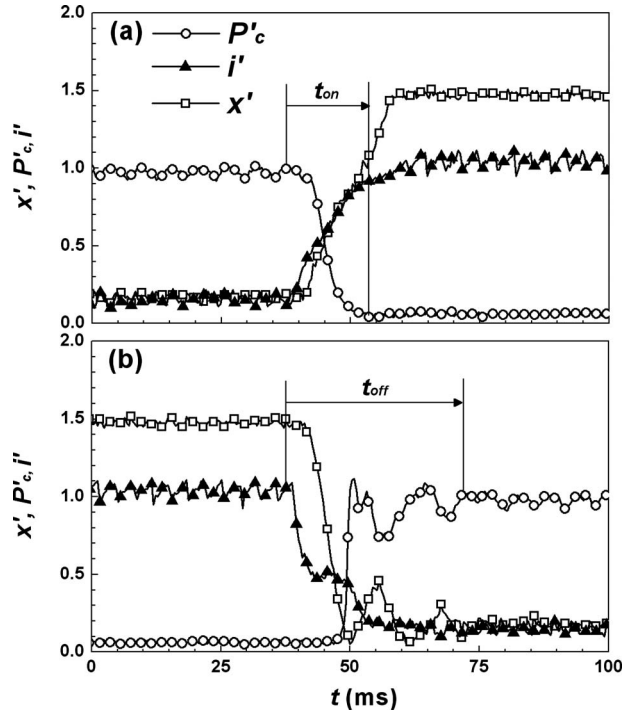

Fig. 14 Response characteristics of the dynamic performance test: (a) on and (*b*) off

component of the spool ($x'=0.25$). On the other hand, at low temperatures, the pressure sensitivity curve is a little steeper than that at high temperatures. In the region of two notches ($x'=0.083-0.416$ and 0.565–0.75), as the spool moves in a forward direction, the seal leakage flow rates due to the radial clearance of the advance component is less than those for other higher temperature conditions, which are due to the strong flow resistance resulting from the high viscosity of the transmission oil. The pressure sensitivity curves are delayed in the region of the delay notch ($x'=0.083-0.416$). The pressure sensitivity curves are then similar to those in the range of valve overlap ($x'=0.416-565$), where flow occurs according to the high viscosity-balanced flow mechanism. In the region of the advance notch ($x'=0.565-0.75$), the pressure sensitivity remains at a lower level than for other conditions due to the strong flow resistance affecting the leakage of the delay component. Since the increase in control current duties makes the spool speed faster at low temperatures, the pressure sensitivity curves with respect to i' are similar. The t-averaged leakage flow rate at $T=100\,^{\circ}\mathrm{C}$ is numerically 0.66 l/min, which is about 6.64 times than at $T=30\,^{\circ}\mathrm{C}$. Although the leakage flow rate is different for different oil temperatures, the behaviors of the seal leakage flow rates with spool displacement are similar, as can be seen in Fig. 13(*b*). Finally, the dynamic response characteristic of the VFS valve is shown in Fig. 14. The data were measured during the on and off operations of the VFS valve. The settling times for the on and off conditions were 16 ms and 34 ms, respectively. As shown in Fig. 14(*b*), because the residual electromagnetic force delayed in the spool departure of off, the settling time is longer than that of on. Some overshoot or ripple pressure appears, once the VFS valve has a backward direction.

4 Conclusions

In this study, numerical simulations were carried out to investigate the flow dynamic behavior of the VFS valves used in automatic transmissions and to analyze the pressure sensitivity and the seal leakage flow rate. The VFS valve can be characterized with the variation in the *EOA* with spool displacement and that the pressure sensitivity can be precisely controlled according to the relation between the depth and the area of the notch in the range of the characteristic length of the valve. The results of model C, which had notches and pressure-compensated hub profile for nonlinear electromagnetic force characteristics, indicated a linear pressure response in the range of valve overlap and a smooth pressure response in the range of two notches. The seal leakage flow through the valve orifice occurred instantly due to the difference between the supplied pressure and the controlled pressure. The seal leakage flow rate was the maximum at the center of the delay notch. The VFS valve with a spool was shown to have an unavoidable and unique hysteresis, which was caused by nonlinear electromagnetic forces at the end of strokes of the spool and by the friction forces in the range of valve overlap. Finally, low oil temperatures significantly affected valve performance characteristics such as the pressure sensitivity curves and the seal leakage flow rates. Although oil temperature increases, the pressure sensitivity curves with respect to i' were not significantly changed because more control current duty is needed to maintain or control the spool displacement due to the increase of the coil resistance.

Acknowledgment

This work was supported by the Creative Research Initiatives of MEST/NRF and partially supported by the Advanced Technology Center Project of MKE.

References

[1] Brejcha, M. F., 1982, *Automatic Transmissions*, Prentice-Hall, Englewood Cliffs, NJ.
[2] Merritt, H. E., 1967, *Hydraulic Control Systems*, Wiley, New York.
[3] Borghi, M., Milani, M., and Paoluzzi, R., 2000, "Stationary Axial Flow Force Analysis on Compensated Spool Valves," Int. J. Fluid Power, **1**(1), pp. 17–25.
[4] Davis, J. A., and Stewart, M., 2002, "Predicting Globe Control Valve Performance-Part I: CFD Modeling," ASME J. Fluids Eng., **124**, pp. 772–777.
[5] Davis, J. A., and Stewart, M., 2002, "Predicting Globe Control Valve Performance-Part II: Experimental Verification," ASME J. Fluids Eng., **124**, pp. 778–783.
[6] Krishnaswamy, K., and Li, P. Y., 2002, "On Using Unstable Electrohydraulic Valves for Control," ASME J. Dyn. Syst., Meas., Control, **124**, pp. 183–190.
[7] Yuan, Q., and Li, P. Y., 2005, "Using Steady Flow Force for Unstable Valve Design: Modeling and Experiments," ASME J. Dyn. Syst., Meas., Control, **127**, pp. 451–462.
[8] Amirante, R., Del Vescovo, G., and Lippolis, A., 2006, "Flow Force Analysis of an Open Center Hydraulic Directional Control Valve Sliding Spool," Energy Convers. Manage., **47**, pp. 114–131.
[9] Amirante, R., Del Vescovo, G., and Lippolis, A., 2006, "Evaluation of the Flow Forces on an Open Centre Directional Control Valve by Means of a Computational Fluid Dynamic Analysis," Energy Convers. Manage., **47**, pp. 1748–1760.
[10] Amirante, R., Moscatelli, P. G., and Catalano, L. A., 2007, "Evaluation of the Flow Forces on a Direct (Single Stage) Proportional Valve by Means of a Computational Fluid Dynamic Analysis," Energy Convers. Manage., **48**, pp. 942–953.
[11] Valdés, J. R., Miana, M. J., Núñez, J. L., and Pütz, T., 2008, "Reduced Order Model for Estimation of Fluid Flow and Flow Forces in Hydraulic Proportional Valves," Energy Convers. Manage., **49**, pp. 1517–1529.
[12] Guillermo, P. S., Pablo, G. A., and Jaime, A. V., 2008, "Three-Dimensional Modeling and Geometrical Influence on the Hydraulic Performance of a Control Valve," ASME J. Fluids Eng., **130**, p. 011102.
[13] Van Doormaal, J. P., and Raithby, G. D., 1984, "Enhancements of the SIMPLE Method for Predicting Incompressible Fluid Flows," Numer. Heat Transfer, Part A, **7**, pp. 147–163.
[14] Fluent Inc., 2006, FLUENT 6.3 User's Guide.

Parametric Design of a Waterjet Pump by Means of Inverse Design, CFD Calculations and Experimental Analyses

Duccio Bonaiuti
Advanced Design Technology Ltd.,
Monticello House,
45 Russell Square,
London WC1B 4JP, U.K.

Mehrdad Zangeneh
Department of Mechanical Engineering,
University College London,
London WC1E 7JE, U.K.

Reima Aartojarvi

Jonas Eriksson

Rolls Royce Marine AB,
Kristinehamn 68129, Sweden

The present paper describes the parametric design of a mixed-flow water-jet pump. The pump impeller and diffuser geometries were parameterized by means of an inverse design method, while CFD analyses were performed to assess the hydrodynamic and suction performance of the different design configurations that were investigated. An initial pump design was first generated and used as baseline for the parametric study. The effect of several design parameters was then analyzed in order to determine their effect on the pump performance. The use of a blade parameterization, based on inverse design, led to a major advantage in this study, because the three-dimensional blade shape is described by means of hydrodynamic parameters, such as blade loading, which has a direct impact on the hydrodynamic flow field. On the basis of this study, an optimal configuration was designed with the aim of maximizing the pump suction performance, while at the same time, guaranteeing a high level of hydrodynamic efficiency, together with the required mechanical and vibrational constraints. The final design was experimentally tested, and the good agreement between numerical predictions and experimental results validated the design process. This paper highlights the contrasting requirements in the pump design in order to achieve high hydrodynamic efficiency or good cavitation performance. The parametric study allowed us to determine design guidelines in order to find the optimal compromise in the pump design, in cases where both a high level of efficiency and suction performance must simultaneously be achieved. The design know-how developed in this study is based on flow field analyses and on hydrodynamic design parameters. It has therefore a general validity and can be used for similar design applications.
[DOI: 10.1115/1.4001005]

1 Introduction

The design of centrifugal and mixed-flow pumps requires the accomplishment of several targets and constraints: A high level of efficiency and suction performance must simultaneously be achieved, while keeping manufacturing costs low and guaranteeing a high level of reliability, as also pointed out by Gopalakrishnan [1] and Hergt [2].

A specific use of mixed-flow pumps is for water-jet applications. The pump is the core of the water-jet propulsion system and directly affects the overall propulsive efficiency. Even if water-jet pumps are required to operate inside a relatively narrow operating range [3], their design is considerably challenging; water-jet pumps must guarantee high hydrodynamic performance, since the propulsive efficiency is directly proportional to the pump efficiency, and they are required to deliver a uniform and axial flow (with small residual swirl), in order to maximize the water-jet thrust.

The pump is dimensioned on the basis of requirements aiming at maximizing the system efficiency, which usually causes the pump to work outside of its optimal operating range. In particular, the pump total head is chosen on the basis of the optimal jet velocity ratio (the ratio between the nozzle exit flow velocity and the vessel speed), and a high rotational speed is used in order to minimize the shaft torque, and therefore, the weight of the whole system. For the given rotational speed, volume flow rate, and pump head, the pump size is chosen considerably smaller than optimal [4], in order to reduce the overall weight of the propulsion system. This causes the pump to operate outside of its best efficiency region. Furthermore, the flow approaching the impeller eye is considerably distorted and with low value of static pressure [5], leading the pump to operate under cavitating conditions. According to Wislicenus [6], water-jet pumps are commonly designed to tolerate some level of cavitation.

With respect to other pump typologies (radial, axial, and inducer type), mixed-flow pumps are the most suitable to accomplish these requirements, and are usually employed in water-jet applications.

As highlighted in several studies [7–11], the flow field in mixed-flow pumps is highly three-dimensional and dominated by secondary flows. Their design is a challenging task, especially in cases like water-jet applications, where cavitation is an issue. A considerable improvement in their design is attained by the use of computational fluid dynamics (CFD). CFD analyses allow a better understanding of the flow phenomena, and nowadays, they are commonly used for the design of water-jet propulsive systems [12–14].

A major improvement in the design of mixed-flow pumps is achieved by the use of inverse design for the parametric representation of the three-dimensional blade shape. Despite conventional CAD methods, where only geometrical parameters are used to describe the blade geometry, inverse design uses hydrodynamic parameters like the blade loading, to describe the blade shape. Such parameters have a direct control of the hydrodynamic flow field and performance, affording a major advantage in the design process. The inverse design technique was widely used to suppress secondary flows in impellers [15–19] of mixed-flow pumps.

Contributed by the Fluids Engineering Division of ASME for publication in the JOURNAL OF FLUIDS ENGINEERING. Manuscript received December 6, 2007; final manuscript received December 21, 2009; published online March 18, 2010. Assoc. Editor: Joseph Katz.

In the present paper, the design of a water-jet pump was carried out in a parametric way, where an inverse design method was used to parametrically describe the impeller and diffuser geometries, and CFD analyses were performed to analyze the hydrodynamic and suction performance of the different design configurations.

First, an initial design was generated, implementing the design experience accumulated from mixed-flow pumps developed in previous studies. Next, the impact of five design parameters on the pump performance was assessed. The aim of this study was to understand the impact of each design parameter on the pump hydrodynamic and suction performance, which usually require opposite settings.

On the basis of the results obtained in the parametric study, a final design was generated, aimed at maximizing the suction performance, while guaranteeing a high level of efficiency and structural and vibrational constraints. An experimental analysis was carried out on this last design and the results were compared with the numerical predictions.

2 Design Method

The commercial software TURBODESIGN-1 was used to parametrically describe the blade geometry. TURBODESIGN-1 [20] is a three-dimensional inviscid inverse design method, in which the blades are represented by sheets of vorticity, whose strength is determined by a specified distribution of bound circulation $2\pi r\bar{V}_\theta$, where $\bar{V}_\theta$ is the circumferentially averaged swirl velocity. In this way, it is possible to find an expression for the bound vorticity in terms of $r\bar{V}_\theta$ and the blade shape. Since the vorticity depends on the blade shape and the blade shape depends on the velocity field, the problem is solved iteratively.

The method starts from an initial blade shape with a specified bound circulation distribution, and the velocity fields throughout the blade passage are calculated, assuming that the flow is 3D and steady. The 3D flow field is solved by decoupling the velocity field into a circumferentially averaged flow and periodic flow (see Ref. [20] for details). Then the blade shape is updated by imposing the inviscid slip condition, which implies that the flow must be aligned to the blade surface. The blade shape, expressed in terms of the angular coordinate of the camber surface $f(r,z)$, is found by integrating a first order hyperbolic partial differential equation along the meridional projections of the streamlines on the blade surface. An initial value of $f(r,z)$ is required to start the integration, and this initial value is called the stacking condition. In this paper, the values of the blade angular coordinate $f(r,z)$ along a quasi-orthogonal are specified as the stacking condition for both impeller and diffuser designs.

Once the updated blade shape is obtained, it is then possible to calculate the vorticity throughout the blade region and the resulting new velocity fields throughout the blade passage. Having a new estimate for the velocity fields, it is then possible to calculate a new blade shape. This iterative process is repeated until changes in blade shapes between two iterations fall below a certain tolerance. In the present paper, such value was set to 10^{-5} rad, which is lower than the blade manufacturing tolerances. The CPU time required to obtain a converged blade shape is very short, typically a few seconds on a modern PC.

The circulation distribution is specified by imposing the spanwise rV_θ distribution at the leading and trailing edges of the blade and the meridional derivative of the circulation drV_θ/dm (blade loading) inside the blade channel. The pressure loading (pressure difference across the blade) is directly related to the meridional derivative of rV_θ through the following equation:

$$p^+ - p^- = (2\pi/B)\rho W_m \frac{\partial(rV_\vartheta)}{\partial m} \tag{1}$$

where p^+ and p^- correspond to the static pressure on the pressure and suction sides of the blade, B is the blade number, ρ is the density, and W_m is the pitch-wise averaged meridional velocity. The following are the input design parameters required by the program.

- Meridional channel shape in terms of hub, shroud, leading and trailing edge contours.
- Normal/tangential thickness distribution.
- Fluid properties and design specifications.
- Number of blades
- Inlet flow conditions in terms of spanwise distributions of total pressure and velocity components.
- Exit rV_θ spanwise distribution. By controlling its value, the Euler work (impeller) or the inviscid flow turning (diffuser) are controlled.
- Blade loading distribution (drV_θ/dm). It is imposed at two or more span locations. The code then automatically interpolates span-wise to obtain the two-dimensional distribution of the blade loading over the whole meridional channel. The blade rV_θ distribution and, consequently, the blade loading distribution are normalized with respect to the value $\omega \cdot r_{2s}^2$, which is the product of the impeller trailing edge shroud radius and the corresponding peripheral velocity.
- Stacking condition. The stacking condition must be imposed at a chord-wise location between leading and trailing edge. Everywhere else the blade is free to adjust itself according to the loading specifications. Conventionally, the stacking is considered positive when it is such that the hub leads the shroud in the direction of rotation (see Fig. 1).

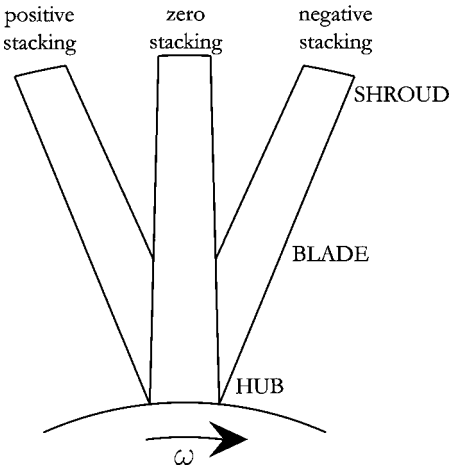

Fig. 1 Schematic representation of the stacking condition

In order to verify the different design configurations that were generated, CFD calculations were performed using the commercial software CFX 10. The CFX solver uses an element-based finite-volume method with second-order discretization schemes in space and time, and a coupled algebraic multigrid algorithm (mass and momentum are solved simultaneously) to solve the pressure and velocity systems. The $k-\varepsilon$ model was imposed for the turbulence closure, with scalable wall-functions. Convergence was based on reducing the maximum of the normalized residuals of the momentum and continuity equations to less than 10^{-4}.

Since the inlet flow distribution of a water-jet pump may vary with the operating conditions, all the configurations were designed and analyzed with CFD, assuming a uniform inlet flow. The average value of total pressure, which occurs at the impeller eye under the actual water-jet operating condition, was imposed as a boundary condition at the inlet of the computational domain.

The computational domain was discretized by means of two H-type blocks, the first describing the impeller vane, and the second describing the diffuser vane. The mixing-plane approach was

Table 1 Grid dependency analysis: Details of the four grids, with number of cells in the stream-wise direction *i*, pitch-wise direction *j*, and span-wise direction *k*; number of cells in the tip impeller clearance region and total grid size

Grid No.	No. of cells in *i*-direction (impeller)	No. of cells in *i*-direction (diffuser)	No. of cells in *j*-direction (impeller and diffuser)	No. of cells in *k*-direction (impeller and diffuser)	No. of cells in the impeller tip clearance region	Total grid size
Grid 1	92	76	48	36	4	290,304
Grid 2	100	84	52	40	4	382,720
Grid 3	108	92	56	44	4	492,800
Grid 4	116	100	60	48	4	650,880

used to exchange information between the two blocks, where the circumferential averaging of the fluxes of the computational variables is calculated at the block interface at each span height. The spanwise distribution of the pitch-averaged fluxes is then used to set the boundary conditions for the adjacent block.

Grid dimensions were chosen after performing a grid dependency analysis on the initial pump configuration (*baseline* design), whose detailed description is reported in the next paragraph. CFD calculations at the pump design point were repeated on four grids with increasing size, whose details are reported in Table 1. The impeller tip clearance gap is around 0.3% of the blade height, and four cells were posed in the tip clearance region to account for the tip clearance flow, in all the grids.

The pump head and the total pressure distribution at the diffuser exit, calculated with the four grids, are reported in Figs. 2(*a*) and 2(*b*), respectively. The pump head is normalized with respect to its value calculated with the finest grid (Grid 4).

The three finest grids present results, which are in good agreement, both in terms of pump head and of total pressure distribution. Grid 3 (see Fig. 2(*c*)) was then selected for this study, and its dimensions and settings were used to generate the grids for all the calculations reported in this paper.

Calculations were performed with a single-phase flow modeling. A cavitation inception criterion was conventionally defined, based on single-phase flow analyses, in order to compare the suction capabilities of the different design solutions. After each calculation, the pressure level was artificially decreased until 5% of the impeller blade surface presented a static pressure lower than the local vapor pressure. The corresponding inlet total pressure was used to compute the net positive suction head required (NPSHR) of the pump at that operating condition (see Ref. [11]).

The final design was also analyzed with the CFX cavitation model [21], which utilizes a homogeneous multiphase approach, based on the volume of fraction (VOF) equations. The governing equations describing the cavitation process assume a two-phase system, with no interphase slip and thermal equilibrium between the phases.

The vapor volume fraction in the flow is determined by a vapor production rate equation, introduced into the source terms of the VOF equations. The form of the source term has been derived by considering the truncated (first order approximation) Rayleigh–Plesset equation for bubble dynamics.

3 Design of the Baseline Configuration

The mixed-flow pump under consideration is composed of an unshrouded impeller and a downstream diffuser. The pump specific speed is $NS=130$, while the shaft power at design point is around 10.5 MW.

The meridional channel, which is reported in Fig. 3, was derived from an existing pump. Modifications were introduced in order to improve the hydrodynamic flow field, while keeping the pump inlet and exit sections unaltered, which must be coupled with the inlet duct and the nozzle of the propulsive system, respectively. The pump maximum diameter is constrained by considerations on the desirable pump weight and it was not changed during the design process.

The numbers of impeller blades (6), diffuser vanes (11), and their normal thickness distributions were determined on the basis of previous experience concerning vibration and stress requirements, and they were not altered in this study. Before proceeding with the parametric study, an initial optimization of the pump was performed in order to generate a design baseline (baseline). A detailed explanation of the baseline impeller and diffuser designs is reported in the sections that follow.

3.1 Impeller Design. The impeller was designed with the inverse design code; design specifications and inlet flow conditions were imposed according to their actual values at the design operating condition. A free-vortex distribution was imposed at the impeller exit (constant value of rV_θ from hub to shroud). The value

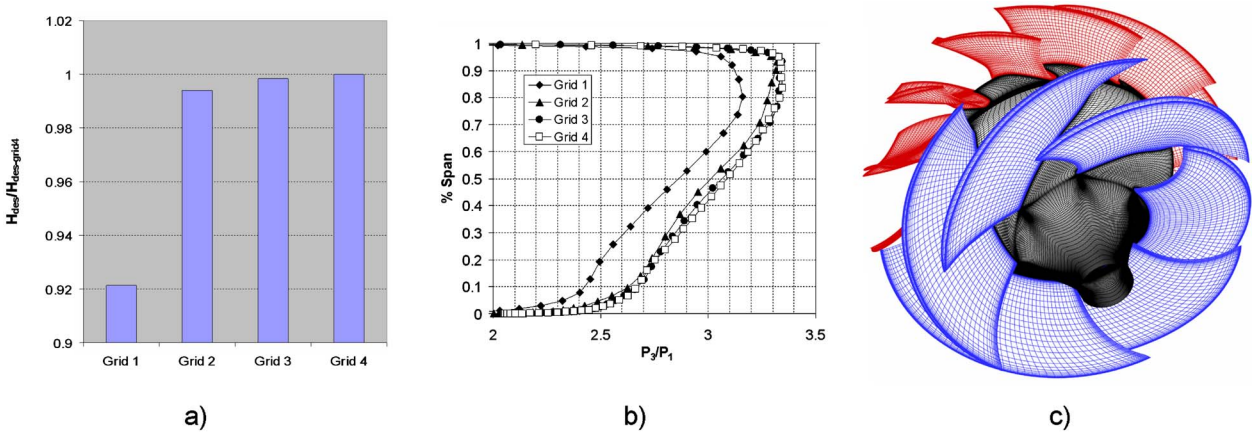

Fig. 2 Grid dependency analysis—(*a*) Normalized pump head at design point, (*b*) spanwise distribution of the total pressure at the diffuser exit, and (*c*) 3D view of Grid 3

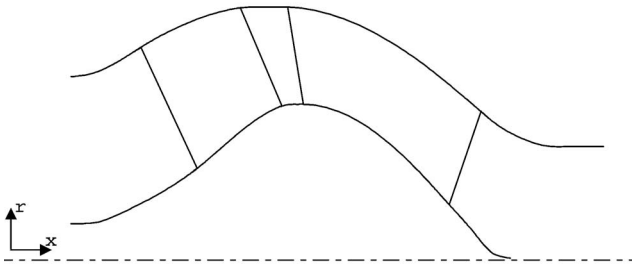

Fig. 3 Sketch of the pump meridional channel

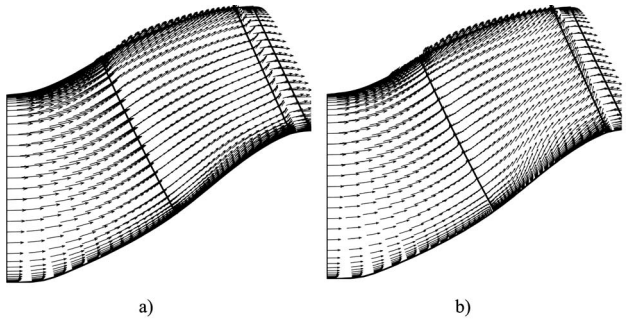

Fig. 5 Baseline—Impeller blade suction side velocity vectors at (*a*) design point and at (*b*) $M/M_{des}=0.9$

of rV_θ was chosen in order to produce the required pump head at design point. A zero stacking condition (radial stacking) was imposed at 90% of the chord.

The pump is characterized by a relatively high specific speed, and friction losses have a larger impact on efficiency than losses deriving from the secondary flow development. Furthermore, in order to minimize the pump weight, a considerably smaller pump size was chosen, rather than the optimal size for that specific speed. As a consequence, the average flow velocity inside the impeller is even higher, further increasing friction losses.

The tip clearance gap is relatively small, compared with the blade height, and the tip clearance vortex does not significantly affect the impeller performance. Secondary flows are quite small and start taking place only at low mass flow rates.

As also found in the axial compressors design [22], when friction losses are predominant, the most efficient loading distribution is the one where the blade is fore-loaded with a loading peak in the first 10–20% of the chord, followed by a gradual unloading of the blade. This type of loading leads to a velocity distribution on the blade suction side, where a strong acceleration is followed by a deceleration, which gradually becomes gentler toward the rear part of the blade. Such a velocity distribution limits the boundary layer growth and its associated losses and also reduces the possibility of flow separation in the trailing edge region. As a drawback, fore-loaded blades are characterized by a considerable pressure drop on the blade suction side, with a detrimental effect on cavitation performance.

The normalized blade loading distribution of the baseline impeller is reported in Fig. 4. The loading is defined at three sections (hub, midspan, and shroud) and it is then interpolated over the meridional channel. Each loading distribution is plotted against the normalized chord from the leading edge (meridional distance=0) to trailing edge (meridional distance=1). All the sections are fore-loaded, with the peak of the loading at 20% of the blade chord.

The value of blade loading at the leading edge controls the flow incidence at design point (see also Ref. [22]). A "zero" value corresponds to designing the blade aligned with the incoming flow, while a positive value determines a positive incidence and vice versa. In this impeller design, it was found that the best efficiency point (BEP) occurred when the flow approaches the blade with some degrees of positive incidence, while the best suction point (BSP) occurred with a negative incidence. Since the shroud is more critical from a cavitation point of view, a negative incidence was imposed in the shroud section and it was gradually increased at the midspan and hub. The incidence values were chosen so that the BSP is centered on the pump design point, while the BEP occurs at a lower mass flow rate (around 95% of design point mass flow rate, as later reported in Fig. 11).

Figure 5 shows the velocity vectors on the blade suction side at design point and at 90% of the design mass flow rate. As is evident, there are some secondary flow migrations along the blade suction side, only at part-flow conditions. No major secondary flows were noticed in other parts of the impeller vane, even at low mass flow rates.

3.2 Diffuser Design. In correspondence with the impeller design, the diffuser was designed by imposing the design point flow field at the impeller exit as inlet conditions to the inverse code.

While friction losses are predominant in the impeller, the diffuser is characterized by strong secondary flows. The major secondary flow migration is the one that moves the low-energy fluid

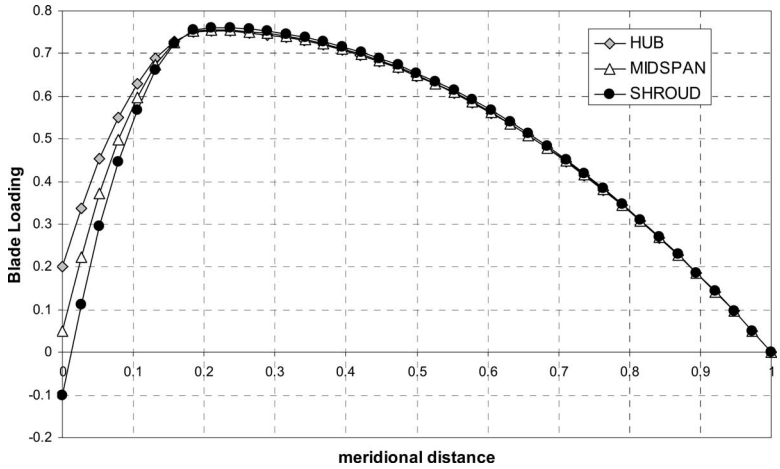

Fig. 4 Baseline—Impeller blade loading

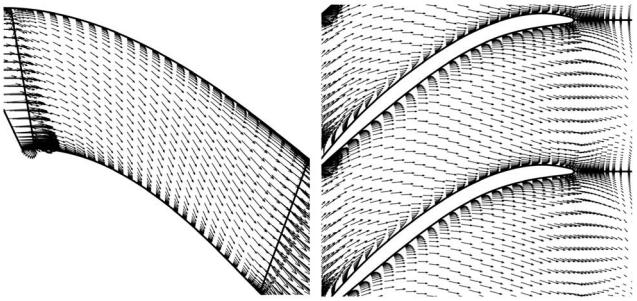

a) b)

Fig. 6 Design point velocity vectors on (*a*) the blade pressure side and (*b*) on the hub section for a diffuser designed with constant blade loading distribution, and zero rV_θ at the diffuser exit

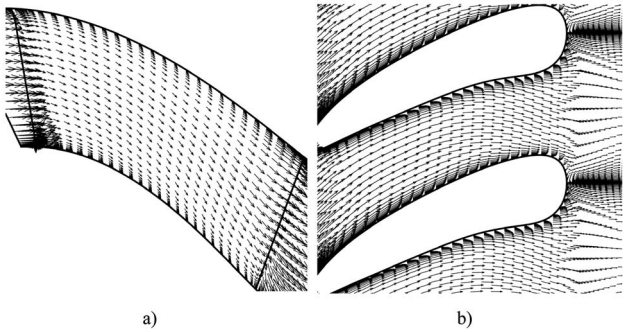

a) b)

Fig. 8 Baseline—Velocity vectors on (*a*) the diffuser blade pressure side and (*b*) on the hub section at design point

along the blade pressure side from the shroud to the hub. On the hub section, the secondary flow then migrates from the pressure side to the suction side, where it tends to accumulate and generates a low-energy wake region on the hub suction side corner in the rear part of the vane. Figure 6 shows the secondary flow development for a diffuser designed with uniform blade loading (constant value along the chord) and with a zero value of rV_θ at the diffuser exit.

The diffuser optimization was aimed at suppressing the secondary flow development and at delivering a uniform flow with minimum residual swirl, in order to maximize the axial thrust and the propulsive efficiency. The optimized blade loading is reported in Fig. 7(*a*). The blade loading was imposed at the hub and shroud sections, using a linear interpolation to obtain the loading distribution over the meridional channel.

As also found in previous works [23,17], fore-loading the hub section and aft-loading the shroud generates a pressure field inside the vane with pressure gradients on blades and walls that counteract the secondary flow migration. On the other hand, a too high fore-loading of the hub may lead to a strong flow deceleration on the hub suction side, with consequent flow separation. For this reason, the hub loading was gradually decreased in the rear part of the blade, so that a gradual deceleration takes place. For the same reason, the diffuser blade was thickened in the hub region (hub fillet) in order to locally accelerate the flow and reduce the risk of separation. A positive incidence was allowed on the hub, while at the shroud, a negative incidence was imposed in order to avoid local pressure spikes, which may lead to cavitation inception on the diffuser leading edge.

The optimized rV_θ distribution, which was imposed at the diffuser exit, is shown in Fig. 7(*b*). The inverse code used in this study is based on an inviscid flow evaluation and does not take into account of the viscous deviation. If an ideal zero value of rV_θ is imposed in the inverse code, the actual flow will present some residual swirl velocity at the diffuser exit, as shown in Fig. 9(*b*). A negative value of rV_θ was then imposed over most of the span, in order to give the blade the necessary overturning required to compensate for the viscous deviation and to deliver an axial flow.

In the hub region, the secondary flow tends to overturn the flow (as shown in Fig. 6(*b*)). If an ideal zero rV_θ is imposed, the flow at the diffuser exit will be characterized by a negative tangential velocity in the hub region (see Fig. 9(*b*)). A positive rV_θ value was then imposed in the lower part of the blade, in order to compensate for this effect. The consequent lower flow turning at the hub section reduces the overall hub loading, further minimizing the secondary flow migration on the hub wall.

As also demonstrated by Zangeneh et al. [16], the blade stacking generates a spanwise force that affects the spanwise pressure distribution on the blade. It can then be used to minimize the spanwise pressure gradients, which cause the secondary flow migration along the blade surface. In this case, 20 deg of stacking were imposed at 90% of the diffuser chord, so that the blade pressure side faces upwards. Such a blade stacking contributed to minimizing the secondary flow migration on the blade pressure side.

The design point velocity vectors on the diffuser pressure side and hub section are reported in Fig. 8. Compared with the flow

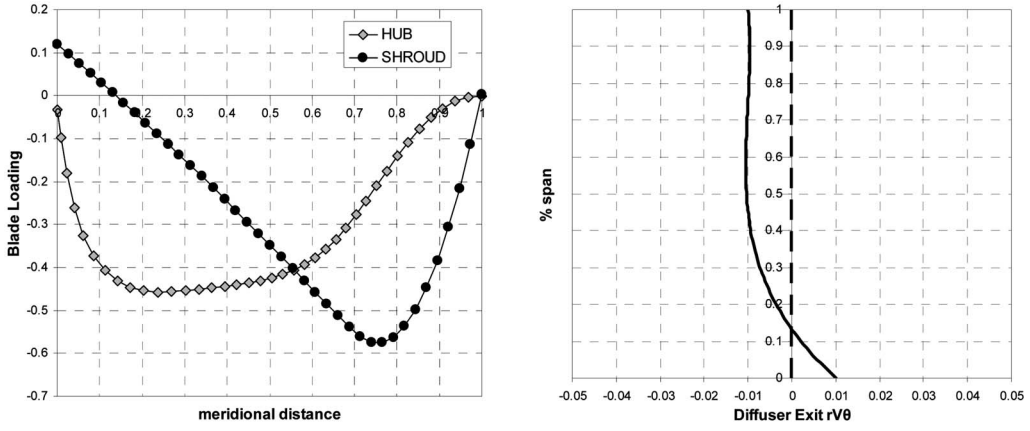

a) b)

Fig. 7 Baseline—(*a*) Diffuser blade loading and (*b*) normalized rV_θ distribution at the diffuser exit, imposed in the inverse design

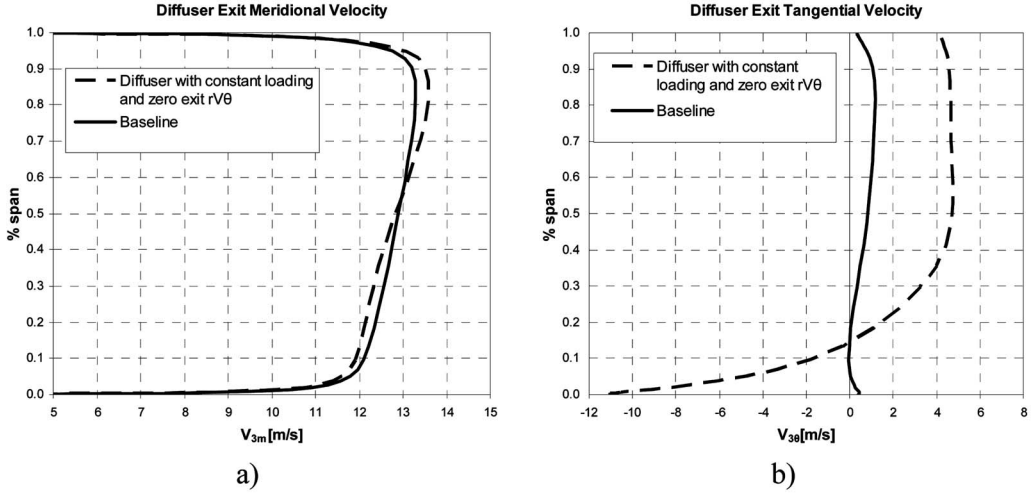

Fig. 9 Pitch-wise averaged, spanwise distribution of (*a*) the axial velocity and (*b*) of the tangential velocity at the diffuser exit at design point

field reported in Fig. 6, the secondary flow migration has been substantially reduced. With respect to the design with *constant loading* and zero rV_θ, the baseline is characterized by a more uniform velocity distribution at the diffuser exit with reduced residual swirl, as shown in Fig. 9.

Using the baseline as reference geometry, the parametric study of five impeller design parameters was carried out in order to assess their impact on the pump hydrodynamic and suction performance. Starting from their baseline value, each parameter was varied on three levels, and the corresponding impeller configurations were generated and compared by means of stage CFD analyses.

The diffuser had already been optimized for maximizing the hydrodynamic efficiency, and its design does not affect the pump suction performance. For this reason, the diffuser geometry was kept unaltered, and modifications were introduced only to adjust its design to the impeller changes.

4 Parametric Analysis of the Impeller Blade Loading

Two configurations (*Des-ld1* and *Des-dl2*) were generated, with identical design parameters to the baseline, apart from the blade loading, which was increasingly aft-loaded, as shown in Fig. 10. Des-ld1 presents a midloaded blade loading distribution (constant loading along the chord), while Des-ld2 is aft-loaded (loading peak located in the rear part of the blade). All the other impeller design parameters were kept unaltered, and the diffuser geometry was not changed with respect to the baseline.

Figure 11 compares the pump efficiency and NPSHR characteristic curves of Des-ld1 and Des-ld2 with the baseline, where the mass flow rate is normalized with respect to the mass flow rate value at design point M_{des}. The empirical evaluation of the NPSHR is derived from single-phase CFD calculations, as described in Sec. 2. The total head curves of the three configurations overlap each other and are not reported.

As expected, aft-loading the impeller blade reduces the impeller efficiency and, as a consequence, the pump efficiency. The drop in peak efficiency of Des-ld2 is about 1% with respect to the baseline.

As far as cavitation is concerned, aft-loading the blade shifts the peak of the loading toward the rear part of the blade and reduces the pressure valley, which occurs in the inlet part of the blade suction side, as shown in Fig. 12. This has a beneficial effect on suction performance, and Des-ld2 presents a NPSHR at design point, which is 0.35m lower than the baseline value.

An aft-loaded loading distribution is therefore preferred in cases where cavitation performance is more important than pump efficiency. The only exception is the hub section, where a high aft-loading (like the one in Des-ld2) leads to a pressure valley in

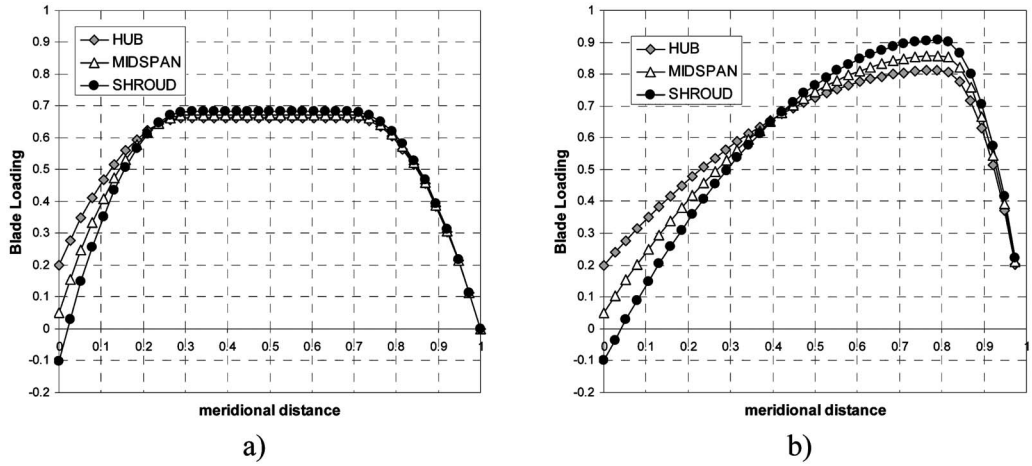

Fig. 10 Impeller blade loading distribution of (*a*) Des-ld1 and (*b*) Des-ld2

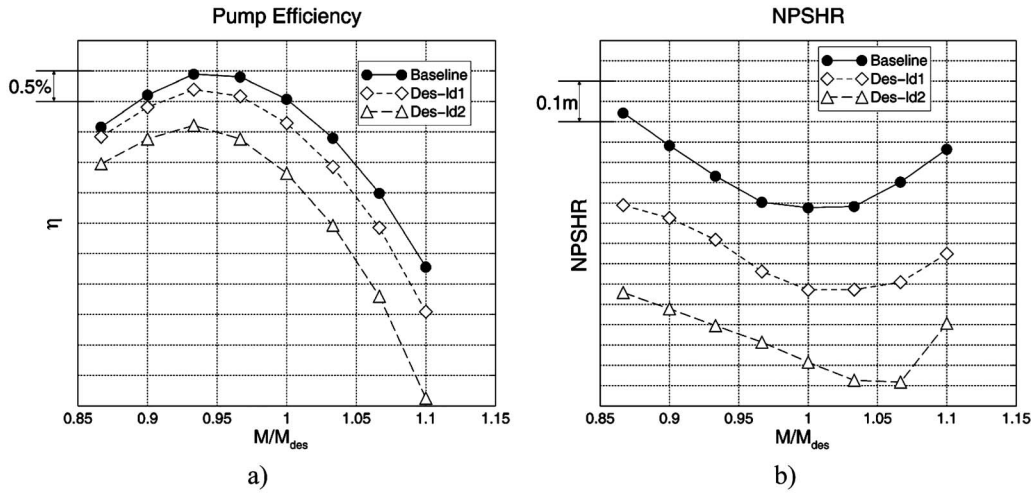

Fig. 11 Comparison of (*a*) pump efficiency and (*b*) NPSHR characteristic curves of baseline, Des-Id1, and Des-Id2

the rear part of the blade, with potential risk of cavitation inception when operating at low mass flow rates. Therefore, it is always preferable to avoid aft-loading the hub section.

5 Parametric Analysis of the Impeller Stacking

Two configurations were generated, with design parameters identical to the baseline, apart from the impeller stacking condition. Des-st1 was designed with a positive stacking of 20 deg, where the hub leads the shroud in the direction of rotation, while an opposite stacking condition was imposed in Des-st2. The stacking location was kept at 90% of the impeller chord.

The characteristic curves, calculated with CFD, are reported in Fig. 13, while Fig. 14 shows the blade pressure distributions at design point.

The main effect of the blade stacking is to change the spanwise profile of the meridional velocity inside the impeller. As shown in Fig. 15(*a*), the radial stacking condition used in the baseline design leads to a constant spanwise distribution of the pitch-averaged meridional velocity inside the impeller. Therefore, the mass flow passing through the impeller is uniformly distributed along the span.

A negative stacking, like the one of Des-st2, increases the meridional velocity in the shroud region, and reduces it at the hub. As a result, the specific mass flow through the impeller increases from hub to shroud. A positive stacking, like the one of Des-st1, generates the opposite effect.

The increase in mass flow through the shroud has a beneficial effect on the pump efficiency, and the peak efficiency of Des-st2 is 0.4% higher than the one of Des-st1.

From Fig. 15(*b*), it can be noticed that the distribution of the tangential velocity inside the impeller is identical for the three configurations. This is in agreement with what was imposed in the design with TURBODESIGN-1 (same rV_θ distribution in the three designs).

The spanwise variation in the meridional velocity also affects the blade pressure distribution (see Fig. 14). Even if the blade loading (drV_θ/dm) is the same in the three designs, the pressure jump across the blade also depends on the meridional velocity W_m, as shown in Eq. (1). For this reason, Des-st2 presents a larger pressure jump in the shroud section and a smaller one in the hub, over the entire blade chord. As a consequence, the minimum pressure on the shroud section is lower, while the hub minimum pressure increases in relation to the baseline. The shroud section is more critical for cavitation, and this causes Des-st2 to have poorer cavitation performance than the baseline. Opposite considerations can be made for Des-st1.

It is to be noticed that, from a mechanical point of view, the imposition of a nonradial stacking, either positive or negative, tends to increase the stress level on the blade.

6 Parametric Analysis of the Impeller Exit Vortex Distribution

The baseline was designed with a free-vortex distribution at the impeller exit (constant value of the impeller exit rV_θ along the span). In this analysis, two pump configurations were designed with opposite profiles of the inter-row rV_θ distribution, as shown in Fig. 16.

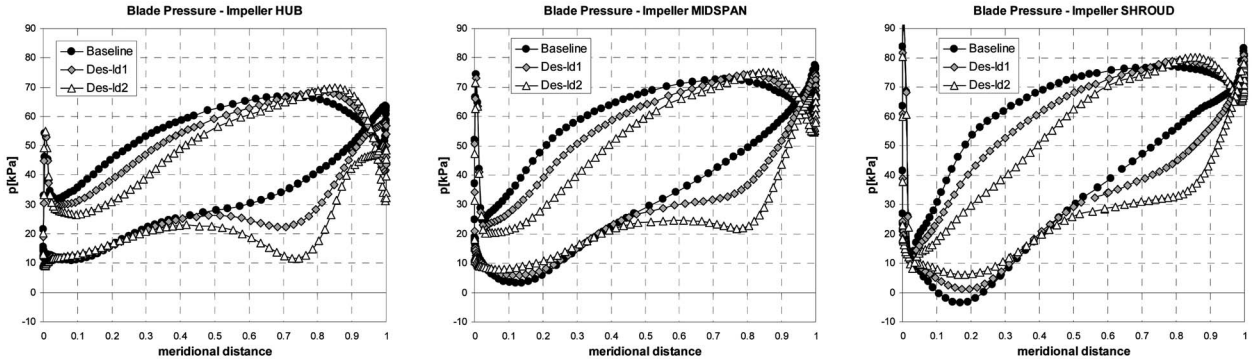

Fig. 12 Impeller blade pressure distributions of baseline, Des-Id1, and Des-Id2 at design point

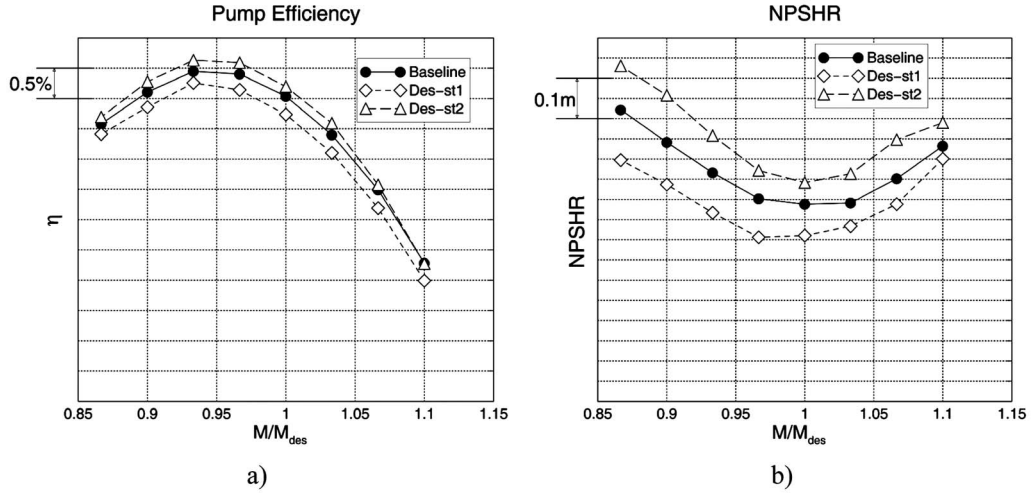

Fig. 13 Comparison of (*a*) pump efficiency and (*b*) NPSHR characteristic curves of baseline, Des-st1, and Des-st2

Des-rvt1 presents a linear rV_θ distribution, where the specific work increases from hub to shroud, while keeping unaltered the overall impeller Euler work (same average value of the impeller exit rV_θ as in the baseline). All the other impeller design parameters were kept unaltered with respect to the baseline. The diffuser design was changed according to the new velocity and total pressure distribution occurring at the impeller exit. Des-rvt2 was designed by imposing an opposite vortex distribution.

The modification of the vortex distribution changes the spanwise distribution of the impeller work, and therefore, the spanwise distribution of the total pressure at the impeller exit, as shown in Fig. 17(*a*). In accord with the results obtained from Ref. [24], the

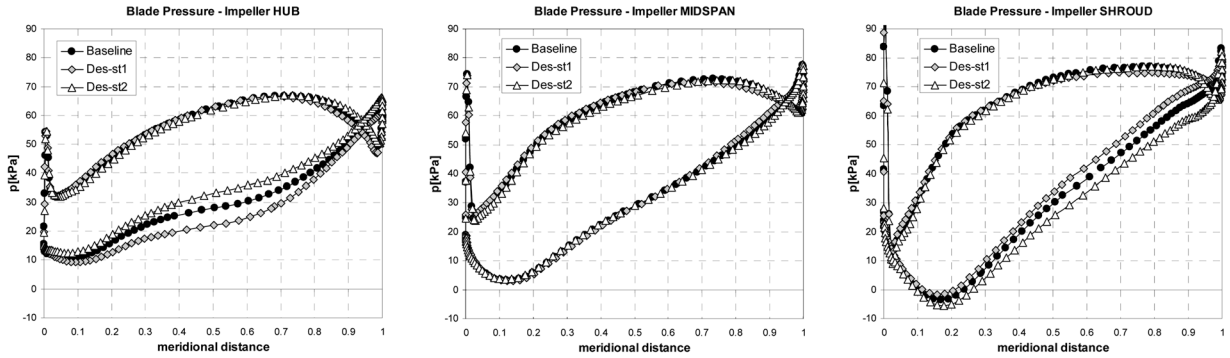

Fig. 14 Impeller blade pressure distribution of baseline, Des-st1, and Des-st2 at design point

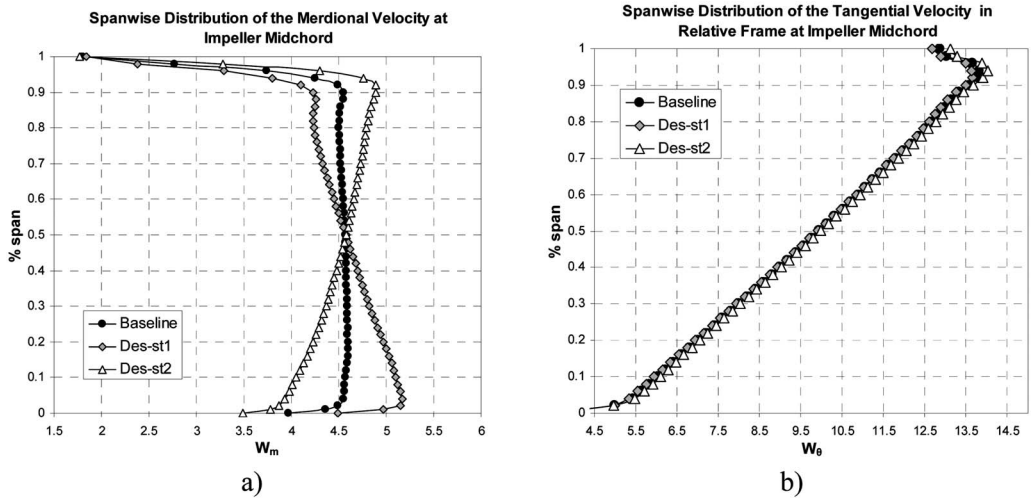

Fig. 15 Pitch-wise averaged, spanwise distribution of (*a*) the meridional velocity and (*b*) of the tangential velocity in relative frame at the impeller midchord at design point

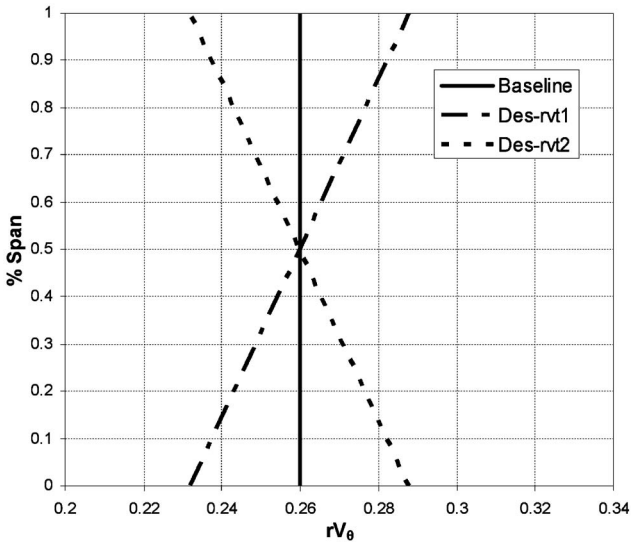

Fig. 16 Normalized spanwise distribution of the impeller exit rV_θ distribution for baseline, Des-rvt1, and Des-rvt2

spanwise distribution of the mass flow passing through the impeller tends to redistribute according to the spanwise distribution of the specific work: The higher the specific work, the higher the portion of mass flow that passes through that section. This is evident from the comparison of the spanwise distributions of meridional velocity at the impeller exit (see Fig. 17(*b*)). A higher meridional velocity corresponds to a larger portion of mass flow rate passing through that section.

Des-rvt1 has a similar efficiency level than the baseline, while Des-rvt2 presents a drop in peak efficiency of 0.5% (see Fig. 18(*a*)). The reason is that the hub is characterized by a considerably smaller radius than the shroud section; therefore, increasing the hub specific work requires a much larger flow turning, with consequent increase in boundary layer losses. Similar results were found by Vad et al. [24].

Cavitation performance is not significantly affected by the change in vortex distribution (see Fig. 18(*b*)), since most of the changes in the blade pressure distributions happen in the rear part of the chord, as shown in Fig. 19.

7 Parametric Analysis of the Leading Edge Sweep Angle

Two designs (Des-sw1 and Des-sw2) were generated with an increasing forward sweep at the impeller leading edge. The hub

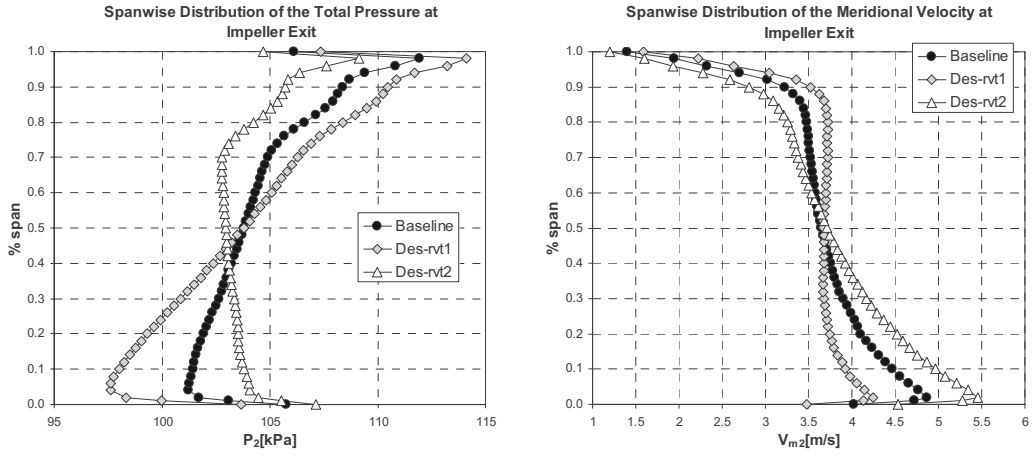

a) b)

Fig. 17 Spanwise distribution of (*a*) total pressure and (*b*) meridional velocity at the impeller exit, at design point

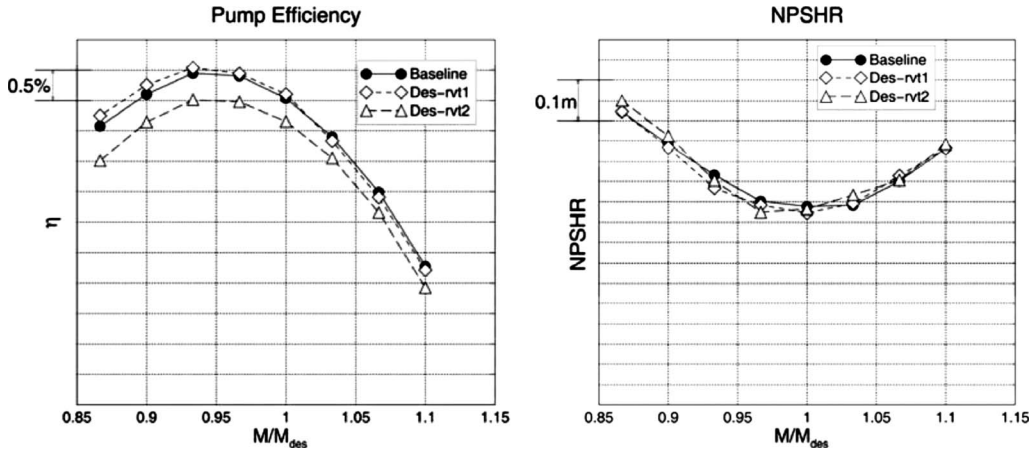

a) b)

Fig. 18 Comparison of (*a*) pump efficiency and (*b*) NPSHR characteristic curves of baseline, Des-rvt1, and Des-rvt2

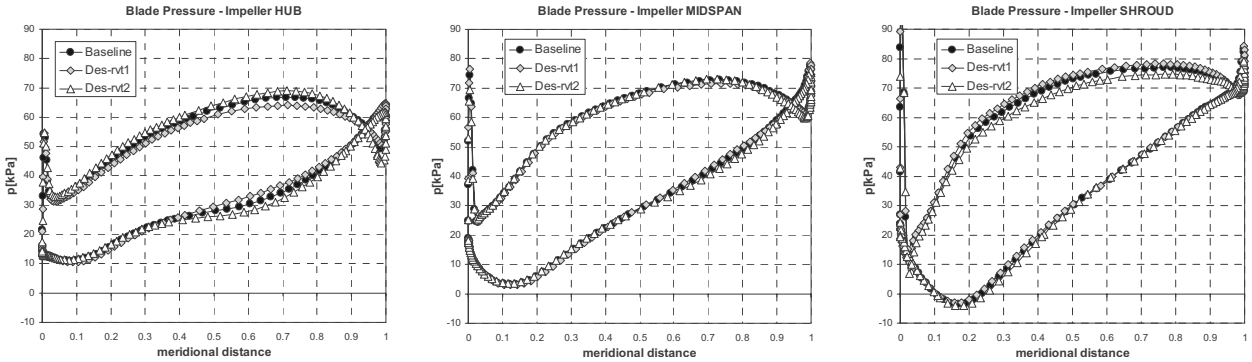

Fig. 19 Impeller blade pressure distribution of baseline, Des-rvt1, and Des-rvt2 at design point

chord was kept unaltered, while the shroud one was increased and a shaped leading edge was imposed, as shown in Fig. 20.

As evident from Fig. 21(*a*), the sweep angle has a marginal effect on the pump efficiency. Only at high mass flow rates, the larger wet area of the forward-swept designs leads to higher friction losses, and Des-sw2 is characterized by a pump efficiency, which is 0.7% lower than for the baseline at $M/M_{des}=1.1$.

On the contrary, the sweep angle has a significant effect on the suction performance. As shown in Fig. 22, the longer chord reduces the specific loading, and the pressure valley on the blade suction side is therefore reduced. As a result, the design point NPSHR value of Des-sw2 is 0.2 m lower than in the baseline (see Fig. 21(*b*)).

A major drawback of such modification is that a high value of the sweep angle also increases the hub-to-shroud lean angle at the impeller leading edge, with a detrimental effect on the stress and vibration performance of the impeller. With respect to the baseline, where the inlet lean angle is 9 deg, this increases up to 20 deg in Des-sw2, leading to an unacceptable stress level on the inlet blade region, as also numerically verified by means of stress analysis calculations.

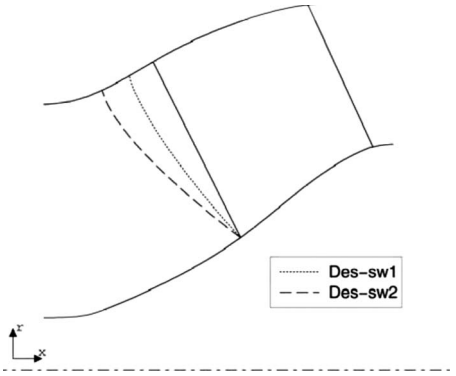

Fig. 20 Leading edge shapes of Des-sw1 and Des-sw2

8 Parametric Analysis of the Impeller Exit Hub Radius

The maximum pump diameter was fixed by considerations on the weight of the pump. An analysis was then performed on the effect of the impeller exit hub radius. Starting from the baseline design, two configurations were generated, one with a lower value (Des-rh1) and one with a higher value (Des-rh2) of the impeller exit hub radius, as shown in Fig. 23. The impeller and diffuser were designed according to the modified meridional geometry, while keeping all the other design parameters unaltered.

The effect of the hub radial development on the pump characteristic curves and pressure distributions is reported in Figs. 24 and 25.

The hub radius variation has a significant effect on the pump efficiency. A smaller impeller exit hub radius (Des-rh1) increases

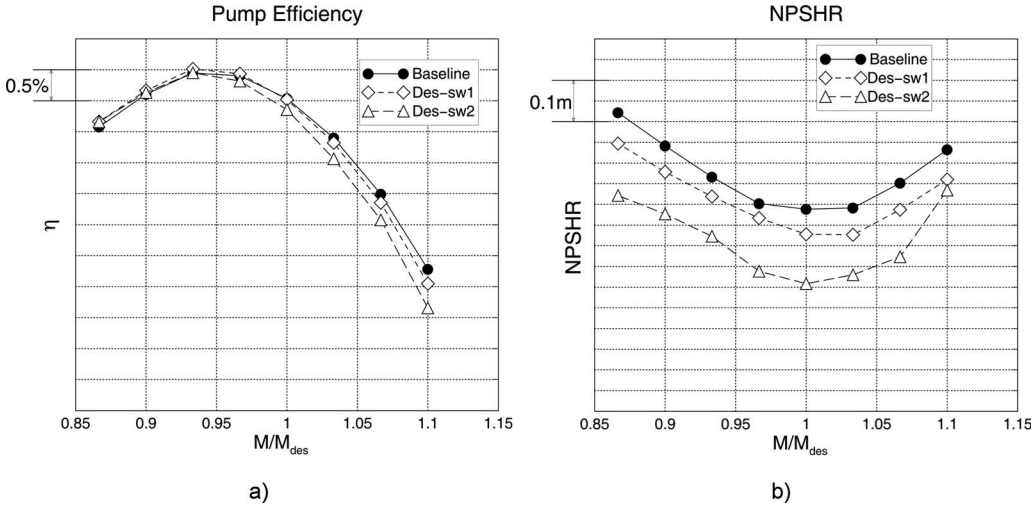

Fig. 21 Comparison of (*a*) pump efficiency and (*b*) NPSHR characteristic curves of baseline, Des-sw1, and Des-sw2

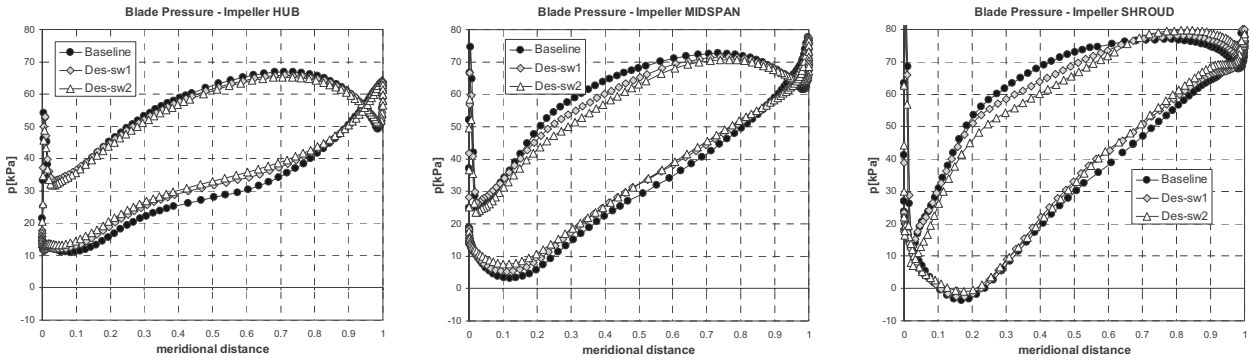

Fig. 22 Impeller blade pressure distribution of baseline, Des-sw1, and Des-sw2, at design point

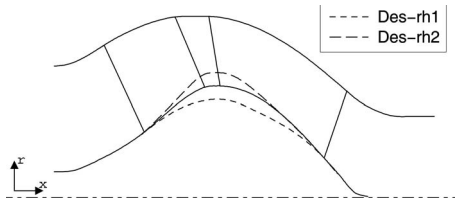

Fig. 23 Meridional channel of baseline, Des-rh1, and Des-rh2

the throat area and reduces the average level of the relative velocity inside the impeller and diffuser. As a result, friction losses are reduced and Des-rh1 presents better efficiency at larger mass flow rates, where friction losses are predominant. The larger throat area also shifts the BEP toward higher mass flow rates.

At lower mass flow rates, a higher hub radius is preferable for two main reasons. A larger hub radial development leads to a higher percentage of the total impeller work performed by centrifugal forces. At low mass flow rates, this effect is predominant over the increase in friction losses, and the overall impeller efficiency is higher. Furthermore, the smaller impeller exit passage

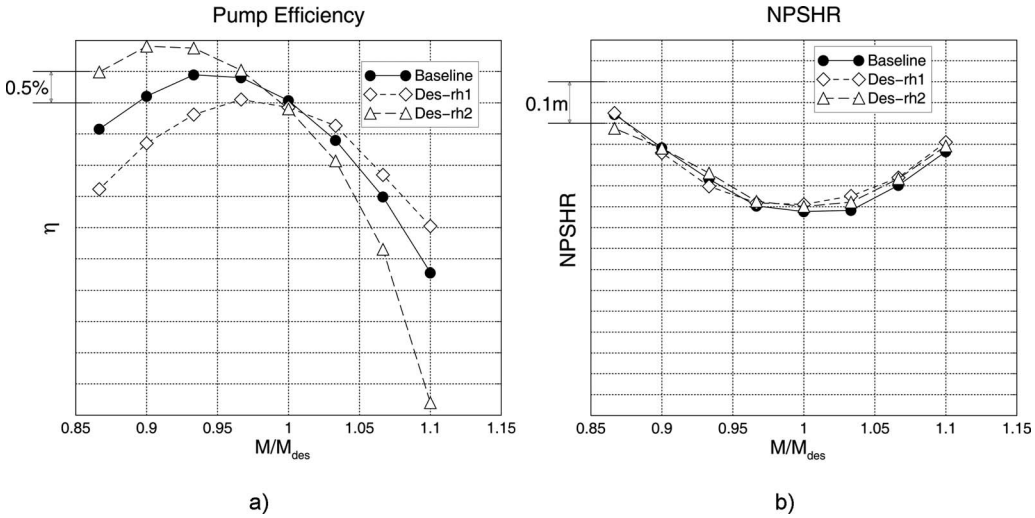

Fig. 24 Comparison of (*a*) pump efficiency and (*b*) NPSHR characteristic curves of baseline, Des-rh1, and Des-rh2

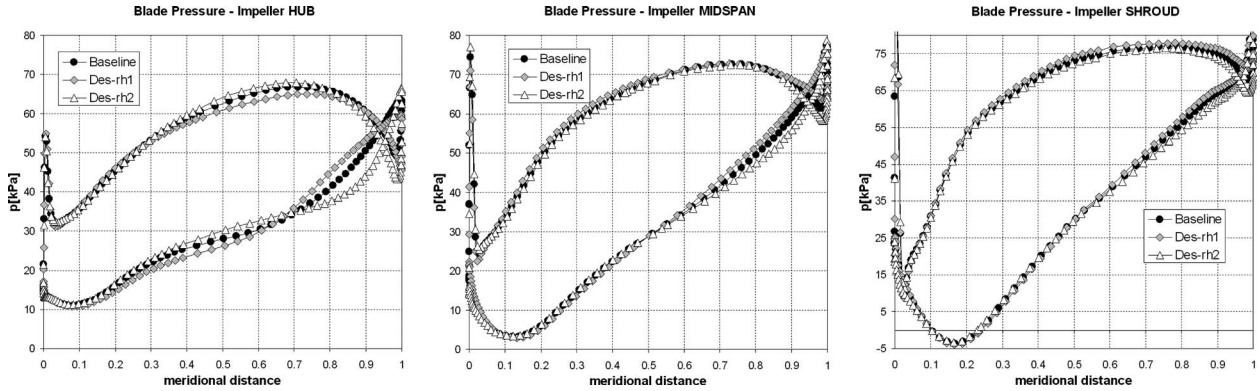

Fig. 25 Impeller blade pressure distribution of baseline, Des-rh1, and Des-rh2 at design point

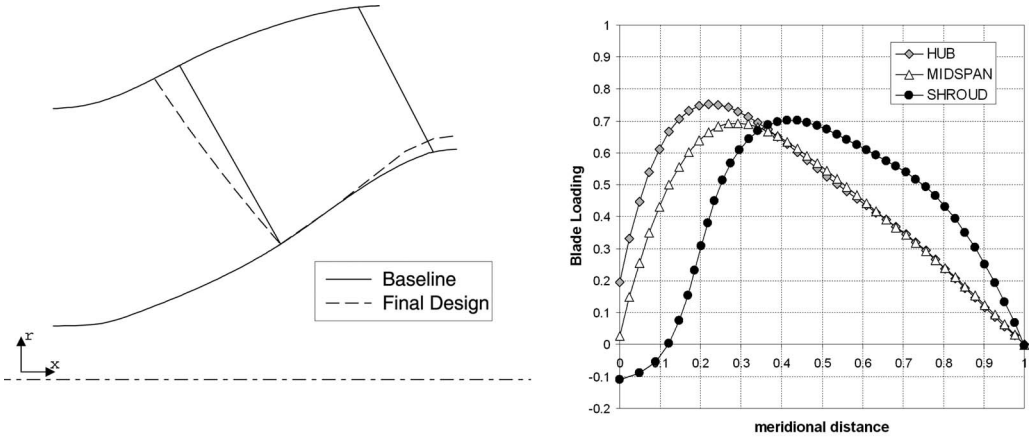

Fig. 26 (*a*) Comparison of the meridional channel development between baseline and final design. (*b*) Blade loading distribution of the final design.

area increases the inter-row meridional velocity, delivering a more axial flow to the downstream diffuser. In the hub region, the impeller exit tangential velocity is smaller (same rV_θ as in the other designs but higher radius), leading to an even more axial flow. The flow turning required by the diffuser in order to deliver an axial flow at the pump exit is then reduced, leading to a smaller secondary flow development. The BEP of Des-rh2 is shifted toward lower mass flow rates, and the peak efficiency is 1% higher than in Des-rh1.

As evident form Fig. 25, changes in the blade pressure distributions occur mostly in the rear part of the blade, where the meridional channel variation is more pronounced, while the minimum pressure level on the blade inlet region is unaltered. Therefore, the cavitation performance is not significantly affected by the meridional channel modifications introduced (see Fig. 24(*b*)).

9 Design of the Final Pump Configuration

Using the design rules developed in the previous sections, a *final design* was generated, aimed at maximizing the cavitation performance, while accepting some loss in efficiency with respect to the baseline design. The impeller exit radius was slightly increased and some degrees of forward sweep were imposed at the impeller leading edge. Even if a more pronounced sweep would have been beneficial for cavitation, it was not used in order to avoid unacceptable levels of stress on the impeller blade. The radial stacking was kept as in the baseline for the same reason. A free-vortex rV_θ distribution was imposed at the impeller exit.

As far as the impeller loading is concerned, the hub and midspan sections, which are less critical for cavitation, were fore-loaded, in order to maximize efficiency. The shroud section was fore-loaded from 40% of the chord to the trailing edge, while its inlet region was unloaded in order to minimize the amount of work performed in the inlet part of the shroud and to reduce the critical pressure drop on the suction side of the blade shroud. The meridional channel and the blade loading of the final design are reported in Fig. 26.

Figure 27 shows the comparison of the characteristic curves between the baseline and final design, while the blade pressure distributions at the design point are compared in Fig. 28.

The final design presents a flat suction curve with a value of NPSHR at the design point, which is 0.27 m lower than in the baseline, at a cost of 0.45% in peak efficiency. At the design point, the efficiency penalty is reduced to only 0.3%.

In the new design, the decreased amount of work performed in the inlet area of the shroud section, together with the effect of the

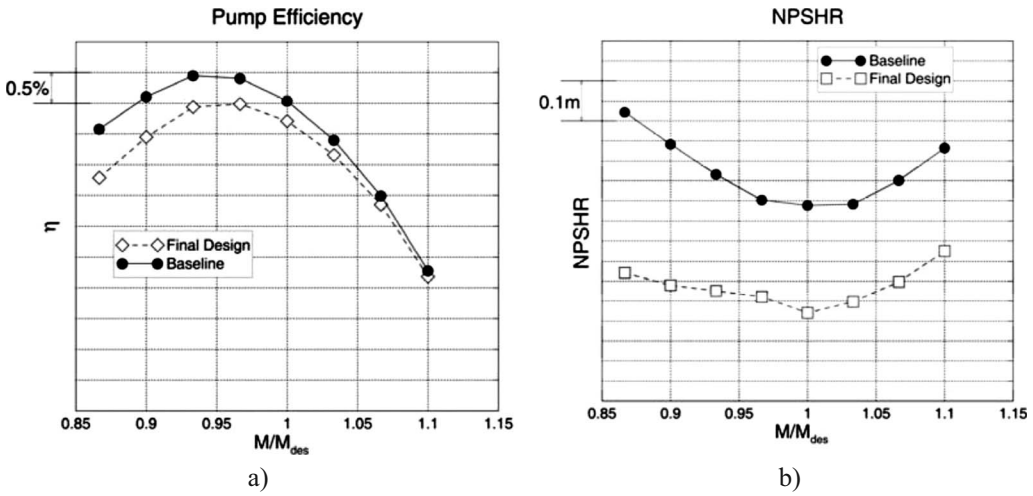

Fig. 27 Comparison of (*a*) pump efficiency and (*b*) NPSHR characteristic curves of baseline and final design

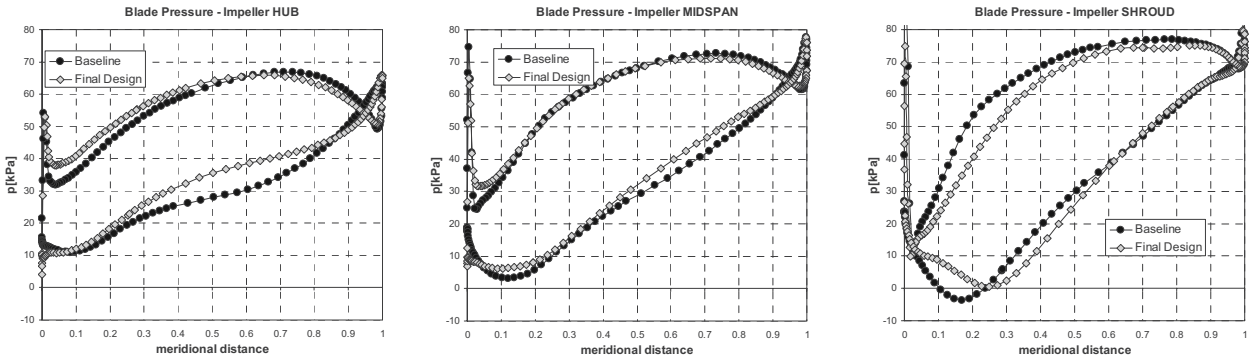

Fig. 28 Impeller blade pressure distribution of baseline and final design at design point

sweep angle, reduces the pressure drop on the blade suction side and shifts backward the location of the minimum pressure on the shroud (see Fig. 28). These combined effects guaranteed the better cavitation performance of the new design.

The cavitation performances of the baseline and of the final design were also analyzed by means of CFD analyses with the cavitation model.

The analysis was first performed at the design operating condition (design mass flow rate and operating inlet total pressure). Figure 29 reports the contours of the vapor volume fraction on the blade. The impeller is orientated so that the suction side of the blade is visible. The final design works under cavitation-free conditions at the design point, while the baseline presents a cavitating region in the shroud area, corresponding to the location of the pressure valley.

Calculations were repeated with an inlet total pressure equal to 60% of the actual operating value. The baseline presents a fully cavitating flow for over 30% of the blade chord, while in the final design, some level of cavitation starts taking place in the hub region downstream of the leading edge and on a small area of the shroud (see Fig. 30).

With respect to the baseline, the final design presents superior cavitation performance, in agreement with the predictions based on the empirical evaluation of the NPSHR, which was used in this study.

10 Experimental Verification of the Final Design

The final design was experimentally analyzed at the Rolls-Royce Hydrodynamic Research Centre (see Ref. [25]). The experimental facility is divided into two parts: a pump loop test in the conventional cavitation tunnel, and a water-jet system test in the free surface cavitation tunnel. In the pump loop test, the general pump performance is measured, whereas in the system test, the overall water-jet system performance is measured. Both facilities are equipped for visualization of cavitation patterns.

The closed-loop experimental facility provides a uniform inlet flow at the impeller eye, giving the pump the same inlet boundary conditions as in the CFD analyses, used in the design process. The pump was then analyzed in this facility in order to validate the CFD results.

Figure 31 compares the experimental head and efficiency characteristic curves to the CFD predictions. The head curves overlap each other, while the numerical prediction of the pump efficiency is about 0.4% higher than the experimental one over the whole operating range. This is in agreement with the authors' experience, considering that mechanical losses are not taken into account in the CFD evaluation.

In accord with the numerical analysis, no evidence of cavitation was found at the design point mass flow rate, over a wide range of inlet total pressures.

In order to detect some level of cavitation, the experimental test was repeated at a partial mass flow rate ($M/M_{des}=0.86$) and with an inlet total pressure equal to 80% of the operating value. CFD calculations with the cavitation model were also performed at the same operating condition. Figure 32 reports the comparison of the flow visualization, obtained with a high-speed camera during the experimental test, and the CFD vapor volume fraction plots on the blade surface.

As evident from the front view picture, which shows the suction side of the blade, CFD predictions are in good agreement with the experimental results. A trapezoidal-shaped attached cavitation region takes place on the lower part of the blade suction side, just downstream of the leading edge. CFD predictions also highlight some level of cavitation on the blade shroud. This is not visible on the photograph, since part of the blade is covered by the impeller shroud.

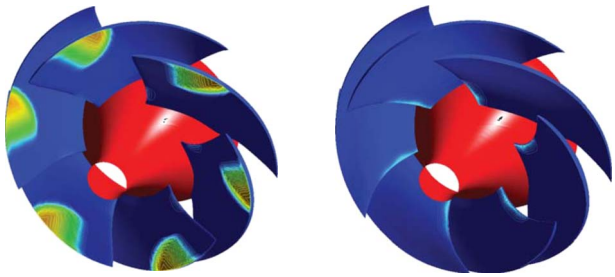

Fig. 29 Cavitation CFD analyses: Visualization of the vapor volume fraction contours on the blade surface for (*a*) the baseline and (*b*) for the final design at design mass flow rate with inlet total pressure $P_1=P_{1-des}$

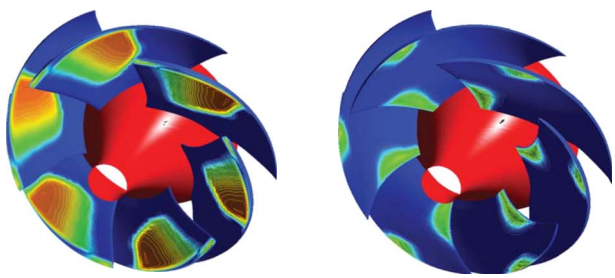

Fig. 30 Cavitation CFD analyses: Visualization of vapor volume fraction contours on the blade surface for (*a*) the baseline and (*b*) for the final design at design mass flow rate with inlet total pressure $P_1=60\%$ of P_{1-des}

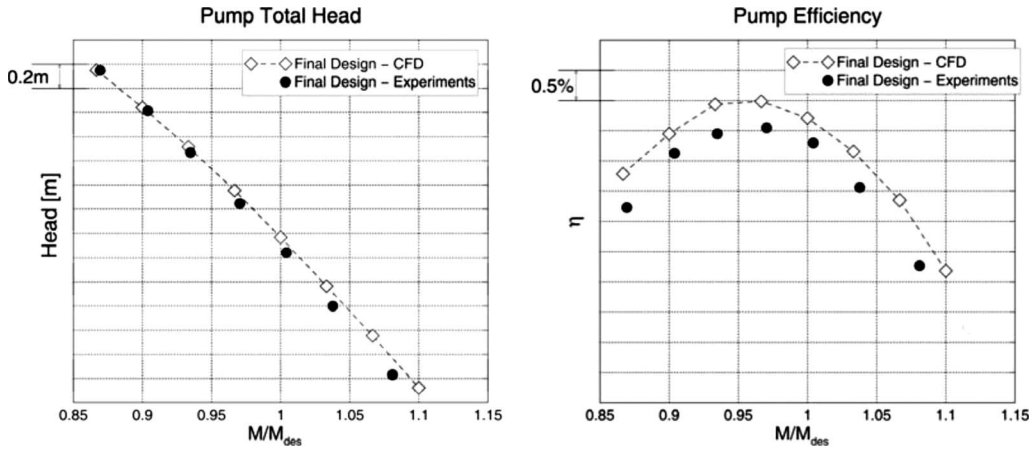

Fig. 31 Comparison between numerical prediction and experimental results of (*a*) the total head and(*b*) efficiency characteristic curves of the final design

In the side view of the impeller, both the experimental visualization and the CFD results highlight the occurrence of some tip clearance cavitation.

The final design was also experimentally tested in an open-system facility, where the complete water-jet propulsion system was simulated. Results from such analysis, not reported in this paper, confirmed the high level of efficiency and suction performance of the final design.

11 Conclusions

The design of a water-jet mixed-flow pump was carried out with the intention of maximizing hydrodynamic and suction performance. The blade shapes of the impeller and diffuser were parameterized by means of an inverse design method, and CFD analyses were performed to address the effect of the design modifications introduced during the design process.

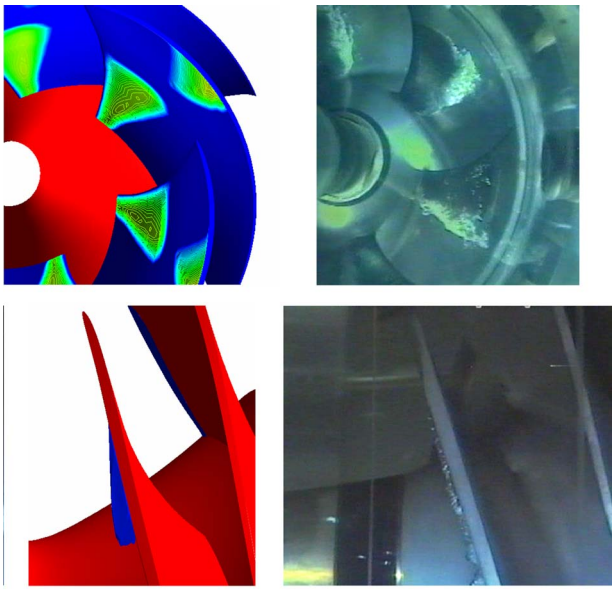

Fig. 32 (*a*) Numerical and (*b*) experimental visualization of cavitation development on the final design at $M/M_{des}=0.86$ and $P_1/P_{1des}=0.8$

The design was carried out in a parametric way. First, an initial pump configuration was generated, exploiting the authors' best experience on the hydrodynamic design of mixed-flow pumps. Then, using the initial design as a baseline, the effect of five impeller design parameters was investigated in a systematic way. Each parameter was varied on three levels in order to asses its impact on the hydrodynamic and suction performance of the pump. The purpose of this study was to determine the different, sometimes opposite, design settings, which are required to maximize the suction performance and the hydrodynamic efficiency of the pump.

The use of a blade parameterization, based on the inverse design, brought a major advantage in this study. The inverse design method used in this paper allowed us to describe the 3D blade shape by using a mix of hydrodynamic parameters (blade loading, exit vortex distribution) and geometrical parameters (meridional channel shape, thickness distribution, and stacking condition). The hydrodynamic parameters have a direct impact on the flow field and performance of the pump: the exit vortex distribution allows the control of the spanwise distribution of work (impeller) or of flow turning (diffuser), while the blade loading determines the shape of the blade pressure distribution. The combination of these two parameters completely determines the distribution of tangential velocity inside the blade. Therefore, the geometrical parameters can only affect the meridional velocity flow field. As highlighted in this paper, such a "decoupled effect" brings a major advantage in the design process, since it makes it easy to understand the impact of each parameter (hydrodynamic or geometrical) on the hydrodynamic flow field and pump performance. In particular, the present analysis led to the development of the following design guidelines.

- The blade loading parametric study showed that such a parameter has a major impact on the hydrodynamic and suction performance of the impeller. In cases, like the present one, where friction losses are predominant, a fore-loaded loading distribution maximizes the impeller efficiency, but, at the same time, it results in a high pressure drop on the blade suction side near the leading edge, with detrimental effect on the suction performance. The direct control of the blade loading, through the inverse design parameterization, allowed us to determine an optimal compromise, where most of the blade is fore-loaded with the exception of the inlet shroud section, which is the most critical for cavitation.
- The parametric analysis of the impeller exit rV_θ showed how, by varying such parameter, it is possible to control the

spanwise distribution of the impeller work, and how this also leads to a spanwise redistribution of the mass flow within the impeller. In the present case, this parameter did not have a major effect on hydrodynamic and suction performance. However, the results show a small drop in performance for the case where the hub rV_θ is higher than the shroud rV_θ. The hub, being at a smaller radius, requires a higher flow turning to produce the same amount of work on the fluid, with the risk of increasing the boundary layer losses.

- By varying the impeller stacking, it is possible to control the meridional velocity flow field inside the impeller, without altering the tangential velocity distribution. As shown in Eq. (1), the pressure jump across the blade is correlated with the meridional velocity field. As a consequence, the stacking condition has an impact also on the pressure field. The analysis highlighted how hydrodynamic and suction performances require opposite settings of the stacking condition.
- With the inverse design method, the overall work performed at a specific span section is determined by the corresponding inlet and exit rV_θ values. As shown by the analysis of the forward sweep angle, extending the shroud blade length distributes the specific work over a longer chord, thus reducing the section blade loading. The pressure valley on the suction side is then reduced with a beneficial effect on the suction performance. As a drawback, the increase in blade length leads to higher friction losses and to penalties in efficiency, when operating at high mass flow rates.
- With the present inverse method, changes in the meridional channel shape affect both the meridional velocity field, by changing the passage area, and the tangential flow field. The analysis of the hub radial development of the pump showed a major impact on the peak efficiency level and location. In the present case, the meridional channel variation was introduced mainly in the rear part of the impeller, and did not impact the pressure distribution in the inlet part of the blade, which is critical for cavitation. Therefore, suction performance was not significantly affected by such modifications.

These design guidelines are based on hydrodynamic considerations, and therefore have a general validity. They can then be exploited for the design of similar mixed-flow pumps.

On the basis of the parametric study, a final configuration was designed, aimed at maximizing cavitation performance, while guaranteeing a high efficiency level, together with mechanical and vibrational constraints. Its performances were analyzed both numerically and experimentally. A very good agreement was found between numerical and experimental results, both in terms of efficiency and cavitation. Such a result validated the design process and also confirmed the excellent cavitation and hydrodynamic performance of the final design.

Nomenclature

η = total-to-total pump efficiency
ρ = fluid density
ω = impeller rotational speed (rad/s)
B = number of blades
H = pump head
M = mass flow rate
N = impeller rotational speed (rpm)
$\mathrm{NPSHR} = (P_1 - p_v)/\rho \cdot g$ = net positive suction head required
$\mathrm{NS} = N \cdot Q^{0.5}/H^{0.75}$ = pump specific speed
p = static pressure
p_v = vapor pressure
P = total pressure
Q = volume flow rate
x, r, θ = cylindrical coordinates
V = absolute velocity
W = relative velocity

Subscripts

1 = impeller inlet
2 = impeller exit
3 = diffuser exit
des = design point
m = meridional direction
θ = tangential direction
h = hub
s = shroud

References

[1] Gopalakrishnan, S., 1999, "Pump Research and Development: Past, Present and Future—An American Perspective," ASME J. Fluids Eng., **121**, pp. 237–247.
[2] Hergt, P. H., 1999, "Pump Research and Development: Past, Present and Future," ASME J. Fluids Eng., **121**, pp. 248–253.
[3] Matsumoto, K., Tanaka, H., and Ozawa, H., 1993, "Optimization of Design Parameters of Water Jet Propulsion System," Proceedings of the FAST93.
[4] Allison, J., 1993, "Marine Water-Jet Propulsion," Soc. Nav. Archit. Mar. Eng., Trans., **101**, pp. 275–335.
[5] Seil, G. J., 2001, "The Effect of the Shaft, Shaft Rotation and Scale on the Flow in Waterjet Inlets," Proceedings of the Waterjet Propulsion III Conference.
[6] Wislicenus, G. F., 1973, "Hydrodynamic Design Principles of Pumps and Ducting for Water-Jet Propulsion," NSRDC Report No. 3990.
[7] Iino, M., Miyagawa, K., Tanaka, K., and Okubo, T., 2002, "Numerical Analysis of Internal Flow in a Mixed-Flow Pump," Proceedings of the Ninth International Symposium on Transport Phenomena and Dynamic of Rotating Machinery.
[8] Goto, A., 1992, "Study of Internal Flows in a Mixed-Flow Pump Impeller at Various Tip Clearances Using Three-Dimensional Viscous Flow Computations," ASME J. Turbomach., **114**, pp. 373–382.
[9] Miner, S. M., 2000, "CFD Analysis of the First-Stage Rotor and Stator in a Two-Stage Mixed Flow Pump," Proceedings of the Isromac 8 Conference.
[10] Kato, C., Mukai, H., and Manabe, A., 2002, "Large Eddy Simulation of Unsteady Flow in a Mixed-Flow Pump," Proceedings of the Isromac 9 Conference.
[11] Bonaiuti, D., Arnone, A., Corradini, U., and Bernacca, M., 2003, "Aerodynamic Redesign of a Mixed-Flow Pump Stage," AIAA Paper No. 2003-3506.
[12] Widmark, C., and Gustafsson, L. T., 1997, "3-Dimensional CFD Calculations on a Complete Waterjet Unit," Proceedings of the International Conference on Power, Performance and Operability of Small Crafts.
[13] Turnock, S. R., Hughes, A. W., Moss, R., and Molland, A. F., 1997, "Investigation of Hull-Water-Jet Flow Interaction," Proceedings of the FAST97.
[14] Huntsman, I., and Hothersall, R., 2001, "Development of Quasi 3D Methods and 3D Flow Solvers for the Hydrodynamic Design of Water Jets," Proceedings of the Waterjet Propulsion III Conference.
[15] Zangeneh, M., Goto, A., and Takemura, T., 1996, "Suppression of Secondary Flows in a Mixed-Flow Pump Impeller by Application of Three-Dimensional Inverse Design Method," ASME J. Turbomach., **118**, pp. 536–561.
[16] Zangeneh, M., Goto, A., and Harada, H., 1998, "On the Design Criteria for Suppression of Secondary Flows in Centrifugal and Mixed Flow Impellers," ASME J. Turbomach., **120**, pp. 723–735.
[17] Goto, A., and Zangeneh, M., 2002, "Hydrodynamic Design of Pump Diffuser Using Inverse Design Method and CFD," ASME J. Fluids Eng., **124**, pp. 319–328.
[18] Sakurai, T., Saito, S., Goto, A., and Ashihara, K., 1999, "Pump Design System Based on Inverse Design Method and Its Application to Development of Diffuser Pump Series," ASME Paper No. FEDSM99-6845.
[19] Goto, A., Ashihara, K., Sakurai, T., and Saito, S., 1999, "Compact Design of Diffuser Pumps Using Three-Dimensional Inverse Design Method," ASME Paper No. FEDSM99-6847.
[20] Zangeneh, M., 1991, "A 3D Design Method for Radial and Mixed-Flow Turbomachinery Blades," Int. J. Numer. Methods Fluids, **13**, pp. 599–624.
[21] Bakir, F., Rey, R., Gerber, A. G., Belamri, T., and Hutchinson, B., 2004, "Numerical and Experimental Investigations of Cavitating Behavior of an Inducer," Int. J. Rotating Mach., **10**, pp. 15–25.
[22] Bonaiuti, D., and Zangeneh, M., 2006, "On the Coupling of Inverse Design and Optimization Techniques for Turbomachinery Blade Design," ASME Paper No. GT90897.
[23] Takemura, T., and Goto, A., 1996, "Experimental and Numerical Study of Three-Dimensional Flows in a Mixed-Flow Pump Stage," ASME J. Turbomach., **118**, pp. 552–561.
[24] Vad, J., Bencze, F., Benigni, H., Glas, W., and Jaberg, H., 2002, "Comparative Investigation on Axial Flow Pump Rotors of Free Vortex and Non-Free Vortex Design," Period. Polytech., Mech. Eng.-Masinostr., **46**, pp. 107–116.
[25] Hager, C., and Styrud, G., 2000, "Kamewa Waterjet 325 World Largest Waterjet Designed for the Fast Ship TG770," Proceedings of the CIMarE High-Speed Vessel Conference.

The Linear Stability Analysis of the Lamb–Oseen Vortex in a Finite-Length Pipe

S. Wang[1]
e-mail: wang@math.auckland.ac.nz

S. Taylor
e-mail: taylor@math.auckland.ac.nz

Department of Mathematics,
University of Auckland,
Auckland 1142, New Zealand

K. Ku Akil
Department of Mathematics and Statistics,
University of Teknologi MARA,
Arau Perlis o2600, Malaysia

*This article extends the perturbation method introduced by Wang (2008, "A Novel Method for Analyzing the Global Stability of Inviscid Columnar Swirling Flow in a Finite Pipe," Phys. Fluids, **20**(7), p. 074101) to determine the global stability of a swirling flow in a straight circular pipe with specified inlet and outlet boundary conditions. To accurately compute the flow stability characteristics, a general procedure to treat the complexity arising from high-order terms is developed. It extends the previous fourth-order method to an eighth-order method. The technique is first applied to the benchmark case of a solid-body rotation flow with a uniform axial speed. It is demonstrated that the eighth-order method is sufficient to construct the growth rate curve between the first and second critical swirls of this flow. Note that this range of swirl is crucial for the study of the vortex breakdown phenomenon since the base flow is unstable and starts the initial stage of transition to a breakdown state. The method is then applied to the Lamb–Oseen vortex to construct the growth rate curve between the first and second critical swirls of this flow. Calculated results are compared with the growth rate curve computed from direct numerical simulations and an overall agreement between the two computations is found. This demonstrates that the Wang and Rusak (1996, "On the Stability of an Axisymmetric Rotating Flow in a Pipe," Phys. Fluids, **8**(4), pp. 1007–1076) instability mechanism captures quantitatively the initial growth of disturbance, which eventually evolves into a breakdown state.* [DOI: 10.1115/1.4001106]

1 Introduction

The study of the stability of an axisymmetric swirling flow in a pipe has a long history. For excellent review papers on this topic, see, for example, Ref. [1] for the stability related to the vortex breakdown phenomenon, and Ref. [2] for a comprehensive review of this topic. Understanding vortex stability can shed light on the stability of rotating flows in vortex tubes and in hydrocyclone separators, swirling flows in modern combustors, and the breakdown of leading-edge vortices above slender wings at high angles of attack.

Rayleigh [3] was the first to establish a fundamental criterion for swirling flows in an infinitely long, straight, circular pipe. His criterion states that a columnar swirling flow with a circumferential velocity component $V(r)$ (here, r is the distance from the vortex axis), a uniform axial velocity component, and zero radial speed is stable to infinitesimal axially symmetric disturbances if and only if the square of the circulation function $K=rV$ decreases nowhere as r increases, i.e.,

$$\Phi \equiv \frac{1}{r^3}\frac{d}{dr}(K^2) > 0 \tag{1}$$

Note that the necessity and sufficiency of Eq. (1) for swirling flow being stable are strongly tied with the assumption imposed on the base swirling flow, namely, a columnar swirling flow in an infinitely long pipe. Such special flows apparently preserve a translational invariant and therefore admit a Fourier mode analysis without losing any generality.

In the study of the vortex breakdown in a finite-length circular pipe, the influence of the physical conditions at the pipe inlet and outlet has been studied by Wang and Rusak [4,5]. It was found that the imposed boundary conditions dramatically alter the stability nature of a swirling flow. In particular, an instability related to the swirl strength above a critical level was found. This cannot be explained by Rayleigh's stability theory. Specifically, a swirling flow, which is stable according to Rayleigh's criterion, can be unstable according to the Wang and Rusak mechanism. This demonstrates that the translational invariancy of the flow is violated. This is a direct consequence of the imposed boundary conditions that is of a different physical nature than the Rayleigh's centrifugal instability.

Additional investigations have demonstrated that the Wang and Rusak instability mechanism has a crucial role in the study of the vortex breakdown phenomenon, see Refs. [4–10] for theoretical works that are based on similar inviscid vortex models in a finite-length pipe. Because of this, it is important to accurately calculate the growth rate of disturbances at swirl levels above critical for vortex flows such as the Lamb–Oseen vortex and the Q-vortex. These model vortices exhibit good matching with the real swirling flows that are prone to vortex breakdown.

An accurate calculation of perturbation growth rate predicts the growth (or decay) of small-amplitude disturbances in the flow and provides the understanding of the primary stage of flow evolution that eventually leads to a breakdown state. However, the stability equation derived in Ref. [5] for general swirling flows is a very complicated differential-integro equation. This problem cannot be reduced in the general case to an ordinary differential eigenvalue problem. The only exception is the case of a solid-body rotation flow. The stability of this flow has been solved in Ref. [5] by using the method of separation of variables, and a formula for the perturbation growth rate as a function of swirl level was obtained.

Wang [11] has recently developed an asymptotic method to solve the Wang and Rusak stability equation for a general columnar swirling flow in a pipe of finite length. The method is based on the perturbation theory of linear operators. The perturbation method leads to a Taylor series formula for the swirl as a function of the growth rate. It was shown in Ref. [11] that the unperturbed operator and the perturbation operators can all be analyzed using

[1]Corresponding author.

Contributed by the Fluids Engineering Division of ASME for publication in the JOURNAL OF FLUIDS ENGINEERING. Manuscript received August 3, 2009; final manuscript received December 15, 2009; published online March 17, 2010. Assoc. Editor: Zvi Rusak.

the method of separation of variables. Thus, the coefficients of the Taylor series formula can be actually calculated in a semi-analytic manner. Wang [11] used this procedure up to fourth-order accuracy and applied it to study the stability of the Lamb–Oseen vortex and the Q-vortex at near critical swirl. It was shown that in the case of a solid-body rotation flow, the approximated growth rate functions accurately represent the exact growth rate computed from the formula for a limited range of swirl levels near the first or the second critical levels. However, in the range between the two critical swirl levels, results are not accurate. Similar problems appeared with growth rate computations of the Lamb–Oseen vortex.

In this article, we extend the perturbation method to improve the approximation of the growth rate function. Our goal is to accurately construct the whole growth rate curve for the entire range of swirl levels between the first and the second critical swirls. The growth rate curve shows quantitatively the change in flow instability when the swirl level is varying above the first critical swirl. This is particularly important for the global stability because the stability is now dependent on the strength of the swirl. We develop an eighth-order calculation method. It is noticed that the perturbation method becomes quickly too complex to be manipulated by hand when the order of the method increases. We thus carefully consider the technical details of the perturbation method and develop a general calculation procedure to build up several thousand terms involved in complicated multiplications of the linear operators. The task then is carried out automatically by using a MATLAB program. After this crucial implementation, the analytic techniques can be readily applied to the high-order method.

We conduct a case study of the solid-body rotation flow with an eighth-order method. It is found that the eighth-order method improves considerably the accuracy of the approximation of the growth rate function as compared to the fourth-order method. Further improvement can be achieved by exploring the Taylor expansions of the inverse function of the growth rate function, and of the function that is derived from a linear transformation of the growth rate function. By applying these techniques to the solid-body rotation flow, we construct the whole growth rate curve between the first and second critical swirls, which is found to be in very good agreement with the exact growth rate curve. The eighth-order method as well as the associated techniques are then applied to the Lamb–Oseen vortex to construct the whole growth rate curve between the first and second critical swirls. The growth rate curve is found to be in good agreement with the direct numerical simulations of the linearized governing flow equations.

The methods developed in this article can be applied to all columnar swirling flows in a finite-length pipe, which can serve as prototypes for real swirling flow apparatus in industry, such as combustors in gas-turbines, swirling testing-rigs in laboratory and hydrocyclone generators, etc. An accurate growth rate curve between the first and second critical swirls is highly desired in the study of vortex breakdown phenomenon, which predominates the initial growth of disturbances leading subsequently to a more complicated nonlinear evolution stage and finally a breakdown state. The analytic nature of the method ensures the accuracy of the resulting growth rate curve. Incorporating the method presented in this paper with direct numerical simulations (DNSs) deepens our understanding of the vortex breakdown phenomenon.

2 Mathematical Model and Stability Equation

We consider an axisymmetric, incompressible, and inviscid flow in a straight, finite-length, circular pipe. We use cylindrical coordinates (r,θ,x), where (u,v,w) are the radial, azimuthal, and axial velocity components, respectively. In a dimensionless form, the pipe radius is set as unity and the pipe length is L, rescaled with respect to the pipe radius. Velocity components are scaled with the characteristic speed of fluid entering the pipe. Let $y=r^2/2$. By virtue of the axisymmetry, a stream function $\psi(x,y,t)$ can be defined such that $u=-\psi_x/\sqrt{2y}$ and $w=\psi_y$. The reduced form of azimuthal vorticity is $\chi=-(\psi_{yy}+\psi_{xx}/2y)$ (where the azimuthal vorticity $\eta=\chi/\sqrt{2y}$). The circulation function K is defined as $K=rv=\sqrt{2y}v$.

The equations that relate the evolution of $\psi(x,y,t)$, $\chi(x,y,t)$, and $K(x,y,t)$ can be written in a compact form (see, for example, Ref. [12])

$$K_t+\{\psi,K\}=0$$

$$\chi_t+\{\psi,\chi\}=\frac{1}{4y^2}(K^2)_x \tag{2}$$

where $\{f,g\}$ denotes the canonical Poisson bracket or Jacobian defined as

$$\{f,g\}=f_yg_x-f_xg_y \tag{3}$$

The first equation in Eq. (2) describes the transport of circulation along a flow path and the second equation describes the interaction between the convection of azimuthal vorticity χ and azimuthal vorticity stretched by the axial gradient of the circulation.

Throughout this article, we consider a steady, columnar swirling base flow with velocity components specified by

$$(u,v,w)=(0,\omega v_0(y),w_0(y)) \tag{4}$$

where $\omega>0$ is the swirl parameter. From this velocity profile, one may find $\psi_0(y)=\int_0^y w_0(y)dy$, $\chi_0=-(\psi_{0yy}+\psi_{0xx}/2y)=-w_{0y}(y)$, and $K=\omega K_0(y)$ with $K_0(y)=\sqrt{2y}v_0(y)$. The extended circulation $I=K^2/2$ can be given by $I=\omega^2 I_0$ with $I_0=K_0^2/2$.

In the study of linear stability, disturbances of the stream function ψ_1 and the circulation K_1 from the base flow (4) are assumed in the forms

$$\psi_1(x,y,t)=\epsilon\phi(x,y)e^{\sigma t}$$

$$K_1(x,y,t)=\epsilon k(x,y)e^{\sigma t} \tag{5}$$

with $\epsilon\ll 1$, where σ is, in general, a complex number, which gives the growth rate. These disturbance terms are superimposed to the base flow state and substituted into the Euler equations (2). By neglecting the second-order perturbation terms, one obtains

$$\left(\phi_{yy}+\frac{\phi_{xx}}{2y}-\left(H''(\psi_0)-\frac{I''(\psi_0)}{2y}\right)\phi\right)_{xx}+\frac{\sigma\chi_{0y}}{w_0^2}\phi_x+\frac{2\sigma}{w_0}\left(\phi_{yy}+\frac{\phi_{xx}}{2y}\right)_x+\frac{\sigma^2}{w_0^2}\left(\phi_{yy}+\frac{\phi_{xx}}{2y}\right)=0 \tag{6}$$

For the detailed derivation of Eq. (6), see Ref. [5]. Equation (6) is the basic stability equation in this study. The eigenvalue problem (6) is solved subject to a set of boundary conditions

$$\phi(x,0)=0,\quad \phi(x,1/2)=0,\quad \text{for}\quad 0\le x\le L$$

$$\phi(0,y)=0,\quad \phi_{xx}(0,y)=0,\quad k(0,y)=0,\quad \text{for}\quad 0\le y\le 1/2$$

$$\phi_x(L,y)=0,\quad \text{for}\quad 0\le y\le 1/2 \tag{7}$$

These boundary conditions are used in Ref. [5]. The problem (6) is reformulated in Ref. [11] as a linear operator perturbation problem

$$\overbrace{-m(y)\left[\left(\phi_{yy}+\frac{\phi_{xx}}{2y}\right)-\frac{w_{0yy}}{w_0}\phi\right]}^{T^{(0)}}$$

$$+\sigma\overbrace{\int_0^x -m(y)\left[\left(\frac{2}{w_0}\left(\phi_{yy}+\frac{\phi_{xx}}{2y}\right)-\frac{w_{0yy}}{w_0^2}\right]dx}^{T^{(1)}}$$

$$+\sigma^2\overbrace{\int_0^x\int_0^x -\frac{m(y)}{w_0^2}\left(\phi_{yy}+\frac{\phi_{xx}}{2y}\right)dxdx}^{T^{(2)}}=\Omega\phi \tag{8}$$

where $\Omega=\omega^2$ and $m(y)$ is the weight function, defined by

$$m(y)=\frac{2w_0^2y^2}{(I_0(\psi_0(y))_y} \tag{9}$$

The solution of Eq. (8) is subject to the following boundary conditions:

$$\phi(x,0)=0,\quad \phi(x,1/2)=0,\quad \text{for}\quad 0\le x\le L$$

$$\phi(0,y)=0,\quad \text{for}\quad 0\le y\le 1/2$$

$$\phi_x(L,y)=0,\quad \text{for}\quad 0\le y\le 1/2 \tag{10}$$

3 The Perturbation Method and Implementation

It has been shown in Ref. [11] that Eq. (8) can be effectively solved for any columnar base flow by the perturbation method. Then, Eq. (8) takes the form

$$T(\sigma)=T^{(0)}+\sigma T^{(1)}+\sigma^2T^{(2)} \tag{11}$$

in which $T^{(0)}$ is an unperturbed self-adjoint linear operator in an appropriate Hilbert space. For the stability problem (Eq. (8)) the spectrum of $T^{(0)}$ is discrete and simple, denoted by $\lambda_0,\lambda_1,\lambda_2,\ldots$, with corresponding orthonormal eigenvectors $\{e_0,e_1,e_2,\ldots\}$

$$T^{(0)}e_0=\lambda_0e_0$$

$$T^{(0)}e_i=\lambda_ie_i,\quad i=1,2,\ldots. \tag{12}$$

We are looking for a local functional dependence $\lambda(\sigma)$ near $\sigma=0$, $\lambda=\lambda_0$. Using the perturbation theory, $\lambda(\sigma)$ can be shown to be an analytic function of σ in a neighborhood of $\sigma=0$, and admits a power series expansion

$$\lambda(\sigma)=\lambda_0+\sum_{n=1}^{\infty}\lambda^{(n)}\sigma^n \tag{13}$$

The coefficients $\lambda^{(n)}$ can be found from the operators $T^{(0)}$, $T^{(1)}$, and $T^{(2)}$.

To proceed, two linear operators related to $T^{(0)}$ must be introduced.

1. The projection P onto the eigensubspace spanned by the eigenvector e_0 is
$$Pu=(u,e_0)e_0 \tag{14}$$
where $(.,.)$ denote the inner product of the Hilbert space.
2. The reduced resolvent S is
$$Su=\sum_{i=1}^{\infty}(\lambda_i-\lambda_0)^{-1}(u,e_i)e_i \tag{15}$$

The coefficients $\lambda^{(n)}$ can be found by (see the detailed derivation in Ref. [13])

$$\lambda^{(n)}=\sum_{p=1}^{n}\frac{(-1)^p}{p}\sum_{v_1+\cdots+v_p=n,\ k_1+\cdots+k_p=p-1}\times\mathrm{tr}[T^{(v_1)}S^{(k_1)}\cdots T^{(v_p)}S^{(k_p)}] \tag{16}$$

where $S^{(k)}=S^k$ for integer $k>0$, $S^{(0)}=-P$, and the symbol tr stands for the trace of a linear operator. Note that in this formula, the sum should be taken over all combinations of positive integers p with $1\le p\le n$ and $v_1,v_2,\ldots,v_p$ with $v_j=1$ or 2, $v_1+\cdots+v_p=n$ and $k_1+\cdots+k_p=p-1$.

In Ref. [13], the terms in Eq. (16) up to $\lambda^{(4)}$ have been explicitly given as

$$\lambda^{(1)}=\mathrm{tr}[T^{(1)}P]$$

$$\lambda^{(2)}=\mathrm{tr}[T^{(2)}P-T^{(1)}ST^{(1)}P]$$

$$\lambda^{(3)}=\mathrm{tr}[-T^{(1)}ST^{(2)}P-T^{(2)}ST^{(1)}P+T^{(1)}ST^{(1)}ST^{(1)}P-T^{(1)}S^2T^{(1)}PT^{(1)}P]$$

$$\begin{aligned}\lambda^{(4)}=\mathrm{tr}[&-T^{(2)}ST^{(2)}P+T^{(1)}ST^{(1)}ST^{(2)}P+T^{(1)}ST^{(2)}ST^{(1)}P\\&+T^{(2)}ST^{(1)}ST^{(1)}P-T^{(1)}S^2T^{(1)}PT^{(2)}P-T^{(1)}S^2T^{(2)}PT^{(1)}P\\&-T^{(2)}S^2T^{(1)}PT^{(1)}P-T^{(1)}ST^{(1)}ST^{(1)}ST^{(1)}P\\&+T^{(1)}S^2T^{(1)}ST^{(1)}PT^{(1)}P+T^{(1)}ST^{(1)}S^2T^{(1)}PT^{(1)}P\\&+T^{(1)}S^2T^{(1)}PT^{(1)}ST^{(1)}P-T^{(1)}S^3T^{(1)}PT^{(1)}PT^{(1)}P]\end{aligned} \tag{17}$$

These formulas can be used to obtain the fourth-order expansion. To obtain up to eighth-order expansions, we must find out the relevant formulas in a feasible way. It was found that the length of the formulas grows very fast: $\lambda^{(5)}$ has 40 terms; $\lambda^{(6)}$ has 144 terms; $\lambda^{(7)}$ has 544 terms; and $\lambda^{(8)}$ has 2128 terms.

Using the identity $\mathrm{tr}\,AB=\mathrm{tr}\,BA$, we can reduce the number of terms in Eq. (16) by combining the similar terms. In fact, we have

$$\begin{aligned}\frac{(-1)^p}{p}\mathrm{tr}[T^{(v_1)}S^{(k_1)}\cdots T^{(v_p)}S^{(k_p)}] &= \frac{(-1)^p}{p}\mathrm{tr}[T^{(v_p)}S^{(k_p)}T^{(v_1)}S^{(k_1)}\cdots T^{(v_{p-1})}S^{(k_{p-1})}]\\ &\cdots\cdots\\ &= \frac{(-1)^p}{p}\mathrm{tr}[T^{(v_2)}S^{(k_2)}T^{(v_3)}S^{(k_3)}\cdots T^{(v_1)}S^{(k_1)}]\end{aligned} \tag{18}$$

where the formula on right-hand side is subsequently obtained by moving each term $T^{(v_{p_0})}S^{(k_{p_0})}$, $1 \le p_0 \le p$ one step to the right in a cyclic way

$$v_1, v_2, \cdots, v_p \mapsto v_p, v_1, \cdots, v_{p-2}, v_{p-1} \mapsto \cdots \mapsto v_2, v_3, \cdots, v_{p-1}, v_1$$

$$k_1, k_2, \cdots, k_p \mapsto k_p, k_1, \cdots, k_{p-2}, k_{p-1} \mapsto \cdots \mapsto k_2, k_3, \cdots, k_{p-1}, k_1 \tag{19}$$

Adding up the p number of such terms in the summand, one obtains

$$(-1)^p \mathrm{tr}[T^{(v_1)}S^{(k_1)} \cdots T^{(v_p)}S^{(k_p)}] \tag{20}$$

This simplifies Eq. (16) to

$$\lambda^{(n)} = \sum_{p=1}^{n} (-1)^p \sum_{v_1+\cdots+v_p=n,\ k_1+\cdots+k_p=p-1} \mathrm{tr}[T^{(v_1)}S^{(k_1)} \cdots T^{(v_p)}S^{(k_p)}] \tag{21}$$

where in the sum, the k_p-tuple should be taken for all possible nonequivalent $(k_1, k_2, \cdots, k_p)$ such that $k_1+k_2+\cdots+k_p=p-1$. Two k_p-tuples are said to be equivalent if they are identical by rotating one of them without changing the order, if necessary. From Eq. (21), we derive the following steps to develop the formulas for various n for the stability problem.

1. For $p=1,2,\ldots,n$, find all the possible nonequivalent nonnegative integer k_p-tuple $(k_1, k_2, \cdots, k_p)$ such that $k_1+\cdots+k_p=p-1$. This can be done, for a valid p, by generating all the k_p-tuples satisfying $k_1+\cdots+k_p=p-1$ and then deleting all the equivalent ones.
2. Find all the possible v_p-tuples $(v_1, v_2, \cdots, v_p)$ such that $v_1+\cdots+v_p=n$ with $v_j=1$ or 2.
3. Write down the term $(-1)^p \mathrm{tr}[T^{(v_1)}S^{(k_1)} \cdots T^{(v_p)}S^{(k_p)}]$, in the summand, for each $(k_1, k_2, \cdots, k_p)$ obtained in step 1, and for all $(v_1, v_2 \cdots, v_p)$ obtained in step 2.

This task is carried out by a MATLAB program. It ultimately relieves us of the burden to write the lengthy formulas.

To evaluate the trace in the formulas, we use

$$\mathrm{tr}\, AP = (APe_0, e_0) = (Ae_0, e_0) \tag{22}$$

Note that the terms in the expansion (21) can be always arranged to end with the projection P, since one of $(k_1, k_2, \ldots, k_p)$ must be zero from $k_1+\cdots+k_p=p-1$. For a term in the summand, the trace can be found by successively using the following formula:

$$\begin{aligned}
\mathrm{tr}[T^{(v_1)}S^{(k_1)} \cdots T^{(v_{p-1})}S^{(k_{p-1})}T^{(v_p)}P] &= (T^{(v_1)}S^{(k_1)} \cdots T^{(v_{p-1})}S^{(k_{p-1})}T^{(v_p)}e_0, e_0) \\
&= \left(T^{(v_1)}S^{(k_1)} \cdots T^{(v_{p-1})}S^{(k_{p-1})} \sum_{i_1} (T^{(v_p)}e_0, e_{i_1})e_{i_1}, e_0\right) \\
&= \begin{cases} \left(T^{(v_1)}S^{(k_1)} \cdots T^{(v_{p-1})} \sum_{i_2, i_2 \neq 0} \sum_{i_1} (\lambda_{i_2} - \lambda_0)^{-k_{p-1}} (T^{(v_p)}e_0, e_{i_1})e_{i_2}, e_0\right), & \text{if } k_{p-1} \neq 0 \\ (T^{(v_1)}S^{(k_1)} \cdots T^{(v_{p-1})}(T^{(v_p)}e_0, e_0)e_0, e_0), & \text{if } k_{p-1} = 0 \end{cases}
\end{aligned} \tag{23}$$

Let $k_{j_1}, k_{j_2}, \ldots, k_{j_q}$ be the nonzero entries in $(k_1, k_2, \ldots, k_p)$. We have $k_{j_1}+k_{j_2}+\cdots+k_{j_q}=p-1$, and an exact formulation for the trace can be obtained as

$$\mathrm{tr}[T^{(v_1)}S^{(k_1)} \cdots T^{(v_{p-1})}S^{(k_{p-1})}T^{(v_p)}P] = \sum_{i_1, i_2, \ldots, i_q} \frac{(T^{(v_1)}e_0, e_{1^*})(T^{(v_2)}e_{1^*}, e_{2^*}) \cdots (T^{(v_{p-1})}e_{(p-1)^*}, e_{p^*})(T^{(v_p)}e_{p^*}, e_0)}{(\lambda_{i_1} - \lambda_0)^{k_{j_1}} (\lambda_{i_2} - \lambda_0)^{k_{j_2}} \cdots (\lambda_{i_q} - \lambda_0)^{k_{j_q}}} \tag{24}$$

where the nested summation indices $i_1, i_2, \ldots, i_q$ run from 1 to infinity, and the subscripts (of e_{l^*}) $l^*, l=1,2,\ldots,p$ stand for

$$i_s, \quad \text{for} \quad l=j_s \ \ 1 \le s \le q, \quad \text{and} \quad \text{for } 0, \text{otherwise} \tag{25}$$

Applying Eq. (24) to Eq. (17), one obtains

$$\begin{aligned}
\lambda^{(1)} &= (T^{(1)}e_0, e_0) \\
\lambda^{(2)} &= (T^{(2)}e_0, e_0) - (T^{(1)}ST^{(1)}e_0, e_0) = (T^{(2)}e_0, e_0) \\
&\quad - \sum_{i, i \neq 0} \frac{(T^{(1)}e_0, e_i)(T^{(1)}e_i, e_0)}{(\lambda_i - \lambda_0)}
\end{aligned} \tag{26}$$

Eq. (24) together with Eq. (21) completely define $\lambda^{(i)}$ and can be implemented to find $\lambda^{(i)}$. Taking advantage of the explicit expression, we develop another MATLAB program that automatically generates the numerical codes to compute $\lambda^{(i)}$.

4 Analysis of the Operators $T^{(0)}$, $T^{(1)}$, $T^{(2)}$

The perturbation method, after the implementation presented in Sec. 3, is readily applied to the stability problem (8). Following the same steps in Ref. [11], we proceed as follows:

1. Solve the eigenvalue problem for $T^{(0)}$, which reads as

$$-m(y)\left[\left(\phi_{yy} + \frac{\phi_{xx}}{2y}\right) - \frac{w_{0yy}}{w_0}\phi\right] = \Omega\phi \tag{27}$$

subject to the boundary conditions (10). The normalized eigenfunctions of Eq. (27) denoted by $\phi^*_{o,n}(x,y)$ are given by

$$\phi^*_{o,n}(x,y) = \sqrt{\frac{2}{L}}\Phi^*_{o,n}(y)\sin\left(\frac{(2n-1)\pi x}{2L}\right) \tag{28}$$

with $\Phi^*_{o,n}(y)$ solving the reduced zeroth-order eigenvalue problem

$$\Phi_{yy} - \frac{(2n-1)^2\pi^2\Phi}{8L^2 y} + \left(\frac{\Omega_{o,n}}{m(y)} - \frac{w_{0yy}}{w_0}\right)\Phi = 0$$

$$\Phi(0) = 0, \quad \Phi\left(\tfrac{1}{2}\right) = 0 \tag{29}$$

and normalized as

$$\left(\int_0^{0.5} \frac{\Phi^{*2}_{o,n}(y)}{m(y)} dy\right)^{1/2} = 1 \tag{30}$$

where $\Omega_{o,n}=\omega^2_{o,n}$ are eigenvalues with $o=1,2,3,\ldots$ and $n=1,2,3,\ldots$ in the order $\Omega_{o_1,n_1} \le \Omega_{o_2,n_2}$ for $o_1 \le o_2$ and $n_1 \le n_2$. The eigenvalues $\Omega_{o,n}$ (or $\omega_{o,n}$) are called critical swirls, see Ref. [14], where neutral modes exist.

2. Two types of inner products $(T^{(1)}\phi^*_{o_1,m}, \phi^*_{o_2,n})$ and $(T^{(2)}\phi^*_{o_1,m}, \phi^*_{o_2,n})$ must be evaluated. As has been shown, these inner products can be evaluated in a remarkably simple way for all columnar swirling flows. In the following, for simplicity, we only consider the swirling flow with a uniform axial flow. Let $I_1(m,n)$ and $I_2(m,n)$ denote

$$I_1(m,n) = \begin{cases} \dfrac{8L}{(2m-1)^2\pi^2} & \text{if } n = m \\ \dfrac{4L}{(2m-1)\pi^2}\left[\dfrac{4}{(2n-1)} + \dfrac{(-1)^{(n+m-1)}-1}{(n+m-1)} + \dfrac{(-1)^{(n-m)}-1}{(n-m)}\right] & \text{if } n \neq m \end{cases} \tag{31}$$

and

$$I_2(m,n) = \begin{cases} \dfrac{4L^2}{\pi^3}\left[\dfrac{-\pi}{(2m-1)^2} + \dfrac{4(-1)^{m+1}}{(2m-1)^3}\right] & \text{if } n = m \\ \dfrac{(-1)^{n+1}16L^2}{(2n-1)^2(2m-1)\pi^3} & \text{if } n \neq m \end{cases} \tag{32}$$

In terms of $I_1(m,n)$ and $I_2(m,n)$, the following useful formulas can be obtained:

$$(T^{(1)}\phi^*_{o_1,m}, \phi^*_{o_2,n}) = \Omega_{o_1,m} I_1(m,n)(\Phi^*_{o_1,m}, \Phi^*_{o_2,n})_1$$

$$(T^{(2)}\phi^*_{o_1,m}, \phi^*_{o_2,n}) = \Omega_{o_1,m} I_2(m,n)(\Phi^*_{o_1,m}, \Phi^*_{o_2,n})_2 \tag{33}$$

where

$$(\Phi^*_{o_1,m}, \Phi^*_{o_2,n})_1 = \int_0^{1/2} \frac{\Phi^*_{o_1,m}\Phi^*_{o_2,n}}{m(y)w_0}dy$$

$$(\Phi^*_{o_1,m}, \Phi^*_{o_2,n})_2 = \int_0^{1/2} \frac{\Phi^*_{o_1,m}\Phi^*_{o_2,n}}{m(y)w_0^2}dy \tag{34}$$

3. At the critical swirl levels $\Omega_{o,m}$, let $\Delta_{o,m}\Omega(\sigma)$ be the swirl increment as a function of σ. The actual swirl can then be written in terms of $\Delta_{o,m}\Omega(\sigma)$ as

$$\Omega = \Omega_{o,m} + \Delta_{o,m}\Omega(\sigma) \tag{35}$$

The perturbation theory of linear operators claims that the function $\Delta_{o,m}\Omega(\sigma)$ is analytic in a complex disc, and has a power series expansion

$$\Delta_{o,m}\Omega(\sigma) = \Omega^{(1)}_{o,m}\sigma + \Omega^{(2)}_{o,m}\sigma^2 + \Omega^{(3)}_{o,m}\sigma^3 + \cdots \tag{36}$$

We will develop an eighth-order approximation of Eq. (36) for the solid-body rotation flow and the Lamb–Oseen vortex.

5 Case Study: The Solid-Body Rotation Flow

5.1 The Approximations of Growth Rate of the Solid-Body Rotation Flow. The solid-body rotation flow is defined as a column of fluid flowing at a constant axial velocity $w_0(r)=W_0=1$, $v_0(r)=r$ and $u_0(r)=0$. For this flow, the stability equation (6) takes a particular simple form

$$\left(\phi_{yy} + \frac{\phi_{xx}}{2y} + \frac{\Omega}{2y}\phi\right)_{xx} + 2\sigma\left(\phi_{yy} + \frac{\phi_{xx}}{2y}\right)_x + \sigma^2\left(\phi_{yy} + \frac{\phi_{xx}}{2y}\right) = 0 \tag{37}$$

where $\Omega=4\omega^2$ is a rescaled swirl parameter. Carefully examining this equation, one can find that all terms except ϕ_{yy} have a common factor $1/2y$. This makes it possible to be solved by the method of separation of variables. For the detailed analysis, we refer to Wang and Rusak [5] and Gallaire and Chomaz [9]. As a well studied case with an accurate growth rate function available, the solid-body rotation flow serves as an ideal vortex model for us to conduct a benchmark case study of the perturbation method.

By using the perturbation method, the stability equation takes the form

$$\overbrace{\left(\phi_{yy} + \frac{\phi_{xx}}{2y} + \frac{\Omega}{2y}\phi\right)}^{T^{(0)}} + \sigma\overbrace{\int_0^x 2\left(\phi_{yy} + \frac{\phi_{xx}}{2y}\right)dx}^{T^{(1)}} + \sigma^2\overbrace{\int_0^x\int_0^x\left(\phi_{yy} + \frac{\phi_{xx}}{2y}\right)dxdx}^{T^{(2)}} = 0 \tag{38}$$

The growth rates of the solid-body rotation flow have been computed by using the high-order method up to the eighth-order. The resulting growth rate curves will be compared to the exact growth rate curves. We focus on the growth rate curve that is located between the first and second critical swirls $\omega_{1,1}$ and $\omega_{1,2}$, respectively. There, the flow loses its stability and undergoes the vortex breakdown process. We will show that the high-order method, reinforced by using special techniques, leads to an accurate reconstruction of the whole growth rate curve in this range of swirl.

We apply the eighth-order perturbation method to the solid-body rotation flow in a pipe of length $L=10$. In Table 1, the coefficients up to the eighth-order approximations of the first two branches are given. All the computations are based on using 20 terms in the summations. Four digits accuracy of these coefficients are therefore reported.

The computational cost depends on the order of the method and the number of terms used in summation. Table 2 shows the CPU usage. Note that all the computations were run on a personal computer with Pentium process 1.5 GHz.

As we see from this table, the computational cost is low for all

Table 1 The computational results of $\Omega^{(i)}_{1,m}$ for $m=1,2$ and $i=1,2,\ldots,8$

	$m=1$	$m=2$
$\Omega^{(1)}_{1,m}$	119.21	13.423
$\Omega^{(2)}_{1,m}$	24,115	−21,876
$\Omega^{(3)}_{1,m}$	1.3679×10^{7}	-1.3839×10^{7}
$\Omega^{(4)}_{1,m}$	1.0267×10^{10}	-1.0390×10^{10}
$\Omega^{(5)}_{1,m}$	8.7748×10^{12}	-8.8025×10^{12}
$\Omega^{(6)}_{1,m}$	8.0876×10^{15}	-8.0904×10^{15}
$\Omega^{(7)}_{1,m}$	7.8315×10^{18}	-7.8310×10^{18}
$\Omega^{(8)}_{1,m}$	7.8559×10^{21}	-7.8557×10^{21}

Table 2 CPU usage in seconds, where *k* is the number of terms used in the summations

	$\Omega_{1,1}^{(5)}$	$\Omega_{1,1}^{(6)}$	$\Omega_{1,1}^{(7)}$	$\Omega_{1,1}^{(8)}$
$k=10$	0.16	0.79	5.16	119
$k=20$	0.2	1.95	43	1363

of the computations. It takes at most about 20 min to complete the computation of $\Omega_{1,1}^{(8)}$, and takes much less time for other lower-order computations.

Various orders of the approximated growth rate curves, emanated from the first and second critical swirls, are plotted in Fig. 1 against the exact growth rate curve. The left plot shows the approximations from the first-order to fourth-order and the right plot shows the approximations from the fifth-order to the eighth-order. Also shown is the exact result from Wang and Rusak [5]. For $\sigma < 0.0005$ the fifth to eighth approximations are virtually identical to the exact growth rate curve. However, a closer examination of the approximations near $\sigma \approx 0.003$, as shown in Fig. 2, reveals the

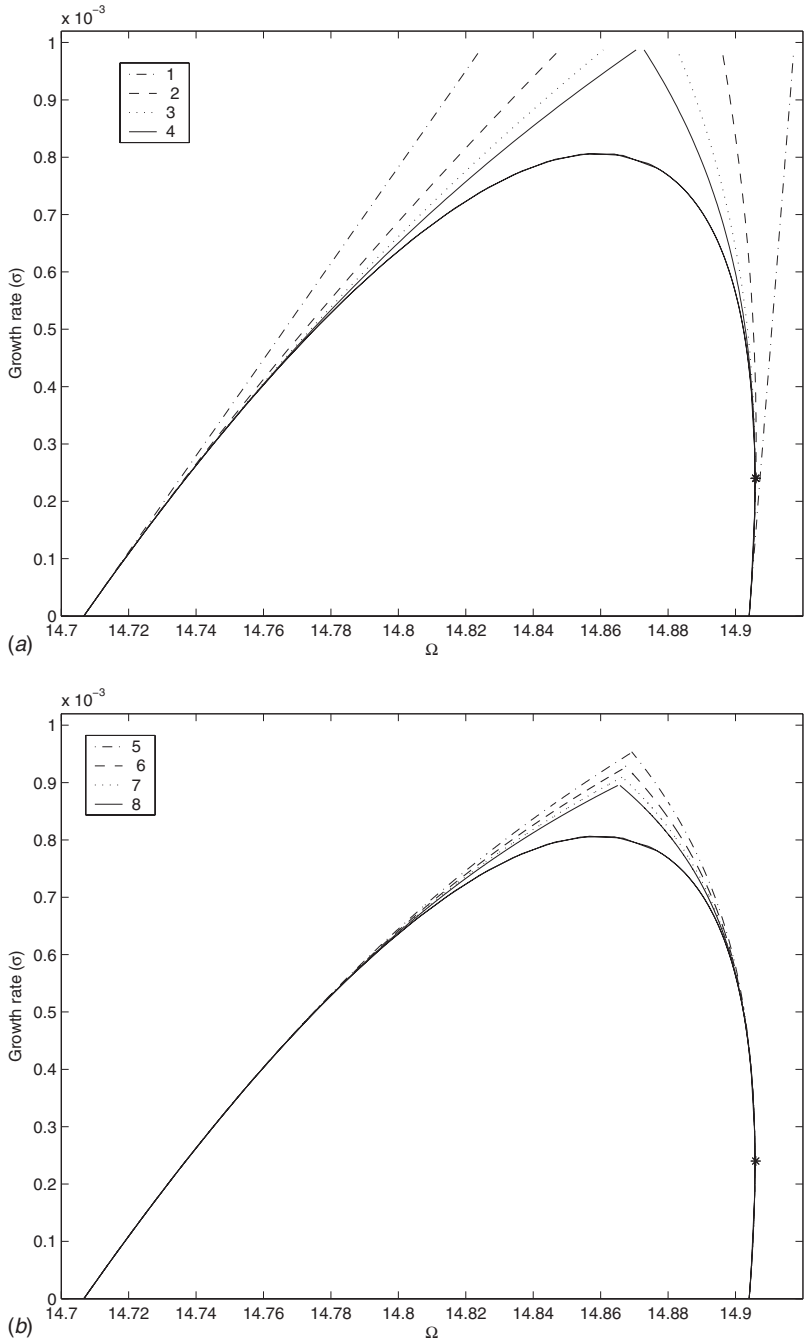

Fig. 1 The first-order to eighth-order approximations of the growth rate curves between first and second critical swirls. The smooth solid black curve indicates the exact solution. (*a*): first-order to fourth-order approximations. (*b*): fifth-order to eighth-order approximations. The asterisk is the branching point (Ω^*, σ^*).

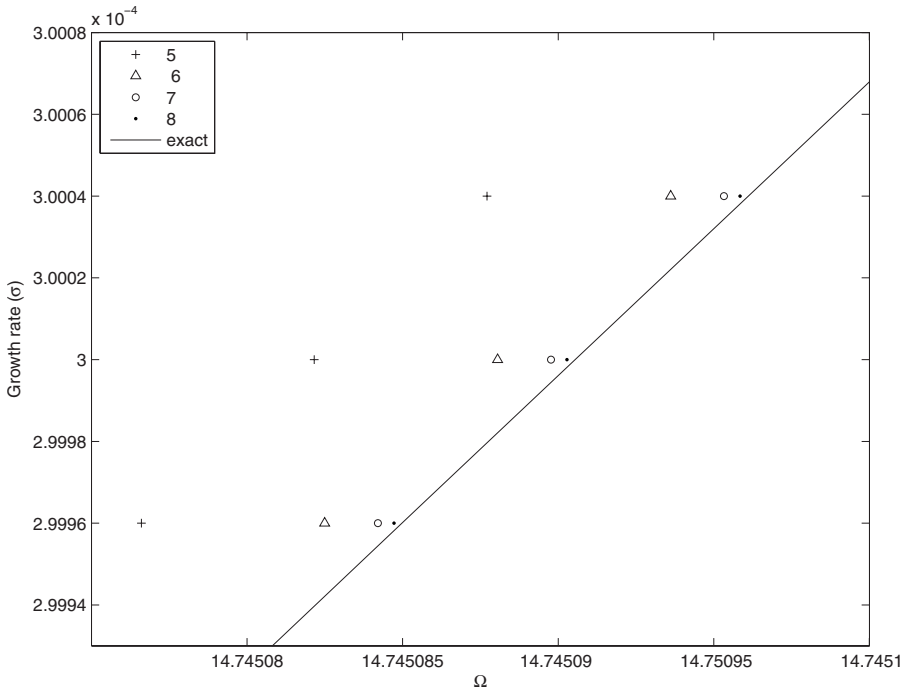

Fig. 2 The convergence history of the approximations from the fifth-order method to the eighth-order method at $\sigma \approx 0.0003$

convergence history from the fifth-order method to the eighth-order method. The improvement of the approximation using higher-order method is clearly observed. However, the errors of the fifth to the eighth approximations are extremely small for this range of growth rate and the advantage of the higher-order method is not really necessary here. The purpose to use higher-order method is to obtain an accurate approximation in a relatively larger range of growth rate. The truncation errors of using finite terms in a Taylor series is determined by the remainder of Taylor series. The quality of the approximation depends, therefore, on the order of the method and also on the rate of convergence of the Taylor series. We will show, in the following, the improvement of the approximation by increasing the order of the method. We will also show the improvement of the approximation by using some novel ideas to accelerate the convergence of the Taylor series in the next section.

The improvement of the approximations from the first-order to the eighth-order method over the interval $(0, \sigma_{\max})$, where $\sigma_{\max}$ is the maximum growth rate between the first and the second critical swirls, has been found to be progressive. One finds, in particular, that the fourth-order method provides accurate results up to the level of about 50% of $\sigma_{\max}$, and the eighth-order method improves the effective coverage up to about 70% of $\sigma_{\max}$. Of these ranges, however, the approximated growth rate curves are seen to be significantly departing from the exact one, and triangle-shaped areas between the approximated growth rate curves and the exact one are observed. It can be seen that the triangle-shaped area in the eighth-order approximation is significantly smaller than that of the fourth-order approximation, a clear indication of the improvement of computations by using a higher-order method. On the second branch of the growth rate curve, an asterisk is shown in Fig. 1, where a complex branch of growth rate curve emerges, see, for example, Ref. [9]. The branching point is denoted by (Ω^*, σ^*).

5.2 Construction of the Growth Rate Curves by Using Novel Approach

5.2.1 Construction of the First Branch of the Growth Rate Curve. We can further improve the approximation by using methods with a few orders higher than the eighth-order (but not more than that, due to the fact that the computational cost rapidly increases, soon beyond current feasibility). However, by carefully examining the approximations in Fig. 1, it can be seen that the improvement from fifth-order to eighth-order is noticeably slower than the improvement from the first-order to the fourth-order. This trend is expected to continue at higher-orders. In fact, according to the present approximations, the function $\Delta_{1,1}\Omega(\sigma)$ is singular at $\sigma_{\max}$ with its derivative becoming infinite. The slow convergence of a power series expansion of an analytic function near a singular point is a common phenomenon and is anticipated. To further improve the approximation of the growth rate function near $\sigma_{\max}$, we propose the following approach. We consider, instead of $\Delta_{1,1}\Omega(\sigma)$, the Taylor series of the inverse function of $\Delta_{1,1}\Omega(\sigma)$, denoted by $\sigma_1(\Delta_1\Omega)$, where $\Delta_1\Omega = \Omega - \Omega_{1,1}$ for the first branch of growth rate function (Similarly, the inverse function of $\Delta_{1,2}\Omega(\sigma)$: $\sigma_2(\Delta_2\Omega)$, where $\Delta_2\Omega = \Omega - \Omega_{1,2}$ for the second branch of the growth rate function). It is apparent that $\sigma_1(\Delta_1\Omega)$ is no longer singular at the swirl Ω_m, where the growth rate reaches the maximum: $\sigma_{\max} = \sigma_1(\Omega_m - \Omega_{1,1})$. One notices that $\sigma_1(\Delta_1\Omega)$ encounters a singular point at Ω^*, slightly above the second critical swirl. There exists now a finite distance between Ω^* and Ω_m. It is, therefore, possible that the power series expansion of $\sigma_1(\Delta_1\Omega)$ may behave better than that of $\Delta_{1,1}\Omega(\sigma)$. As will be demonstrated, this idea works very well for the solid-body rotation flow.

The coefficients of the Taylor expansion of $\sigma_1(\Delta_1\Omega)$ (or $\sigma_2(\Delta_2\Omega)$) can be found from the eighth-order expansion of $\Delta_{1,1}\Omega(\sigma)$ (or $\Delta_{1,2}\Omega(\sigma)$) through the inverse function relationship. In general, if $y = f(x)$ is smooth function at $x_0, y_0 = f(x_0)$ and $f'(x_0) \neq 0$, we have, by direct differentiation

$$[f^{-1}(y_0)]' = \frac{1}{f'(x_0)}$$

$$[f^{-1}(y_0)]'' = -\frac{f''(x_0)}{f'(x_0)^3}$$

Table 3 The computational results of $C_m^{(i)}$ for $m=1,2$ and $i=1,2,\ldots,8$

	$m=1$	$m=2$
$C_m^{(1)}$	8.388×10^{-3}	7.450×10^{-2}
$C_m^{(2)}$	2.847×10^{-2}	1.809×10^{2}
$C_m^{(3)}$	-1.166×10^{-1}	1.578×10^{4}
$C_m^{(4)}$	-1.3739	2.2879×10^{7}
$C_m^{(5)}$	-2.296×10^{2}	4.645×10^{10}
$C_m^{(6)}$	-5.482×10^{3}	1.212×10^{14}
$C_m^{(7)}$	-1.427×10^{4}	3.868×10^{17}
$C_m^{(8)}$	-5.050×10^{5}	1.458×10^{21}

$$[f^{-1}(y_0)]^{[3]}=\frac{3f''(x_0)^2}{f'(x_0)^5}-\frac{f^{[3]}(x_0)}{f'(x_0)^4}$$

$$[f^{-1}(y_0)]^{[4]}=-\frac{15f''(x_0)^3}{f'(x_0)^7}-\frac{f^{[4]}(x_0)}{f'(x_0)^5}+\frac{10f''(x_0)f^{[3]}(x_0)}{f'(x_0)^6}$$

$$[f^{-1}(y_0)]^{[5]}=\frac{105f''(x_0)^4}{f'(x_0)^9}-\frac{105f''(x_0)^2f^{[3]}(x_0)}{f'(x_0)^8}+\frac{15f''(x_0)f^{[4]}(x_0)}{f'(x_0)^7}+\frac{10f^{[3]}(x_0)^2}{f'(x_0)^7}-\frac{f^{[5]}(x_0)}{f'(x_0)^6}$$

$$\ldots\ \ldots \tag{39}$$

The lengthy formulas for $[f^{-1}(y_0)]^{[6]}$, $[f^{-1}(y_0)]^{[7]}$, $[f^{-1}(y_0)]^{[8]}$ are obtained in a straightforward manner and are omitted here. By using Eq. (39) and the data presented in Table 2, we can find the first eight coefficients in the Taylor series expansions

$$\sigma_1(\Delta_1\Omega)\approx\sum_{i=1}^{8}C_1^{(1)}(\Delta_1\Omega)^i \quad \text{and} \quad \sigma_2(\Delta_2\Omega)\approx\sum_{i=1}^{8}C_2^{(1)}(\Delta_2\Omega)^i \tag{40}$$

for the first and second branches, and the results are listed in Table 3.

The resulting growth rate curves are shown in Fig. 3, together with the eighth-order approximation of $\Delta_{1,1}\Omega(\sigma)$. It is found that the first branch of approximation is remarkably improved. The new growth rate approximation is much closer to the exact one than the eighth-order approximation of $\Omega_{1,1}(\sigma)$. However, the approximation of the second branch by the new approach is apparently worse than the original expansion. This can be explained as that $\sigma_2(\Delta_2\Omega)$ encounters a singular point at Ω^*, where the derivative of $\sigma_2(\Delta_2\Omega)$ becomes infinite and its Taylor expansion must diverge. This gives a much smaller interval of convergence than that of the original function $\Delta_{1,2}\Omega(\sigma)$.

5.2.2 Construction of the Second Branch of the Growth Rate Curve. We seek further improvement of the approximation of the second branch of growth rate function by extending the "inverse function" method. Consider a linear transformation of the coordinates

$$y=a(x-\bar{x}),\quad y=\bar{y} \tag{41}$$

where a is a constant. Equation (41) can be written in matrix form as

$$\begin{bmatrix}x\\y\end{bmatrix}=\begin{bmatrix}1 & a^{-1}\\0 & 1\end{bmatrix}\begin{bmatrix}\bar{x}\\\bar{y}\end{bmatrix} \tag{42}$$

A differentiable function $y=f(x)$ can be transformed to the new coordinates $(\bar{x},\bar{y})$ by

$$\bar{y}=f(x(\bar{x};a)) \tag{43}$$

where $x(\bar{x};a)$ is implicitly determined by

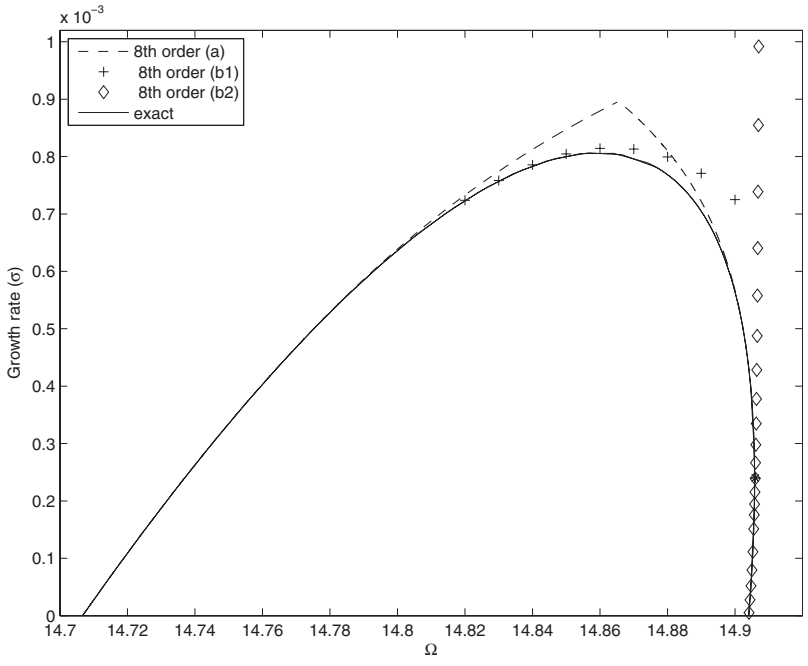

Fig. 3 The comparison of $\Delta_{1,1}\Omega(\sigma)$ (dashed line − − denotes eighth-order (a)), $\Delta_{1,2}\Omega(\sigma)$ (dashed line − − denotes eighth-order (a)), $\sigma_1(\Delta_1\Omega)$ (plus sign + denotes eighth-order (b1)), and $\sigma_2(\Delta_2\Omega)$ (diamond ◇ denotes eighth-order (b2)). The solid line indicates the exact solution.

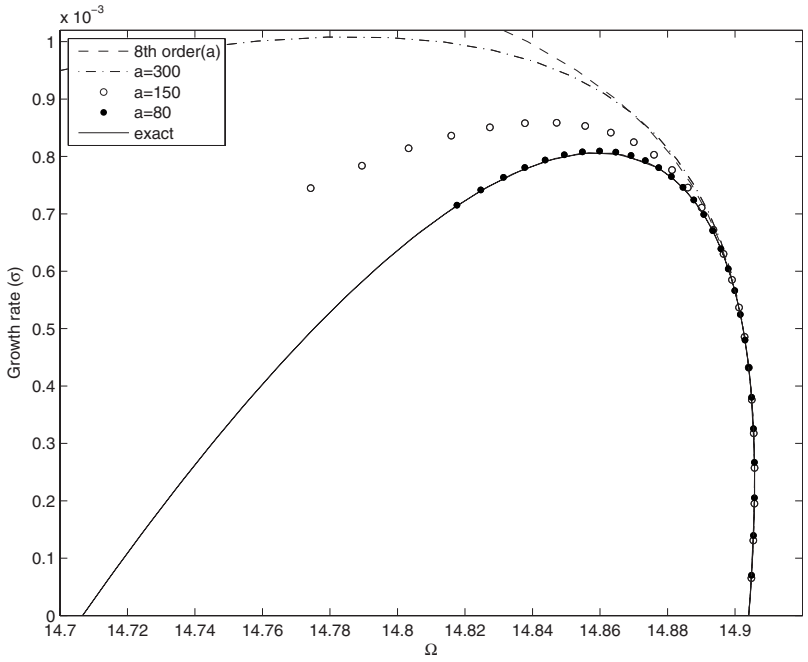

Fig. 4 The comparison of the approximation by using the original eighth-order Taylor expansion $\Delta_{1,2}\Omega(\sigma)$ (dashed line − − denotes eighth-order (a)) and the approximations by using the new approach with $a=300,150,80$. The solid line indicates the exact solution.

$$a(x-\bar{x}) = f(x) \tag{44}$$

The inverse function approach can be regarded to correspond to the linear transformation

$$\begin{bmatrix} x \\ y \end{bmatrix} = \begin{bmatrix} 0 & 1 \\ 1 & 0 \end{bmatrix} \begin{bmatrix} \bar{x} \\ \bar{y} \end{bmatrix} \tag{45}$$

The crucial fact is that $f(x(\bar{x};a))$ may admit a Taylor series with better approximation than that of $f(x)$. From Eq. (44) we find, by differentiations

$$[f(x(\bar{x};a))]' = a(x'(\bar{x};a)-1), \quad \text{where} \quad x'(\bar{x};a) = \frac{a}{a-f'(x)}$$

$$[f(x(\bar{x};a))]'' = x'(\bar{x};a)^3 f''(x)$$

$$[f(x(\bar{x};a))]''' = 3x'(\bar{x};a)^2 x''(\bar{x};a) f''(x) + x'(\bar{x};a)^4 f'''(x)$$

$$\begin{aligned}[f(x(\bar{x};a))]^{[4]} &= 6x'(\bar{x};a)x''(\bar{x};a)^2 f''(x) + 3x'(\bar{x};a)^2 x'''(\bar{x};a) f''(x) \\ &\quad + 7x'(\bar{x};a)^3 x'' f'''(x) + x'(\bar{x};a)^5 f^{[4]}(x)\end{aligned}$$

$$\begin{aligned}[f(x(\bar{x};a))]^{[5]} &= 6x''(\bar{x};a)^3 f''(x) + 18x'(\bar{x};a)x''(\bar{x};a)x'''(\bar{x};a) f''(x) \\ &\quad + 27x'(\bar{x};a)^2 x''(\bar{x};a)^2 f'''(x) + 3x'(\bar{x};a)^2 x^{[4]} \\ &\quad \times(\bar{x};a) f''(x) + 10x'(\bar{x};a)^3 x'''(\bar{x};a) f'''(x) \\ &\quad + 12x'(\bar{x};a)^4 x''(\bar{x};a) f^{[4]}(x) + x'(\bar{x};a)^6 f^{[5]}(x)\end{aligned} \tag{46}$$

and the recursive relationship

$$x^{[n]}(\bar{x};a) = \frac{[f(x(\bar{x};a))]^{[n]}}{a} \quad \text{for} \quad n \geq 2 \tag{47}$$

We apply the linear transformation to the second branch of growth rate function $\Delta_{1,2}(\sigma)$ and define the function $\Delta_{1,2}(\sigma(\bar{\sigma},a))$, where $\sigma(\bar{\sigma})$ is implicitly defined by

$$a(\sigma-\bar{\sigma}) = \Delta_{1,2}(\sigma) \tag{48}$$

Using the derivatives $\Delta_{1,2}^{[n]}\Omega(\sigma)$ at $\sigma=0$ for $n\leq 5$, and Eqs. (46) and (47), we may evaluate the first five orders of derivatives for the function $\Delta_{1,2}(\sigma(\bar{\sigma},a))$, and thus obtain a fifth-order Taylor expansion for this function. $\Delta_{1,2}\Omega(\sigma)$ can be re-established by transferring back to the original variable σ.

Our computations show that the parameter a critically affects the convergence behaviors and we can optimize a to achieve a satisfactory approximation with the fifth-order Taylor expansion. Figure 4 demonstrates the successive improvements from $a=300$ to $a=80$. Note that the original expansion corresponds to the case $a=\infty$. This explains why the approximation at $a=300$ is very close to the original eighth-order approximation. The matching between the exact solution and its approximation at $a=80$ is excellent. Complementing this with the eighth-order method, namely, by using the approximation of $\sigma_1(\Delta_1\Omega)$ for the first branch and using the current approximation with $a=80$ for the second branch, the growth rate curve can be accurately approximated for the whole range of swirl between the first and second critical levels, as shown in Fig. 5. This figure also shows that the two branches of approximations are nicely overlapped in a range of swirl. This suggests a practical method to optimize the parameter a when an exact growth rate curve is not available, as is always the situation in applications of the current method. Namely, optimization of a can be achieved by matching the two branches of approximations in the overlapped range.

6 The Growth Rate Curve of the Lamb–Oseen Vortex

In this section, we apply the high-order method, together with the associated techniques for further improving the approximation, to the Lamb–Oseen vortex. We construct the growth rate curve between the first and second critical swirls for the Lamb–Oseen vortex. It should be noted that the Lamb–Oseen vortex is a more realistic vortex model than the solid-body rotation flow and is widely used in the study of the vortex breakdown phenomenon

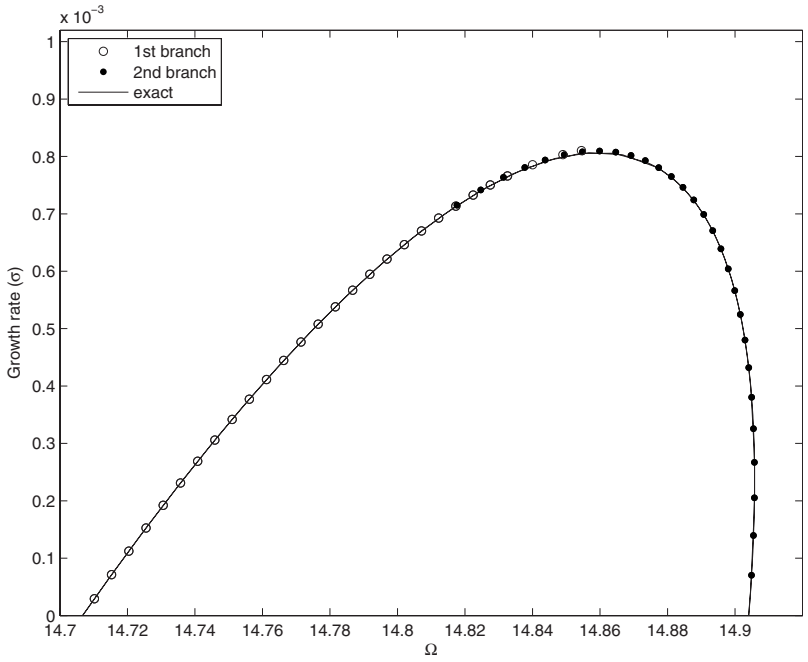

Fig. 5 The construction of the growth rate curve by jointly using the improved first branch (○) and second branch (·) of approximations. The solid line indicates the exact solution.

(see Ref. [15]). The growth rate curve obtained in this section provides crucial information for the incipience of the bubble type of vortex breakdown in swirling flows close to the real physics.

6.1 The Eighth-Order Approximation of the Growth Rate Curve. The circumferential velocity component of the Lamb–Oseen vortex contains a vortical core at the center in which the flow is similar to the solid-body rotation flow whereas outside this vortex core the flow is close to an irrotational (potential) rotating flow. The axial velocity of the Lamb–Oseen vortex is uniform. The flow is specified by its axial and circumferential velocity components

$$w_0(r) = W_0 = 1$$

$$\omega v_0(r) = \omega \frac{(1 - e^{-r^2/r_c^2})}{r} \tag{49}$$

in which ω is the swirl and r_c is the vortex core.

For convenience, let $\beta = 1/r_c^2$, one finds from Eq. (49)

$$v_0(y) = \frac{1 - e^{-2\beta y}}{\sqrt{2y}} \tag{50}$$

The stability equation is formulated as the following perturbation problem:

$$\overbrace{-m(y)\left(\phi_{yy} + \frac{\phi_{xx}}{2y}\right)}^{T^{(0)}} + \sigma \overbrace{\int_0^x \left[-2m(y)\left(\phi_{yy} + \frac{\phi_{xx}}{2y}\right)\right] dx}^{T^{(1)}}$$

$$+ \sigma^2 \overbrace{\int_0^x \int_0^x \left[-m(y)\left(\phi_{yy} + \frac{\phi_{xx}}{2y}\right)\right] dx dx}^{T^{(2)}} = \Omega\phi \tag{51}$$

subject to the boundary conditions (10), where

$$m(y) = \frac{y^2}{\beta(1 - e^{-2\beta y})e^{-2\beta y}} \tag{52}$$

By using the eighth-order method, we perform the computation of $\Omega_{1,m}^{(k)}$ for a case study of the Lamb–Oseen vortex with $\beta = 4$ and pipe length $L = 6$. The results are presented in Table 4. Figure 6 shows the first and second branches of the growth rate curves based on the coefficients shown in Table 4. The approximations from the first to the eighth-order methods exhibit a similar behavior to what has been found in the case of the solid-body rotation flow. It was found that the approximation of the growth rate curve progressively converges as the order of approximation increases. However, the rate of convergence slows down as the order increases.

6.2 Reconstruction of the Growth Rate Curve. In the following, we apply the techniques, which are effectively used in the solid-body rotation flow to improve the approximation, to the Lamb–Oseen vortex. The first step is to find the inverse function expansion, using the same technique

Table 4 The computational results of $\Omega_{1,m}^{(i)}$ for $m=1,2$ and $i=1,2,\ldots,8$

	$m=1$	$m=2$
$\Omega_{1,m}^{(1)}$	3.8049	0.43526
$\Omega_{1,m}^{(2)}$	214.70	−192.81
$\Omega_{1,m}^{(3)}$	3.2837×10^4	-3.3778×10^4
$\Omega_{1,m}^{(4)}$	6.7487×10^6	-6.8683×10^6
$\Omega_{1,m}^{(5)}$	1.5807×10^9	-1.5863×10^9
$\Omega_{1,m}^{(6)}$	3.9891×10^{11}	-3.9109×10^{11}
$\Omega_{1,m}^{(7)}$	1.0560×10^{14}	-1.0560×10^{14}
$\Omega_{1,m}^{(8)}$	2.8981×10^{16}	-2.8981×10^{16}

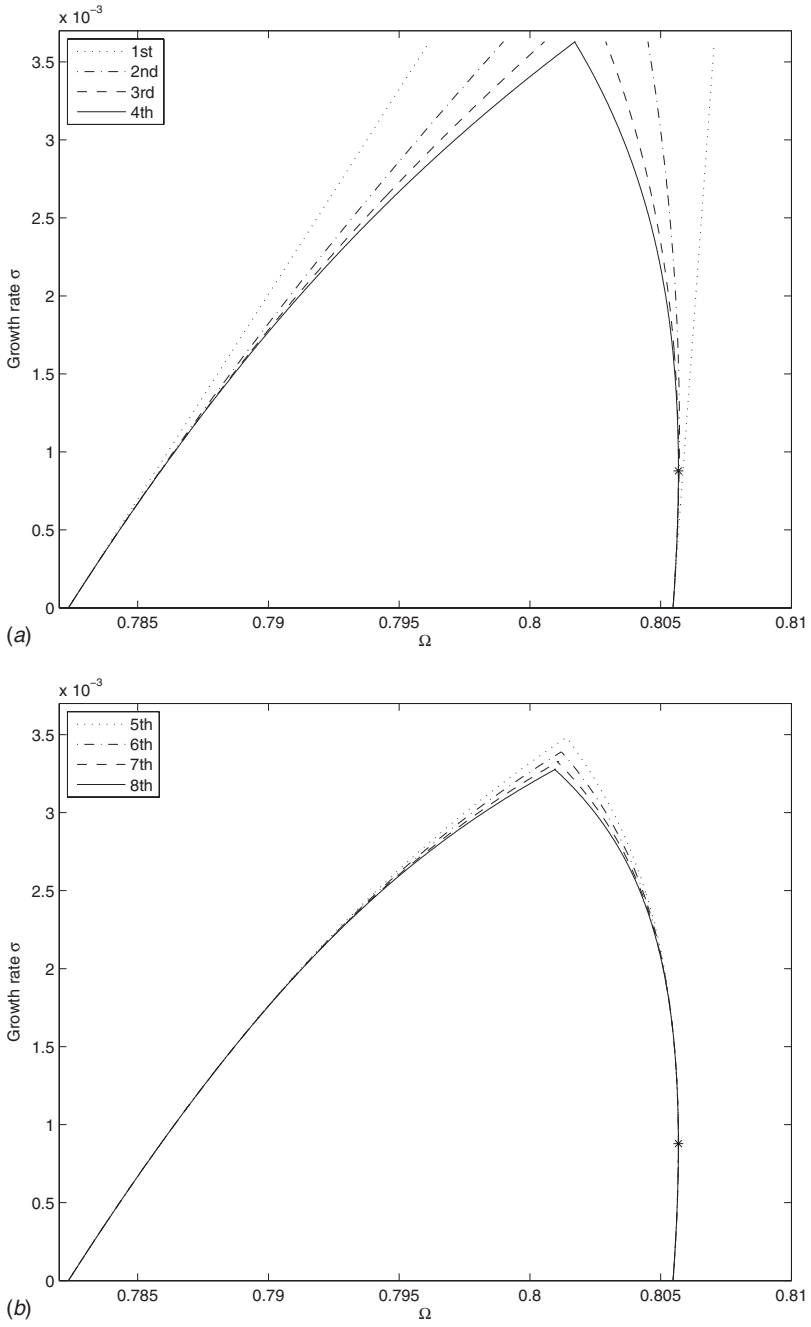

Fig. 6 The first-order to eighth-order approximations of the growth rate curves between first and second critical swirls. (*a*): first-order to fourth-order approximations. (*b*): fifth-order to eighth-order approximations.

$$\sigma_1(\Delta_1\Omega) \approx \sum_{i=1}^{8} C_1^{(i)}(\Delta_1\Omega)^i \tag{53}$$

The coefficients $C_1^{(i)}$ are presented in Table 5. The resulting approximated growth rate curves, together with the original eighth-order approximation of $\Delta_{1,1}\Omega(\sigma)$ and $\Delta_{1,2}\Omega(\sigma)$, are shown in Fig. 7. Although an exact growth rate curve is missing in the case, comparing Fig. 7 to Fig. 3 reveals a similar behavior of the approximations. A significant improvement of the approximation by using the expansion of Eq. (53) is achieved. However, the inverse function expansion of the second branch of growth rate function is once again worth than the original eighth-order approximation.

Table 5 The computational results of $C_1^{(i)}$ for $i=1,2,\ldots,8$

$C_1^{(1)}$	$C_1^{(2)}$	$C_1^{(3)}$	$C_1^{(4)}$	$C_1^{(5)}$	$C_1^{(6)}$	$C_1^{(7)}$	$C_1^{(8)}$
0.2628	−7.795	-2.464×10^{2}	-2.715×10^{4}	-4.008×10^{6}	-7.532×10^{8}	-1.616×10^{11}	-5.449×10^{13}

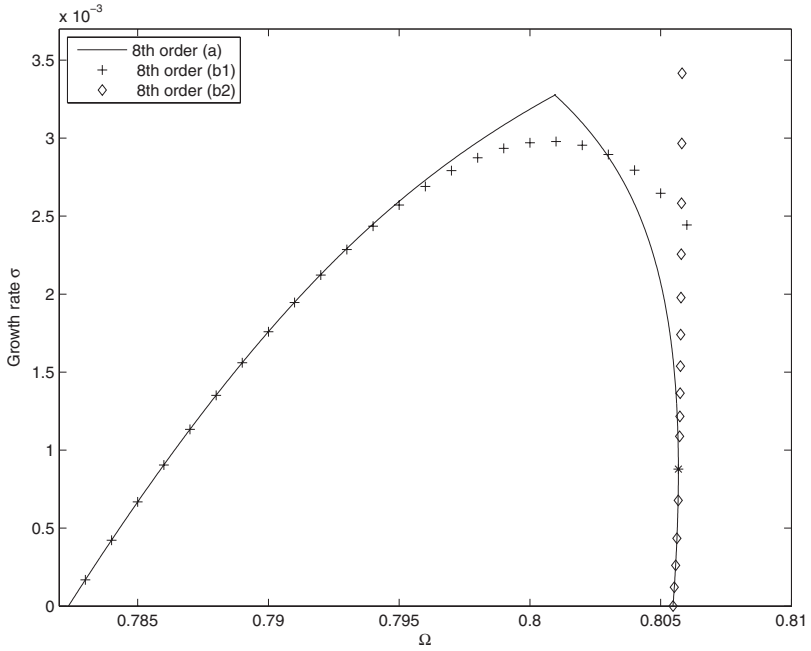

Fig. 7 The eighth-order approximations of the growth rate curve by using different approaches: $\Delta_{1,1}\Omega(\sigma)$ (solid line denotes eighth-order (a)), $\Delta_{1,2}\Omega(\sigma)$ (solid line denotes eighth-order (a)), $\sigma_1(\Delta_1\Omega)$ (plus sign + denotes eighth-order (b1)), and $\sigma_2(\Delta_2\Omega)$ (diamond ◇ denotes eighth-order (b2))

We then construct the second branch of growth rate curve by using the method stated in Sec. 5.2.2. we optimize a to achieve a satisfactory approximation with the fifth-order Taylor expansion. Figure 8 demonstrates the successive improvements from $a=10$ to $a=2.57$. It is found that the approximation of $a=10$ is very close to the original approximation by using eighth-order method. The matching between the first branch approximation and the second branch approximation with $a=2.57$ is excellent. The complete growth rate curve between the first and second critical swirl levels is, thereby, reconstructed, as shown in Fig. 9.

We have done numerical simulations of the linearized equations of Eq. (2). Starting from a given but rather arbitrary initial disturbance, the flow eventually evolves into a flow state corresponding to the unstable mode with the largest growth rate. As in this case,

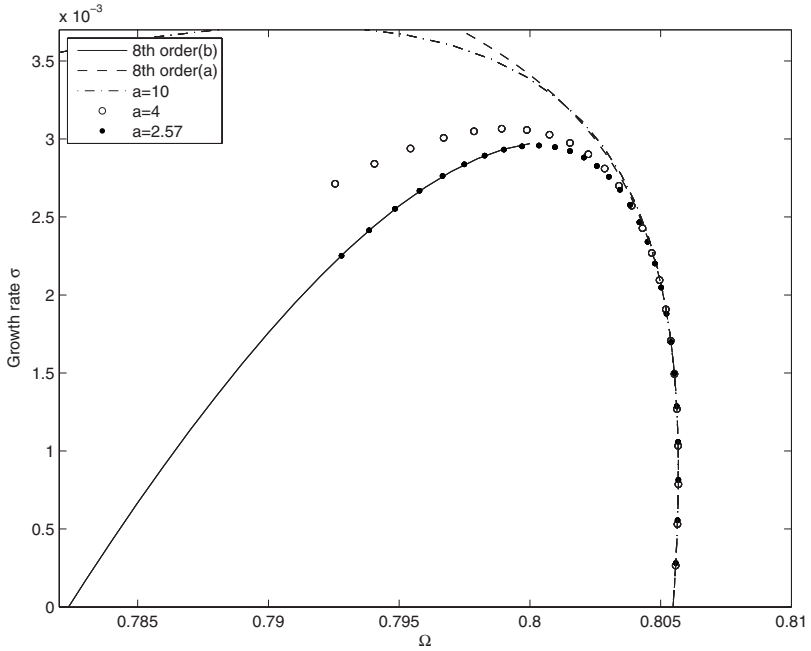

Fig. 8 The comparison of the approximation by using the original eighth-order Taylor expansion $\Delta_{1,2}\Omega(\sigma)$ (dashed line − − denotes eighth-order (a)) and the approximations by using the new approach with $a=10,4,2.57$. The first branch approximation $\sigma_1(\Delta_1\Omega)$ (solid line denotes eighth-order (b)) is used in the matching process to optimize the second branch approximation.

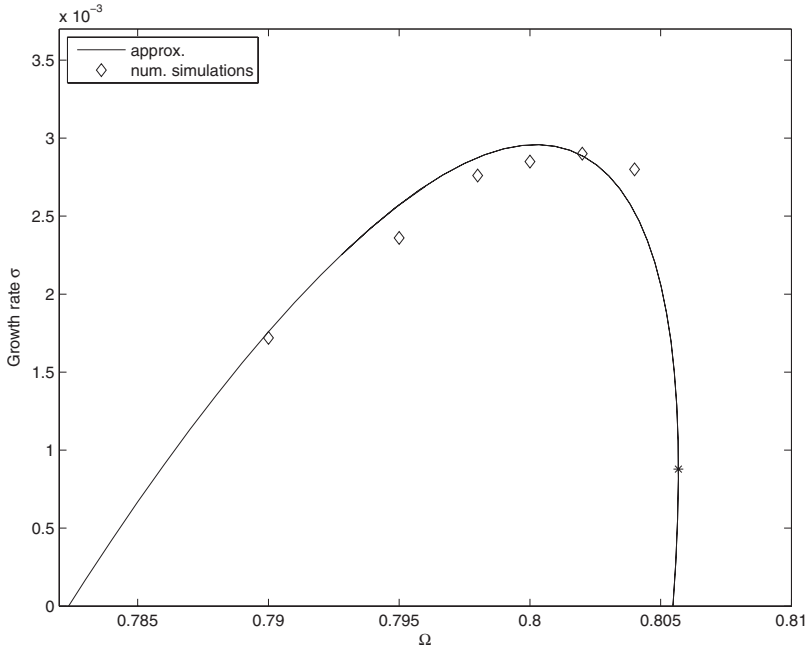

Fig. 9 Reconstruction of the whole growth rate curve: the solid line is the approximated growth rate curve and the diamond (◇) is the direct numerical simulation result. The asterisk is the branching point.

only one unstable mode exists and its growth rate can then be found in terms of this long time behavior. The second-order central difference scheme is used in spatial discretization and the time evolution is integrated by using a fourth-order Rungs–Kutta method. The simulated growth rates are plotted in Fig. 9 with diamonds. The agreement of the direct numerical simulations and the growth rate found in this study is of physical significance: The primary dynamical evolution of the bubble type of vortex breakdown has been quantitatively confirmed. This is particularly important in the vortex breakdown problem, as the fundamental physical mechanism is still a debating issue.

7 Conclusions

We develop in this paper a calculation method to accurately construct the growth rate curve of the Lamb–Oseen vortex (as a representative of a vortex flow model) for swirl levels between the first and second critical swirls. This range of swirl is crucial for the study of the vortex breakdown phenomenon, as the base flow starts the initial stage of transition to the vortex breakdown state. The method is based on the perturbation theory of linear operators. On the basis of the work presented in Ref. [11], an eighth-order method has been developed to improve the accuracy of the approximation of the growth rate curve.

We conduct a benchmark case study of the solid-body rotation flow. It is found that the eighth-order method associated with some special techniques is sufficient to accurately construct the growth rate curve in the range of swirl between the first and second critical swirls. The method is then applied to the Lamb–Oseen vortex to construct the growth rate curve between the first and second critical swirls for this vortex flow. As a direct application, we compare the growth rate curve to the direct numerical simulation results and an overall agreement between the two has been found.

The present paper demonstrates that the Wang and Rusak instability mechanism captures quantitatively the initial disturbance growth in the Lamb–Oseen vortex, which evolves eventually into a breakdown state. Understanding the vortex flow dynamics at the initial stages of instability and transition to breakdown is crucial for the design of future control systems to delay (or to enhance) the appearance of vortex breakdown in swirling flows.

Acknowledgment

This research was carried out with the support of the University of Auckland under Grant No. 3622940/9844.

References

[1] Leibovich, S., 1984, "Vortex Stability and Breakdown: Survey and Extension," AIAA J., **22**(9), pp. 1192–1206.
[2] Ash, R. L., and Khorrami, M. R., 1995, "Vortex Stability," *Fluid Vortices*, S. I. Green, ed., Kluwer, Dordrecht, The Netherlands, pp. 317–372.
[3] Rayleigh, L., 1917, "On the Dynamics of Revolving Fluids," Proc. R. Soc. London, Ser. A, **93**, pp. 148–154.
[4] Wang, S., and Rusak, Z., 1997, "The Dynamics of a Swirling Flow in a Pipe and Transition to Axisymmetric Vortex Breakdown," J. Fluid Mech., **340**, pp. 177–223.
[5] Wang, S., and Rusak, Z., 1996, "On the Stability of an Axisymmetric Rotating Flow in a Pipe," Phys. Fluids, **8**(4), pp. 1007–1076.
[6] Rusak, Z., 1998, "The Interaction of Near-Critical Swirling Flows in a Pipe With Inlet Vorticity Perturbations," Phys. Fluids, **10**(7), pp. 1672–1684.
[7] Rusak, Z., Wang, S., and Whiting, C. H., 1998, "The Evolution of a Perturbed Vortex in a Pipe to Axisymmetric Vortex Breakdown," J. Fluid Mech., **366**, pp. 211–237.
[8] Rusak, Z., and Judd, K. P., 2001, "The Stability of Non-Columnar Swirling Flows in Diverging Streamtubes," Phys. Fluids, **13**(10), pp. 2835–2844.
[9] Gallaire, F., and Chomaz, J.-M., 2004, "The Role of Boundary Conditions in a Simple Model of Incipient Vortex Breakdown," Phys. Fluids, **16**(2), pp. 274–286.
[10] Gallaire, F., Chomaz, J.-M., and Huerre, P., 2004, "Closed-Loop Control of Vortex Breakdown: A Model Study," J. Fluid Mech., **511**, pp. 67–93.
[11] Wang, S., 2008, "A Novel Method for Analyzing the Global Stability of Inviscid Columnar Swirling Flow in a Finite Pipe," Phys. Fluids, **20**(7), p. 074101.
[12] Szeri, A., and Holmes, P., 1988, "Nonlinear Stability of Axisymmetric Swirling Flows," Philos. Trans. R. Soc. London, Ser. A, **326**, pp. 327–354.
[13] Kato, T., 1966, *Perturbation Theory for Linear Operators. Die Grundlehren der mathematischen Wissenschaften*, Vol. 132, Springer-Verlag, New York.
[14] Benjamin, T. B., 1962, "Theory of the Vortex Breakdown Phenomenon," J. Fluid Mech., **14**, pp. 593–629.
[15] Faler, J. H., and Leibovich, S., 1978, "An Experimental Map of Internal Structure of a Vortex Breakdown," J. Fluid Mech., **86**, pp. 313–335.

G. P. Willems

J. P. Kroes[1]
e-mail: j.p.kroes@tue.nl

Department of Mechanical Engineering,
Technische Universiteit Eindhoven,
P.O. Box 513,
5600 MB Eindhoven, The Netherlands

M. Golombok
Department of Mechanical Engineering,
Technische Universiteit Eindhoven,
P.O. Box 513,
5600 MB Eindhoven, The Netherlands;
Shell Exploration and Production,
Kessler Park 1,
2288 GS Rijswijk, The Netherlands

B. P. M. van Esch

H. P. van Kemenade

J. J. H. Brouwers

Department of Mechanical Engineering,
Technische Universiteit Eindhoven,
P.O. Box 513,
5600 MB Eindhoven, The Netherlands

Performance of a Novel Rotating Gas-Liquid Separator

A novel gas separation process makes use of a rotating phase separator to separate micron-sized droplets from a gas stream. Based on an industrial scale design, a water/air separator is constructed and tested. The first experiment concerns the drainage of large fractions of separated liquid. During operation, drainage is observed via windows and a descriptive model is formulated. Because of the major influence on overall separation efficiency, liquid drainage is a key issue in the separator design. The second experiment comprises a droplet collection efficiency measurement using micron-sized droplets dispersed within the airstream. The separation efficiency of fine droplet removal is measured. This is an important factor in reducing capital costs. [DOI: 10.1115/1.4001008]

Keywords: rotational separation, separation efficiency, liquid drainage

1 Introduction

Condensed rotational separation (CRS) is a new centrifugal method for separating bulk mixtures of gases [1–4]. The mixture is cooled to a temperature at which the contaminant condenses to micron-sized mist particles, which are removed by mechanical separation. A potential application of this technology is removing CO_2 and/or H_2S from contaminated natural gas wells with typical flow rates of 30–300 m_n^3/s (i.e., normal cubic meters per second). Measurements on a laboratory scale experimental setup at a flow rate of 16×10^{-3} m_n^3/s [5] have delivered the proof of principle. The resulting liquid droplets, which have to be separated, are on the order of microns. To remove fine particles from a gas stream the rotating phase separator (RPS) has been developed. The basic idea behind the RPS is a rotating cylinder consisting of a multitude of axially oriented channels (Fig. 1). The channels are only a couple of millimeters in diameter so that particles as small as 1 μm can be effectively centrifugated to the walls. At equal external dimensions and energy consumption (either electrical or due to pressure drop), the particles collected are typically ten times smaller than those separated in a corresponding cyclone [2]. The RPS was originally applied for air filtration, water purification in utilities, (hot) flue gas filtering, drying of (natural) gas, and sanitary particle recovery [6–10]. The cocurrent arrangement and high liquid load are new aspects in the application for condensed rotational separation.

In applying the CRS concept for cleaning natural gas, the cooling of the contaminated gas mixture is obtained by expanding to a lower pressure and temperature. After expansion, the fraction of the condensed liquid to be separated is typically in the range 0.5–5% v/v. For example, a 50% CO_2/CH_4 mixture condensed at −50°C and 30 bars has a liquid volume fraction of 4% v/v. The example stated in Table 1 (70% CH_4 and 30% CO_2 at $p=30$ bars and $T=-60$°C) has a liquid volume fraction of 1.6%. Given the density increase during condensation, there is thus a considerable liquid loading (in mass terms) of the downstream RPS unit. Experiments with a large liquid loading on a small-scale unit showed losses in separation efficiency due to clogging and back-up of liquid CO_2 [5]. Liquid removal was then recognized as one of the key design challenges. This led to several design modifications, which were implemented in a large-scale RPS design. The design is suited for large liquid loads and is schematically shown in Fig. 2. We now describe the details.

Gas containing a mist of droplets enters the unit via a tangential inlet. First coarse droplets (larger than 10 μm) are separated in the preseparator section. The preseparator acts as a cyclone and collects the droplets in a stationary volute. This liquid leaves via a tangentially connected exit (liquid exit 1).

The gas stream, containing the remaining mist of mainly micron-sized droplets, enters the rotating element (Fig. 1). While traveling in the axial direction through the rotating channels, the droplets are driven to the channel walls by centrifugal force (see Fig. 1, right hand side). On the walls the mist droplets coagulate into a thin film. The rotating element thus acts as a droplet coalescer. For optimal film behavior and minimal pressure drop the flow direction through the element is downward [11]. Due to gravitational and shear forces, the film is forced out of the channels.

[1]Corresponding author.

Contributed by the Fluids Engineering Division of ASME for publication in the JOURNAL OF FLUIDS ENGINEERING. Manuscript received May 26, 2009; final manuscript received January 5, 2010; published online March 17, 2010. Assoc. Editor: Theodore Heindel.

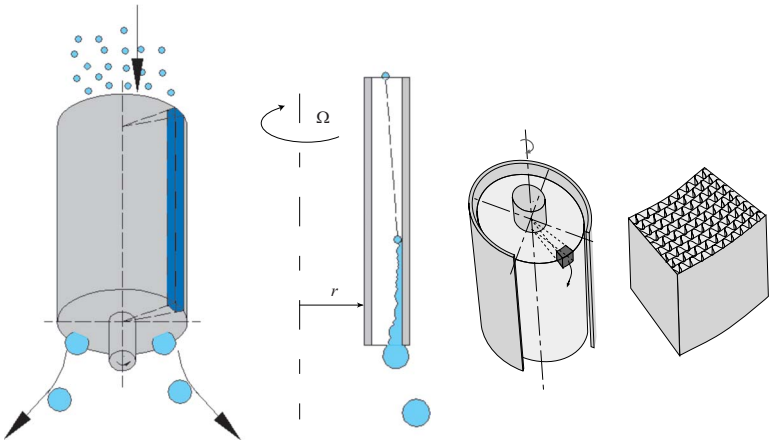

Fig. 1 Schematic of the RPS rotating element and droplet separation in a channel

At the end of the channels (Fig. 2, pos. A) the film breaks up into droplets of typically 50 μm. The outer wall of the rotating element extends in the axial direction beyond the end of the channels. This ensures that the solid body rotation of the gas stream leaving the element is maintained. Droplets that break off at the end of the channels are centrifugally separated from the gas in this rotating field (B), and collected in a film on the rotating outer wall (C).

Downstream of the element the postseparator section is entered, where the liquid is actually separated from the gas stream. The liquid film leaves the gas stream at the end of the extended outer wall of the rotating element (Fig. 2, pos. D) toward a nonrotating collection volute. The liquid still contains significant momentum, which drives a standing film (F) within the stationary volute. Via a tangentially connected large diameter exit (liquid exit 2) the liquid leaves towards a collection vessel. The inner wall of the collection volute (G) keeps the liquid separated from the product gas flow. This wall prevents re-entrainment of liquid due to splashing in the postseparator.

Table 1 Operating parameters comparing field application conditions to the experimental test unit

	Field application	Test rig analog
Gas	CH_4 (70 mol % of feed)	Air
Contaminant	CO_2 (30 mol % of feed)	Water
Product gas flow rate	0.45 m^3/s	0.50 m^3/s maximum
Liquid waste loading	7.5 l/s	9 l/s maximum
Pressure	30 bars	1 bar
Temperature	−60°C	20°C

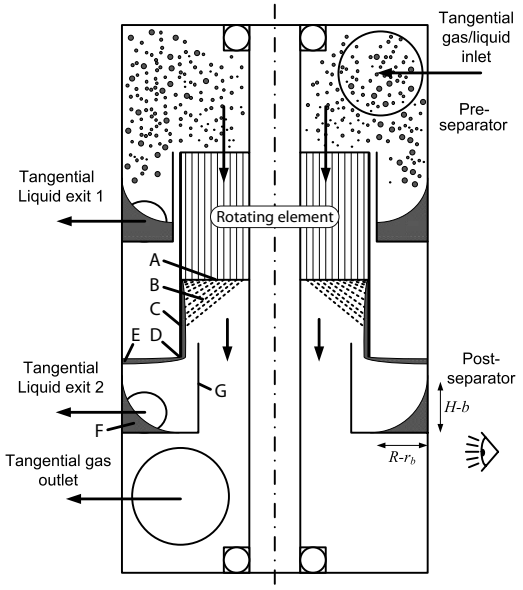

Fig. 2 Schematic of a rotating phase separator

In order to obtain a better understanding of the dominating physical phenomena during liquid drainage, a visually accessible industrial scale prototype has been built, based on the upscale design described above. In this way potential flaws in the design can be tackled before final construction. The prototype was connected to an atmospheric test rig with water and air as working fluids. The test setup approximately models a 24 m_n^3/s (80 MMscf/d) equivalent installation on a natural gas well with 30% v/v contamination (see comparison in Sec. 3 below). This article reports two different experiments concentrating, respectively, on removal of separated liquid and on droplet separation efficiency.

The goal of the liquid removal measurement is to determine whether the designed separator can cope with the large amounts of liquid that will be encountered under real process conditions (up to 7.5 kg/s). A model is developed to describe the hydrodynamic behavior of the liquid in the collecting volute of the postseparator.

The separation efficiency measurements are used to validate whether the design calculations concerning the capture fraction of small droplets are correct. The advantage of a RPS compared with cyclones in terms of separation efficiency only becomes significant in large-scale units [2], and this prototype is the first industrial scale unit for this application. Existing centrifugal technology is based on cyclone systems often with some sort of ancillary droplet entrapment mechanism such as a mist mat [2]. These systems have been predominantly used for either water removal or removal of condensate from natural gas. The pressure and temperature conditions are reasonably close to ambient. Such cyclone systems, however, require that the liquid droplets have achieved a size of 15–20 μm prior to swirling, and this requires considerable growth and agglomeration times. Smaller droplets can only be removed if the residence times are increased. Compared with water or condensate removal, the pressure is higher and temperatures lower for removal of CO_2 from gas. Maintaining these conditions over extended pipe lengths is not practicable for the high flow conditions associated with gas processing (30–300 m_n^3/s). An alternative is then to go to a multicyclone configuration—however, this leads to complex and expensive batteries of systems, which require careful dividing of streams and then separa-

tion and combining of the resultant product and waste streams. By contrast, the separator described here has been shown to be able to separate small droplets at the high throughput rates associated with gas fields [12]. In fact, it can be instructively viewed as an integrated cheap multicyclone because each of the ~15,000 channels itself functions as a minicyclone with similar separation performance. From an engineering point of view the rotation is an order of magnitude lower than in turbomachinery, being typically on the order of 1000 rpm. In addition, the tangentially induced input swirl is sufficient to drive the rotation. Thus no external drive is necessary in a full scale system. In the prototype developed here, we do have an external drive simply for having more control over experimental variables during development.

To measure the separation efficiency curve, a droplet mist is injected at the inlet, and particle volume concentrations and size distributions after separation are measured in the gas stream using particle light diffraction [13]. A significant amount of droplets in the range 0–10 μm was created, and the size distributions of these droplets could be measured sufficiently accurate.

In Sec. 2 a theoretical model is presented, describing the hydrodynamics of the liquid in the postseparator. Section 3 describes the experimental setup and measurement methods. In Sec. 4 the results of the liquid removal measurements are compared with the theoretical model. Also the measured efficiencies are compared with previous theoretical predictions.

2 Liquid Drainage

The postseparator significantly affects the overall separation efficiency. As discussed above, in the postseparator section, rotating liquid emerges from the end of the filter element (Fig. 2, pos. A) and collects on the rotating extended sleeve (Fig. 2, pos. C). The important thing is to get the film from the rotating sleeve, into the stationary volute scoop (G). This results in momentum dissipation. There are thus two impulse transfer effects that need to be considered.

- The fluid exits the rotating element and hits the stationary volute at E (Fig. 2) losing impulse.
- The remaining impulse is effectively fed to the film and drives the film (F) into the tangential liquid exit 2.

The aim of the derivations that follow is to model the liquid drainage from the stationary postseparator liquid collection volute sufficiently accurately to come to a reliable design. The main question is the amount of liquid that can be drained from the volute via a tangential outlet. The liquid flow rate is mainly determined by the fluid velocity at the tangential outlet (Fig. 2, liquid exit 2).

Because the drainage relies on the fluid momentum, the momentum dissipation in the volute is of importance. In order to determine the momentum dissipation within the collection bucket, the contact area between the fluid and the wall has to be estimated. The contact area in combination with the local velocity and friction factor determine the local momentum dissipation. The incoming feed momentum, in combination with the momentum dissipation, yields the outflow conditions.

2.1 Liquid Film Dimensions. Within the liquid collection volute of the postseparator a liquid film forms (Fig. 2, pos. F), which is supported by the bottom and outer wall of the *stationary* volute. As a first step, the geometry of the liquid film interface is determined. Defining a cylindrical coordinate system (r,θ,z) with the volute bottom and the shaft rotation axis (see Fig. 2) as the r- and z-axes, respectively, the coordinate definition through a cross section of the film can be found in Fig. 3. The following relation for the pressure within the liquid at a position (r,z) below the liquid-gas interface at $z_i(r)$ can be derived [14]:

$$p(r,z) = p_g + \rho_l g(z_i(r) - z) \tag{1}$$

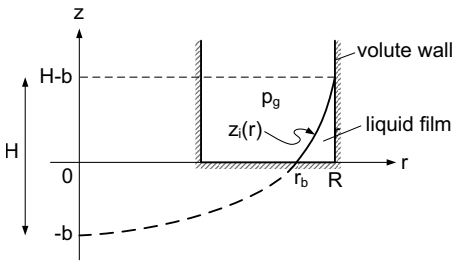

Fig. 3 Coordinate definition, cross section through liquid film. Coordinate θ is perpendicular to the plane of drawing.

where ρ_l is the density of the liquid phase, p_g is the pressure of the gas phase, and g is the gravitational acceleration. Consequently, the derivative in the radial direction becomes

$$\frac{\partial p}{\partial r} = \rho_l g \frac{dz_i}{dr} \tag{2}$$

The pressure variation in the radial direction due to the centrifugal force, in the case of a stationary flow, can also be described by

$$\frac{\partial p}{\partial r} = \rho_l \frac{v_\theta^2}{r} \tag{3}$$

Combining the two gives

$$\frac{dz_i}{dr} = \frac{v_\theta^2}{gr} \tag{4}$$

Within a radial cross section of the film in Fig. 3 the liquid rotates as a solid body. The solid body assumption is confirmed by measurement in Sec. 4.1. It is only required to estimate the contact surface between the moving film and the stationary volute wall in order to estimate momentum dissipation. The tangential velocity is given by $v_\theta = \omega r$, with $\omega = \omega(\theta)$. Integration of Eq. (4) then gives the shape of the liquid film interface as

$$z_i(r) = \frac{\omega^2 r^2}{2g} - b \tag{5}$$

This parabolic profile can be fully described in terms of the geometric variables $H(\theta)$ and $b(\theta)$ as

$$z_i(r) = H\left(\frac{r}{R}\right)^2 - b, \quad r_b < r < R, \quad r_b = R\sqrt{\frac{b}{H}} \tag{6}$$

It follows from this definition that the profile (see Fig. 3) intersects the vertical axis at $z_i(0) = -b$, and that H is the sum of b and the maximum film height $z_i(R)$: $H = b + z_i(R)$. The actual film interface only runs between the volute bottom ($z=0$) and the outer wall ($r=R$). Combination of Eqs. (5) and (6) yields an expression for the angular velocity ω, which is directly related to H as

$$\omega^2 = \frac{2gH}{R^2} \tag{7}$$

and from which fluid tangential velocity v_θ can be calculated as

$$v_\theta = \omega r = \sqrt{2gH}\frac{r}{R} \tag{8}$$

The mass flow rate $\dot{m}$ and the rate of angular momentum $\dot{I}$ through a cross section of the liquid layer at angular position θ can be determined by integration using Eqs. (6) and (8). The transport of mass in the film equals

$$\dot{m}(\theta) = \rho_l \int_{r_b}^{R} \int_0^{z_i(r)} v_\theta dz dr = \frac{1}{2}\rho_l R\sqrt{2gH}\left(\frac{H}{2} - b + \frac{b^2}{2H}\right) \tag{9}$$

with H and b as functions of θ. Similarly, an expression for the transfer of angular momentum can be found. Angular momentum

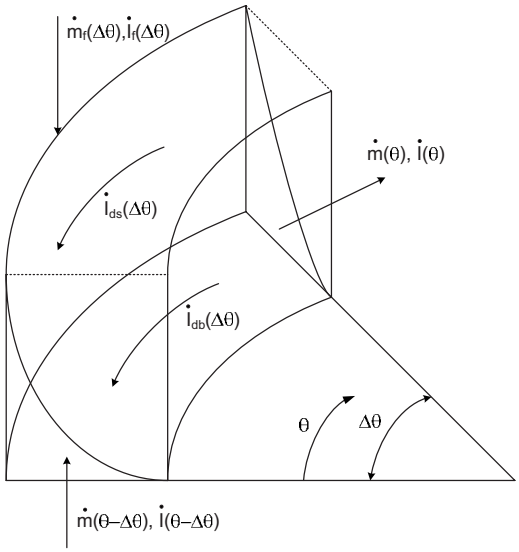

Fig. 4 Definitions within a volume segment

$\dot{I}$ can be described as momentum in the tangential direction, multiplied by the radius.

$$\dot{I}(\theta) = \rho_l \int_{r_b}^{R} \int_{0}^{z_i(r)} v_\theta^2 r dz dr = 2\rho_l g H R^2 \left(\frac{H}{6} - \frac{b}{4} + \frac{b^3}{12H^2} \right) \quad (10)$$

The shape of the liquid layer at angular position θ is determined by the parameters $H(\theta)$ and $b(\theta)$, the values of which can now be calculated from Eqs. (9) and (10) once $\dot{m}(\theta)$ and $\dot{I}(\theta)$ are known.

2.2 Momentum Dissipation. Using conservation of mass and angular momentum, the mass flow rate $\dot{m}$ and the rate of angular momentum $\dot{I}$ at position θ can be related to transfer of mass and momentum at a previous angular position $\theta - \Delta\theta$ via the feed of mass and the feed and dissipation of momentum in the small interval $\Delta\theta$ (see Fig. 4). The mass balance is given as follows:

$$\dot{m}(\theta) = \dot{m}(\theta - \Delta\theta) + \dot{m}_f(\Delta\theta) \quad (11)$$

The balance for the rate of angular momentum is described by

$$\dot{I}(\theta) = \dot{I}(\theta - \Delta\theta) + \dot{I}_f(\Delta\theta) - \dot{I}_{ds}(\Delta\theta) - \dot{I}_{db}(\Delta\theta) \quad (12)$$

with $\dot{m}_f(\Delta\theta)$ and $\dot{I}_f(\Delta\theta)$ the influxes of mass and angular momentum, and $\dot{I}_{ds}(\Delta\theta)$ and $\dot{I}_{db}(\Delta\theta)$ the dissipations of angular momentum through shear forces at the side and bottom walls, respectively. The mass and the momentum that are fed into the system by the liquid entering at the top in the interval $\Delta\theta$ can be described by

$$\dot{m}_f(\Delta\theta) = \dot{m}_f \frac{\Delta\theta}{2\pi} \quad \dot{I}_f(\Delta\theta) = \dot{m}_f v_{\theta f} R \frac{\Delta\theta}{2\pi} = \dot{m}_f(\Delta\theta) v_{\theta f} R \quad (13)$$

with $\dot{m}_f$ the total liquid feed to the postseparator, and $v_{\theta f}$ its tangential velocity.

In general, momentum dissipation can be described by

$$\dot{I}_d(\Delta A) = \int_{\Delta A} \tau r dA = \frac{1}{2} f \rho_l \int_{\Delta A} v_\theta^2 r dA \quad (14)$$

with τ the shear stress and f the friction coefficient.

For the side wall, the dissipation of angular momentum is equal to

$$\dot{I}_{ds}(\Delta\theta) = f\rho_l g R^2 \int_{\theta-\Delta\theta}^{\theta} H(H-b) d\theta' \cong f\rho_l g R^2 \Delta\theta (\bar{H}^2 - \bar{H}\bar{b}) \quad (15)$$

of which the final result is a first order approximation after linearization in H and b. Similarly, the dissipation at the bottom wall $\dot{I}_{db}(\Delta\theta)$ is found in a first order approximation as

$$\dot{I}_{db}(\Delta\theta) = \frac{f\rho_l g R^3}{5} \int_{\theta-\Delta\theta}^{\theta} H d\theta' - \frac{f\rho_l g}{5R^2} \int_{\theta-\Delta\theta}^{\theta} H r_b^5 d\theta' \cong \left(\frac{\rho_l f g \bar{H} \Delta\theta}{5R^2} \right) \times (R^5 - \bar{r}_b^5) \quad (16)$$

with $\bar{H}$, $\bar{b}$, and $\bar{r}_b$ averages in the interval $\Delta\theta$.

With the derived relations, the momentum and mass balance can now be solved. The liquid film is solved numerically, starting from $\dot{m}=0$ and $\dot{I}=0$ at $\theta=0$. The entire film is divided into small enough segments $\Delta\theta$ to justify the approximation in Eqs. (15) and (16). The mass flow rate $\dot{m}$ and momentum $\dot{I}$ are obtained at angular position θ, using Eqs. (11) and (12). From these values, $H(\theta)$ and $b(\theta)$ are obtained using Eqs. (9) and (10). Since the momentum dissipation depends on the average value for H, b, and r_b in interval $\Delta\theta$, a subiteration procedure is required to solve the problem. The model gives a theoretical prediction for the film height, width, and fluid velocity, which together determine the theoretical liquid drainage capacity. The model will be validated with the help of laboratory experiments in Sec. 4.1.1.

3 Experimental Setup

An atmospheric test setup is built using air and water as working fluids. As shown in Table 1, the test setup is based on a contaminated gas field installation with a feed of 24 m_n^3/s (80 MMscf/d), contaminated with 30 mol % of CO_2. Expansion of the natural gas (to 20 bars and $-60°C$) leads to a methane-rich gas flow rate of 0.45 m^3/s and a CO_2-rich liquid flow rate of 7.5 l/s in the form of micron-sized condensate droplets entrained in the gas stream. On our test rig similar volume flow rates of air (up to 0.50 m^3/s) and water (up to 9 l/s) can be provided to the RPS unit. But because we could not achieve high liquid loading with *micron-sized* water droplets, coarse spray nozzles are utilized to examine the effects of a high load on liquid removal in the postseparator volute, and the separation efficiency is measured separately using a smaller amount of micron-sized droplets.

1. *Liquid drainage capacity.* A large amount of water (up to 9 l/s) in the form of coarse droplets is sprayed directly on the RPS element using three large nozzles. The large droplet size does not affect the loading of the postseparator volute because as with micron-sized droplets, in the end all the liquid is collected on the extended wall of the rotating element (see Fig. 2). Drainage of this water in the postseparator volute is studied and its performance and hydrodynamic behavior are measured.
2. *Separation efficiency.* In principle, separation of small droplets in the channels of the rotating element is not affected by the amount of droplets. Therefore the separation efficiency is determined separately with a smaller loading. High pressure nozzles inject a mist containing a large amount of micron-sized droplets into the airstream in the inlet piping. Based on particle diffraction, the volume concentration and size distribution of droplets are measured in the airstream leaving the unit. From the results a separation efficiency curve is derived.

Section 3.1 gives a general detailed description of the test setup, whereas Secs. 3.2 and 3.3 deal with the liquid drainage and separation efficiency measurements.

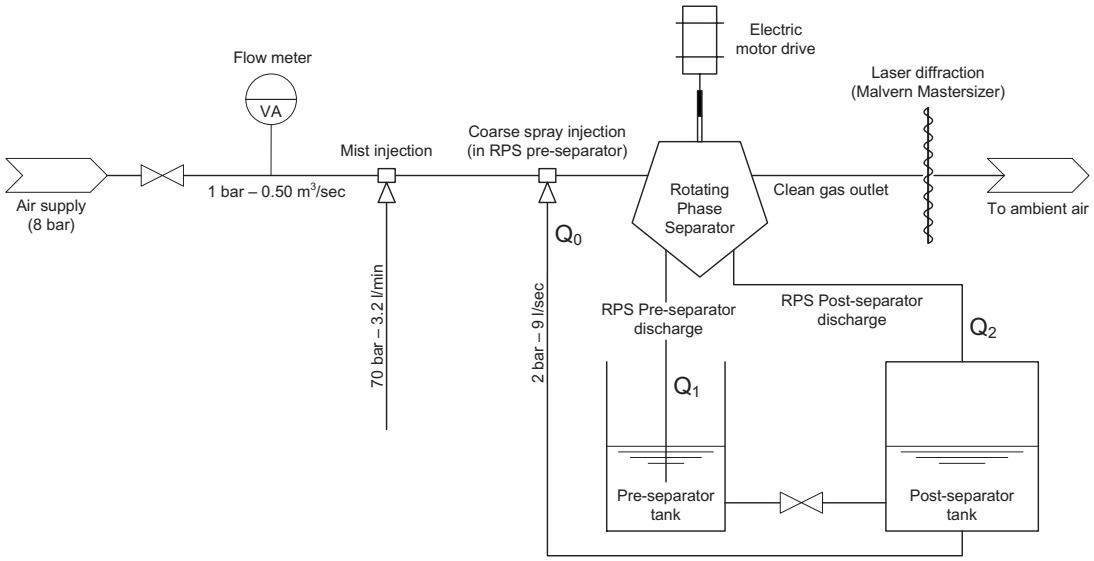

Fig. 5 Schematic of the test rig

3.1 Description of the Test Setup. A schematic of the experimental setup is introduced in Fig. 5. The components will be described in more detail in Secs. 3.1.1–3.1.3, dealing with the feed streams, the separation unit, and the discharge streams.

3.1.1 Feed Streams. Air supply. Pressurized air from a supply at 8 bars is expanded over a globe valve to approximately 1 bar. In this way a flow rate up to 0.50 m^3/s can be provided to the RPS unit. The valve is actuated via pressurized air and operated manually. A Coriolis-type mass flow meter is used to monitor the flow.

Large liquid loading. A large storage tank (capacity 1 m^3) is filled with ordinary tap water. A 5.5 kW multistage centrifugal pump provides up to 9 l/s of water (Q_0) to three large spray nozzles, which spray the large liquid load directly on the RPS element in the axial direction. Produced droplet sizes are in the millimeter-range. The nozzles are mounted on the top flange; see Fig. 6. The volume flow is monitored by a variable area (VA) flow meter, and can be adjusted via a frequency converter that controls the rotational speed of the pump motor.

Fine mist supply. Demineralized water from another smaller storage tank is pressurized by a plunger pump. A pressure reducing control valve keeps the pressure in the upstream line at 70 bars, bypassing the surplus of water back to the tank. A mist is generated in a mechanical way by 28 so-called pin jet nozzles (manufactured by BETE, Greenfield, MA, USA, type PJ6), and injected in the airflow entering the RPS unit. A pin jet nozzle forces water through an orifice of 152 μm, and the resulting jet subsequently breaks up against a metal pin that is situated right in front of the orifice. A substantial amount of generated droplets is in the micron-range. From the specifications of the nozzle manufacturer it can be estimated that water will be injected at a constant rate of approximately 3.2 l/min. To prevent material blockage of the orifice, demineralized water was used.

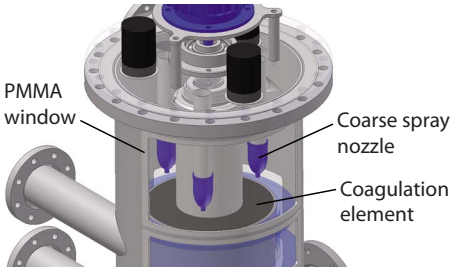

Fig. 6 Close-up of the Eindhoven laboratory unit

3.1.2 Separation Unit. The core of the test rig is a vertically mounted RPS unit, with downward flow direction through the rotating element. This unit is a dedicated test version of an industrial design. The actual gas throughput is 0.5 m_n^3/s maximum. The corresponding contaminated natural gas flows would depend on the liquid extraction and thus on the levels of contamination. For example, Table 1 shows the corresponding conditions of liquid and gas throughput for a 30% CO_2 in natural gas mixture with optimal separation at 30 bars and −60°C, as discussed in the Introduction. The original design is for typical natural gas postexpansion pressures and temperatures of around 20 bars and −60°C. Because the test unit operates at atmospheric pressure, the casing walls are thinner. The conditions are noncryogenic, and material constraints for air-water are far less severe than for CH_4 and CO_2, not to mention H_2S. We use ball bearings, rubber seals, and flanges constructed out of stainless steel.

The method of manufacturing the RPS element follows the manufacturing process of corrugated paper [6]. Taking two 0.1 mm thick stainless steel foils, one foil is corrugated and the other is not. Then the two foils together are wound up many times around an axis, and welded together continuously. The end result is a complete element with inner and outer diameters of 180 mm and 340 mm, respectively, and a length of 155 mm. The shape of the channels in the element is approximately trapezoidal (Fig. 1) with a maximum channel height of 1.9 mm. Approximately 10% of the frontal surface of the element is covered by the channel walls.

A unique feature of this RPS test unit is that it has been made optically accessible. In the shell a total of six holes are cut out that have been covered by transparent PMMA windows; see Fig. 6.

In a prescribed industrial unit the gap between the element and the cylindrical housing by which it is surrounded is smaller than 1 mm. However, our prototype has a gap of 4–5 mm between the rotating element and stationary wall. This is due to difficulties in making the housing. This results in a relatively large leak flow bypassing the rotating element.

In a field application, a condensed liquid mist is entrained in the inlet gas stream. Because it enters the unit tangentially (Fig. 7), the momentum contained in the liquid is not lost but will be employed to drive the element. In our test application though, the three nozzles spray the liquid load in the axial direction on the RPS element, and the complete liquid load has to be brought into

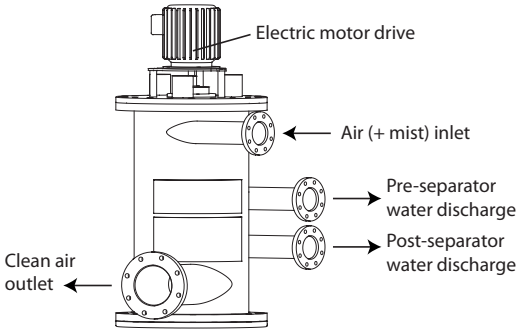

Fig. 7 Connections of the RPS unit

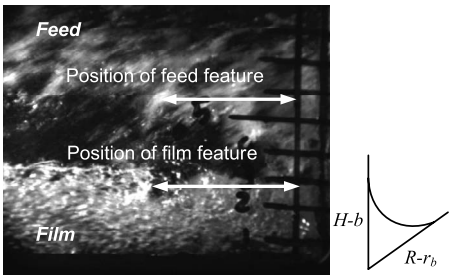

Fig. 8 A typical high speed exposure taken through the window of the stationary volute (880 frames/s, $\Delta t \approx 1$ ms). On the right a schematic isometric view of the film is shown, with the film height ($H-b$) and width ($R-r_b$) indicated. The bottom of the volute is present at the bottom edge of the exposure (see Fig. 2).

rotation together with the element. The consequence is that the RPS element in the test unit has to be driven by a relatively large motor. A 15 kW electric motor is mounted on top of the unit (see Fig. 7), and a frequency converter controls its shaft speed. An advantage of this system is that the rotational speed of the RPS element is controllable.

3.1.3 Discharge Streams. Water discharge. Water separated in the postseparator is discharged directly into the main storage tank, whereas water from the preseparator ends as a dip pipe in a secondary tank (see Fig. 5). This dip pipe acts as a siphon water lock so that the entire airflow is forced to flow through the RPS element. The preseparator flow rate Q_1 (Fig. 5) is derived from the rising water level in the secondary tank. Subsequently, this flow rate is subtracted from the feed rate Q_0 to obtain the postseparator flow rate $Q_2 = Q_0 - Q_1$. The pre- and postseparator discharge pipes are connected tangentially to the separator casing (Fig. 7). Adequate drainage is ensured by using large diameter pipes over a short horizontal distance.

Air outlet. The air outlet pipe passes through the sample area of a Malvern Mastersizer S, which measures the distribution properties of droplets entrained in the airstream leaving the unit (see Sec. 3.3). A short distance downstream, the stream is discharged into the ambient air.

3.2 Liquid Drainage Measurement. Flow rates up to 9 l/s (Q_0 in Fig. 5) are metered and sprayed into the rotating airstream just before it enters the RPS element; see Fig. 6. Not all the liquid sprayed on the RPS element reaches the postseparator because a substantial amount Q_1 is drained via the preseparator drainage system. For this reason the liquid flow rate Q_2 within the postseparator only reaches up to 5 l/s.

Because of the proximity of the three nozzles (see Fig. 6), the element is not homogenously loaded. This does not affect the loading of the postseparator because on the extended outer wall of the rotating element (Fig. 2, pos. C) the collected liquid is redistributed before it leaves toward the postseparator volute.

The liquid that is expelled from the rotating element collides with the wall (Fig. 2, pos. E) and loses some of its momentum. The remaining momentum drives a standing liquid film (F) that rotates within the volute. Since the volute is located lower than the point where the liquid leaves the element, the film is fed from the top.

The height and width of the rotating liquid film in the postseparator are determined via scales, which are placed on the volute side wall and bottom. These scales can be read through the polymethylmethacrylaat (PMMA) windows.

Using a high speed camera the feed and film are recorded via the postseparator window from aside, as indicated by the eye in Fig. 2. The position is opposite to the liquid exit 2 (at 180 deg). The velocities of the feed (which is the liquid entering the liquid film) and film in horizontal direction are calculated from the change in position of a visually distinguishable feature within subsequent exposures. Figure 8 clearly shows the turbulent, unstructured flow patterns in the rotating film and in the feed supply. The feed is located at the point where the liquid enters the film.

3.3 Separation Efficiency Measurement. A constant amount of mist is injected into the airstream entering the RPS unit; see Sec. 3.1.1. Droplets that could not be separated by the RPS unit are entrained in the airstream leaving the unit. The volume concentration and volume distribution of these droplets are measured by a Malvern Mastersizer S 300, making use of particle diffraction. As will be explained in this section, a separation efficiency curve is derived from the measurement results [13].

The Mastersizer contains a laser source, which emits a parallel laser beam with a diameter of approximately 15 mm, and a lens mounted at a distance of 240 mm from the source. The air outlet pipe (∅110 mm) coming from the RPS unit passes through the Mastersizer. The distance from the pipe wall to the lens is approximately 25 mm in order to have some clearance for cleaning the lens. The laser beam passes perpendicularly through the middle of the gas stream via two holes (∅35 mm) in the wall of the pipe. These holes are open to prevent distortion of the laser signal. The laser exposed area is closed with a cardboard cover.

The Mastersizer measures two quantities.

1. *Concentration.* The total volume concentration c is the fraction occupied by droplets. The Mastersizer measures the extinction of laser light, and the associated software uses the Lambert–Beer law [15] to compute the concentration. To this end it uses the measured droplet size distribution and a given path length of the laser beam through the sample. The laser beam passes through the pipe perpendicular to the flow. This path length is thus the internal pipe diameter with a small correction for lateral droplet leakage.
2. *Size distribution.* A monodisperse mist produces a diffraction pattern consisting of a series of alternate light and dark concentric rings, the spacing of which depends on the droplet diameter [16]. The Mastersizer registers the diffraction pattern of droplets with a series of detectors, and the MALVERN software uses Mie theory to derive the volume distribution of a polydisperse mist.

The distribution is obtained as a histogram of volume fractions Δf_i, distributed over 49 intervals i with droplet sizes ranging from d_{pi1} to d_{pi2}. The intervals are equally spaced on a logarithmic scale between 0.5 μm and 880 μm. On the logarithmic scale their midsize can be derived as the geometric mean of the interval limits: $d_{pi} = \sqrt{d_{pi1} d_{pi2}}$. The sum of the fractions equals unity as follows:

$$\sum_{i=1}^{49} \Delta f_i(d_{pi}) = 1 \tag{17}$$

For any gas flow rate, droplet volume concentrations are measured for two situations: c is the concentration with the separator in operation, and c_0 is the concentration with the nonrotating element. The separation efficiency due to the rotating element is given by

$$\eta = 1 - \frac{c}{c_0} \tag{18}$$

Note that this is different from the overall separation efficiency. As we shall see, even a stationary element has a removal effect due to droplet impaction at the channel entrance (see Sec. 4.2.1). Except for the volume concentration, the shape of the distribution as represented by the fractions Δf_i also changes with rotational speed of the element. The separation tends to cut off the right part of the distribution first, because large droplets are separated more efficiently than small droplets. Equation (18) can now be combined with the 49 monodisperse volume fractions Δf_i with droplet sizes d_{pi}. Because the concentration of one monodisperse fraction is $c\Delta f_i$, the separation efficiency of the monodisperse fractions as a function of their droplet size can be expressed as

$$\eta(d_{pi}) = 1 - \frac{c\Delta f_i}{c_0 \Delta f_{0i}} \tag{19}$$

where subscript 0 refers to the situation at 0 rpm. Because the measured droplets are in the low range 1–10 μm, the measurement is very sensitive. To prevent artificial peaks in the distribution (typically above 100 μm) the background noise has to be recorded at the same airflow, and it must be verified that the lens remains clean. To ensure a reproducible state and a stationary situation, the unit is flushed at maximum throughput before each measurement, and after switching on mist injection measurements are only taken after stabilization. Measurement and background recording were both taken to last 20 s, which means that their final signal is averaged from 10,000 instantaneous sweeps.

4 Results and Discussion

This section is divided into two parts: First the results concerning the liquid drainage are discussed and compared with predictions. Subsequently the separation efficiency of the separator is discussed.

4.1 Liquid Drainage. The liquid drainage is measured with a water/air mixture to validate the theoretical model developed in Sec. 2. The measurements of the liquid film have been performed for increasing liquid loading at various shaft speeds Ω.

From the observed parabolic shape of the film we conclude that the tangential velocity profile in a cross section of the film can be described by a solid body rotation $v_\theta = \omega r$. The measurements of the film width $(R - r_b)$ and height $(H - b)$ (see Fig. 8) were done at three positions along the circumference, located at 90 deg, 180 deg, and 270 deg from the outlet. The tangential velocity of the film v_θ was measured at 180 deg (halfway the film) using the high speed camera (see Fig. 8).

In order to predict the velocity of the film, the velocity of the feed should be measured or estimated and used as an input parameter for the model. As well as the film velocity, the tangential velocity $v_{\theta f}$ of liquid entering the liquid film was measured at 180 deg using the high speed camera.

4.1.1 Comparison With Theory and Discussion. In Fig. 9 the predicted film velocities are compared with the measured velocities at shaft speeds of 800 rpm and 1200 rpm of the RPS element. The errors of approximately 0.4 m/s are mainly due to the velocity determination with high speed exposures. The velocities within the turbulent flow vary substantially in time and place.

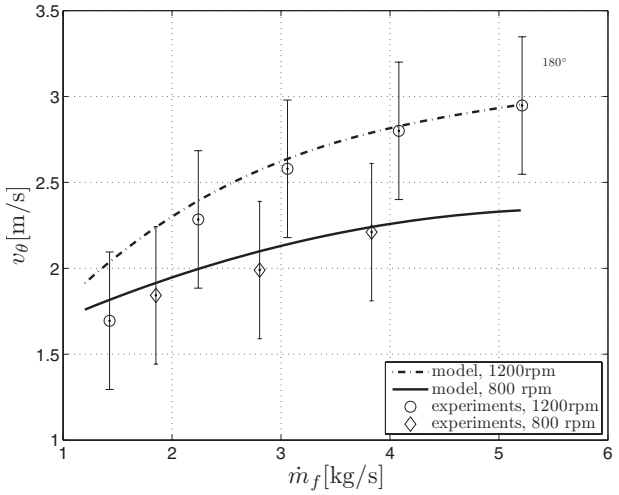

Fig. 9 Measured and predicted tangential liquid film velocities at the outer wall ($r = R$) as a function of total liquid mass flow rate, halfway the film (at 180 deg from the outlet), for shaft speeds 800 rpm and 1200 rpm. Predictions are based on measured feed velocities of $v_{\theta f} = 6.6$ m/s at 800 rpm and $v_{\theta f} = 9.1$ m/s at 1200 rpm, and a friction factor $f = 0.05$.

In the model, the friction factor f (see Eqs. (14)–(16)) can be used to fit predictions (based on measured feed velocities) to measured film velocities. Figure 9 shows that the film velocity is rather well predicted with a friction factor of 0.05. This value is quite high, when compared with the flat plate analogy [17]. However, since the liquid film is an unsteady, decelerating flow through a highly curved volute, a substantial increase in the friction factor is expected [17]. The turbulence intensity corresponding to a friction factor of 0.05 is approximately 16%, which seems reasonable when observing the high speed exposures.

Comparing the measured film width and height with predictions, the model typically overpredicts the height and underpredicts the width of the film. The reason is that the film is deformed, because the water fed into the film alongside the wall contains a significant vertical momentum. This results in a lower height and a larger width of the film.

The model is intended as a design tool for the sizing of the liquid collection volute, and an accurate description of the turbulent liquid film is not required. Using a friction factor of 0.05, the model is sufficiently accurate to design the liquid collection volutes for a known feed velocity.

4.2 Separation Efficiency. In the Sec. 4.1 the performance of the RPS postseparator at large liquid loads was discussed. This section concentrates on measuring the separative performance of the RPS rotating element with regard to micron-sized mist droplets. In Sec. 4.2.1 we show the separative power of the RPS element. In Sec. 4.2.2 an example of a measured separation efficiency curve is discussed, and in Sec. 4.2.3 measured curves for a number of airflow settings and rotational speeds are compared with theory.

4.2.1 Separative Power. We inject mist droplets in the airstream entering the RPS unit, and measure the size distribution and volume concentration of droplets in the airstream after the RPS unit (see Fig. 5 and Sec. 3.3). With a stationary (nonrotating) element, measured size distributions after the unit are plotted in Fig. 10 as a probability density function (PDF) for various airflow settings. Note that because the PDF is plotted on a logarithmic axis, volume fractions are normalized by the interval width of the natural logarithm of the particle diameter [15] (see caption). It can be seen that droplets are mainly in the range 0–11 μm. Volume concentrations (or fractions) in air corresponding to these distri-

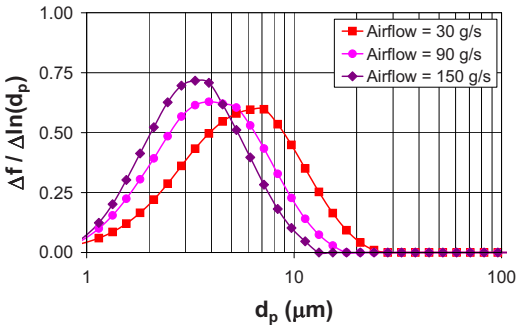

Fig. 10 Droplet distributions at $\Omega=0$ rpm. Volume fractions Δf_i are normalized as follows: For each interval i with droplet sizes ranging from d_{pi1} to d_{pi2}, the PDF is expressed as $\Delta f_i/(\ln d_{pi2}-\ln d_{pi1})$ with d_p expressed in microns. The airflow is measured in grams per second (g/s).

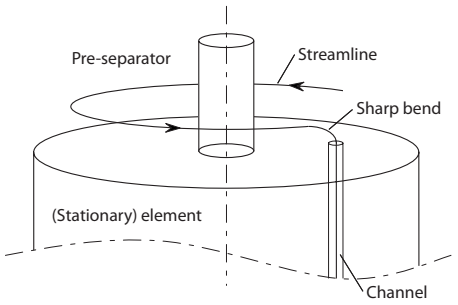

Fig. 12 Impaction at the channel entrance

butions are 1.8×10^{-6}–5.4×10^{-6} v/v. When these concentrations are compared with the water injected into the airstream before the RPS unit it appears that approximately 99.5% is already separated, even when the element is not rotating.

Apparently these droplets in the range 0–11 μm are not separated effectively by cyclone action in the preseparator. Shortly after expansion of natural gas, a significant fraction of the condensed contaminant droplets falls within this size range. This means that we can simulate droplet sizes of the field application. The fact that it concerns only 0.5% of our total injected mist volume explains why a relatively large number of nozzles (28) are needed.

Taking the volume concentration with the nonrotating element ($\Omega=0$ rpm) as reference c_0, the separation efficiency due to the rotating element according to Eq. (18) is shown in Fig. 11 for increasing rotational speed. It can be concluded that, in contrast to the preseparator cyclone, the rotating element is capable of effectively removing micron-sized droplets at large gas volume flows.

In the preseparator the airflow rotates due to the tangential air inlet. When the tangential velocity of this inlet airflow does not match with the tangential velocity of the element, the airflow undergoes a sharp bend at the entrance of the channels (see Fig. 12). Due to this bend droplets will be separated in a manner similar to an inertial impactor. This effect is most significant when the element is stationary. When the element starts rotating the mismatch in tangential velocity between the preseparator airflow and the element becomes smaller (smoother transition), and separation by impaction at the channel entrance reduces.

According to Eq. (18) the separation efficiency due to the rotating element at a fixed airflow is derived as $\eta=1-c/c_0$. The reduction in c_0 (stationary element) due to impaction is stronger than the reduction in c (element at some speed Ω), which leads to an underestimation of the separation efficiency η. Impaction at 0 rpm reduces c_0, but has a relatively little effect on c. This underestimation will be more perceptible at low speeds Ω, where the efficiency of the rotating element is low and c is large. This is understood better considering the following example: When $c_0=5.5\times10^{-6}$ and $c=4.0\times10^{-6}$ v/v (at low speed), the separation efficiency is 27%. Suppose that c_0 is reduced to 5.0×10^{-6} as a result of impaction on the stationary element, whereas c remains unaltered (no impaction because the transition from preseparator to channels is smooth when the element rotates). The measured efficiency η will then be reduced from 27% to 20%. But when $c=1.0\times10^{-6}$ (at high speed) the efficiency only goes from 82% to 80%.

Thus the effect of impaction with a stationary element on the derived separation efficiency with rotating element is larger in percent points at low Ω. Note that the trend of the lines in Fig. 11 extrapolates to a collection efficiency of 0% at a speed $\Omega>0$ rpm. At this point the separation in the channels of the rotating element compensates for the impaction in the stationary case (c equal to c_0).

4.2.2 Separation Efficiency Curve. Figure 13 shows an example of a measured separation efficiency curve as a function of the droplet size. The separation efficiency is plotted on the left axis. According to Eq. (19), the efficiency as a function of the droplet size is based on the volume concentrations of monodisperse fractions $c\Delta f_i$. In normalized form, the latter can be read out on the right axis. These normalized volume concentrations can also be seen as the total volume concentration c, multiplied by the PDF (as in Fig. 10).

Figure 13 shows that for droplet diameters <2 μm the efficiency curve increases with decreasing particle size. This unexpected result is a general trend in all measured curves. The measurement accuracy for $d_p<2$ μm is too low to draw meaningful

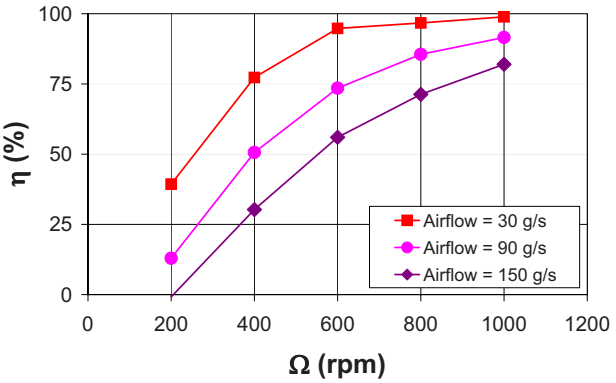

Fig. 11 Measured separation efficiency due to the rotating element, using the situation with a stationary element ($\Omega=0$ rpm) as a reference

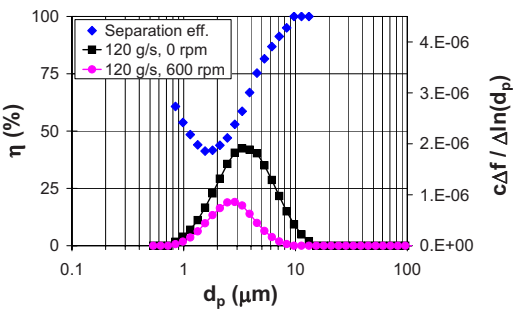

Fig. 13 Example of the analysis of a separation efficiency curve (600 rpm, airflow 120 g/s). Separation efficiency (diamonds) is indicated on the left axis, and normalized volume concentrations (squares and circles) are shown on the right axis. Volume concentrations $c\Delta f_i$ are normalized in the same way as the volume fractions in Fig. 10; see caption.

Table 2 Predicted values of $d_{p50\%}$ (μm) for the range of operational settings. The units of airflow settings are grams per second (g/s).

Airflow (g/s)	Rotational speed (rpm)				
	200	400	600	800	1000
30	3.8	1.9	1.3	0.9	0.8
60	5.4	2.7	1.8	1.3	1.1
90	6.6	3.3	2.2	1.6	1.3
120	7.6	3.8	2.5	1.9	1.5
150	8.5	4.2	2.8	2.1	1.7

conclusions, because the two distributions on which the efficiency is based (Eq. (19)) are both on the low edge (the relative size of both volume fractions is small). Besides, we are mainly interested in the part of the curve where efficiencies of 100% are approached. We therefore disregard results below 2 μm.

4.2.3 Comparison With Theory and Discussion. Separation efficiency curves were measured at 25 different operational settings (airflow and rotational speed). As explained in Sec. 1, the separation efficiency is a function of the airflow rate through the RPS element and its rotational speed. So in order to compare the measured curves to theory a parameter is needed that accounts satisfactorily for both airflow and rotational speed. This is the particle diameter that should theoretically be collected with 50% efficiency within the channels of the RPS, $d_{p50\%}$. We now estimate this.

The basis for theoretical prediction of the separation efficiency of the rotating element is the following [9]. The moment a particle enters a separation channel (Fig. 1), its radial velocity will be determined by equilibrium between centrifugal force, buoyancy force, and drag force according to Stokes' law. Originally the separation efficiency was described in terms of $d_{p100\%}$ [9], the smallest particle diameter that is separated with 100% efficiency. In practice it is more convenient to use $d_{p50\%}$. In contrast to $d_{p100\%}$, $d_{p50\%}$ always exists. Also the value of $d_{p50\%}$ is less variable and can be measured more reliably.

For the simplifying assumptions of concentric channels and laminar Poiseuille flow (no turbulent velocity fluctuations) over the complete length of the channels, $d_{p50\%}$ of the rotating element can be written as [9]

$$d_{p50\%}^2 = \frac{13.5\mu_g d_c}{(\rho_p - \rho_g)\pi L(1-\epsilon)(R_o^3 - R_i^3)}\frac{\phi}{\Omega^2} \tag{20}$$

The operational parameters are flow rate through the element ϕ (m^3/s) and angular velocity of the element Ω (rad/s). In the equation d_c is the maximum channel height and ϵ is the fraction of the frontal surface of the element that is covered by channel walls. For the other symbols, refer to the Nomenclature. Equation (20) holds for either a uniform flow distribution over the element, or a linear distribution, which means that the axial velocity is proportional to the distance from the rotation axis. The predicted values of $d_{p50\%}$ for all our operational settings are listed in Table 2.

For a uniform flow distribution over the element, analytical expressions of the separation efficiency have previously been derived for both concentric and triangular channels [9]. The efficiency appears to be a function of the dimensionless particle diameter $d_p/d_{p50\%}$, with $d_{p50\%}$ based on concentric channels and calculated according to Eq. (20). Because $d_{p50\%}$ is a function of the operational parameters' flow rate and rotational speed, there is only a single predicted curve as a function of particle size for all operational settings. Subsequently we can also normalize our measured curves with their corresponding calculated value of $d_{p50\%}$, as listed in Table 2. This makes it possible to plot the measured curves for all operational settings on the same axis.

The flow distribution over the element can be assumed uniform (equal loading of all channels), because the element acts as a flow straightener. Since no analytical predictions are available for trapezoidal channels, we assume triangular channels. Differences resulting from a slightly different channel shape or a possibly slightly nonuniform flow distribution are only in the order of a few percent.

Describing the flow in the channels as laminar Poiseuille flow with a superimposed rigid rotation, a bulk Reynolds numbers Re_z and a so-called rotation Reynolds number Re_Ω can be defined [18] as

$$\mathrm{Re}_z = \frac{v_c d_h}{\nu_g}, \quad \mathrm{Re}_\Omega = \frac{\Omega d_h^2}{4\nu_g} \tag{21}$$

with v_c the mean channel velocity, d_h the channel hydraulic diameter, and ν_g the kinematic viscosity of the gas. Flow instabilities can be expected in circular channels when both $\mathrm{Re}_\Omega > 27$ and $\mathrm{Re}_z > 83$ [18]. Direct numerical simulations [10] then show a decrease in separation efficiency for large particle diameters in comparison with pure laminar flow [9]. Taking for the hydraulic diameter d_h the maximum channel height d_c, $\mathrm{Re}_\Omega < 7$ for all our measurement settings, and therefore flow instabilities are not expected. This means that the usual limit $\mathrm{Re}_z < 2000$ for laminar flow holds. Because in our measurements $\mathrm{Re}_z < 300$ we can safely base predictions on laminar Poiseuille flow.

Figure 14 shows the measured separation efficiency curves at low rotational speeds, together with the above mentioned prediction for the rotating element. The large difference between the measured and predicted efficiencies can be explained by the impaction-induced separation at the channel entrance when the element is stationary, as explained in Sec. 4.2.1. This leads to an underestimation of the measured separation efficiency with the rotating element, which is most significant at low rotational speeds. Note also that $d_{p50\%}$ is based on concentric instead of triangular channels. As a result, the predicted efficiency at $d_p/d_{p50\%} = 1$ is slightly different from 50%.

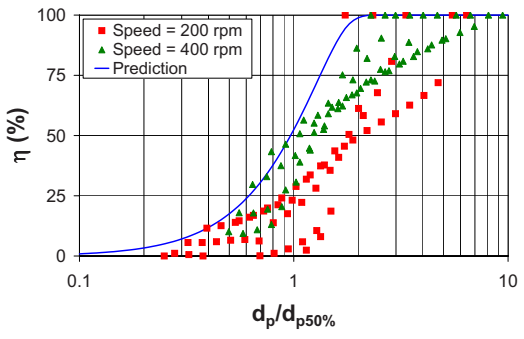

Fig. 14 Measured and predicted separation efficiency curves at low rotational speeds. Table 2 shows values of $d_{p50\%}$. All ten curves measured at speeds 200 rpm and 400 rpm are plotted. The prediction is for a rotating element with triangular channels, laminar channel flow, and a uniform flow distribution over the element.

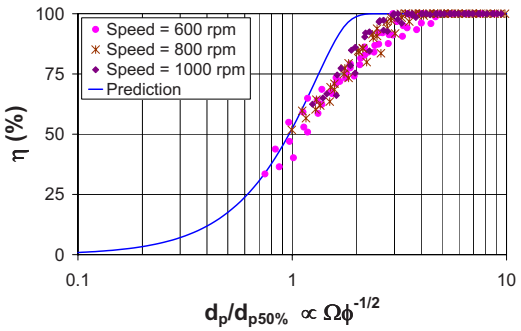

Fig. 15 Measured and predicted separation efficiency curves at high rotational speeds. Table 2 shows values of $d_{p50\%}$. All 15 curves measured at speeds 600 rpm, 800 rpm, and 1000 rpm are plotted. The prediction is for a rotating element with triangular channels, laminar channel flow, and a uniform flow distribution over the element.

At higher rotational speeds, Fig. 15 shows good consistency of the measured efficiency curves. All measured curves are on one line, which indicates that $d_{p50\%}$ accounts successfully for both airflow and rotational speed. When rotating fast, the RPS element separates efficiently and the deviations caused by impaction at the channel entrance are small. The measured curves go through 50% at $d_{p50\%}$, which means that Eq. (20) gives a good prediction of the value of $d_{p50\%}$.

Efficiencies at droplet diameters higher than $d_{p50\%}$ are 10–20% lower than the predicted curve. This can be explained by the leak over the gap between housing and rotating element (see Sec. 3.1.2). This gap with a width of 4–5 mm covers roughly 8% of the total surface, and it is estimated that this causes over 10% of the gas flow to bypass the element. This easily results in more than a 10% decrease in separation efficiency, as seen in Fig. 15. It seems counterintuitive that separation efficiencies of 100% are reached. However, the rotating element also causes rotation within the gap resulting in separation of (large) droplets.

Separation efficiencies around 100% are only reached at three to four times $d_p/d_{p50\%}$. For a specific airflow and particle diameter this means a rotational speed of three to four times the speed at 50% efficiency. From a design point of view it should be realized that when it is required that the prototype completely removes all droplets larger than, for example, 5 μm from the gas stream, $d_{p50\%}$ should thus be 1.25 μm.

5 Conclusions

Using large collection volutes in combination with large diameter tangential liquid outlets, the RPS is capable of handling large liquid loads.

In a rotating phase separator liquid can be drained with the help of a tangential liquid outlet, making use of the intrinsic fluids' angular momentum. Using a friction factor of 0.05, the presented model can be used to predict film velocity and corresponding dimensions accurately enough to size the liquid collection device.

Measurements show that the RPS is capable of removing micron-sized droplets effectively, which distinguishes it from cyclones. It proves that the droplet separation step in the concept of removing contaminants from natural gas by condensation is feasible.

The rotating element effectively enlarges droplets to a separable size via accelerated coagulation. This eliminates the need for a long induction section in which droplets grow to a size that can be separated by cyclones. In a field application using a cryogenic gas stream, this keeps capital costs low.

We have measured separation efficiencies down to 2 μm in agreement with theoretical predictions. The measured efficiencies are 0–20% lower than previous theoretical predictions, which can be explained by the leak flow via the gap between rotating element and housing. This is the subject of future study.

When removing liquid carbon dioxide, some CH_4 will be dissolved in the liquid CO_2. This may give rise to foam forming if the CH_4 acts as a surfactant lowering the surface tension of the liquid. Currently we are planning a test in which we agitate such liquid in a closed vessel, to reveal whether foaming occurs. The results of the test will be used to assess whether the liquid removal in the postseparator is sufficiently effective to prevent accumulation of foam and re-entrainment. By adding a surfactant to the injected water in the test setup described in this article, we will assess the effects of a low surface tension on droplet break-off and collection after the rotating element.

Nomenclature

A = surface area (m^2)
b = profile offset from the r-axis in the negative z-direction (m)
c = droplet volume concentration (m^3/m^3)
d_c = maximum channel height (m)
d_h = channel hydraulic diameter (m)
d_p = particle or droplet diameter (m)
$d_{p50\%}$ = diameter of a particle collected with 50% theoretical efficiency (m)
f = friction factor
Δf = volume fraction (m^3/m^3)
g = gravitational acceleration (m/s^2)
H = sum of profile offset and film height at the outer radius (m)
$\dot{I}$ = rate of angular momentum (N m)
$\dot{I}_{db}$ = dissipation of angular momentum at the volute bottom (N m)
$\dot{I}_{ds}$ = dissipation of angular momentum at the volute side wall (N m)
L = channel length (m)
$\dot{m}$ = mass flow rate (kg/s)
p = pressure within the liquid (Pa)
p_g = gas pressure (Pa)
R = collection volute outer radius (m)
R_i = element inner radius (m)
R_o = element outer radius (m)
Re_z = bulk Reynolds number
Re_Ω = rotation Reynolds number
r = radial coordinate (m)
r_b = radial position of the profile r-axis intersection (m)
v_c = mean channel velocity (m/s)
v_θ = tangential velocity (m/s)
z = axial coordinate (m)
z_i = z-position of the film interface (m)

Greek

ϵ = element surface fraction occupied by channel walls (m^2/m^2)
η = separation efficiency (m^3/m^3)
θ = angular position (rad)
μ = dynamic viscosity kilogram per meter second (kg/ms)
ν = kinematic viscosity $\nu=\mu/\rho$ (m^2/s)
ρ = density (kg/m^3)
ρ_p = particle or droplet density (kg/m^3)
τ = shear stress (Pa)
ϕ = feed gas volume flow rate (m^3/s)
Ω = element angular velocity (rad/s)
ω = film angular velocity (rad/s)

Subscripts

0 = reference situation with a nonrotating element
f = feed of the postseparator liquid film
g = gas
l = liquid

Appendix

In this article we have used standard SI units. Flows are often referred to as "normal" (denoted m_n^3/s) with respect to equivalent flows at standard temperature and pressure. However, practical application motivates us here to add a note regarding standard usage, which engineers in the field recognize as the "scf"—the standard cubic foot. Typical gas wells will produce in the range $30-300$ m_n^3/s more familiar to facilities' personnel as the unit million scf per day, i.e., a corresponding range $\sim 100-1000$ MMscf/d.

References

[1] Brouwers, J. J. H., van Wissen, R. J. E., and Golombok, M., 2006, "Novel Centrifugal Process Removes Gas Contaminants," Oil Gas J., **104**(42), pp. 37–41.
[2] van Wissen, R. J. E., Brouwers, J. J. H., and Golombok, M., 2007, "In-Line Centrifugal Separation of Dispersed Phases," AIChE J., **53**(2), pp. 374–380.
[3] van Wissen, R. J. E., 2006, "Centrifugal Separation for Cleaning Well Gas Streams: From Concept to Prototype," Ph.D. thesis, Eindhoven University of Technology, Eindhoven, The Netherlands.
[4] Willems, G. P., 2009, "Condensed Rotational Cleaning of Natural Gas," Ph.D. thesis, Eindhoven University of Technology, Eindhoven, The Netherlands.
[5] Willems, G. P., Golombok, M., Tesselaar, G., and Brouwers, J. J. H., 2010, "Condensed Rotational Separation of CO_2 From Natural Gas," AIChE J., **56**(1), pp. 150–159.
[6] Brouwers, J. J. H., 2002, "Phase Separation in Centrifugal Fields With Emphasis on the Rotational Particle Separator," Exp. Therm. Fluid Sci., **26**, pp. 325–334.
[7] van Kemenade, H. P., Mondt, E., Hendriks, A. J. A. M., and Verbeek, P. H. J., 2003, "Liquid-Phase Separation With the Rotational Particle Separator," Chem. Eng. Technol., **26**(11), pp. 1176–1183.
[8] Brouwers, J. J. H., 1996, "Rotational Particle Separator: A New Method for Separating Fine Particles and Mists From Gases," Chem. Eng. Technol., **19**(1), pp. 1–10.
[9] Brouwers, J. J. H., 1997, "Particle Collection Efficiency of the Rotational Particle Separator," Powder Technol., **92**(2), pp. 89–99.
[10] Kuerten, J. G. M., van Esch, B. P. M., van Kemenade, H. P., and Brouwers, J. J. H., 2007, "The Effect of Turbulence on the Efficiency of the Rotational Phase Separator," Int. J. Heat Fluid Flow, **28**(4), pp. 630–637.
[11] Willems, G. P., van Esch, B. P. M., Brouwers, J. J. H., and Golombok, M., 2008, "Creeping Film Model for Condensed Centrifugal Separation Processes," Chem. Eng. Sci., **63**(13), pp. 3358–3365.
[12] Kohl, A. L., and Nielsen, R. B., 1997, *Gas Purification*, 5th ed., Gulf Professional, Houston, TX.
[13] Brunazzi, E., Paglianti, A., and Talamelli, A., 2003, "Simplified Design of Axial-Flow Cyclone Mist Eliminators," AIChE J., **49**(1), pp. 41–51.
[14] Bird, R. B., Stewart, W. E., and Lightfoot, E. N., 2002, *Transport Phenomena*, 2nd ed., Wiley, Hoboken, NJ.
[15] Hinds, W. C., 1999, *Aerosol Technology*, 2nd ed., Wiley, New York.
[16] Lefebre, A. H., 1989, *Atomization and Sprays, Combustion: An International Series*, Taylor & Francis, Bristol, PA.
[17] Schlichting, H., 1979, *Boundary-Layer Theory*, 7th ed., McGraw-Hill, New York.
[18] Mackrodt, P. A., 1976, "Stability of Hagen-Poiseuille Flow With Superimposed Rigid Rotation," J. Fluid Mech., **73**(1), pp. 153–164.

Asymptotic Generalizations of the Lockhart–Martinelli Method for Two Phase Flows

Y. S. Muzychka
Professor
Mem. ASME

M. M. Awad
Mem. ASME

Faculty of Engineering and Applied Science,
Memorial University of Newfoundland,
St. John's, NF, A1B 3X5, Canada

*The Lockhart–Martinelli (1949, "Proposed Correlation of Data for Isothermal Two Phase Flow, Two Component Flow in Pipes," Chem. Eng. Prog., **45**, pp. 39–48) method for predicting two phase flow pressure drop is examined from the point of view of asymptotic modeling. Comparisons are made with the Lockhart–Martinelli method, the Chisholm (1967, "A Theoretical Basis for the Lockhart-Martinelli Correlation for Two Phase Flow," Int. J. Heat Mass Transfer, **10**, pp. 1767–1778) method, and the Turner–Wallis (1969, One Dimensional Two Phase Flow, McGraw-Hill, New York) method. An alternative approach for predicting two phase flow pressure drop is developed using superposition of three pressure gradients: single phase liquid, single phase gas, and interfacial pressure drop. This new approach allows for the interfacial pressure drop to be easily modeled for each type of flow regime such as bubbly, mist, churn, plug, stratified, and annular, or based on the classical laminar-laminar, turbulent-turbulent, laminar-turbulent, and turbulent-laminar flow regimes proposed by Lockhart and Martinelli.* [DOI: 10.1115/1.4001157]

Keywords: two phase flow, gas-liquid flow, interfacial effects, porous media, fractured media, microchannels, microgravity flow, asymptotic modeling, Martinelli parameter

1 Introduction

It has been 60 years since the publication of Lockhart and Martinelli's [1] seminal paper on two phase or two component flows. This paper has essentially defined the methodology for presenting two phase flow data in non-boiling and boiling flows. The mere fact that it has received nearly 1000 citations in journal papers alone is a testament to its contribution to the field of two phase flow. Since the publication of Lockhart and Martinelli's paper [1], a number of extensions, modifications, and closures have been proposed for simple two phase flow modeling assuming separated flows.

In the present work, analysis of two phase flows using asymptotically based correlation methods is examined. The proposed method is distinguished from the classic Lockhart–Martinelli approach, which is shown to be a special case in the present method since it includes a general means of accounting for interfacial pressure drop effects, i.e., those resulting from the interaction of the two phases. Closure is provided by means of two coefficients, which are determined by means of comparison with experimental data. The proposed models are compared with two phase and two component flow data found in a variety of gas-liquid applications including pipes and micro- and minichannels. However, the approach can also be applied to two phase flow in porous media, fractured media, microgravity, and with proper attention, liquid-liquid applications.

2 Review of Models

A general overview of a number of related methodologies is first given. We consider three classical approaches in detail, which are all somewhat related. These are the original *Lockhart–Martinelli* method, the *Turner–Wallis* method also known as the separate cylinders model, and the Chisholm method. Additional models from the recent literature are also examined.

Contributed by the Fluids Engineering Division of ASME for publication in the JOURNAL OF FLUIDS ENGINEERING. Manuscript received September 20, 2009; final manuscript received January 5, 2010; published online March 18, 2010. Assoc. Editor: Olivier Coutier-Delgosha.

2.1 Lockhart–Martinelli Method.

In 1949, Lockhart and Martinelli [1] proposed a correlation scheme for two phase flows. Using a simple analysis founded on the premise that the static pressure drop for the liquid and gas phases flowing simultaneously is equal at any point along the duct, they developed expressions for predicting the two phase pressure drop, which contained four variables: D_l/D, D_g/D, α, and β. The first two represented the ratio of the hydraulic diameter to pipe diameter for each phase flowing in the pipe, while the latter two represented the ratio of the true area occupied by each phase to the hydraulic area determined from the hydraulic diameters of each flowing phase. Using the simple pressure drop calculations,

$$\left.\frac{dp}{dx}\right|_{tp} = \frac{2f_l}{D_l}\rho U_l^2 = \frac{2f_g}{D_g}\rho U_g^2 \tag{1}$$

based on simple friction laws, i.e., $f_l \sim C_l/\mathrm{Re}_l^n$ and $f_g \sim C_g/\mathrm{Re}_g^m$, Lockhart and Martinelli [1] deduced that the two phase pressure drop could be predicted using

$$\left.\frac{dp}{dx}\right|_{tp} \sim \left.\frac{dp}{dx}\right|_l \alpha^{n-2}\left(\frac{D}{D_l}\right)^{5-n} \tag{2}$$

or

$$\phi_l^2 \sim \frac{\left.\frac{dp}{dx}\right|_{tp}}{\left.\frac{dp}{dx}\right|_l} \sim \alpha^{n-2}\left(\frac{D}{D_l}\right)^{5-n} \tag{3}$$

Without a loss in generality, one can now stipulate that

$$\phi_l^2 \sim \text{const} \tag{4}$$

A similar analysis for ϕ_g^2 leads to

$$\left.\frac{dp}{dx}\right|_{tp} \sim \left.\frac{dp}{dx}\right|_g \beta^{m-2}\left(\frac{D}{D_g}\right)^{5-m} \tag{5}$$

or

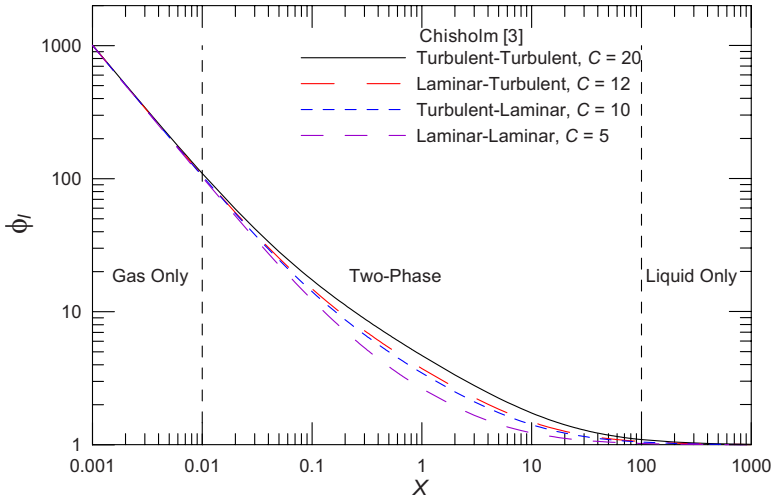

Fig. 1 Lockhart and Martinelli's [1] curves for the four flow regimes showing ϕ_l versus X

$$\phi_g^2 \sim -\frac{\left.\frac{dp}{dx}\right|_{tp}}{\left.\frac{dp}{dx}\right|_g} \sim \beta^{m-2}\left(\frac{D}{D_g}\right)^{5-m} \tag{6}$$

and

$$\phi_g^2 \sim \text{const} \tag{7}$$

In Eqs. (3) and (6), the constants m and n represent the exponent on the Reynolds number in the simple friction models. Thus, given that for any particular combination of mass flow rates for the liquid and gas phases, a unique value for D_l and D_g would arise, and hence α and β also, giving rise to a constant value for ϕ_l^2 and ϕ_g^2 for the given flow conditions.

Lockhart and Martinelli [1] further showed through their analysis that the generalized variable

$$X^2 \sim -\frac{\left.\frac{dp}{dx}\right|_l}{\left.\frac{dp}{dx}\right|_g} \sim \frac{\frac{2f_l}{D_l}\rho U_l^2}{\frac{2f_g}{D_g}\rho U_g^2} \sim \frac{\mathrm{Re}_g^m \; C_l \rho_g \dot{m}_l^2}{\mathrm{Re}_l^n \; C_g \rho_l \dot{m}_g^2} \tag{8}$$

is also a required correlating parameter. The parameter X has come to be known as the *Martinelli* parameter, and is sometimes also denoted as χ and Ma. The latter being discouraged to avoid confusion with the Mach number.

As a result of this simple analysis, Lockhart and Martinelli [1] established four flow regimes based on the values of m and n in the simple friction laws. These correspond to the laminar-laminar (ll), turbulent-turbulent (tt), laminar liquid–turbulent gas (lt), and turbulent liquid-laminar gas (tl) flow combinations of the liquid and gas. While both convenient and simple, these four flow regimes say nothing with regard to the type of flow pattern. Lockhart and Martinelli [1] devised four separate correlations, one for each flow regime, as shown in Fig. 1. These were presented both graphically and in tabular form in the original paper in the form of a family of curves:

$$\phi^2 \sim \phi_l^2(X), \quad \phi_g^2(X) \tag{9}$$

As a correlating scheme, the Lockhart–Martinelli [1] approach represents an asymptotic normalization of two phase flow data, given the Eqs. (3), (6), and (8). The scheme can be summarized as follows:

$$\left.\begin{array}{lll} \phi_l^2 \to \dfrac{1}{X^2}, & X \to 0 & \text{gas flow} \\ \phi_l^2 \sim f(X), & 0.01 < X < 100 & \text{two phase flow} \\ \phi_l^2 \to 1, & X \to \infty & \text{liquid flow} \end{array}\right\} \tag{10}$$

In the region of $0.01 < X < 100$, the results are strongly dependent on the nature of the flow, i.e., the four flow regimes of Lockhart and Martinelli [1], in addition to the type of flow, i.e., bubbly, stratified, churn, slug, annular, and mist. In this region, the interfacial effects are strongest and hence most dependent on the type of flow or flow pattern. Addressing these issues phenomenologically is best dealt with using empirical models utilizing one or more closure constants. However, as we shall see shortly, a simple theoretical closure can be found, which is independent of the type flow and only depends on which of the four flow regimes is assumed. The Lockhart–Martinelli curves are plotted in Fig. 1.

The Lockhart–Martinelli [1] scheme can be viewed as universal for any flow regime. The influence of the flow pattern or regime generally only manifests itself in the transition region due to interfacial effects. In the asymptotic region, the plot is universal in that it returns the single phase flow pressure drop regardless of flow regime, i.e., laminar or turbulent. Thus two flows having the same X value are only distinguishable as a result of interfacial effects. This is clearly seen in Fig. 1. In the original analysis of Lockhart and Martinelli, these interfacial effects are stronger for turbulent flows than for laminar flows, as expected. But within a given flow regime such as turbulent-turbulent, the type of flow pattern should also lead to distinguishable interfacial effects, for example, annular flow versus churn flow.

2.2 Turner–Wallis Method. More than a decade had passed since Lockhart and Martinelli's [1] paper had been published when Turner and Wallis [2] had developed a theoretical approach that allowed for an analytical closure of the Lockhart–Martinelli [1] equations. Turner and Wallis [2] proposed that the two phase flow could be analyzed by modeling the flow as two parallel single phase streams flowing in separate pipes, each with a cross-sectional area equal to its actual flow area. This approach is also referred to as the "separate cylinders" model [2]. By assuming that the pressure gradient across the parallel streams was equal to that in the two phase flow, and that the cross-sectional areas of the two smaller pipes equaled the area of the actual pipe carrying the combined stream, they were able to develop simple analytical

Table 1 Turner–Wallis closure coefficients

Liquid	Gas	p
$m=0$	$n=0$	2.5
$m=0.2$	$n=0.2$	2.4
$m=0.25$	$n=0.25$	2.375
$m=1$	$n=1$	2
$m=1$	$n=0.25$	2.10
$m=0.25$	$n=1$	2.05

relationships for the laminar-laminar, turbulent-turbulent, and constant friction factor flow regimes. For the mixed flow regimes, the approach leads to implicit relationships for ϕ_l^2 and ϕ_g^2, which can easily be solved numerically.

Assuming that the simple friction models are stated as before, i.e., $f_l \sim C_l/\mathrm{Re}_l^n$ and $f_g \sim C_g/\mathrm{Re}_g^m$, it is easy to show that the following expression can be obtained:

$$\left(\frac{1}{\phi_l^2}\right)^{2/(5-n)} + \left(\frac{1}{\phi_g^2}\right)^{2/(5-m)} = 1 \tag{11}$$

Introducing $X^2 = \phi_g^2/\phi_l^2$, we can solve for a number of special cases, which yield both explicit and implicit forms for ϕ_l^2. Turner and Wallis [2] suggested that for any two phase flow, the "separate cylinders" analysis, Eq. (11), could be generalized in the following way:

$$\left(\frac{1}{\phi_l^2}\right)^{1/p} + \left(\frac{1}{\phi_g^2}\right)^{1/p} = 1 \tag{12}$$

such that any value of p could be chosen to fit a particular data set. This leads to a one parameter empirical closure model. This generalization was proposed in Ref. [2], but no physical basis was given. Given that $X^2 = \phi_g^2/\phi_l^2$, one can rearrange the above expression to obtain:

$$\phi_l^2 = \left[1 + \left(\frac{1}{X^2}\right)^{1/p}\right]^p \tag{13}$$

The value of p has been found using the separate cylinders approach to equal $p=2$ for laminar-laminar flow, $2.375 < p < 2.5$ for turbulent-turbulent flows based on friction factor, and $2.5 < p < 3.5$ turbulent-turbulent flows calculated on a mixing length basis [2]. These are summarized in Table 1 and in Fig. 2.

In the case of the two mixed flow regimes, the Turner–Wallis [2] method leads to the following implicit expressions:

$$\phi_l^2 = \left[1 + (\phi_l^2)^{3/38}\left(\frac{1}{X^2}\right)^{1/2.375}\right]^2 \tag{14}$$

for the laminar-turbulent case and

$$\phi_l^2 = \left[1 + (\phi_l^2)^{-3/38}\left(\frac{1}{X^2}\right)^{1/2}\right]^{2.375} \tag{15}$$

for the turbulent-laminar case. These can be solved numerically and fit to simple relationships, such as Eq. (13).

Using the data of Lockhart and Martinelli [1], Turner and Wallis [2] found that $p=2.75$ fit the laminar-laminar flow data better, while $p=4$ fit the turbulent-turbulent flow data better. Irrespective of the four Lockhart–Martinelli [1] flow regimes, Turner and Wallis [2] found that $p=3.5$ fit all data in a best fit sense, i.e., equal scatter about Eq. (13). Equation (13) also has the advantage of overcoming the implicit formulation, which results from Eq. (11) in the mixed flow regimes. However, in these cases, it now becomes an *empirical* closure rather than an *analytical* closure. In any event, the fact that the results of the analytical closure are not in full agreement with the better empirical closure suggests that additional attention is required to better predict and understand the interfacial interactions. As stated by Wallis [2], there is no rationale for the modest agreement between their analytical results and the empirical results of Lockhart and Martinelli [1]. Despite this, the method is still widely accepted due in part to its simplicity, and in the opinion of the present authors, its analytical elegance.

2.3 Chisholm Method. Not long after Turner and Wallis [2] proposed the separate cylinder model, Chisholm [3] proposed a more rigorous analysis, which was an extension of the Lockhart–Martinelli [1] approach, except that a *semi-empirical* closure was adopted. Chisholm's [3] rationale for his study was the fact that the Lockhart–Martinelli [1] approach failed to produce suitable equations for predicting the two phase pressure gradient, given that the empirical curves were only presented in graphical and tabular forms. Despite Chisholm's [3] claims, he developed his approach in much the same manner as Lockhart and Martinelli [1]. After several algebraic manipulations, Chisholm [3] proposed that the two phase flow pressure gradient could be predicted using only

$$A = A_g + A_l \tag{16}$$

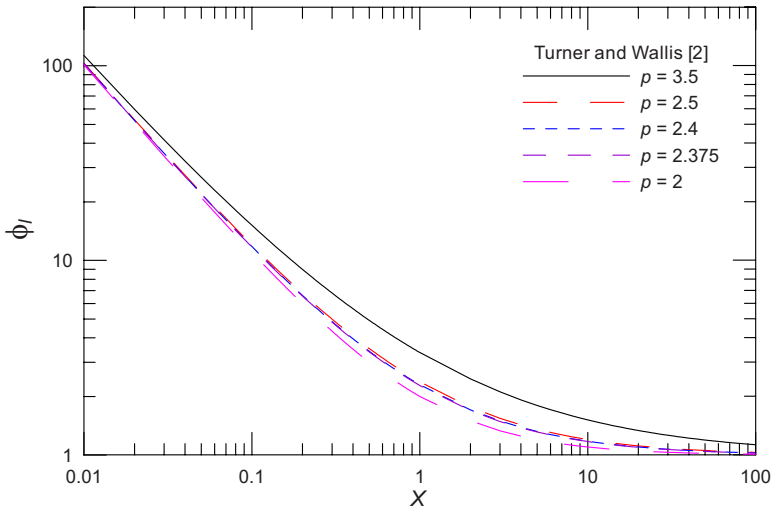

Fig. 2 Turner and Wallis's [2] method for ϕ_l versus X for various derived and empirical values of p

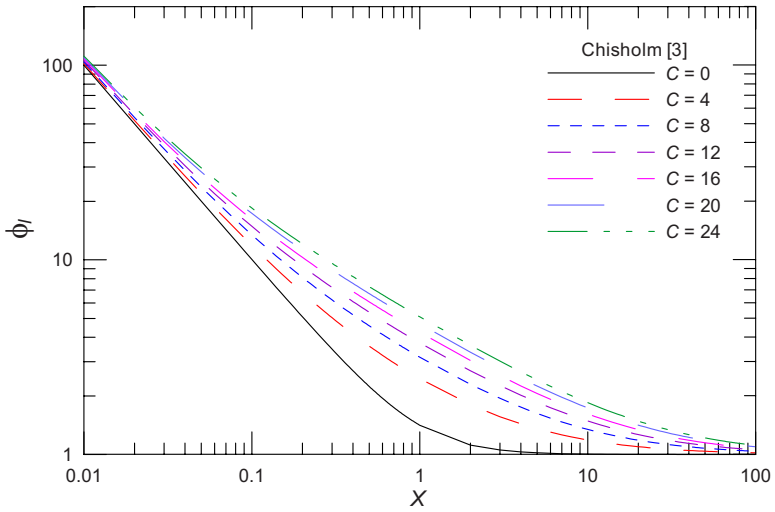

Fig. 3 Chisholm's [3] equation for ϕ_l versus X for various values of C

$$\frac{1}{\beta} = \frac{A}{A_g} - \frac{A_l}{\alpha A_g} \tag{17}$$

$$\left(\frac{A_l}{A}\right)^{(2-n)/2}\left(\frac{1}{1-A_l/A}\right)^{(2-m)/2} = \frac{X\beta^{(1+m)/2}}{Z\alpha^{(1+n)/2}} \tag{18}$$

$$\phi_l^2 = \frac{1}{\alpha^{1+n}}\left(1+\frac{A_g}{A_l}\right)^{1-n}\left(\frac{A_g}{A_l Z^2}+1\right) \tag{19}$$

where Z is physical parameter related to the interfacial stress referred to as a "shear force function" by Chisholm [3]. In general, Z can only be derived analytically for special cases such as annular flow and homogeneous flow. With Z known analytically or empirically, along with A_l/A and X, the above equations could be solved for α, β, A_g/A_l, and ϕ_l^2. Chisholm [3] solved the above equations using a value $Z \approx 14$, which he determined by "trial and error," and values of A_l/A, i.e., the liquid volume fraction, as suggested by Lockhart and Martinelli [1]. Chisholm's [3] semitheoretical analysis predicted the tabulated values of the Lockhart–Martinelli [1] curves in the realm of -21% and $+16\%$ depending the flow regime.

Chisholm [3] felt that above equations were "unnecessarily complicated as far as the design engineer is concerned," and as such, in the same study he proposed the now widely adopted equations:

$$\phi_l^2 = 1 + \frac{C}{X} + \frac{1}{X^2} \tag{20}$$

and

$$\phi_g^2 = 1 + CX + X^2 \tag{21}$$

where C was chosen to be equal to $C_{ll}=5$ for laminar-laminar flow, $C_{tt}=20$ for turbulent-turbulent flow, $C_{tl}=10$ for turbulent-laminar flow, and $C_{lt}=12$ for laminar-turbulent flow to provide agreement with the curves presented graphically in Lockhart and Martinelli's original paper [1]. These curves are shown in Fig. 1 to represent the original Lockhart–Martinelli [1] tabulated data. It should also be pointed out that the Chisholm constants have remain unchanged when Eqs. (20) and (21) are reported in the literature. They are based only on the reported data of Lockhart and Martinelli [1], as they are fits to the original tabulations presented in Ref. [1] for the four flow regimes.

However, as a one parameter model, C can be chosen to fit any one data set with greater accuracy. This is frequently done by researchers in the open literature. The meaning of the coefficient C can be easily seen if one expands the Chisholm equations to obtain

$$\left.\frac{dp}{dx}\right|_{tp} = \left.\frac{dp}{dx}\right|_l + C\left(\left.\frac{dp}{dx}\right|_l \left.\frac{dp}{dx}\right|_g\right)^{1/2} + \left.\frac{dp}{dx}\right|_g \tag{22}$$

where we may now write that

$$\left.\frac{dp}{dx}\right|_i = C\left(\left.\frac{dp}{dx}\right|_l \left.\frac{dp}{dx}\right|_g\right)^{1/2} \tag{23}$$

is the *interfacial* contribution to the total two phase flow pressure drop. Thus, the constant C in Chisholm's model can be viewed as a weighting factor for the geometric mean of the single phase gas and liquid only pressure gradients (Fig. 3).

The constant C can be derived analytically for a number of special cases. For example, Whalley [4] obtained for a homogeneous flow having constant friction factor:

$$C = \left(\frac{\rho_l}{\rho_g}\right)^{1/2} + \left(\frac{\rho_g}{\rho_l}\right)^{1/2} \tag{24}$$

which for an air/water combination gives $C \approx 28.6$, which is in good agreement with Chisholm's value for turbulent-turbulent flows. Whalley [4] also showed that for laminar and turbulent flows with no interaction between phases the values of $C \approx 2$ and $C \approx 3.66$ are obtained, respectively. Furthermore, if a laminar plug flow is assumed, a value of $C=0$ can be easily derived, which implies that the total pressure gradient is just the sum of the component pressure gradients based on plug length and component flow rate. This is a reasonable approximation provided that plug lengths are longer than 15 diameters [5]. This observation is also in agreement with recent models [6,7] in microchannel flows, which have yielded

$$C = 21[1 - \exp(-319 D_h)] \tag{25}$$

where the hydraulic diameter D_h must be specified in m. In the case of microchannels, it can be seen that $C \to 0$ as hydraulic diameter becomes small, $D_h \to 0$. English and Kandlikar [7] extended the Mishima and Hibiki [6] model to laminar-laminar flow by replacing their constant, 21, with the Chisholm value for laminar-laminar flow of 5. In general, a correlation such as Eq. (25) should be discouraged due to the "dimensional" specification of D_h, as it is easy to miscalculate C if the proper dimensions are not used for D_h, which is occasionally reported erroneously in the

open literature.

Zhang [8] found that C was dependent on the Laplace number La because of the large effect of surface tension and gap size for mini- and microchannels, As a result, the Laplace number was used instead of the hydraulic diameter D_h in the Mishima and Hibiki [6] correlation as follows:

$$C = 21\left[1 - \exp\left(-\frac{0.358}{\mathrm{La}}\right)\right] \tag{26}$$

where

$$\mathrm{La} = \frac{\sqrt{\sigma/g(\rho_l - \rho_g)}}{D} \tag{27}$$

is the Laplace number. The above equation has the advantage of being in a dimensionless form.

Additional formulations and correlations for the closure parameter C have functions of properties, mass flux, and quality that can be found in the open literature [9]. For example, Sun and Mishima [9] found that C was strongly affected not only by La but also by Re_l in the laminar flow region. As a result, the following expression was obtained for C in the laminar flow region:

$$C = 26\left(1 + \frac{\mathrm{Re}_l}{1000}\right)\left[1 - \exp\left(-\frac{0.153}{0.27\ \mathrm{La} + 0.8}\right)\right] \tag{28}$$

Their statistical analysis showed that C changed with Reynolds number. Moreover, the term C/X in the Chisholm correlation strongly depended on the ratio $\mathrm{Re}_g/\mathrm{Re}_l$, especially when Re_l or Re_g is over 2000. In addition, it can be found that the data points become more scattered with the increase in the ratio $\mathrm{Re}_g/\mathrm{Re}_l$. Based on the statistical analysis, they modified the Chisholm correlation as follows:

$$\phi_l^2 = 1 + \frac{1.79\left(\frac{\mathrm{Re}_g}{\mathrm{Re}_l}\right)^{0.4}\left(\frac{1-x}{x}\right)^{0.5}}{X^{1.19}} + \frac{1}{X^2} \tag{29}$$

They pointed out that the C value calculated by Eq. (29) would not sharply change while $x \to 1$ or $x \to 0$ because Re_l or Re_g changed inversely with x and $1-x$, respectively. Particularly, for their database, x ranged from 1.5×10^{-5} to 0.98, while the calculated value of C was found to vary from 29.9 to 3.2, accordingly. Despite this extensive correlation of C, Sun and Mishima [9] concluded that their model is only marginally better than other models in many cases, and only slightly less accurate than the widely adopted Mueller–Stainhagen and Heck model [9]. Thus, correlating C as a function of other variables appears to offer little added value.

Additional extended Chisholm type models are reviewed by Sun and Mishima [9] and Awad [10].

2.4 Modified Turner–Wallis Model. Awad and Muzychka [11] arrived at the same simple form as the empirical Turner and Wallis [2] model, but with a different physical approach. Rather than model the fluid as two distinct fluid streams flowing in separate pipes, they proposed that the two phase pressure drop could be predicted using a nonlinear superposition of the component pressure drops that would arise from each stream flowing alone in the *same* pipe, through application of the Churchill–Usagi asymptotic correlation method [12]. This form was asymptotically correct for either phase as the mass quality varied from $0 < x < 1$. Furthermore, rather than approach the Martinelli parameter from the point of view of the four flow regimes using simple friction models, they proposed using the Churchill [13] model for the friction factor in smooth and rough pipes for all values of the Reynolds number. In this way, the proposed model was more general and contained only one empirical coefficient, the Churchill–Usagi [12] blending parameter. The resulting model takes the form

$$\left.\frac{dp}{dx}\right|_{tp} = \left[\left(\left.\frac{dp}{dx}\right|_l\right)^q + \left(\left.\frac{dp}{dx}\right|_g\right)^q\right]^{1/q} \tag{30}$$

or when written as a two phase liquid multiplier:

$$\phi_l^2 = \left[1 + \left(\frac{1}{X^2}\right)^q\right]^{1/q} \tag{31}$$

which is the same as Eq. (13) from the Turner–Wallis approach, when $q = 1/p$. The main exception is that the authors [11,14–16] developed values of q for different flow regimes using the following friction model to calculate X^2:

$$f = 2\left[\left(\frac{8}{\mathrm{Re}_D}\right)^{12} + \left(\frac{1}{(A_1 + A_2)^{3/2}}\right)\right]^{1/12} \tag{32}$$

where

$$A_1 = \left\{2.457 \ln\left[\frac{1}{(7/\mathrm{Re}_D)^{0.9} + (0.27k/D)}\right]\right\}^{16} \tag{33}$$

and

$$A_2 = \left(\frac{37530}{\mathrm{Re}_D}\right)^{16} \tag{34}$$

The principal advantages of the above approach over the Turner–Wallis [2] method are twofold. First, all four Lockhart–Martinelli flow regimes can be handled with ease since the Turner–Wallis [2] method leads to implicit relationships for the two mixed regimes. Second, since the friction model used is only a function of Reynolds number and roughness, broader applications involving rough pipes can be easily modeled. Using the above equations, Awad [10] found that $q \approx 0.307$ for large tubes and $q \approx 0.5$ for microchannels, minichannels, and capillaries. The general characteristics of Eq. (31) are shown in Fig. 4 for a range of values of q. Thus, the extended Turner–Wallis approach is also a one parameter correlating scheme. Awad and Butt [14–16] showed that the method works well for liquid-liquid flows and flows through porous and fractured media for petroleum industry applications.

Approximate equivalence between Eq. (20) and Eq. (31) can be found when $q = 0.36$, 0.3, 0.285, and 0.245 when $C = 5$, 10, 12, and 20, respectively. This yields differences of 3–9% rms. The special case of $q = 1$ leads to a linear superposition of the component pressure drops, which corresponds to $C = 0$. This limiting case is only valid for plug flows when plug length to diameter ratios exceed 15 [5].

2.5 Modified Chisholm Models. Finally, in a recent series of studies by Saisorn and Wongwises [17–19], a new correlation was proposed having the form

$$\phi_l^2 = 1 + \frac{6.627}{X^{0.761}} \tag{35}$$

for experimental data for slug flow, throat-annular flow, churn flow, and annular-rivulet flow [17], and

$$\phi_l^2 = 1 + \frac{2.844}{X^{1.666}} \tag{36}$$

for experimental data for annular flow, liquid unstable annular alternating flow (LUAAF), and liquid/annular alternating flow (LAAF) [18]. These correlations neglect the $1/X^2$ term, which represents the limit of primarily gas flow in the Lockhart–Martinelli [1] formulation. Neglecting this term ignores this important limiting case, which is an essential contribution in the Lockhart–Matrinelli modeling approach. As a result, at low values of X, the proposed correlations undershoot the trend of the data, limiting their use in the low X range. Thus, a more appropriate and generalized form of the above correlations should be

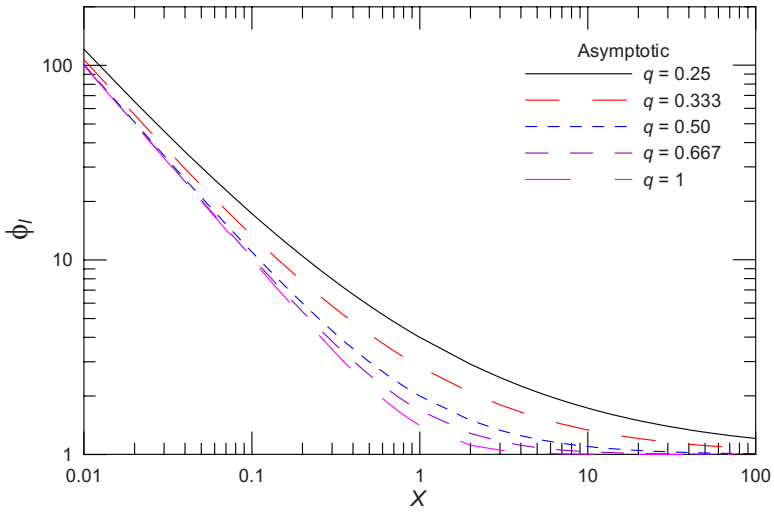

Fig. 4 Comparison of Awad and Muzychka [8] equation for various q

$$\phi_l^2 = 1 + \frac{A}{X^m} + \frac{1}{X^2} \tag{37}$$

or

$$\phi_g^2 = 1 + AX^m + X^2 \tag{38}$$

which are the focus of Sec. 3 for decomposing two phase flow pressure drop into three basic components.

3 Asymptotic Decomposition of Two Phase Flow

Gas-liquid two phase flow will be examined from the point of view of interfacial pressure drop. Recognizing that in a Lockhart–Martinelli [1] reduction scheme single phase flow characteristics must be exhibited in a limiting sense, they will be subtracted from the experimental data being considered to illustrate some benefits of using the one and two parameter models. For this purpose, we utilize some recent data for microtubes and the original data presented in the paper of Lockhart and Martinelli [1]. While not exhaustive, the general idea of this modeling approach is illustrated.

We can define the two phase flow pressure drop as a linear combination of three simple pressure drops or pressure gradients. These are the single phase liquid, single phase gas, and interfacial pressure drop. The rationale for such a choice lies in the definition of the Lockhart–Martinelli approach, whereby, for small and large values of the Martinelli parameter X, one obtains single phase flow, while in the transitional region between $0.01 < X < 100$, the interfacial effects result in an increase in ϕ^2 over the simple linear superposition of the single phase flow contributions. This is where a large scatter in data occurs depending upon flow regime or pattern.

Beginning with

$$\left.\frac{dp}{dx}\right|_{tp} = \left.\frac{dp}{dx}\right|_{l} + \left.\frac{dp}{dx}\right|_{i} + \left.\frac{dp}{dx}\right|_{g} \tag{39}$$

Introducing the two phase liquid multiplier as proposed by Lockhart and Martinelli [1], we obtain

$$\phi_l^2 = 1 + \phi_{l,i}^2 + \frac{1}{X^2} \tag{40}$$

where

$$\phi_{l,i}^2 = \frac{\left.\frac{dp}{dx}\right|_i}{\left.\frac{dp}{dx}\right|_l} \tag{41}$$

is a two phase multiplier for the interfacial pressure drop. This can be viewed as an extended form of the Chisholm model, where the interfacial contribution is what is to be modeled.

3.1 One Parameter Models. Comparison with the Chisholm [3] formulation gives

$$\phi_{l,i}^2 = \frac{C}{X} \tag{42}$$

for the liquid multiplier formulation or

$$\phi_{g,i}^2 = CX \tag{43}$$

for the gas multiplier formulation.

This represents a simple one parameter model, whereby closure can be found with comparison with experiment. In addition, the simple asymptotic form of Eq. (31) also represents a one parameter model. If the interfacial effects can be modeled by Chisholm's proposed model or Eq. (31), then all of the reduced data should show trends indicated by Eq. (42) or Eq. (43). However, if data do not scale according to Eq. (42) or Eq. (43), i.e., a slope of -1 or $+1$, then a two parameter model is clearly required. This is shown in Fig. 5, which shows that all interfacial effects have the same slope but their intensity is governed by the value of C.

3.2 Two Parameter Models. The above equations may be extended to develop a simple two parameter power law model such that

$$\phi_{l,i}^2 = \frac{A}{X^m} \tag{44}$$

or

$$\phi_{g,i}^2 = AX^m \tag{45}$$

leading to Eq. (37) or Eq. (38).

These forms have the advantage that experimental data for a particular flow regime can be fitted to the simple power law after the removal of the single phase pressure gradients from the experimental data. Additional modifications may be introduced if the coefficients A and m can be shown to depend on other variables

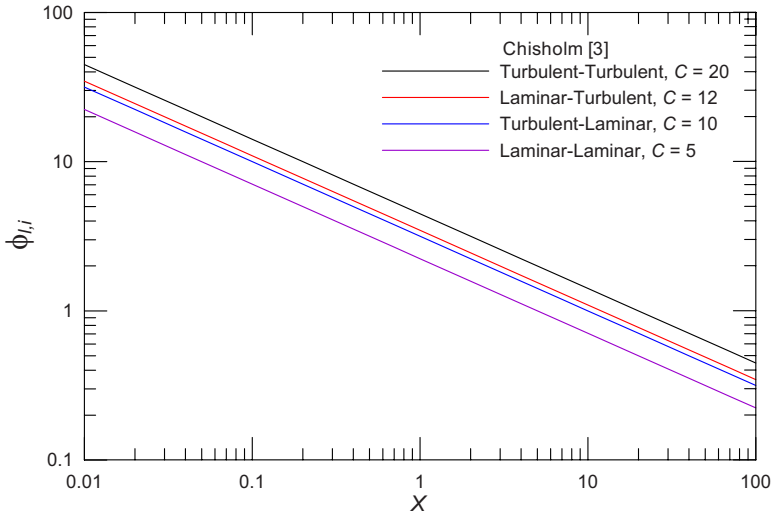

Fig. 5 Interfacial two phase multiplier for different flow regimes for the Chisholm model

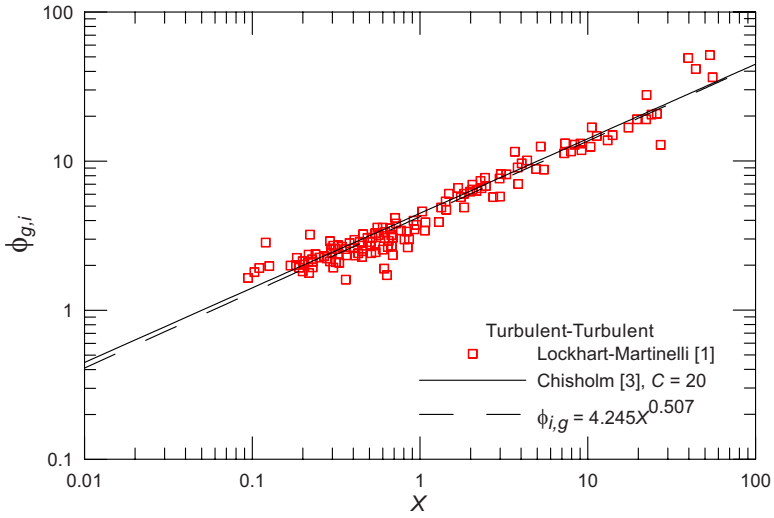

Fig. 6 Interfacial two phase multiplier for different flow regimes

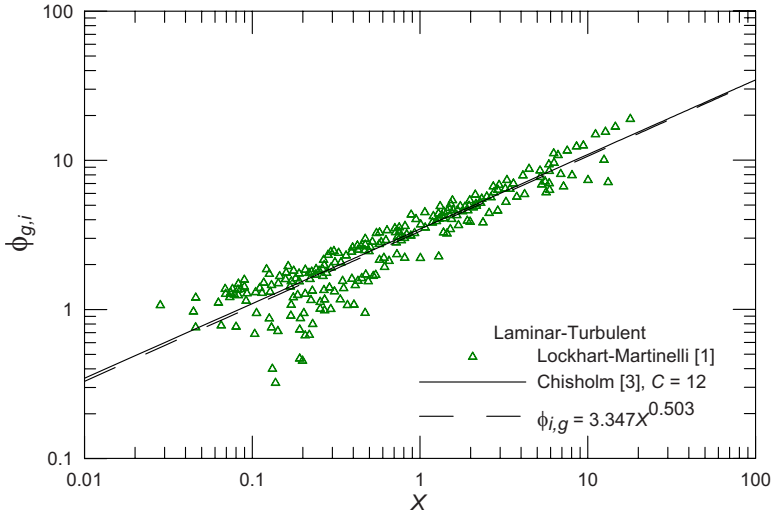

Fig. 7 Interfacial two phase multiplier for different flow regimes

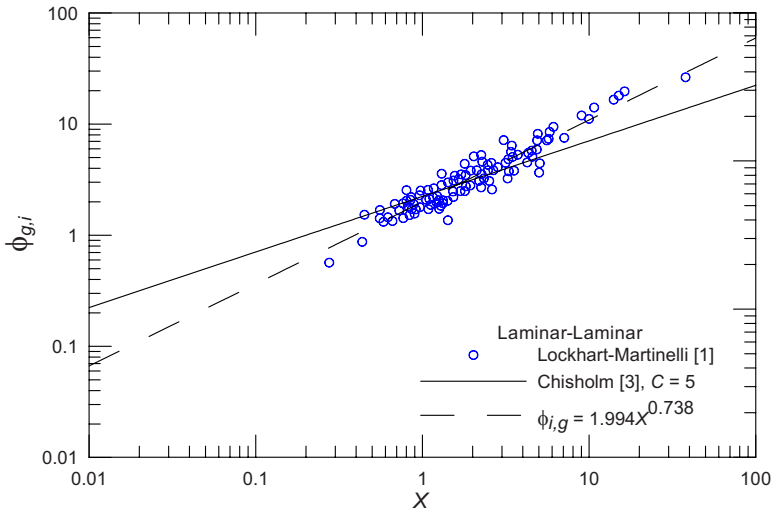

Fig. 8 Interfacial two phase multiplier for different flow regimes

such as mass flow rate, fluid properties, and mass quality or void fraction. These issues will be examined next considering a few data sets from the open literature.

4 Comparisons With Data

In this section, we will apply the approach outlined above to a few selected data sets. Given that two phase flow data are widely reported using the Lockhart–Martinelli parameters ϕ_l and X, we can present two phase flow data simply as an interfacial two phase multiplier using

$$\phi_{l,i}^2 = \phi_l^2 - 1 - \frac{1}{X^2} \tag{46}$$

Beginning with the data originally reported in Lockhart and Martinelli's [1] original paper, we consider the interfacial two phase multiplier for the flow regimes defined by Lockhart and Martinelli. Figures 6–8 present the data for turbulent-turbulent, laminar-turbulent, and laminar-laminar flows. In the first two cases, one can see that the Chisholm one parameter model, which is proportional to X, gives good results. In the case of laminar-laminar flow, better agreement can be found with the two parameter modeling approach since the data are not directly proportional to X, as Eq. (43) implies. The results are summarized in Table 2 along with comparisons to the original Chisholm and Turner–Wallis one parameter models. Additionally, we present the best values of the Chisholm coefficient for each data set, given that the original Chisholm constants were not based on a more substantial data set.

All of the data in Figs. 6–8 are plotted with the alternate two parameter model for the full two phase flow multiplier in Fig. 9. Additional data in the Appendix of Lockhart and Martinelli's paper [1] was provided by Jenkins [20], which highlight the fact that even within the turbulent-turbulent flow regime, trends can be seen if the data are grouped by liquid mass flow rate. These data

Table 2 Comparison of one and two parameter models for ϕ

	Two parameter			One parameter[a]		One parameter[b]		One parameter	
Flow	A	m	%rms	C	%rms	C	%rms	q	%rms
Lockhart and Martinelli [1] for ϕ_g									
Laminar/laminar	3.98	1.476	13.49	5	16.35	5	16.35	0.370	15.53
Laminar/turbulent	11.20	1.060	20.01	12	20.87	10	19.51	0.290	19.62
Turbulent/turbulent	18.02	1.014	15.76	20	17.67	16	15.08	0.244	14.21
All data	10.97	1.000	25.61	8	23.86	8	23.86	0.299	23.12
Jenkins [20] for ϕ_g									
$\dot{m}$=75.75 kg/h	4.24	0.300	5.13	20	17.94	15	15.36	0.260	10.65
$\dot{m}$=333.39 kg/h	11.53	0.558	7.87	20	22.37	14	16.22	0.253	14.19
$\dot{m}$=726.65 kg/h	19.56	0.832	4.24	20	7.42	19	7.15	0.227	7.36
All data	15.26	0.811	13.50	20	17.34	16	14.64	0.247	12.99
Saisorn and Wongwises [17–19] for ϕ_l									
Slug	2.06	0.453	13.69	5	24.35	2	15.13	0.465	14.44
Churn	6.27	0.278	8.11	5	17.40	8	10.01	0.303	9.34
Throat-annular	2.69	1.740	11.71	5	26.38	2	11.93	0.476	11.45
Annular-rivulet	0.0795	1.075	22.50	5	26.14	1	6.28	0.606	6.08
Annular flow	2.45	0.308	24.45	5	19.41	3	10.73	0.465	10.30
LUAAF	0.908	0.870	18.43	5	47.50	1	7.53	0.645	7.36
LAAF	1.49	0.678	9.82	5	37.08	2	6.65	0.541	4.59
All data	3.21	1.042	18.14	5	27.16	2	14.26	0.488	14.13

[a]Actual Chisholm constant.
[b]Best Chisholm constant.

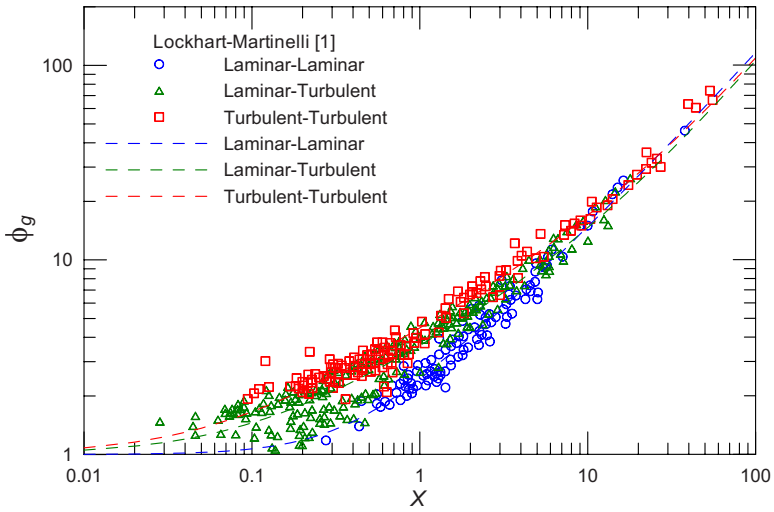

Fig. 9 Two phase multiplier for all data based on different flow regimes

are re-analyzed using Eq. (38) and the two parameter interfacial two phase multiplier is given in Fig. 10 along with the single parameter Chisholm model.

It is easily seen that as mass flow rate increases, the interfacial pressure drop increases with an observed increase in the slope of the curve. All of the data are plotted in Fig. 11 as a full two phase flow multiplier. The accuracy of the various approaches are given in Table 2 for all of the data reported in Ref. [1]. It is seen that the two parameter empirical approach is somewhat better for correlating data.

Finally, we present some data for capillary tubes obtained from Refs. [17,18]. These data are reported based on the flow pattern, i.e., slug, annular, and churn. Data are plotted in Figs. 12–14 for the two parameter model, where it can be seen that the various annular flow patterns have similar interfacial behavior. The greatest variation is observed with the drastically different flow patterns of slug, churn, and annular, as shown in Fig. 12. The various accuracies for both one and two parameter models are given in Table 2. It can be seen as the flow rate increases and hence a tendency toward turbulent flow, the interfacial effects increase the two phase flow multiplier systematically, hence an increase in the Chisholm parameter C and increases in the A and m. Similarly, a decrease in q is observed in the asymptotic based one parameter model. This is not as evident with the subjective flow pattern analysis using the data of Saisorn and Wongwises [17,18]. Also shown in Figs. 12–14 is the interfacial parameter derived from the correlations given in Refs. [17,18]. The correlation departs from the trends of the given data and fits due to the fact that the authors [17,18] did not include the single phase gas flow limit in their development. When presented in this manner, one can see that large errors will occur in the region of $0.01 < X < 1$. It can also be seen that the correlation does not adequately account for the interfacial effects at higher values of X as the trend in the data do not follow the correlation properly. Thus, any two phase flow modeling using empirical or semi-empirical models must include the asymptotic limits of single phase flow for both the gas and liquid phases.

5 Summary and Conclusions

Two phase flows in pipes, minichannels, and microchannels was considered. A review of the classic Lockhart–Martinelli method and other asymptotic representations of two phase flow was examined. These approaches can all be considered one and two parameter models. The two parameter models offer more flexibility for developing empirical models for specific flow regimes when the simple Chisholm model fails to capture the slope of the interfacial two phase multiplier. The above approaches were com-

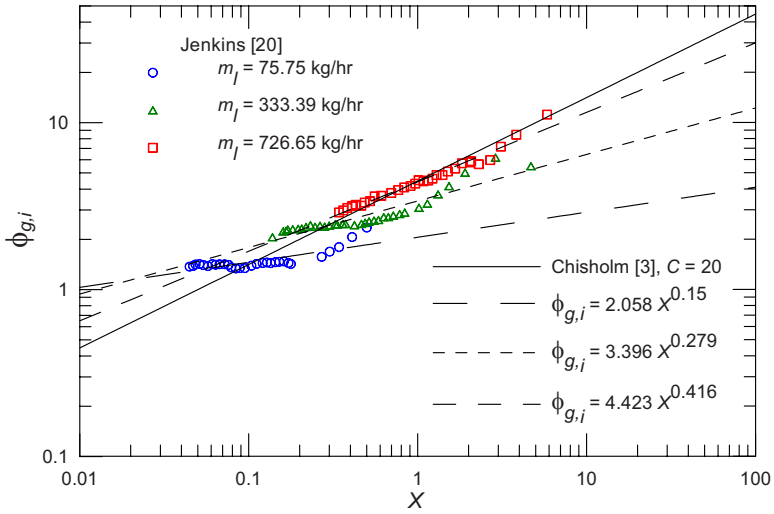

Fig. 10 Interfacial two phase multiplier for different flow rates

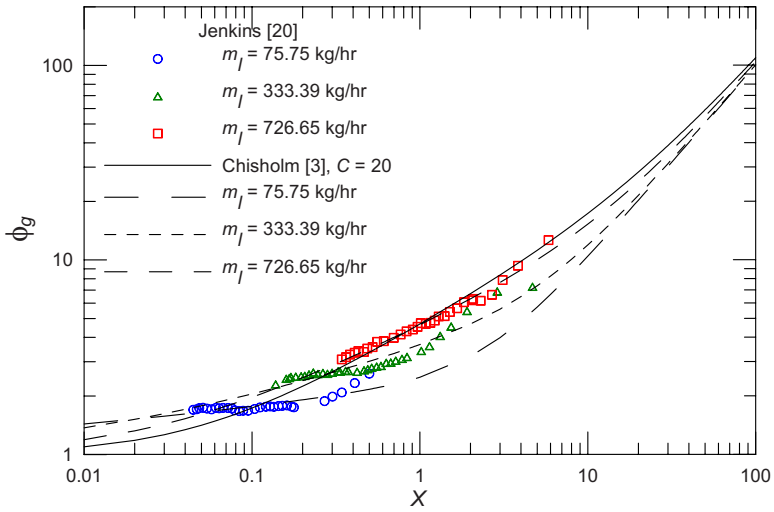

Fig. 11 Two phase multiplier for different flow rates

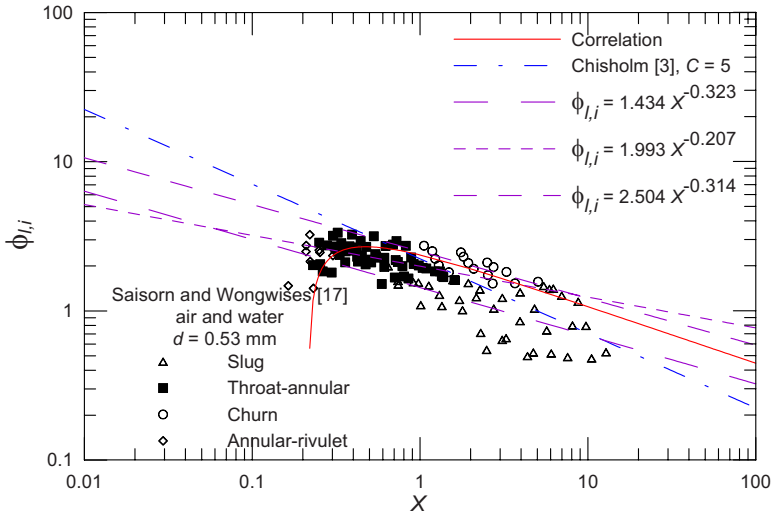

Fig. 12 Interfacial two phase multiplier for different flow patterns

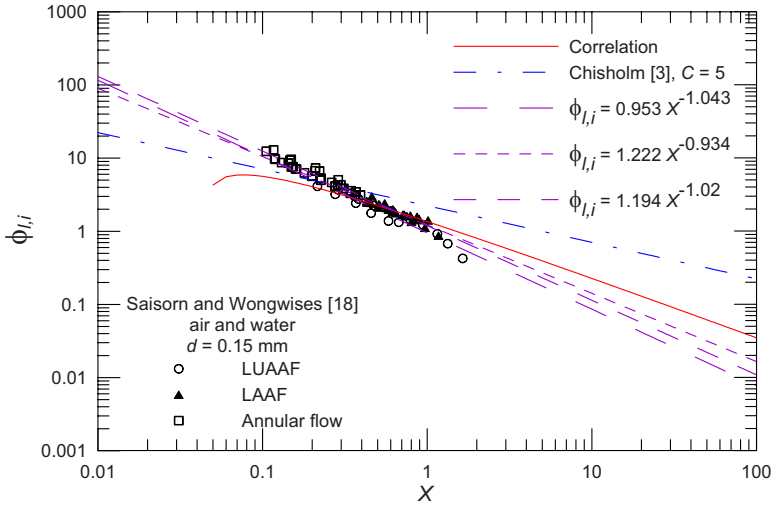

Fig. 13 Interfacial two phase multiplier for different flow patterns

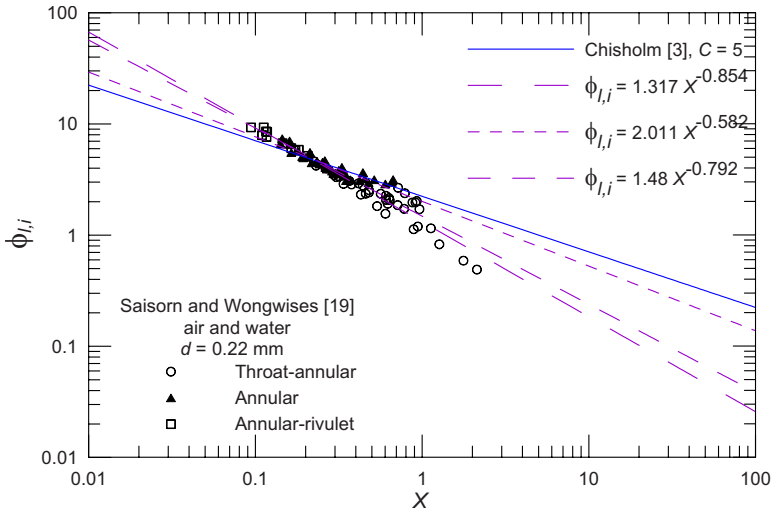

Fig. 14 Interfacial two phase multiplier for different flow patterns

pared for a few selected data sets and it was found that the proposed two parameter modeling approach is the best and offers the greatest flexibility. However, the modified Turner–Wallis approach of Awad and Muzychka [11] also provides comparable prediction of data sets.

Furthermore, as shown by Sun and Mishima [9], the return on investment in more complicated empirical modeling schemes, which include additional physical variables in the prediction of Chisholm constants, is not always positive, making the simple approaches reviewed in this paper a more viable approach. In fact, the approach used by Sun and Mishima [9] cannot guarantee better accuracy unless it is applied to a phenomenological case, such as a two phase plug flow, as shown in Ref. [5]. Sun and Mishima [9] even concluded their paper with the statement that their model only provides comparable accuracy to the popular Mueller–Steinhagen and Heck model despite having many more variables.

Two phase flow modeling from the point of view of interfacial phenomena is deemed to be a better approach from the standpoint of understanding what variables will affect the data in the interfacial region. The true impact of the two phase flow interfacial effects are more clearly seen, only after the removal of the single phase flow contributions from the Lockhart–Martinelli two phase multiplier. This is evident from Figs. 12–14, where the assumed Chisholm model clearly does not model the interfacial effects adequately. Decomposing the Lockhart–Martinelli approach into single phase and interfacial components would appear to provide better understanding of experimental data and lead to better model/correlation development.

Acknowledgment

The authors acknowledge the financial support of the Natural Sciences and Engineering Research Council of Canada (NSERC) through the Discovery Grants program.

Nomenclature

A = flow area, m^2
C = Chisholm constant
C_g = gas phase friction constant
C_l = liquid phase friction constant
D_h = hydraulic diameter, m
D = diameter of circular duct, m
f = fanning friction factor
k = pipe roughness, m
L = length of tube, m
La = Laplace number
$\dot{m}$ = liquid mass flow rate, kg/s
m = gas phase friction exponent
n = liquid phase friction exponent
p = pressure, Pa
p, Eq. (13) = blending parameter, Eq. (13)
P = perimeter, m
q = blending parameter, Eq. (31)
Re_D = Reynolds number, $\equiv UD/\nu$
U = average liquid velocity, m/s
x = mixture mass quality
x = axial position in a duct
X = Martinelli parameter

Greek Symbols

α = liquid area ratio
β = gas area ratio
ϕ = two phase multiplier
ρ = fluid density, $\mathrm{kg/m^3}$
σ = surface tension, N/m

Superscripts

* = dimensionless
$\overline{(\cdot)}$ = mean value

Subscripts

g = gas
i = interfacial
l = liquid
tp = two phase

References

[1] Lockhart, R. W., and Martinelli, R. C., 1949, "Proposed Correlation of Data for Isothermal Two Phase Flow, Two Component Flow in Pipes," Chem. Eng. Prog., **45**, pp. 39–48.
[2] Wallis, G., 1969, *One Dimensional Two Phase Flow*, McGraw-Hill, New York.
[3] Chisholm, D., 1967, "A Theoretical Basis for the Lockhart-Martinelli Correlation for Two Phase Flow," Int. J. Heat Mass Transfer, **10**, pp. 1767–1778.
[4] Whalley, P. B., 1996, *Two-Phase Flow and Heat Transfer*, Oxford University Press, New York pp. 22–25.
[5] Kreutzer, M. T., Kapteijn, F., Moulijin, J. A., Kleijn, C. R., and Heiszwolf, J. J., 2005, "Inertial and Interfacial Effects on Pressure Drop of Taylor Flow in Capillaries," AIChE J., **51**(9), pp. 2428–2440.
[6] Mishima, K., and Hibiki, T., 1996, "Some Characteristics of Air-Water Two Phase Flow in Small Diameter Vertical Tubes," Int. J. Multiphase Flow, **22**, pp. 703–712.
[7] English, N. J., and Kandlikar, S. G., 2006, "An Experimental Investigation into the Effect of Surfactants on Air-Water Two-Phase Flow in Minichannels," Heat Transfer Eng., **27**, pp. 99–109.
[8] Zhang, W., 2006, "Study on Constitutive Equations for Flow Boiling in Mini-Channels," Ph.D. thesis, Kyoto University, Japan.

[9] Sun, L., and Mishima, K., 2009, "Evaluation Analysis of Prediction Methods for Two-Phase Flow Pressure Drop in Mini-Channels," Int. J. Multiphase Flow, **35**, pp. 47–54.
[10] Awad, M. M., 2007, "Two Phase Flow Modelling in Pipes," Ph.D. thesis, Memorial University of Newfoundland, Canada.
[11] Awad, M. M., and Muzychka, Y. S., 2004, "A Simple Asymptotic Compact Model for Two-Phase Frictional Pressure Gradient in Horizontal Pipes, *Proceedings of the IMECE 2004*, Anaheim, CA, Nov. 13–19, Paper No. IMECE2004-61410.
[12] Churchill, S. W., and Usagi, R., 1972, "A General Expression for the Correlation of Rates of Transfer and Other Phenomena," AIChE J., **18**, pp. 1121–1128.
[13] Churchill, S. W., 1977, "Friction-Factor Equation Spans all Fluid-Flow Regimes," Chem. Eng. (New York, NY), **84**, pp. 91–92.
[14] Awad, M. M., and Butt, S. D., 2009, "A Robust Asymptotically Based Modeling Approach for Two-Phase Flow in Porous Media," ASME J. Heat Transfer, **131**, p. 101014.
[15] Awad, M. M., and Butt, S. D., 2009, "A Robust Asymptotically Based Modeling Approach for Two-Phase Gas-Liquid Flow in Fractures," 12th International Conference on Fracture (ICF12), Session: Oil and Gas Production and Distribution, Ottawa, Canada, Jul. 12–17, Paper No. ICF2009-646.
[16] Awad, M. M., and Butt, S. D., 2009, "A Robust Asymptotically Based Modeling Approach for Two-Phase Liquid-Liquid Flow in Pipes," ASME Paper No. OMAE2009-79072.
[17] Saisorn, S., and Wongwises, S., 2008, "Flow Pattern, Void Fraction and Pressure Drop of Two-Phase Air-Water Flow in a Horizontal Circular Micro-Channel," Exp. Therm. Fluid Sci., **32**, pp. 748–760.
[18] Saisorn, S., and Wongwises, S., 2009, "An Experimental Investigation of Two-Phase Air-Water Flow Through a Horizontal Circular Micro-Channel," Exp. Therm. Fluid Sci., **33**, pp. 306–315.
[19] Saisorn, S., and Wongwises, S., 2010, "The Effects of Channel Diameter on Flow Pattern, Void Fraction and Pressure Drop of Two-Phase Air-Water Flow in Circular Micro-Channels," Exp. Therm. Fluid Sci., **34**, pp. 454–462.
[20] Jenkins, R., 1947, "Two-Phase Two-Component Flow of Water and Air," Master of Chemical Engineering thesis, University of Delaware, Newark, DE.

Mahdi Nili-Ahmadabadi
School of Mechanical Engineering,
Center of Excellence in Energy Conversion,
Sharif University of Technology,
P.O. Box 14588-89694,
Tehran, Iran
e-mail: nili@mech.sharif.edu

Ali Hajilouy-Benisi
e-mail: hajilouy@sharif.edu

Farhad Ghadak
e-mail: fghadak@yahoo.com

Qadr Aerodynamic Research Center,
Imam Hossein University,
P.O. Box 14588-89694,
Tehran, Iran

Mohammad Durali
School of Mechanical Engineering,
Center of Excellence in Design,
Robotics and Automation,
Sharif University of Technology,
P.O. Box 14588-89694,
Tehran, Iran
e-mail: durali@sharif.edu

A Novel 2D Incompressible Viscous Inverse Design Method for Internal Flows Using Flexible String Algorithm

In this investigation, the flexible string algorithm (FSA), used before for inverse design of subsonic and supersonic ducts in compressible flows with and without normal shock, is developed and applied for inverse design of 2D incompressible viscous internal flow with and without separation. In the proposed method, the duct wall shape is changed under an algorithm based on deformation of a virtual flexible string in flow. At each modification step, the difference between current and target wall pressure distributions is applied to the string. The method is an iterative inverse design method and utilizes the analysis code for the flow field solution as a black-box. Some validation test cases and design examples are presented here, which show the robustness and flexibility of the method in handling complex geometries. In cases with separated flow pressure distribution, a unique solution for inverse design problem does not exist. The design algorithm is a physical and quick converging approach and can efficiently utilize commercial flow analysis software.
[DOI: 10.1115/1.4001072]

Keywords: inverse design, 2D ducts, viscous incompressible flows, flexible string algorithm

1 Introduction

One of the optimal shape design methods is the surface shape design (SSD), which in fluid flow problems usually involves finding a shape associated with a prescribed distribution of surface pressure or velocity. It should be noted that the solution of a SSD problem is not generally an optimum solution in a mathematical sense. It just means that the solution satisfies a target pressure distribution (TPD), which resembles a nearly optimum performance.

There are basically two different algorithms for solving SSD problems: decoupled (iterative) and coupled (direct or noniterative) techniques. In coupled solution approach, an alternative formulation of the problem is used in which the surface coordinates appear (explicitly or implicitly) as dependent variables. In other words, coupled methods tend to find the unknown part of the boundary and the flow field unknowns simultaneously in a (theoretically) single-pass or one-shot approach.

The traditional fully coupled approaches usually transform the flow equations to a computational domain in which the unknown coordinates appear as dependent variables. Stanitz [1–3] solved two- and three-dimensional potential flow duct design problems using stream and potential functions as independent variables. Zanetti [4] considered two-dimensional and axisymmetric Euler equations and mapped the physical domain to a fixed computational region.

A novel direct shape design method was proposed by Ashrafizadeh et al. [5]. They basically showed that a fully coupled formulation of the SSD problem could be solved in the physical domain using a simple extension of commonly used computational fluid dynamics (CFD) algorithms. Since the proposed direct design method does not need any transformation to or from a computational domain, it is applicable, in principle, to any flow model in 2D or 3D domains. Ghadak [6] extended the application of this method to the design of ducts carrying flows governed by the nonlinear coupled Euler equations.

On the other hand, the iterative shape design approach relies on repeated shape modifications such that each iteration consists of flow solution followed by a geometry updating scheme. In other words, a series of sequential problems is solved in which the surface shape is altered during iterations so that the desired TPD is finally achieved.

Iterative methods have been by far the most widely used to solve practical SSD problems. The traditional iterative methods used for SSD problems are often based on trial and error or optimization algorithms. The trial and error process is very time consuming and computationally expensive and hence needs designer experience to reach minimum costs. Optimization methods [7,8] are commonly used to automate the geometry modification in each iteration cycle. In such methods, an objective function (e.g., the difference between a current pressure distribution (CPD) and the TPD [9]) is minimized, subjected to the flow constraints, which have to be satisfied. Although the iterative methods are general and powerful, they are often computationally costly and mathematically complex. These methods can utilize the analysis methods for the flow field solution as a black-box.

Other iterative methods presented use the physical algorithms instead of mathematical algorithms to automate the geometry modification in each iteration cycle. One of these physical algorithms is governed by a transpiration model, in which one can assume that the wall is porous and hence the mass can be fictitiously injected through the wall in such a way that the new wall satisfies the slip boundary condition. Aiming the removal of nonzero normal velocity on the boundary, a geometry update deter-

Contributed by the Fluids Engineering Division of ASME for publication in the JOURNAL OF FLUIDS ENGINEERING. Manuscript received August 13, 2009; final manuscript received January 16, 2010; published online March 17, 2010. Assoc. Editor: Rajat Mittal.

mined by applying either the transpiration model based on mass flux conservation [10–14] or the streamline model based on alignment with the streamlines [15], must be adopted.

An alternative algorithm is based on the residual-correction approach. In this method, the key problem is to relate the calculated differences between the actual pressure distribution on the current estimate of the geometry and the TPD (the residual) to required changes in the geometry. Obviously, the art in developing a residual-correction method is to find an optimum state between the computational effort (for determining the required geometry correction) and the number of iterations needed to obtain a converged solution. This geometry correction may be estimated by means of a simple correction rule, making use of relations between geometry changes and pressure differences known from linearized flow theory.

The residual-correction decoupled solution methods try to utilize the analysis methods as a black-box. Barger and Brooks [16] presented a streamline curvature method in which they considered the possibility of relating a local change in surface curvature to a change in local velocity. Since then, a large number of methods have been developed following that concept. For example, in Garbedian–McFadden (GM) design method (elastic membrane concept) presented in Ref. [17], an auxiliary partial differential equation was solved iteratively in the computational plane, together with the fluid flow equation, to achieve the given TPDs. In the GM method, the surface pressure distribution or the flow velocity on the surface (i.e., just outside the boundary layer) depends on the surface ordinate, the surface slope, and the surface second derivative. Linear combination of these three parameters is related to the change in velocity squared on the surface. Malone et al. [18] solved the GM equation directly in a physical domain rather than in the computational domain. A modified GM (MGM) design algorithm was presented by Malone et al. [19], which removed some limitations of the original GM method. Subsequent refinements and modifications made MGM applicable to design problems based on the full potential [20], the Euler [21], and the Navier–Stokes equations [22,23]. Takanashi [24] developed a 3D wing design method based on this approach. In Ref. [25], Takanashi's method is linked with a Navier–Stokes solver to design transonic airfoils. Two major problems with the classical MGM approach were its slow convergence at leading and trailing edges of the airfoil, and its slower convergence in conjunction with the flow field analysis codes of increasing nonlinearity [26]. In order to alleviate these problems, Dulikravich [26] developed a mathematical formulation for MGM in shape inverse design using an analytical Fourier series solution. Also, he showed that 3D subsonic wings can be reliably designed using a panel code, an Euler solver, or a turbulent Navier–Stokes solver.

The main idea behind decoupling the flow and the geometry solutions in inverse design in most cases is to take maximum advantages of the available analysis methods. Another advantage of decoupled solution methods is the fact that, in general, the constraints can be implemented much more easily in a separate geometry updating process than in a complete system of equations for flow, as well as geometry variables.

In recent years, inverse design methods have been extremely developed for industrial application. An optimization approach for improving turbomachinery performance was proposed by Ashihara [27] based on a 3D inverse design method, a CFD code, and optimization algorithm. By combining the 3D inverse design method and CFD predictions, the blade loading parameters, which is the major inputs for the 3D inverse design method, were treated as design variables and the impeller performance predicted by CFD was treated as an objective function of the optimization problem. Min [28] presented a 3D viscous semi-inverse design method built on a time-marching Reynolds-averaged Navier–Stokes solver for subsonic mixed-flow and radial impellers. In Ref. [29], Roidl and Ghaly modified the method originally developed by Daneshkhah and Ghaly [30,31] for single blade rows in 2D viscous flow, and extended by Roidl and Ghaly [32] to handle one or more stages for dual point inverse design of axial turbine (for design and off-design point).

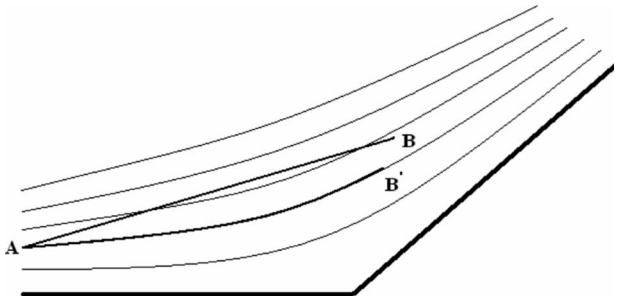

Fig. 1 The string deformation in a 2D flow

In this research, the flexible string algorithm (FSA) introduced by Nili et al. [33,34], for inverse design of subsonic and supersonic ducts in compressible flows with and without normal shock, is developed for incompressible viscous flow regimes. Also, the FSA treatment in separated flow is investigated.

The new feature of FSA consists of considering the duct wall as a flexible string having mass. The difference between TPD and CPD at each modification step is applied to the string as an actual force that accelerates and moves the string. Having achieved to the target shape, the difference between TPD and CPD vanishes and finally the string deformation is stopped automatically. Solving the string kinematic equations together with Navier–Stokes equations at each modification step updates the duct shape to achieve the TPD.

Instead of the other residual-correction methods with mathematical base that use flow equation for inverse design problems, FSA turns the inverse design problem into a fluid-solid interaction scheme with physical sense that uses pressure to deform the flexible wall. Therefore, higher calculation efficiency and time savings will be expected.

2 Fundamentals of the Method

Assume a 2D flow, as shown in Fig. 1. If a flexible string is fixed at point A in the flow, pressure applied to the sides of the string will deform it to lay on a streamline passed through the point A (A-B' curve). This phenomenon occurs because it is assumed that no mass flux can pass across the string.

Throughout the inverse design procedure to achieve the target wall geometry, the unknown contour duct walls, such as flexible strings, are assumed to have fixed starting point and free end point. The wall geometry is modified by pressure difference between TPD and CPD. When target wall shape is obtained, this pressure difference logically vanishes. The flow field is analyzed using the Navier–Stokes equation solution by mean of collocated method at each modification step [35].

3 String Governing Equations

To derive the string kinematic relations, the string is approximated by a chain with n links of equal lengths with joints bearing no moment. Supposing uniform mass distribution along each link, the mass center is located at its midpoint. Free body diagram of an arbitrary link of the chain is shown at Fig. 2. Assuming 2D motion of the chain for each link, three kinematic relations can be derived as follows.

1. Moment equation about mass center of an arbitrary link (Fig. 2(a)):

$$\tfrac{1}{2}(F_{xi}^{j2}+F_{xi}^{j1})\Delta s_i \sin\theta_i - \tfrac{1}{2}(F_{yi}^{j2}+F_{yi}^{j1})\Delta s_i \cos\theta_i = \tfrac{1}{12}\rho_i(\Delta s_i)^3\alpha_i \quad (1)$$

2. Newton's second law in the x direction (Fig. 2(b)):

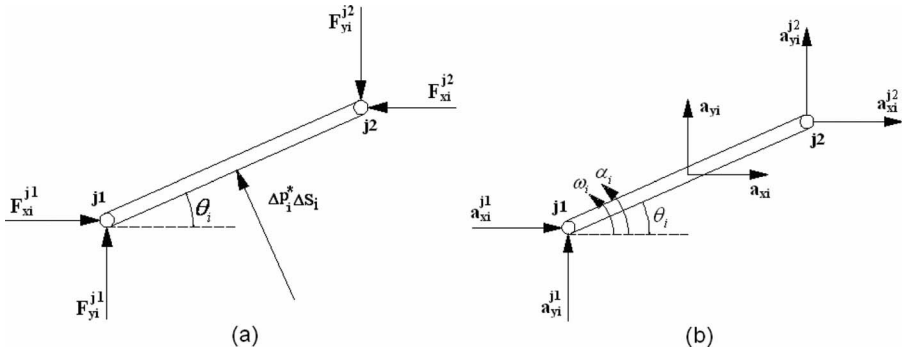

Fig. 2 Free body diagram of an arbitrary link i of the chain: (*a*) kinematics and (*b*) forces

$$F_{xi}^{j1} - F_{xi}^{j2} - \Delta p_i^* w \Delta s_i \sin\theta_i = \rho_i \Delta s_i a_{xi} \tag{2}$$

3. Newton's second law in the y direction (Fig. 2(b)):

$$F_{yi}^{j1} - F_{yi}^{j2} + \Delta p_i^* w \Delta s_i \cos\theta_i = \rho_i \Delta s_i a_{yi} \tag{3}$$

As it will be explained in Sec. 4, the effect of viscous force due to wall shear stress is neglected.

$$\rho_i \Delta s_i a_{xi} = \rho_i \Delta s_i \left(a_{xi}^{j1} - \tfrac{1}{2}\Delta s_i \sin\theta_i \alpha_i - \tfrac{1}{2}\Delta s_i \cos\theta_i \omega_i^2\right) \tag{4}$$

$$\rho_i \Delta s_i a_{yi} = \rho_i \Delta s_i \left(a_{yi}^{j1} + \tfrac{1}{2}\Delta s_i \cos\theta_i \alpha_i - \tfrac{1}{2}\Delta s_i \sin\theta_i \omega_i^2\right) \tag{5}$$

Equations (6) and (7) indicate the relations between the linear accelerations of two consecutive joints of each link:

$$a_{xi}^{j2} = a_{xi}^{j1} - \Delta s_i \sin\theta_i \alpha_i - \Delta s_i \cos\theta_i \omega_i^2 \tag{6}$$

$$a_{yi}^{j2} = a_{yi}^{j1} + \Delta s_i \cos\theta_i \alpha_i - \Delta s_i \sin\theta_i \omega_i^2 \tag{7}$$

Furthermore, the consistency equations at each joint are as follows:

$$a_{xi}^{j2} = a_{xi+1}^{j1}, \quad a_{yi}^{j2} = a_{yi+1}^{j1}, \quad F_{xi}^{j2} = -F_{xi+1}^{j1}, \quad F_{yi}^{j2} = -F_{yi+1}^{j1} \tag{8}$$

The boundary conditions include fixed starting and free end points of the chains (links). Therefore, zero acceleration and force are attributed to the starting and end points, respectively.

$$a_{x1}^{j1} = a_{y1}^{j1} = 0 \tag{9}$$

$$F_{xn}^{j2} = F_{yn}^{j2} = 0 \tag{10}$$

To study the chain kinematics, it is enough to calculate angular acceleration of each link (α_i) and there is no need to calculate the other unknowns such as the forces and linear acceleration components. Having eliminated the forces and linear accelerations and solving the linear system of equations, the angular accelerations are calculated exactly. Then, the angular velocity (ω_i) and the angle change of each link ($\Delta\theta_i$) are obtained as follows:

$$\omega_i^{t+\Delta t} = \omega_i^t + \alpha_i \Delta t \tag{11}$$

$$\Delta\theta_i = 1/2\alpha_i \Delta t^2 + \omega_i \Delta t \tag{12}$$

Starting from the first link toward the end one, the new positions of joints ($j+1$) are obtained by adding the angle change of each link to the calculated position of the previous joint (j). The solution starts with an initial guess such that the duct's main characteristics (e.g., length and inlet or outlet area) are known and fixed. In this method, one of the joints coordinates (say, x) is fixed.

$$x_j^{t+\Delta t} = x_j^t \tag{13}$$

$$y_{j+1}^{t+\Delta t} = y_j^{t+\Delta t} + \Delta s_i \sin(\theta_i + \Delta\theta_i) \tag{14}$$

In this research, the boundary conditions are the inlet velocity and outlet pressure. Therefore, at each shape modification step, the outlet pressure remains constant, while the inlet pressure changes according to the pressure in the first interior cell. Since, the inlet area is fixed, the string starting point must be stationary and therefore, $\Delta p_{\text{first-joint}}$ must be zero. Thus, the pressure difference applied to the string at any other point must be gauged with respect to the pressure difference at the first joint. This is shown in Eq. (15). The basis of the method requires that for incompressible internal flows, TPD be applied to the string from inside of duct and CPD, from outside of duct.

$$\Delta p_j = (p_{\text{Tar}(j)} - p_j) - [p_{\text{Tar}(1)} - p_1]$$

$$::j = 1, n+1 \quad ::p_{n+1} = p_{\text{Tar}(n+1)} = P_{\text{back}} \tag{15}$$

Finally, the pressure difference applied to each link of the string is obtained from the following equation:

$$\Delta p_i^* = (\Delta p_j + \Delta p_{j+1})/2 \quad ::i = j = 1, n$$

$$i\text{:index of each link}, \quad j\text{: index of each joint} \tag{16}$$

Figure 3 shows how the string equations are typically incorporated into existing flow solution procedures.

4 Validation Cases

For validation of the proposed method, a given shape such as a nozzle, diffuser, 90 deg bended duct or an S-shaped duct is analyzed here to obtain the solid wall pressure distributions. Then, these pressure distributions are considered as the TPD for the SSD problems. The method starts with an arbitrary (initial) shape, and after several shape modifications, the difference between TPD and CPD vanishes and thus, the target shape satisfying the TPD is reached. In all test cases, the iterations were stopped after the pressure differences were reduced by three orders of magnitude. After each geometry modification, the analysis code is run until the residuals were reduced by three orders of magnitude.

As mentioned before, the viscous force applied to the duct wall is neglected in the string equations. In this research, for validation cases, in addition to the TPD, target shear stress was entered into the string equations. It was found that the shear stress effects are negligible (two orders of magnitude less) compared with the pressure effect (Fig. 8). Moreover, target shear stress distribution is not known in real design cases. Therefore, the viscous force effects were neglected in the design algorithm.

4.1 Nozzle Case. A nozzle shape duct, as shown in Fig. 4(a), is assumed. In order to test the capability of the proposed method, the flow field of the nozzle is analyzed and the wall pressure distribution is determined for specified boundary conditions. Starting from a straight converging wall as the initial guess (Fig. 4(a)), the design program algorithm is converged after 100 modification steps (Fig. 4(c)). The wall pressure distributions of the initial and final shapes are shown in Fig. 4(b).

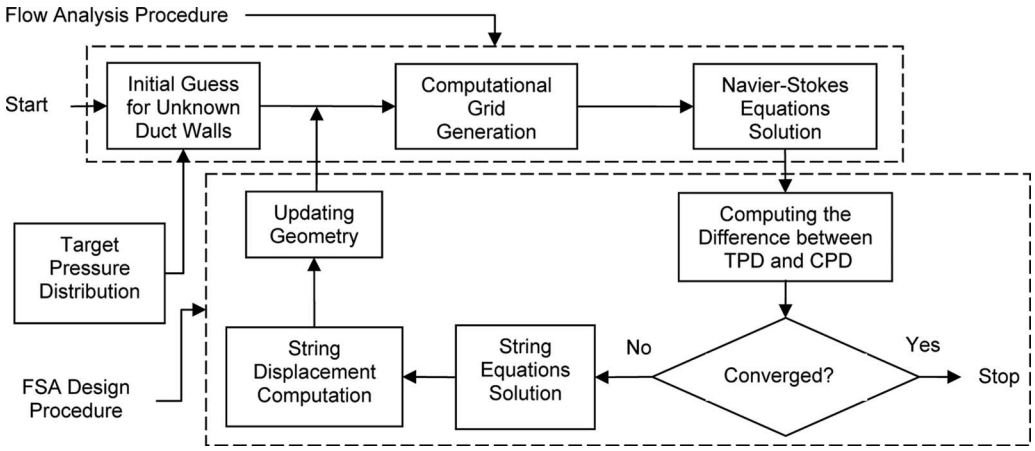

Fig. 3 Implementation of the inverse design algorithm

4.2 Diffuser Case Without Separation. In Fig. 5(*a*), a diffuser with an area ratio of 1.2 and an inlet velocity of 30 m/s as the target shape and a straight duct as the initial guess are shown. Also, the wall pressure distributions of the initial and target shape are shown in Fig. 5(*b*). The flow field analysis in this diffuser indicates that no separation occurs. The design program algorithm is converged after 380 modification steps (Fig. 5(*c*)).

4.3 90 deg Bended Duct With Two Unknown Walls. In the cases presented earlier, horizontal length of duct remains constant through the shape modification steps. In the case of bended duct, outlet section is not perpendicular to the x coordinate and hence, it is not possible to fix horizontal length of duct. In such cases, instead of horizontal length, the duct centerline length is assumed known and remains constant during the evolution.

In a bended duct, the duct is asymmetric and both upper and lower duct walls are unknown. These two walls are modeled as two strings deforming from initial guess to the target shape. During the shape modification procedure, the length of each string is

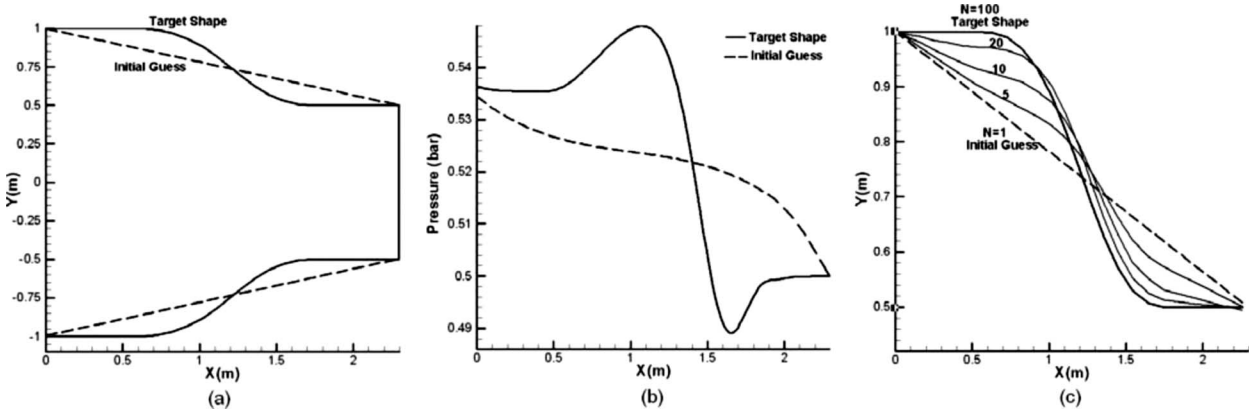

Fig. 4 (*a*) Geometry of the nozzle with initial guess, (*b*) wall pressure distribution of the initial guess and target shape, and (*c*) modification steps of the nozzle wall from the initial guess to the target shape

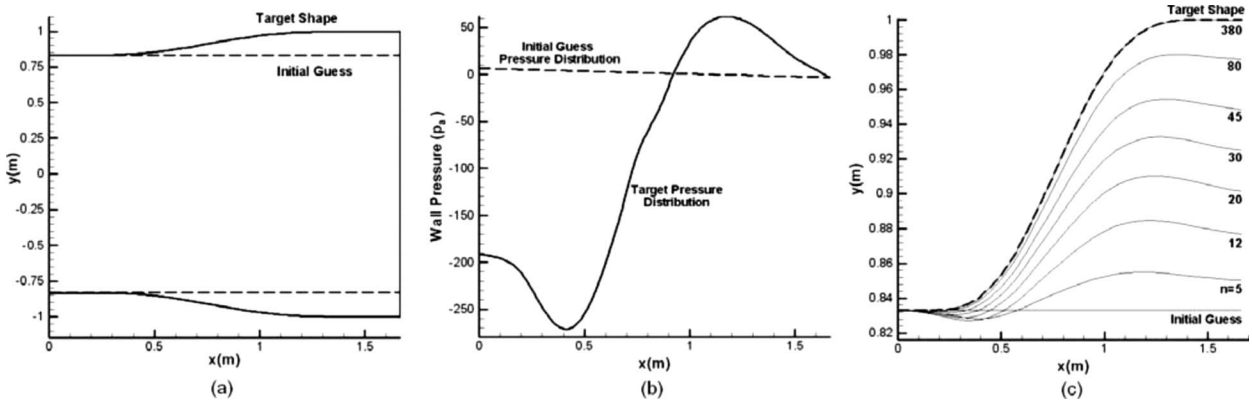

Fig. 5 (*a*) Geometry of the diffuser with initial guess, (*b*) wall pressure distribution of the initial guess and target shape, and (*c*) modification steps of the diffuser wall from the initial guess to the target shape

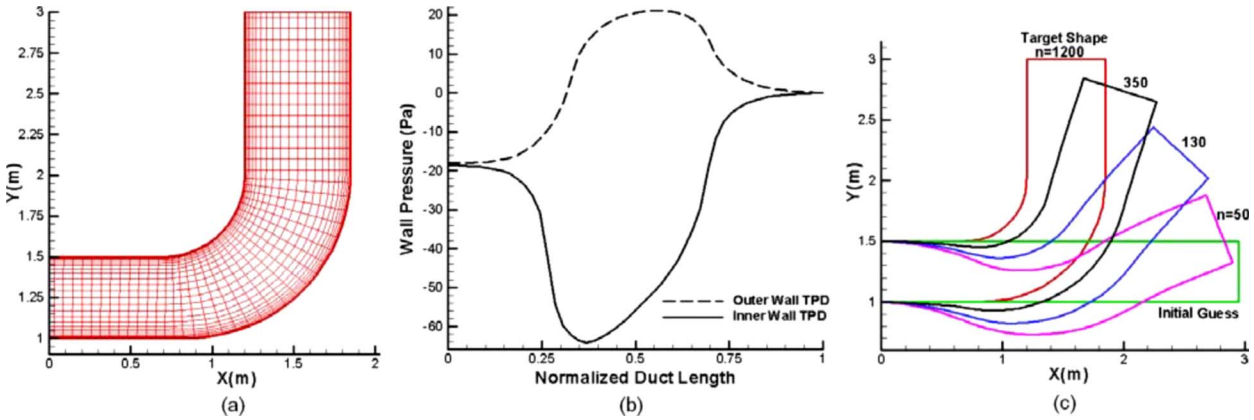

Fig. 6 (*a*) **Geometry of the 90 deg bended diffuser with its grid,** (*b*) **wall pressure distribution of the 90 deg bended diffuser along the inner and outer walls, and** (*c*) **modification steps from the initial guess to the target shape**

modified based on the fixed centerline length. In such cases, a large number of modification steps are required to converge design algorithm since the pressure is highly sensitive to the wall shape change.

Considering a virtual string on the duct centerline with a constant length and applying the difference between the upper and lower pressures to centerline string, the convergence rate of the design algorithm will be increased significantly. In other words, in the case of ducts with two unknown walls, three strings can be modeled on the upper wall, lower wall, and centerline whereby the centerline string as an auxiliary string causes to speed up the duct shape modification. The pressure difference applying to the centerline string is obtained from the following equation for each link:

$$\Delta p^*_{\text{centerline}} = \Delta p^*_{\text{upper wall}} - \Delta p^*_{\text{lower wall}} \tag{17}$$

In this part, we would like to redesign a 90 deg bended diffuser. The TPD (Fig. 6(*b*)) for this validation test case is obtained from the numerical analysis of the flow through it with a 50×25 grid (Fig. 6(*a*)). The inlet velocity and outlet gauge pressures are considered 10 m/s and zero, respectively. Figure 6(*c*) illustrates the initial guess and the evolution of the shape after 50, 130, 350, and 1200 modification steps. As shown in this figure, since the initial guess is not a suitable one, severe shape changes occur during their evolutions.

4.4 Diffuser Case With Separation. Figure 7(*a*) shows the flow field of a diffuser with an area ratio of 1.4 and an inlet velocity of 30 m/s in which the separation phenomenon occurs. The wall pressure distribution of the diffuser shown in Fig. 7(*a*) is considered as the target pressure distribution. Starting from a rectangular duct as the initial guess, the design algorithm is converged to the diffuser shown in Fig. 7(*b*) after 400 modification steps. Although the difference between the target and calculated pressure distribution decreases three orders of magnitude, the final shape (Fig. 7(*b*)) is converged to a configuration with no separation in Fig. 7(*a*). This is due to the negligible pressure difference between the inner and outer regions of separated flow. As shown in Fig. 8(*a*), wall pressure distributions related to Figs. 7(*a*) and 7(*b*) are coincided with each other, while wall shear stress distributions are not (Fig. 8(*b*)). Therefore, for duct inverse design with separation, in addition to satisfy the wall pressure distribution, it is necessary to satisfy the shear stress distribution. It is noticeable that for viscous flows with no separation and nonviscous flows, the shape related to a TPD is unique or at least no example has been observed against it up to now. But for viscous flow regimes with separation, the shape related to a TPD is not unique.

If a diffuser with separation (an area ratio of 1.44 and an inlet velocity of 30 m/s) is considered as the initial guess, the design procedure is converged to the same shape but after 1400 modification steps, as shown in Fig. 9. If separation occurs during the string deformation, due to the string oscillation in the separation region, the convergence will be postponed. In other words, in the cases with separation probability, an initial guess without separation is better than that with separation.

5 Design Examples

5.1 Diffuser Shape Modification. Improving the diffuser shown in Fig. 10(*a*) is the goal of this example. For diverging

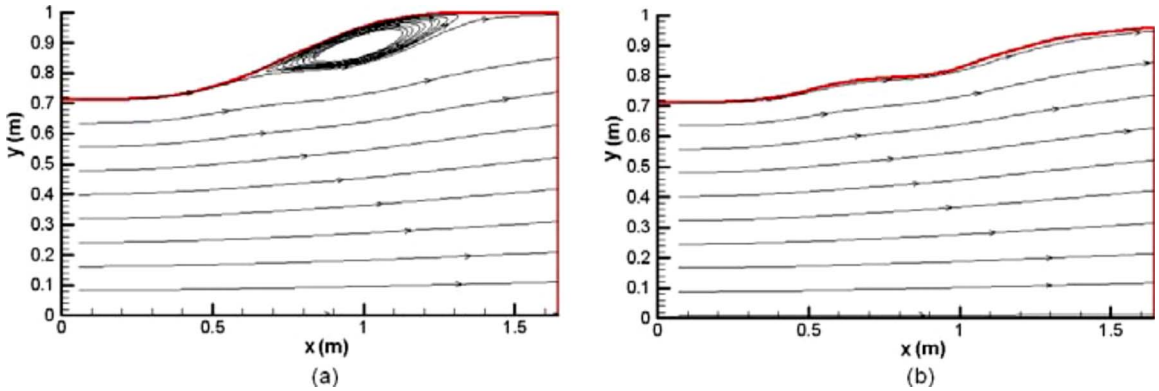

Fig. 7 (*a*) **Flow field of the diffuser with area ratio of 1.4.** (*b*) **Final shape after 400 modification steps with corresponding streamlines.**

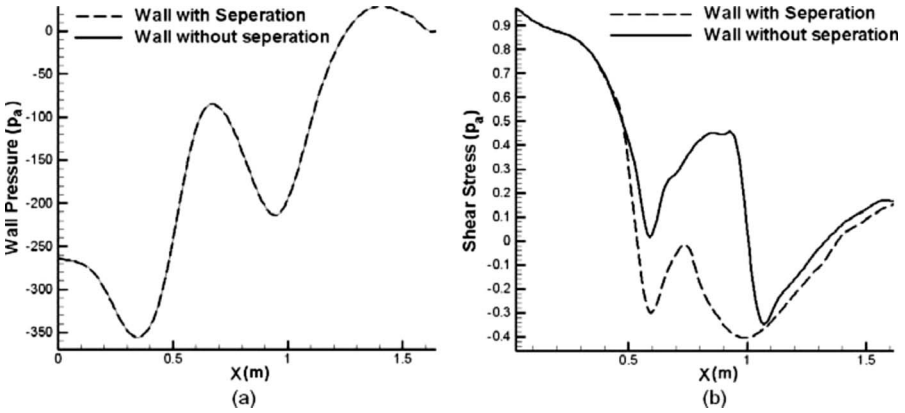

Fig. 8 (*a*) **Wall pressure and** (*b*) **wall shear stress distribution of the diffusers shown in Fig. 7**(*a*) **and 7**(*b*)

incompressible flow, there is an overall flow deceleration ($p_2 > p_1$) and hence an overall adverse pressure gradient. If one proposes the diffuser shape in Fig. 10(*a*), a flow solution gives the wall pressure indicated by the solid curve in Fig. 10(*b*). The designer general goal is to eliminate extreme pressure changes along the duct wall and to increase pressure coefficient as much as possible. In the optimization process, one would come up with different arbitrary pressure distributions, one of which is shown in Fig. 10(*b*) as an example. The proceeding flow calculations will examine this choice and will result a new shape for the duct. At this stage, the designer can plan for further duct geometrical change toward specific design goals. The wall pressure given by

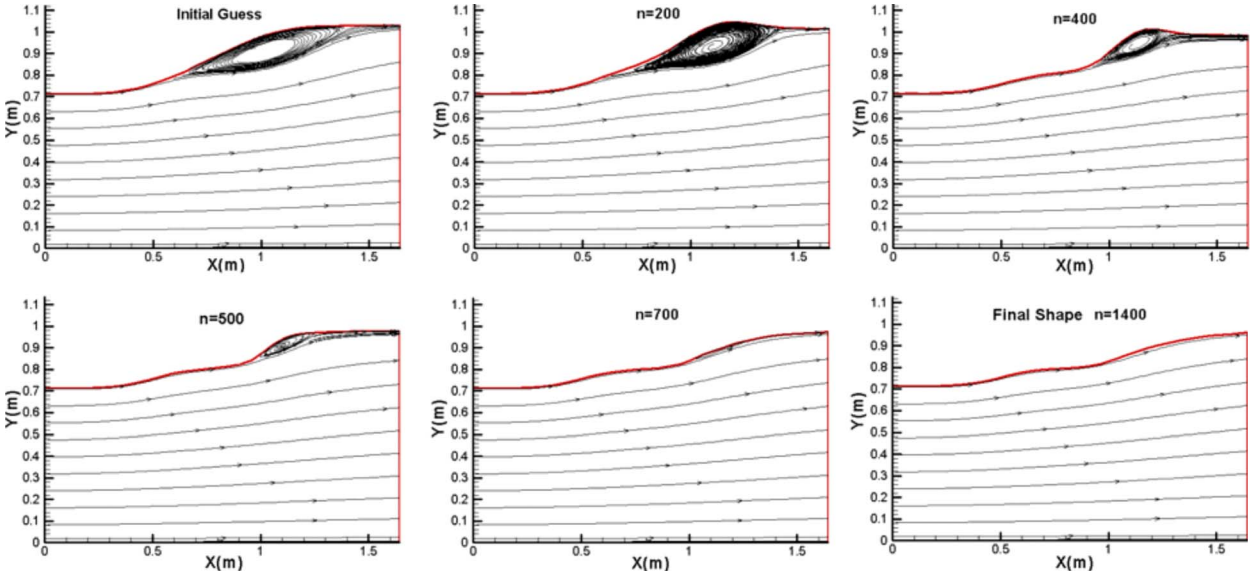

Fig. 9 Shape modification steps from the initial guess to the target shape

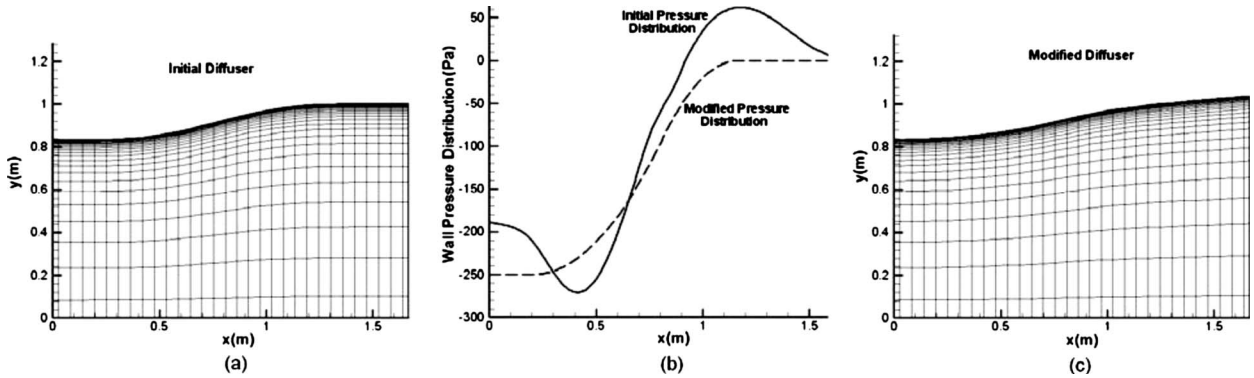

Fig. 10 (*a*) **Diffuser with area ratio of 1.2 as the initial guess,** (*b*) **wall pressure profile of the initial diffuser and modified pressure profile as the target pressure distribution, and** (*c*) **modified shape after 420 modification steps**

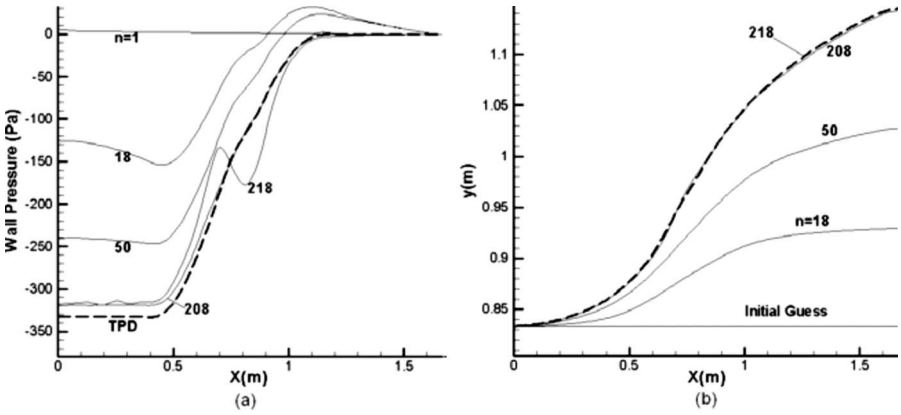

Fig. 11 (***a***) **Changes in wall pressure profile.** (***b***) **Wall shape equivalent to the corresponding pressure profile.**

the dashed curve in Fig. 10(*b*) eliminates the pressure extremes and hence, the boundary layer is more capable of withstanding the adverse pressure gradient. As it can be seen, the TPD results a pressure coefficient, which is increased by 30%. The resulting duct shape after 420 modification steps is shown in Fig. 10(*c*).

In Fig. 11(*a*), the pressure rise of TPD is considered 330 Pa producing high pressure gradient and inlet velocity is considered 30 m/s. Starting from a rectangular duct, the duct wall deforms smoothly so that wall pressure profile closes to TPD after 208 modification steps. But, due to high pressure gradient, after the 208th step, separation occurs and design algorithm is not converged. But, after 208 modification steps, a pressure rise of 320 Pa is obtained, which is relatively a high pressure gradient. This example shows that FSA is capable to obtain the approximate maximum pressure rise of a diffuser. Wall shape equivalent to the pressure profile is shown in Fig. 11(*b*).

5.2 S-Shaped Diffuser Design. Using the inverse design method, one can find the appropriate geometry for S-shaped diffusers. Because of considerable adverse pressure gradients along their walls, the possibility of flow separation is very high in such ducts. Figure 12(*a*) shows the streamlines inside an S-shaped diffuser with an area ratio of 1.92 and an inlet velocity of 30m/s. A considerable separation region is seen at the lower wall of the S-shaped diffuser. Pressure distributions of the lower and upper walls of the diffuser are shown as the solid lines in Fig. 12(*b*). Having modified the wall pressure distribution, the dash lines shown in Fig. 12(*b*) are considered as TPD. It is clear that the undershoot and overshoot have been removed from the wall pressure profile and the possibility of separation to decrease is expected. The pressure rise of the modified pressure distribution is about 16% more than that of the initial pressure distribution. Starting with the diffuser shown in Fig. 12(*a*) as the initial guess and applying the target pressure distribution, the design algorithm is converged to S-shaped diffuser shown in Fig. 12(*c*) after 2200 modification steps. As seen, in addition to eliminate the separation region, the area ratio increases from 1.92 to 2.17. Also, as opposed to the initial S-shaped diffuser in which the exit velocity vectors are not horizontal, for the designed S-shaped diffuser, they are horizontal. This will be explained later.

Figure 13 shows the pressure contour and grid of the designed S-shaped duct. Figure 14 shows the difference between designed S-shaped diffuser for viscous and nonviscous flow regimes. This difference can be regarded to boundary layer thickness.

The remaining question is the relation between the upper and lower wall pressure profiles of the S-ducts. To answer this question, a control volume, as shown in Fig. 15, is considered inside the S-duct. To simplify the problem, the viscous forces are neglected and only pressure and momentum terms are considered. Writing the momentum equation in the y direction, the following relation is obtained:

$$\sum F_y = 0 \Rightarrow \int_0^L (P_{up} - P_{low})dx = 0 \tag{18}$$

Equation (18) implies that the area surrounded between the upper and lower wall pressure profiles at the graph of pressure versus x is zero. Thus, the upper and the lower wall pressure profiles should cross each other at a point. In other words, the area sur-

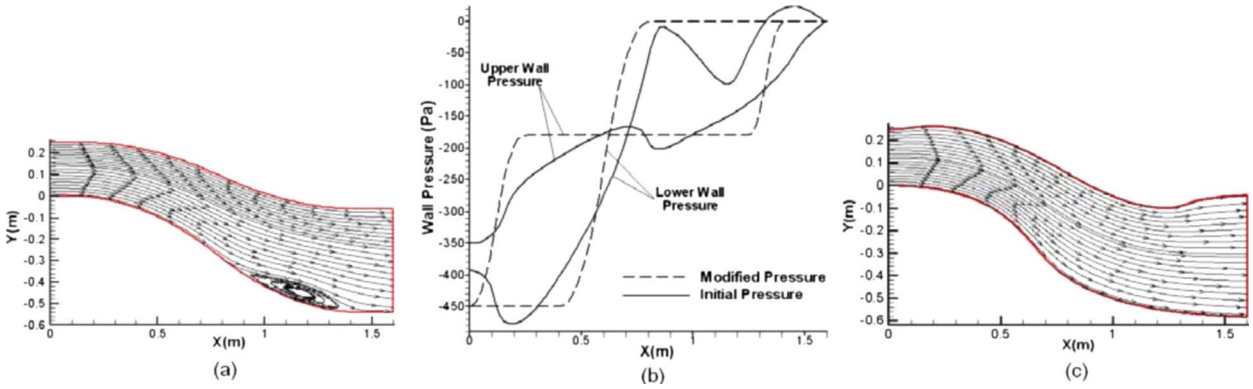

Fig. 12 (***a***) **Streamlines inside the S-shaped diffuser with area ratio of 1.92 as the initial guess,** (***b***) **wall pressure profile of the initial diffuser and modified pressure profile as the target pressure distribution, and** (***c***) **designed S-shaped diffuser with area ratio of 2.17 after 2200 modification steps**

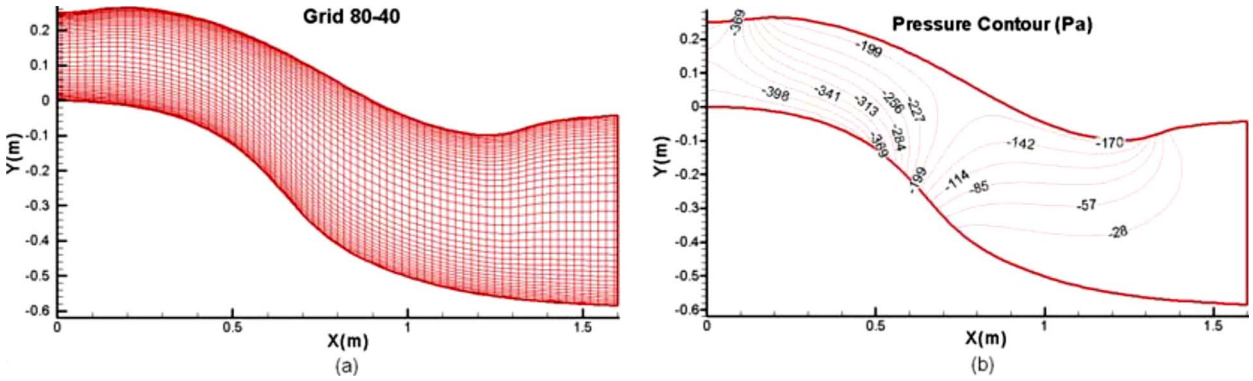

Fig. 13 (*a*) Generated grid and (*b*) pressure contour inside the designed S-shaped diffuser

rounded before and after intersection point should be equal. This idea is used for the modified pressure distribution shown in Fig. 12(*b*). As mentioned before, the velocity vectors at the initial S-shaped diffuser outlet are not in line with the duct longitudinal axis (Fig. 12(*a*)). This is because the corresponding two surrounded areas are not equal as a result of local separation (Fig. 12(*b*)).

In order to study the grid size effect on the designed shape, the S-shaped diffuser is redesigned for four grid sizes; 32×15, 64×32, 80×40, and 100×50 with the same TPD in Fig. 12(*b*). Figure 16 compares three designed shapes. The shape related to 100×50 grid is not shown in Fig. 16 because it coincides with the shape corresponding to 80×40 grid.

5.3 Bended Diffuser Design. In this part, we would like to design a 90 deg bended diffuser with an inlet velocity of 10 m/s and a pressure rise of 45 Pa without separation. A simple 90 deg bended diffuser as initial guess is shown in Fig. 17(*a*). The streamlines inside the diffuser shows a separation region at the end of inner wall. The solid lines in Fig. 17(*b*) indicate the inner and outer wall pressure profiles of the initial guess diffuser.

For curved diffusers, the best performance is obtained by heavily overloading the outer wall [36]. On the contrary to this recommendation, the pressure loading on the inner wall of the initial diffuser is more than that on the outer wall and hence, the separation occurs. Increasing the outer wall pressure gradient compared with the inner one and eliminating the undershoot of the initial pressure (dashed lines in Fig. 17(*b*) as TPD), the 90 deg bended diffuser shown in Fig. 17(*c*) is obtained. The obtained diffuser has no separation for the same pressure rise. About 1300 modification steps are required to achieve from Fig. 17(*a*) to Fig. 17(*c*).

Figure 18 shows the difference between the exit velocity profile of the initial guess and the designed diffuser. As seen, in the designed diffuser, the velocity profile is almost uniform.

In Fig. 19(*a*), the pressure rise of TPD is 11% more than that of the initial pressure distribution. The diffuser shown in Fig. 19(*b*) is obtained from the TPD shown in Fig. 19(*a*). As seen in this figure, in addition to eliminate the separation region in Fig. 17(*a*), the area ratio increases.

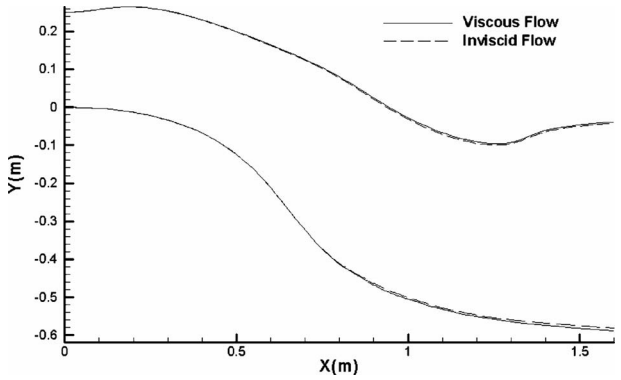

Fig. 14 The difference between designed S-shaped diffuser in viscous flow and ideal flow

6 Conclusion

FSA design procedure is incorporated into an existing Navier–Stokes code with collocated method. The FSA turns the inverse design problem into a fluid-solid interaction scheme that has a physical base. The method converges quickly and can efficiently utilize commercial flow analysis software as a black-box. The results show that the method can be very promising in duct and other flow conduit design for viscous and nonviscous flow regimes. As opposed to inviscid and viscous flows with no separa-

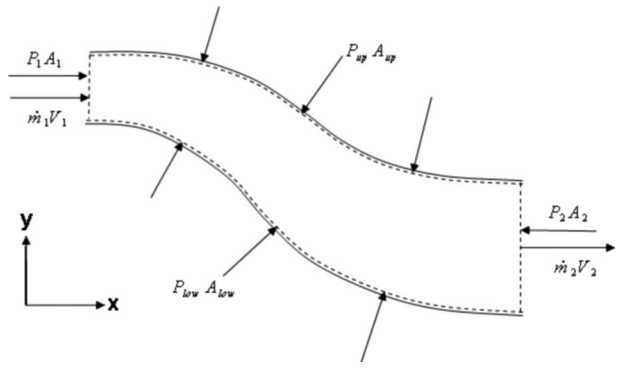

Fig. 15 Control volume inside an S-duct

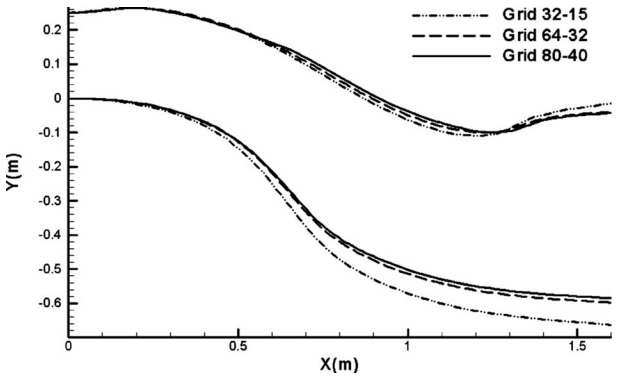

Fig. 16 The grid study for design of S-shaped diffuser

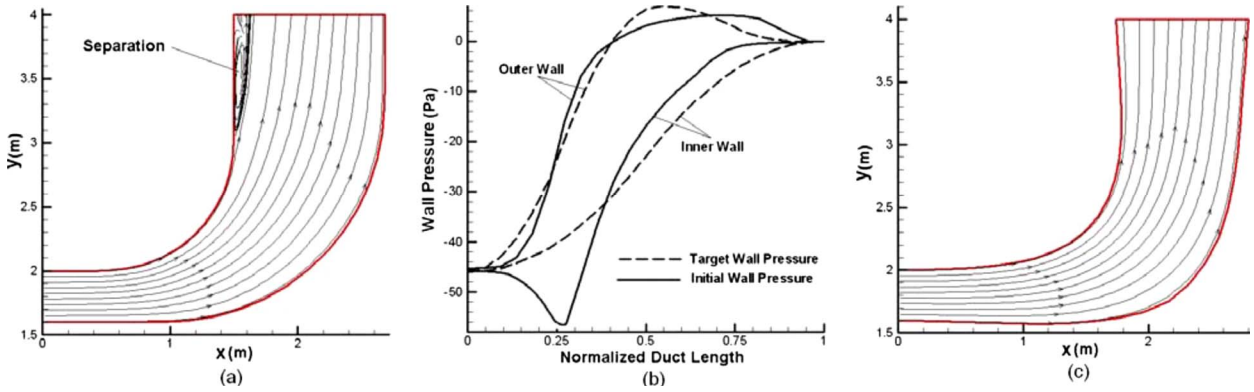

Fig. 17 (*a*) Streamlines inside the 90 deg bended diffuser as the initial guess, (*b*) wall pressure profile of the initial diffuser and modified pressure profile as the target pressure distribution, and (*c*) designed 90 deg bended diffuser after 1300 modification steps

tion, in which there is a unique solution for inverse design problems, in viscous flows with separation, the solution is not unique.

Nomenclature

a = linear acceleration (m s^{-2})
A = area (m^2)
F = force vector (N)
L = duct length (m)
$\dot{m}$ = mass flow rate (kg/s)
N = number of shape modifications
n = number of links
p_i = pressure calculated at cell center near the wall (Pa)
Q = sum of the conserved flow variables such as ρ, ρu, ρv, and ρe in Euler equations
t = time (s)
x = x position of joints (m), x coordinate
y = y position of joints (m), y coordinate
V = flow velocity (m/s)
w = width of duct (m)
Δ = difference
Δs = link length (m)
Δp_i^* = pressure difference applied to each link (Pa)
Δp_i = difference between TPD and CPD at each link (Pa)
α = angular acceleration (rad s^{-2})
θ = link angle (deg)
ρ = mass per unit length (kg m^{-1})
ω = angular velocity (rad s^{-1})

Subscripts

1 = duct inlet

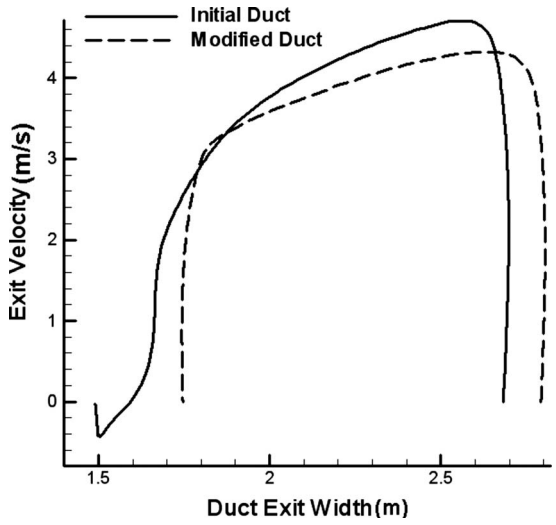

Fig. 18 The difference between exit velocity profile of the initial guess and the designed diffuser

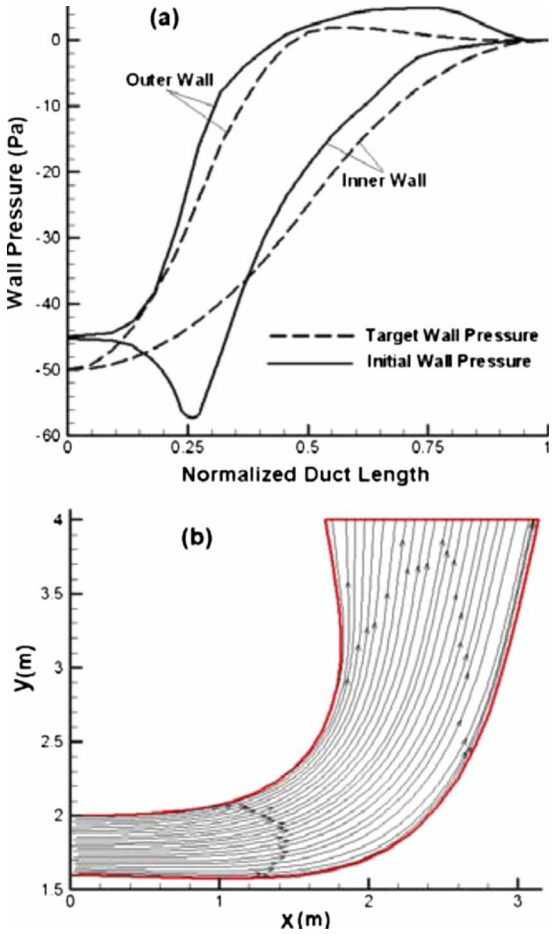

Fig. 19 (*a*) Initial pressure distribution and modified TPD for 90 deg bended diffuser and (*b*) designed 90 deg bended diffuser without separation

2 = duct outlet
i = links index
j = joints index
low = lower wall
max = maximum
up = upper wall
Tar = Target
x = x component, x coordinate
y = y component, y coordinate

Superscript

I.G. = initial guess
$j1$ = starting point of each link
$j2$ = end point of each link
n = iteration number at analysis code
$t+\Delta t$ = related to updated geometry
t = related to current geometry

References

[1] Stanitz, J. D., 1953, "Design of Two-Dimensional Channels With Prescribed Velocity Distributions Along the Duct Walls," Lewis Flight Propulsion Laboratory Technical Report No. 1115.

[2] Stanitz, J. D., 1980, "General Design Method for Three-Dimensional, Potential Flow Fields, I—Theory," NASA Technical Report No. 3288.

[3] Stanitz, J. D., 1987, "A Review of Certain Inverse Methods for the Design of Ducts With 2- or 3-Dimensional Potential Flows," Proceedings of the Second International Conference on Inverse Design Concepts and Optimization in Engineering Sciences (ICIDES-II), G. S. Dulikravich, ed., Pennsylvania State University, University Park, PA, Oct. 26–28.

[4] Zannetti, L., 1986, "A Natural Formulation for the Solution of Two-Dimensional or Axis-Symmetric Inverse Problems," Int. J. Numer. Methods Eng., **22**, pp. 451–463.

[5] Ashrafizadeh, A., Raithby, G. D., and Stubley, G. D., 2003, "Direct Design of Ducts," ASME J. Fluids Eng., **125**, pp. 158–165.

[6] Ghadak, F., 2005, "A Direct Design Method Based on the Laplace and Euler Equations With Application to Internal Subsonic and Supersonic Flows," Ph.D. thesis, Sharif University of Technology, Iran.

[7] Cheng, C.-H., and Wu, C.-Y., 2000, "An Approach Combining Body Fitted Grid Generation and Conjugate Gradient Methods for Shape Design in Heat Conduction Problems," Numer. Heat Transfer, Part B, **37**(1), pp. 69–83.

[8] Jameson, A., 1994, "Optimum Aerodynamic Design Via Boundary Control," Optimum Design Methods for Aerodynamics, AGARD Report No. R-803, pp. 3.1–3.33.

[9] Kim, J. S., and Park, W. G., 2000, "Optimized Inverse Design Method for Pump Impeller," Mech. Res. Commun., **27**(4), pp. 465–473.

[10] Dedoussis, V., Chaviaropoulos, P., and Papailiou, K. D., 1993, "Rotational Compressible Inverse Design Method for Two-Dimensional Internal Flow Configurations," AIAA J., **31**(3), pp. 551–558.

[11] Demeulenaere, A., and van den Braembussche, R., 1998, "Three-Dimensional Inverse Method for Turbomachinery Blading Design," ASME J. Turbomach., **120**(2), pp. 247–255.

[12] de Vito, L., and Van den Braembussche, R., 2003, "A Novel Two-Dimensional Viscous Inverse Design Method for Turbomachinery Blading," ASME J. Turbomach., **125**, pp. 310–316.

[13] Demeulenaere, A., Leonard, O., and Van den Braembussche, R., 1997, "A Two-Dimensional Navier–Stokes Inverse Solver for Compressor and Turbine Blade Design," Proc. Inst. Mech. Eng., Part A, **211**, pp. 299–307.

[14] Henne, P.A., 1980, "An Inverse Transonic Wing Design Method," AIAA Paper No. 80-0330.

[15] Volpe, G., 1989, "Inverse Design of Airfoil Contours: Constraints, Numerical Method Applications," Computational methods for Aerodynamic design (Inverse) and Optimization, AGARD CP-463, Paper No. 4.

[16] Barger, R.L. and Brooks, C.W., 1974, "A Streamline Curvature Method for Design of Supercritical and Subcritical Airfoils," NASA Report No. TN D-7770.

[17] Garabedian, P., and McFadden, G., 1982, "Design of Supercritical Swept Wings," AIAA J., **30**(3), pp. 444–446.

[18] Malone, J., Vadyak, J., and Sankar, L. N., 1987, "Inverse Aerodynamic Design Method for Aircraft Components," J. Aircr., **24**(1), pp. 8–9.

[19] Malone, J., Vadyak, J., and Sankar, L. N., 1985, "A Technique for the Inverse Aerodynamic Design of Nacelles and Wing Configurations," AIAA Paper No. 85-4096.

[20] Campbell, R. L., and Smith, L. A., 1987, "A Hybrid Algorithm for Transonic Airfoil and Wing Design," AIAA Paper No. 87-2552.

[21] Bell, R. A., and Cedar, R. D., 1991, "An Inverse Method for the Aerodynamic Design of Three-Dimensional Aircraft Engine Nacelles," Proceedings of the Third International Conference on Inverse Design Concepts and Optimization in Engineering Sciences, ICIDES-III, G. S. Dulikravich, ed., Washington, DC, Oct. 23–25, pp. 405–417.

[22] Malone, J.B., Narramore, J.C., and Sankar, L.N., 1989, "An Efficient Airfoil Design Method Using the Navier–Stokes Equations," Computational methods for Aerodynamic design (Inverse) and Optimization, AGARD CP-463, Paper No. 5, pp. 5.1–5.18.

[23] Malone, J. B., Narramore, J. C., and Sankar, L. N., 1991, "Airfoil design method using the Navier–Stokes equations," J. Aircr., **28**(3), pp. 216–224.

[24] Takanashi, S., 1985, "Iterative Three-Dimensional Transonic Wing Design Using Integral Equations," J. Aircr., **22**, pp. 655–660.

[25] Hirose, N., Takanashi, S., and Kawai, N., 1987, "Transonic Airfoil Design Procedure Utilizing a Navier–Stokes Analysis Code," AIAA J., **25**(3), pp. 353–359.

[26] Dulikravich, G.S. and Baker, D.P., 1999, "Aerodynamic Shape Inverse Design Using a FOURIER SERIES METHOD," AIAA Paper No. 99-0185.

[27] Ashihara, K. and Goto, A., 2001, "Turbomachinery Blade Design Using 3-D Inverse Design Method, CFD and Optimization Algorithm," ASME Paper No. GT2001-0358.

[28] Min, J., Dang, T. Q., and Cave, M. J., 2009, "Fully Three-Dimensional Viscous Semi-Inverse Method for Subsonic Mixed-Flow and Radial Impeller Design," ASME Paper No. GT2009-59679.

[29] Roidl, B. and Ghaly, W., 2009, "Dual Point Redesign of Axial Turbines Using a Viscous Inverse Design Method," ASME Paper No. GT2009-59707.

[30] Daneshkhah, K., and Ghaly, W., 2007, "Aerodynamic Inverse Design for Viscous Flow in Turbomachinery Blading," J. Propul. Power, **23**(4), pp. 814–820.

[31] Daneshkhah, K., and Ghaly, W., 2006, "An Inverse Blade Design Method for Subsonic and Transonic Viscous Flow in Compressors and Turbines," Inverse Probl. Sci. Eng., **14**(3), pp. 211–231.

[32] Roidl, B. and Ghaly, W., 2008, "Redesign of a Low Speed Turbine Stage Using a New Viscous Inverse Design Method," ASME Paper No. GT2008-51468.

[33] Nili-Ahmadabadi, M., Durali, M., Hajilouy, A., and Ghadak, F., 2009, "Inverse Design of 2D Subsonic Ducts Using Flexible String Algorithm," Inverse Probl. Sci. Eng., **17**(8), pp. 1037–1057.

[34] Nili-Ahmadabadi, M., Hajilouy, A., Durali, M. and Ghadak, F., 2009, "Duct Design in Subsonic & Supersonic Flow Regimes With & Without Shock Using Flexible String Algorithm," ASME Paper No. GT2009-59744.

[35] Farhanieh, B., and Davidson, L., 1992, "Numerical Calculation of Navier-Stokes Equations in Biological Ducts," Proceedings of the Sixth Biomechanics Seminar, Gothenburg, Apr., Vol. 6, pp. 154–167.

[36] Sagi, C. J., and Johnston, J. P., 1967, "The Design of Performance of Two Dimensional, Curved Diffusers," ASME J. Basic Eng., **89**, pp. 715–731.

Development Length Requirements for Fully Developed Laminar Pipe Flow of Yield Stress Fluids

R. J. Poole
Department of Engineering,
University of Liverpool,
Brownlow Street,
Liverpool L69 3GH, United Kingdom
e-mail: robpoole@liv.ac.uk

R. P. Chhabra
Department of Chemical Engineering,
Indian Institute of Technology,
Kanpur 208016, India
e-mail: chhabra@iitk.ac.in

In this technical brief, we report the results of a systematic numerical investigation of developing laminar pipe flow of yield stress fluids, obeying models of the Bingham-type. We are able to show that using a suitable choice of the Reynolds number allows, for high Reynolds number values at least, the development length to collapse to the Newtonian correlation. On the other hand, the development length remains a weak, nonmonotonic, function of the Bingham number at small values of the Reynolds number (Re≤40). [DOI: 10.1115/1.4001079]

1 Introduction

Notwithstanding the long (and continuing) debate about the very existence of a "true" yield stress, it is readily acknowledged that the notion of an apparent yield stress is a very useful engineering empiricism for a wide range of materials [1–3]. These materials appear solidlike below some critical (yield) stress but flow above this value. Here we are interested in the development length problem for such fluids, i.e., the length of pipe required for the flow of such fluids to become "fully developed." Although this problem is classical, and has been investigated repeatedly, only relatively recently have accurate results become available even for Newtonian [4] and non-Newtonian inelastic fluids (obeying the power-law model [5]). For pipe flow, Durst et al. [4] proposed the following correlation for Newtonian fluids

$$X_D/D = [(0.619)^{1.6} + (0.0567\ \mathrm{Re})^{1.6}]^{1/1.6} \tag{1}$$

where X_D is the development length (m), D is the pipe diameter (m), and Re is the Reynolds number. For power-law fluids a modification to Eq. (1) was proposed to account for the low Reynolds number dependence on the power-law index (consult Ref. [5] for details).

For visco-plastic fluids, although a number of studies have investigated this issue either analytically or numerically [6–11], with the exception of Ookawara et al. [11], the results of these studies have ignored the diffusion-dominated case (i.e., low Reynolds number) and proposed correlations of the form $X_D/D = C(\mathrm{Re})$, where C is a function of the nondimensional yield stress (usually represented as a Bingham number). Thus they incorrectly predict that for creeping flows (i.e., $\mathrm{Re}\to 0$) the flow instantaneously develops. In addition, as Ref. [11] highlight, the occurrence of the "plug" region means that although the centerline velocity reaches 99% of its fully developed value in a rather shorter distance than the Newtonian case, the complete radial variation in the velocity at this location is not yet fully developed (see their Fig. 1 for example). Thus one of the conclusions of Vradis et al. [9] that "the velocity profiles develop faster with higher values of the yield (Bingham) number" is essentially incorrect. To overcome this difficulty, Ookawara et al. [11] redefined the entry length as the axial distance where the velocity at a radial position of 95% of the plug radius reaches 99% of the calculated maximum velocity (at the same radial location). Although Ookawara et al. [11] highlighted this important issue and provided a correlation that also predicts the development length for low Reynolds numbers (<10), their yield stress results (obtained using the Bingham model) are restricted to just five simulations and their correlation is independent of the Bingham number, something which, at low Reynolds number at least, seems unrealistic, given the results for the power-law model [5]. In this technical brief we report the results of a detailed numerical study, of quantified accuracy, which attempts to reconcile these issues.

2 Nondimensional Groups

To investigate the yield stress effects in the laminar developing pipe flow, we use here a Bingham-type approach, e.g., a model of the form $\tau = \tau_0 + \mu_p \dot{\gamma}$, where τ is the shear stress (Pa), τ_0 is the yield stress (Pa), $\dot{\gamma}$ is the shear rate (s^{-1}), and μ_p is the plastic viscosity (Pa s). To quantify the importance of the yield stress we use the well-known Bingham number

$$\mathrm{Bn} = \frac{\tau_0 D}{\mu_p U_B} \tag{2}$$

where D is the pipe diameter (m), U_B is the bulk velocity (m/s), and ρ is the density (kg/m^3).

Guided by the results of Ookawara et al. [11] we use the following definition for the Reynolds number based on the momentum correction coefficient method[1] [11]

$$\mathrm{Re}(\mu_a, \zeta) = \frac{\rho U_B D}{\mu_a}\zeta \tag{3}$$

where $\mu_a = 3\mu_p/(a^4 - 4a + 3)$, $\zeta = 9(5 + 6a - 11a^2)/5(3 + 2a + a^2)^2$, and a is the relative plug radius for the Bingham model [12].

3 Numerical Method

We assume that the flow is laminar, incompressible, steady, and axisymmetric (i.e., two-dimensional). We utilize the commercial package FLUENT to solve the governing equations of the conservation of mass and momentum. The differencing schemes used are both formally second-order in accuracy: central differencing is used for the diffusive terms and a second-order up-winding scheme for the convective terms. Coupling of the pressure and velocity was achieved using the well-known semi-implicit method for pressure-linked equations (SIMPLE) implementation of Patankar [13]. The default "Bingham" model in FLUENT utilizes a bi-viscosity model (see Ref. [14] for example) of the form

$$\tau = \mu_{\mathrm{yield}}\dot{\gamma} \quad \dot{\gamma} < \frac{\tau_0}{\mu_{\mathrm{yield}}}$$

$$\tau = \tau_0 + \mu_P\left[\dot{\gamma} - \frac{\tau_0}{\mu_{\mathrm{yield}}}\right] \quad \dot{\gamma} \geq \frac{\tau_0}{\mu_{\mathrm{yield}}} \tag{4}$$

i.e., for low shear rates the material acts as a very viscous liquid (equal to the "yielding" viscosity μ_{yield}) rather than a true solid.

Contributed by the Fluids Engineering Division of ASME for publication in the JOURNAL OF FLUIDS ENGINEERING. Manuscript received July 22, 2009; final manuscript received December 14, 2009; published online March 17, 2010. Assoc. Editor: Hassan Peerhossaini.

[1]This is the Reynolds number obtained when the friction-factor Reynolds number relationship is forced to be equal to the Newtonian one in a laminar flow (e.g., $f(\mathrm{Re}) = 16$ for a pipe). It is the Bingham model equivalent of the Metzner-Reed Reynolds number for power-law fluids.

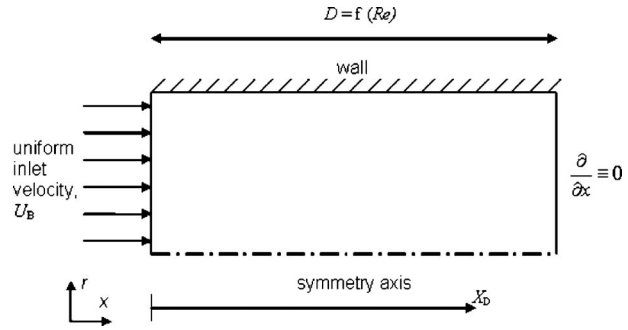

Fig. 1 Schematic of the computational domain and boundary conditions

We also investigate here the role played by the exact value of this yielding viscosity. As the default model is discontinuous, we also developed a user defined function (UDF) for the apparent viscosity to incorporate the exponential model due to Papanastasiou [15]

$$\tau = \tau_0(1 - e^{-m\dot{\gamma}}) + \mu_P\dot{\gamma} \tag{5}$$

where m is the stress growth exponent, which has the dimensions of time. Again this model transforms the "solid" region to a viscous one of high viscosity. It is usually thought that $mU/D > 500$ is sufficient for Eq. (5) to mimic the Bingham model successfully [15]. We also note that although Eqs. (4) and (5) approximate the true Bingham model over a wide range of shear rates [3], both models are fundamentally different to a true "yield stress" model as deformation occurs below the yield stress. As recent analytical work [16] has suggested that for a true Bingham model the development length may be "infinitely delayed," and the continuing debate regarding the existence of a true yield stress [2], we feel that the use of Eqs. (4) and (5) to approximate a yield stress fluid is reasonable.

A schematic representation of the computational domain is given in Fig. 1. At inlet ($x=0$), we apply a uniform velocity U_B and as discussed in the introduction, we define the development length X_D as the axial distance required for the velocity to reach 99% of the calculated maximum value at a radial location corresponding to 95% of the plug radius. We use the well-known no-slip boundary condition at the wall and impose zero axial gradients at the outlet. The length of the domain is dependent on the Reynolds and Bingham numbers of the flow in question ($L = f(\mathrm{Re}, \mathrm{Bn})$). Broadly, longer domain lengths were necessary than in the case of Newtonian or power-law fluids [5].

A preliminary series of calculations at low Re (=0.001) were carried out to assess the effects of mesh refinement, domain length, choice of Bingham-like model (i.e., Eq. (4) and (5)), value of yielding viscosity, and nondimensional value of the m parameter. Our coarse mesh, which is 10 diameters in length, corresponds to mesh M2 of our previous study [5] and comprises 20×200 cells, our base mesh "M3" comprises 40×400 cells, and our refined mesh "M4" comprises 80×800 cells. The cells are quadrilateral and of constant dimension $\Delta x = 2\Delta r$. We note that our base mesh here is of lower refinement than our results for the power-law model: a consequence of the longer domain lengths and the significantly increased time for convergence required for the Bingham-type models used here. In addition to the variation in X_D, to allow us to estimate the accuracy of the various conditions, we define a relative error

$$E = \frac{u_c - U_{C,\mathrm{FD}}}{U_{C,\mathrm{FD}}} \tag{6}$$

where u_c is the calculated centerline velocity (m/s) at the outlet plane and $U_{C,\mathrm{FD}}$ is the corresponding fully developed analytical value (m/s). The analytical solution for fully developed pipe flow of a Bingham fluid is well-known (see Ref. [12] for example) and so is not repeated here. The results of this series of calculations are shown in Tables 1–4 and from these information, we conclude the following: (a) Our coarse mesh (M2) shows discrepancies with the analytical fully developed solution, and therefore, all remaining calculations were conducted using M3 (simulations using M4 were prohibitively expensive and were not pursued above creeping-flow conditions, limited results are provided in Table 4); (b) although for a given mesh E exhibited little sensitivity to the yielding viscosity and stress growth exponent, the development length was more effected; (c) despite the bi-viscosity and exponential models becoming independent of these parameters in a given mesh, there is still a difference of about 2% between the development lengths predicted for nominally identical conditions (Re and Bn); and (d) although at low Reynolds numbers X_D is shorter for yield stress fluids than in the Newtonian case, longer

Table 1 Effect of various parameters using mesh M2 and domain length of 10*D* (NC=4000 cells, Re=0.001)

	u_c/U_B	E (%)	X_D/D
	Bi-viscosity (Bn=1)		
$\mu_{\mathrm{yield}}/\mu_p = 10^1$	1.865	0.26	0.6282
$\mu_{\mathrm{yield}}/\mu_p = 10^2$	1.852	−0.45	0.5832
$\mu_{\mathrm{yield}}/\mu_p = 10^3$	1.850	−0.53	0.5757
$\mu_{\mathrm{yield}}/\mu_p = 10^4$	1.850	−0.53	0.5753
	Exp. model (Bn=1)		
$mU/D = 37$	1.852	−0.43	0.6269
$mU/D = 370$	1.850	−0.53	0.5916
$mU/D = 3700$	1.850	−0.54	0.5899
	Bi-viscosity (Bn=10)		
$\mu_{\mathrm{yield}}/\mu_p = 10^4$	1.427	−0.59	0.5834
$\mu_{\mathrm{yield}}/\mu_p = 10^5$	1.426	−0.60	0.5804
	Exp. model (Bn=10)		
$mU/D = 1050$	1.426	−0.61	0.6267
$mU/D = 10{,}500$	1.426	−0.60	0.6044
$mU/D = 105{,}000$	1.426	−0.63	0.5985

Table 2 Effect of various parameters using mesh M3 and domain length of 10*D* (NC=16,000 cells, Re=0.001)

	u_c/U_B	E (%)	X_D/D
	Bi-viscosity (Bn=1)		
$\mu_{\mathrm{yield}}/\mu_p = 10^1$	1.872	0.67	0.6305
$\mu_{\mathrm{yield}}/\mu_p = 10^2$	1.859	−0.06	0.6000
$\mu_{\mathrm{yield}}/\mu_p = 10^3$	1.857	−0.14	0.5923
$\mu_{\mathrm{yield}}/\mu_p = 10^4$	1.857	−0.16	0.5922
	Exp. model (Bn=1)		
$mU/D = 37$	1.859	0.04	0.6297
$mU/D = 370$	1.858	−0.13	0.6077
$mU/D = 3700$	1.858	−0.13	0.6066
	Bi-viscosity (Bn=10)		
$\mu_{\mathrm{yield}}/\mu_p = 10^4$	1.434	−0.10	0.5852
$\mu_{\mathrm{yield}}/\mu_p = 10^5$	1.431	−0.30	0.5695
$\mu_{\mathrm{yield}}/\mu_p = 10^6$	1.432	−0.23	0.5731
	Exp. model (Bn=10)		
$mU/D = 10{,}500$	1.432	−0.23	0.5916
$mU/D = 105{,}000$	1.432	−0.23	0.5910

Table 3 Effect of domain length and the Bingham number for M3 using the bi-viscosity model and $\mu_{yield}/\mu_p=10^4$ (Re=0.001)

Bn=1	X_D/D	Bi=3.16	X_D/D	Bi=10	X_D/D
2*D*	0.5703	2*D*	0.4839	2*D*	0.5371
5*D*	0.5904	5*D*	0.5033	5*D*	0.5620
10*D*	0.5922	10*D*	0.5087	10*D*	0.5852
Bn=2		Bi=5			
2*D*	0.5008	2*D*	0.4997		
5*D*	0.5352	5*D*	0.5182		
10*D*	0.5440	10*D*	0.5258		

Table 4 Effect of mesh refinement using the bi-viscosity model and Re=0.001

Bn=1 ($\mu_{yield}/\mu_p=10^4$)	X_D/D	Bn=3.16 ($\mu_{yield}/\mu_p=10^4$)	X_D/D	Bn=10 ($\mu_{yield}/\mu=10^5$)	X_D/D
M2 10*D*	0.5753	M2 10*D*	0.5238	M2 10*D*	0.5804
M3 10*D*	0.5922	M3 10*D*	0.5087	M3 10*D*	0.5695
M4 10*D*	0.6011	M4 10*D*	0.5113	M4 10*D*	0.5766
Extrapolated	0.6047	Extrapolated	0.5123	Extrapolated	0.5975
Bn=2 ($\mu_{yield}/\mu_p=10^4$)		Bn=5 ($\mu_{yield}/\mu_p=10^4$)			
M2 10*D*	0.5417	M2 10*D*	0.5361		
M3 10*D*	0.5440	M3 10*D*	0.5258		
M4 10*D*	0.5498	M4 10*D*	0.5320		
Extrapolated	0.5521	Extrapolated	0.5345		

domain lengths are required for X_D to become independent of this domain length (see data in Table 3).

We use the bi-viscosity model for the rest of our simulations with a yield viscosity ratio (μ_{yield}/μ_p) of at least 10^4 and 10^5 for Bn=10. The data in Tables 1 and 2 show that the use of the Papanastasiou model would produce very similar results. Given all of the effects investigated we believe that the uncertainty in our estimation of X_D is no better than 2%.

To highlight the quality of the simulations, in Fig. 2, we show the radial variation in the outlet axial velocity profile from our simulations for Re=0.001 (bi-viscosity model, $\mu_{yield}/\mu_p=10^4$, mesh M3 and domain length of 10*D*) compared with the analytical solutions for the fully developed flow. Excellent agreement can be seen with $|E|$ at most 0.3%.

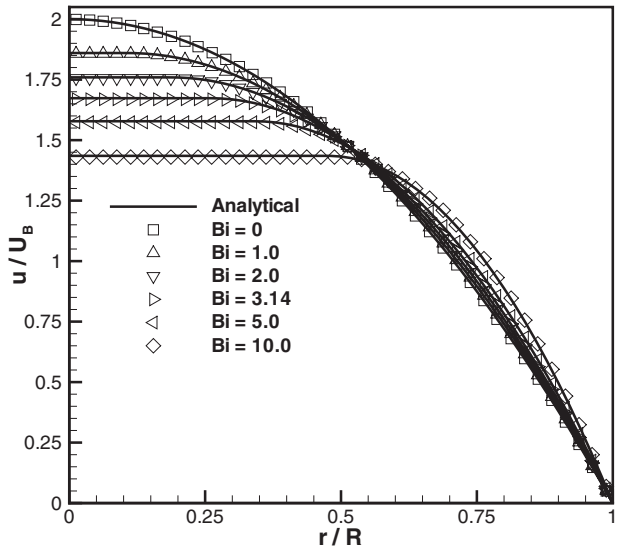

Fig. 2 Comparison of the numerical simulation velocity profiles at the pipe exit with the fully developed analytical solution at Re=0.001 for a range of Bingham numbers (bi-viscosity model, $\mu_{yield}/\mu_p=10^4$, mesh M3 10*D* length)

4 Results and Conclusions

The nondimensional development length is plotted as a function of the modified Reynolds number, Eq. (3), in Fig. 3 for a range of Bingham numbers $1<\mathrm{Bn}<10$. At higher values of Bn convergence became increasingly difficult and, as discussed in Ref. [3], as most interesting viscoplastic phenomena occuring in the range $1<\mathrm{Bn}<10$ simulations at higher Bn were not pursued. For Bn =0.1 we found that the results were practically indistinguishable from our Newtonian data (Bn=0) and are, therefore, not included

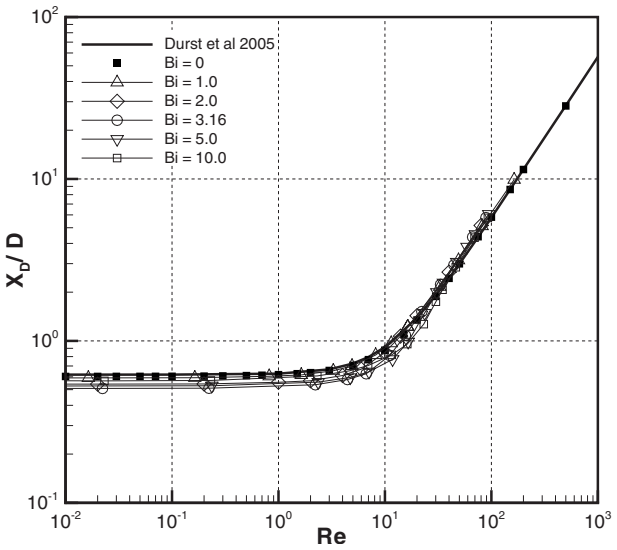

Fig. 3 Development length variation for Bingham fluids

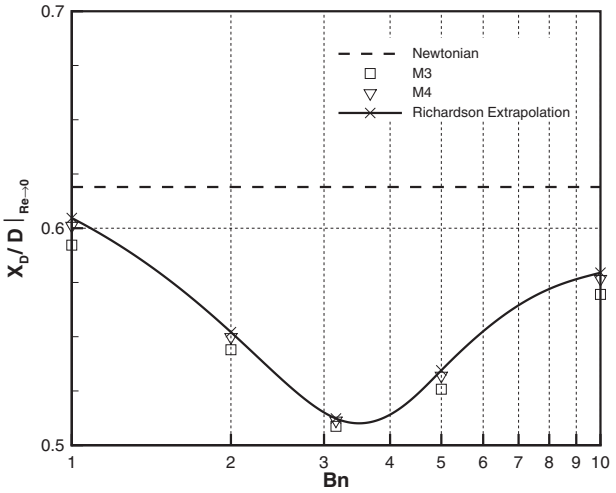

Fig. 4 Variation in the creeping-flow development length with the Bingham number

here. Much as was observed for non-Newtonian power-law fluids [5], above a critical value of Re, the data collapse to the Newtonian correlation [4]. Below this critical value of Re, which appears to be about 40 at the highest Bn, the development length departs from the Newtonian correlation in a nonmonotonic fashion dependent on the Bingham number. To highlight this variation in Fig. 4 we plot the creeping flow development length (i.e., $\mathrm{Re} \to 0$) versus the Bingham number (the Richardson extrapolation values shown in Fig. 4 and quantified in Table 4 were determined using the method outlined in Ref. [5]). The variation in the development length with Bn is complex; as the yield stress effects increase (i.e., as Bn increases) the central solid "plug" region grows—effectively changing the pipe diameter that the fluid "sees"—and the characteristic diffusion velocity also changes. Simple scaling arguments such as that used for power-law fluids [5] did not help reconcile this behavior. As the differences are relatively small—the maximum departure from the Newtonian correlation being about 20%—we propose that the Newtonian correlation (Eq. (1)) can be used for engineering purposes (estimating entrance effects, for example, when designing pipe flow systems [17]), provided that the momentum corrected Reynolds number is used in lieu of the Newtonian Reynolds number.

References

[1] Bird, R. B., Dai, G. C., and Yarusso, B. J., 1983, "The Rheology and Flow of Viscoplastic Materials," Rev. Chem. Eng., **1**, pp. 2–70.

[2] Barnes, H. A., 1999, "The Yield Stress—A Review or '$\pi\alpha\nu\tau\alpha\ \rho\varepsilon\iota$'—Everything Flows?," J. Non-Newtonian Fluid Mech., **81**, pp. 133–178.

[3] Mitsoulis, E., 2007, "Flows of Viscoplastic Materials: Models and Computations," *Rheology Reviews*, D. M. Binding, N. E. Hudson, and R. Keunings, eds., The British Society of Rheology, Glasgow, pp. 135–178.

[4] Durst, F., Ray, S., Unsal, B., and Bayoumi, O. A., 2005, "The Development Lengths of Laminar Pipe and Channel Flows," ASME J. Fluids Eng., **127**, pp. 1154–1160.

[5] Poole, R. J., and Ridley, B. S., 2007, "Development Length Requirements for Fully-Developed Laminar Pipe Flow of Inelastic Non-Newtonian Liquids," ASME J. Fluids Eng., **129**, pp. 1281–1287.

[6] Chen, S. S., Fan, L. T., and Hwang, C. L., 1970, "Entrance Region Flow of the Bingham Fluid in a Circular Pipe," AIChE J., **16**, pp. 293–299.

[7] Shah, V. L., and Soto, R. J., 1975, "Entrance Flow of a Bingham Fluid in a Tube," Appl. Sci. Res., **30**, pp. 271–278.

[8] Nowak, Z., and Gajdeczko, B., 1983, "Laminar Entrance Flow of a Bingham Fluid," Acta Mech., **49**, pp. 191–200.

[9] Vradis, G. C., Dougher, J., and Kumar, S., 1993, "Entrance Pipe Flow and Heat Transfer for a Bingham Plastic," Int. J. Heat Mass Transfer, **36**, pp. 543–552.

[10] Min, T., Choi, H. G., Yoo, J. Y., and Choi, H., 1997, "Laminar Convective Heat Transfer of a Bingham Plastic in a Circular Pipe—II. Numerical Approach—Hydrodynamically Developing Flow and Simultaneously Developing Flow," Int. J. Heat Mass Transfer, **40**, pp. 3689–3701.

[11] Ookawara, S., Ogawa, K., Dombrowski, N., Amooie-Foumeny, E., and Riza, A., 2000, "Unified Entry Length Correlation for Newtonian, Power Law and Bingham Fluids in Laminar Pipe Flow at Low Reynolds Number," J. Chem. Eng. Jpn., **33**, pp. 675–678.

[12] Chhabra, R. P., and Richardson, J. F., 2008, *Non-Newtonian Flow and Applied Rheology*, 2nd ed., Butterworth-Heinemann, Oxford.

[13] Patankar, S. V., 1980, *Numerical Heat Transfer and Fluid Flow*, Hemisphere, Washington, DC.

[14] O'Donovan, E. J., and Tanner, R. I., 1984, "Numerical Study of the Bingham Squeeze Film Problem," J. Non-Newtonian Fluid Mech., **15**, pp. 75–83.

[15] Papanastasiou, T. C., 1987, "Flow of Materials With Yield," J. Rheol., **31**, pp. 385–404.

[16] Al Khatib, M. A. M., and Wilson, S. D. R., 2001, "The Development of Poiseuille Flow of a Yield Stress Fluid," J. Non-Newtonian Fluid Mech., **100**, pp. 1–8.

[17] Escudier, M. P., Poole, R. J., Presti, F., Dales, C., Nouar, C., Desaubry, C., Graham, L., and Pullum, L., 2005, "Observations of Asymmetrical Flow Behaviour in Transitional Pipe Flow of Yield-Stress and Other Shear-Thinning Liquids," J. Non-Newtonian Fluid Mech., **127**, pp. 143–155.

Adjustment of Aerodynamic-Compensation Characteristics of a Pitot Tube by Rear-Body Shape Manipulation

Jehanzeb Masud
Department of Mechanical and Aerospace Engineering,
Institute of Avionics and Aeronautics,
Air University,
Islamabad 44000, Pakistan
e-mail: jehanzeb.masud@mail.au.edu.pk

Farooq bin Akram
School of Aerospace Engineering,
Georgia Institute of Technology,
Atlanta, GA 30332

In this paper we present a methodology for adjustment of subsonic compensation characteristics of an aerodynamic-compensation Pitot tube. This methodology is based on manipulation of a Pitot tube profile (shape) downstream of the static pressure port such that its subsonic characteristics are modified while the supersonic characteristics remain unchanged. Due to this "rear-body" shape adjustment, complete redesign of a developed or in service Pitot tube is not required. We have used computational fluid dynamics tools in the analysis and design refinement of a Pitot tube by rear-body shape adjustment. The complete Mach number regime ($M<2$) has been computationally analyzed for three different rear-body profiles. The results of our study indicate that significant variation in subsonic compensation characteristics of a Pitot tube is possible by this method. [DOI: 10.1115/1.4001156]

Keywords: Pitot tube, air data, aerodynamic compensation, CFD

1 Introduction

Pitot-static tube (referred commonly as Pitot tube) is one of the important air data sensors and is designed to measure correct ambient static and total pressure corresponding to aircraft flight conditions [1]. These pressure measurements translate into aircraft speed, pressure altitude, Mach number, vertical velocity information, etc., that are necessary for multiple aircraft subsystems. The measurement of correct ambient (atmospheric) static pressure by the Pitot tube over the whole Mach number regime (subsonic to supersonic) of the aircraft is the most critical aspect in its design. Generally, a Pitot tube is placed ahead of the aircraft where the local static pressure in the subsonic regime is higher than the ambient static pressure, i.e., positive Cp value [1], and is referred to as the Cp "position error." In the supersonic regime the local static pressure ahead of the aircraft equals the ambient static pressure; i.e., Cp position error value is zero. An "aerodynamic-compensation" Pitot tube is designed to "compensate" for the position error by generating "opposite" local Cp by a carefully contoured profile [1–6], as shown in Fig. 1. This presents multiple challenges to the designer due to the inherently different nature of subsonic and supersonic flows [7–9] as well as the sensitivity of the Pitot tube to minor factors such as mounting angle, pressure ports, etc. [10–13]. An ideal Pitot tube would fully compensate for the aircraft presence, and thus the static pressure measured by it over the whole flight regime, subsonic through supersonic, would be the corresponding atmospheric (ambient) pressure.

A designed and tested aerodynamically compensating Pitot tube for a supersonic aircraft can be subjected to subsequent modifications that arise as a part of aircraft development process. These modifications can affect the compensating characteristics of the Pitot tube. Since complete redesign of the Pitot tube is expensive in terms of verification and testing, therefore for small modifications, an alternate approach may be cost effective. In this paper one such technique, i.e., "rear-body compensation," is applied to adjust the pressure sensing characteristics of a compensating Pitot tube in the subsonic regime. The Pitot tube (Fig. 1) used in the present study was originally designed and developed for a supersonic fighter aircraft [14] and was later subjected to a flush angle-of-attack (AOA) interface modification [10] that had detrimental effect on its compensation characteristics. The influence of the AOA interface modification and subsequent adjustment of Pitot tube's compensation characteristics by rear-body shape adjustment are the subjects of the present study. Computational fluid dynamics (CFD) techniques are used in the analysis and redesign of this Pitot tube.

2 Computational Setup

The Pitot tube is symmetric about its longitudinal axis; therefore, steady-state, 2D axisymmetric analysis is done to evaluate its aerodynamic characteristics. This corresponds to zero AOA and zero side-slip angle (β) of the Pitot tube during flight. Aircraft Pitot tubes are generally oriented such that these flow conditions (AOA=β=0) prevail in their vicinity for most part of aircraft designed mission profile. The coordinate system and other parameters of the basic Pitot tube used in the present study are shown in Fig. 1. In addition to the Pitot tube, for CFD analysis, the complete flow domain is modeled and shown in Fig. 2. The flow domain includes the freestream far field, the Pitot tube, and the symmetry axis.

Mapped quadrilateral elements were used to mesh the computational domain. Elements were graded toward the surface of the Pitot tube in order to accurately resolve flow phenomena in its vicinity. Representative mesh in the vicinity of the Pitot tube is shown in Fig. 3.

In the present work, compressible Reynolds averaged Navier-Stokes (RANS) system of equations with constant property air (except density) was solved using the SIMPLEF algorithm of ANSYS® FLOTRAN [15,16]. No-slip velocity boundary condition was enforced at the surfaces/walls of the Pitot tube (Figs. 1 and 2). Pressure/velocity boundary conditions were used at upstream, far-stream, and downstream locations (Fig. 2) corresponding to the desired Mach number. Symmetry boundary condition was specified on the symmetry axis.

2.1 Turbulence Modeling. The flow field in the vicinity of the Pitot tube at zero AOA and β (axisymmetric case) is relatively straightforward without wakes, separation regions, or recirculating flow, and therefore is not expected to be sensitive to turbulence modeling. In our earlier study [5], we had shown that the two-equation standard K-ε (SKE) turbulence model [17] with standard wall treatment (law-of-the-wall) is adequate for computation of axisymmetric flow around a Pitot tube. Therefore, all the computed results presented in this study are based on the SKE turbulence model with standard wall function.

2.2 Grid Independence Analysis. Numerically computed results change with the type and fineness of the mesh/grid used for computations. In order to determine the dependence of the computational result on the mesh/grid used, two cases with different grids (Grids 1 and 2) were computed each at Mach numbers 0.9 and 1.8; Grid 1 had 40,500 elements (40,921 nodes) and Grid 2 had 77,000 elements (77,586 nodes). The results indicate percentage changes of less than 1.8% and 2.3% in the computed Cp value

Contributed by the Fluids Engineering Division of ASME for publication in the JOURNAL OF FLUIDS ENGINEERING. Manuscript received June 13, 2009; final manuscript received January 13, 2010; published online March 18, 2010. Assoc. Editor: Paul Durbin.

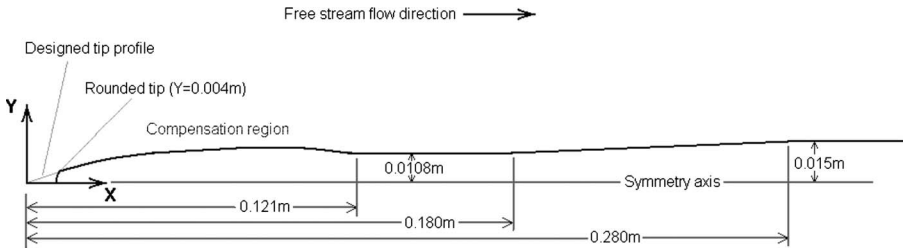

Fig. 1 Geometric profile of the original Pitot tube

at the design static port location (0.069 m from the Pitot tube front tip, Figs. 1 and 9) between the two grids at subsonic and supersonic speeds, respectively. The value of computed turbulent law y^+ remains below 200 and 300 at subsonic and supersonic speeds [9], respectively, for both the grids. These values of turbulent law y^+ show a reasonable resolution of grid near the walls with respect to the usage of standard wall functions [9,15,16]. Majority of the computations for the present work were done with a mesh having grid density equivalent to Grid 2 or better (Fig. 3).

3 Wind Tunnel Test Data

The designed original Pitot tube shown in Fig. 1 was tested in a high speed wind tunnel as part of aircraft [14] air data system development process. The high speed wind tunnel test section was 0.6×0.6 m^2 while the Pitot tube model (1:1 scale) had a maximum diameter of 0.030 m; therefore wind tunnel corrections to the measured Cp were considered unnecessary, and direct comparison between the computed results and the corresponding wind tunnel test data can be made. The original Pitot tube (Fig. 1) and its wind tunnel model (1:1 scale) had a design static pressure port placed at 0.069 m from the designed tip profile. During wind tunnel testing, static pressure (and corresponding Cp) was measured and recorded for a range of Mach numbers and AOAs at this static pressure port (sideslip was fixed at zero for these tests). All wind tunnel test (WTT) runs included a measurement point at AOA=0, which corresponds to the axisymmetric condition of the present computations. For computations, care was taken to place a node at the Pitot tube static port location so that computed results are directly available for comparison with wind tunnel test data without resorting to data interpolation. Comparison between computed and corresponding WTT data is quite satisfactory as shown later in this paper.

4 Results and Discussion

In the present analysis, computations were carried out at Mach numbers of 0.6, 0.8, 0.9, 1.3, 1.5, and 1.8 in order to adequately cover the wind tunnel test (experimental) data range as well as the aircraft flight envelope. The axisymmetric geometry used for the present computations is practically valid at zero angle-of-attack with no sideslip, as discussed earlier.

The basic flow field around the Pitot tube for all cases of the present study consists of freestream flow being modified by the presence of the tube. The flow adjacent to the Pitot tube generally follows its contour while far away it merges with the freestream flow. There is no separation/recirculation region near the Pitot

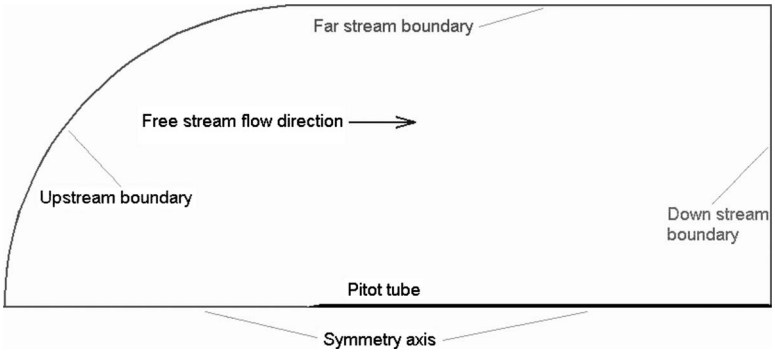

Fig. 2 Layout of the computational domain

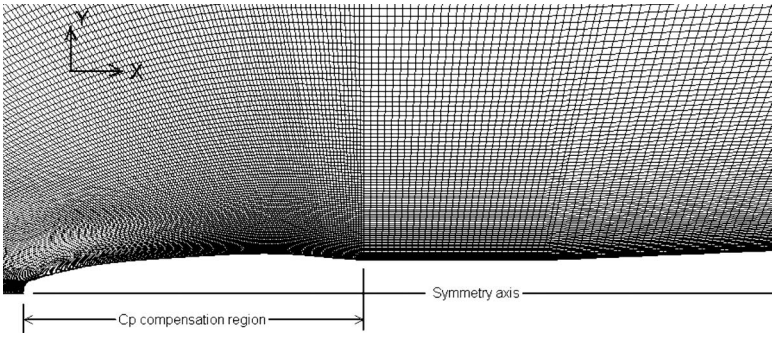

Fig. 3 Representative mesh in the vicinity of the Pitot tube

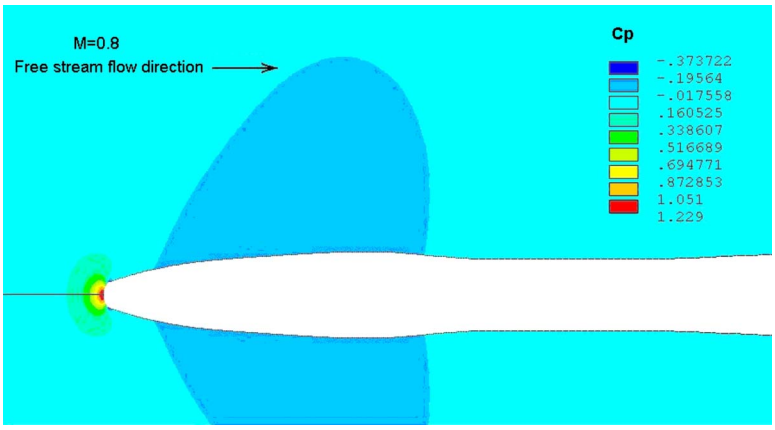

Fig. 4 Subsonic Cp variation near the compensation region of the Pitot tube

tube; therefore streamline or vector plots are not necessary to visualize this simple flow field. Some representative computed pressure field results are discussed next.

The computed pressure coefficient "Cp" variation in the vicinity of the original Pitot tube (Fig. 1) "compensation" region is shown in Figs. 4 and 5 for freestream Mach numbers of 0.8 and 1.5, respectively. Large pressure changes in the shock wave and near the front tip stagnation point are evident. The static pressure in the compensation region (Fig. 1) is lower than the freestream pressure in the subsonic regime (Fig. 4), which is a desirable characteristic [5]. While in the supersonic regime it is close to the freestream value (Fig. 5), which is again a desirable characteristic [5]. Detailed Cp variation along the Pitot surface is not evident from Figs. 4 and 5, and is discussed later in this paper.

4.1 Pitot Tube Design Refinement: Placement of AOA Interface. The first step in the original Pitot tube (Fig. 1) design refinement was to see the influence of pressure differential AOA measurement system conical interface [10] on the compensation region Cp characteristics. The conical interface is required between 0.0108 m radius tube at the end of the Pitot compensation region and 0.021 m radius tube at the rear joint with the aircraft nose radome [10]. For this purpose the interface under consideration is shown in Fig. 6. This interface is designated the "AOA interface," the starting point of this conical interface is 0.220 m from the designed tip, and it has a half-cone-angle (HCA) of 25 deg.

This AOA interface is likely to influence the subsonic Cp characteristics of the compensation region at design static pressure

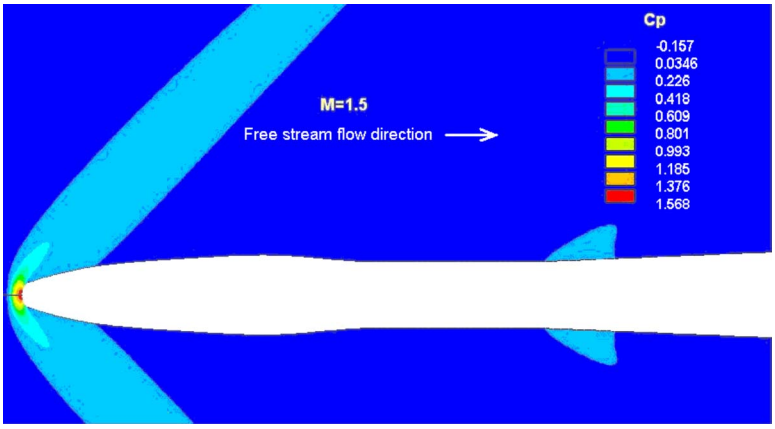

Fig. 5 Supersonic Cp variation near the compensation region of the Pitot tube

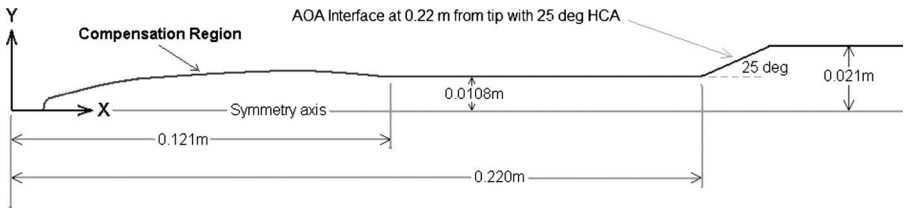

Fig. 6 Geometry of the proposed AOA interface

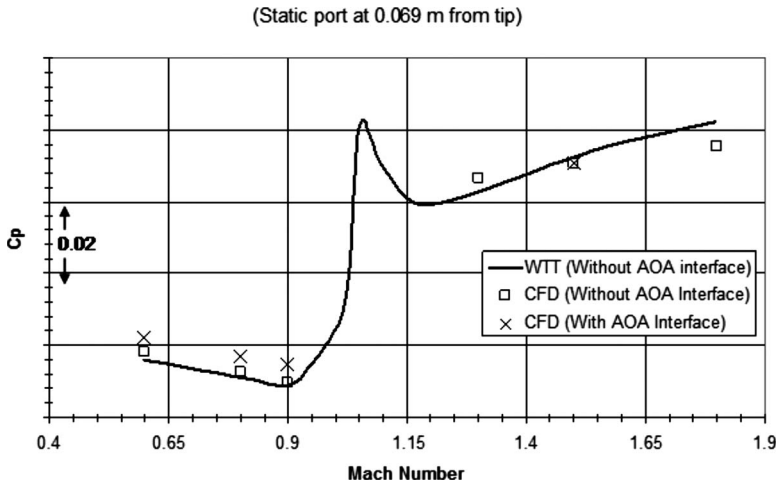

Fig. 7 Computed effect of the AOA interface on Cp at the design static pressure port

port; however, it would not have any effect in the supersonic regime as it is located downstream of the compensation region (Fig. 6). In order to computationally evaluate the effect of the proposed AOA interface, the computational procedure discussed earlier was followed. The complete geometry of the original Pitot tube with an AOA interface was recreated and analyzed for a range of subsonic and supersonic Mach numbers.

The results of the CFD analysis for the original Pitot tube with an AOA interface are shown in Fig. 7 in terms of pressure coefficient (Cp) at design static pressure port (0.069 m from the tip). The wind tunnel test data and computed results for the original Pitot tube without an AOA interface (Fig. 1) are also plotted for comparison. The agreement between the computed and WTT data is satisfactory given the sensitivity of tested Cp (WTT) to tolerances (errors) in Pitot tube wind tunnel model compensation region profile, its static pressure port location, and its alignment in the wind tunnel. Since the AOA interface is behind (downstream) of the Pitot tube compensation region (Fig. 6), therefore its effect on compensation region Cp would exist only in the subsonic regime as discussed earlier. This is confirmed for a single point CFD analysis at freestream Mach number of 1.5 as shown in Fig. 7. The computed Cp with an AOA and without an AOA interface is the same at $M=1.5$; therefore for design refinement analysis no further computations were done in the supersonic regime.

The change in subsonic Cp in the Pitot tube compensation region (at design static port, 0.069 m from the tip) due to the AOA interface, shown in Fig. 7, translates into an increase of about 7–8% of Cp value without the AOA interface. This represents inadequate compensation by the Pitot tube, which can cause significant errors in indicated altitude, Mach number, etc. However, the detrimental effect of the AOA interface on subsonic Cp of the compensation region may be reduced to acceptable levels without complete redesign by techniques that target subsonic Cp in the region of interest, i.e., rear-body compensation. As the name suggests, some changes in the compensation region (body) profile downstream (rear) of the area of interest (design static port) may be incorporated to counter the effect of the AOA interface. This aspect is discussed next in the paper.

4.2 Cp Adjustment by Rear-Body Compensation. The increase in Cp in the compensation region (design static port) due to the presence of the AOA interface is limited to the subsonic regime only. The supersonic Cp characteristics remain unchanged (Fig. 7) and are acceptable. The aim in this situation is to influence the subsonic Cp in the compensation region without disturbing its supersonic behavior. This suggests some change in the Pitot tube compensation region profile rear (downstream) of the area of interest, which is the design static port at 0.069 m from the tip. For the original Pitot tube with an AOA interface three rear-body compensation profiles were designed, as shown in Fig. 8. These profiles target changes in the basic compensation region profile rear (downstream) of the design static port at 0.069 m in the region between 0.089 m and 0.121 m from the designed tip. The three rear-body compensation profiles are designated RC1, RC2, and RC3 (Fig. 8) and are formed by a curve that is tangent both to the upstream profile at $x=0.089$ m and the downstream straight edge at $x=0.121$ m. The different curvatures are achieved by varying the stiffness of the fitted curve at the rear point ($x=0.121$ m). As can be seen from Fig. 8, all the profile changes (RC1, RC2, and RC3) result first in an increased expansion region in the flow direction (flow turning away from itself on a convex surface) followed by an increased compression region (flow turning into itself on a concave surface) compared with the original compensation profile in the same area ($0.089\ \text{m} \leq x \leq 0.121$ m). The first expansion region is expected to locally create a region of relatively low pressure of increasing magnitude from RC1 to RC3 profiles, which, due to subsonic nature of the flow, is expected to correspondingly reduce the upstream static pressure at the design static port ($x=0.069$ m) as well. The subsequent (further downstream) compression region is expected to result in a local region of relatively higher pressure, but since this high pressure region is downstream of the expansion region, therefore, the net effect at the design static port is expected to be dominated by the expansion region. The magnitude of this phenomenon is expected to progressively increase from RC1 to RC2 to RC3 profile due to difference in local profile curvatures in the region $0.089\ \text{m} \leq x \leq 0.121$ m (Fig. 8).

The complete geometry of the original Pitot tube with an AOA interface and RC1, RC2, and RC3 profiles (Figs. 6 and 8) was recreated for each combination and analyzed for a range of subsonic Mach numbers following the computational procedure discussed earlier. The results of computations with various rear-body compensation profiles (i.e., RC1, RC2, and RC3, Fig. 8) are shown in Fig. 9. The original Pitot tube CFD results (without an AOA interface or rear-body compensation profiles, Fig. 1) and wind tunnel test data (without an AOA interface) are also included for reference.

As can be seen from Fig. 9, the RC1, RC2, and RC3 profiles counter the influence of the AOA interface to increasing levels, as qualitatively discussed earlier. The RC3 profile completely eliminates the influence of the AOA interface at the designed static port (0.069 m from the Pitot tube designed tip, Fig. 8) and restores the Cp behavior to the original Pitot tube wind tunnel test level (with-

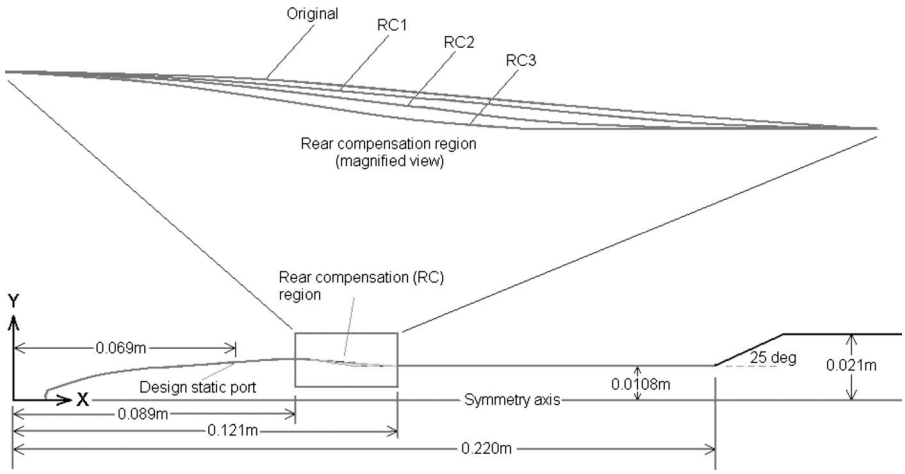

Fig. 8 Geometry of three proposed rear-body compensation (RC) profiles for a Pitot tube with AOA interface

out an AOA interface, Fig. 9). In order to get greater insight into the rear-body compensation phenomenon and the working of the local expansion and compression regions, as briefly discussed earlier, the Cp variation along the Pitot tube compensation region surface is plotted in Fig. 10 for a freestream Mach number of 0.6. It can be seen that the RC3 profile (Pitot tube with an AOA interface and an RC3 profile) first creates a region of locally low Cp at the expansion region followed by a region of locally high Cp at the compression region further downstream (between 0.089 m and 0.121 m, Fig. 8). The net effect of this is that the subsonic Cp in the rest of the compensation region upstream of RC3 is lowered to its original level (Figs. 9 and 10), as is proposed by rear-body compensation concept. The RC3 profile leaves the supersonic Cp at design static pressure port unaffected since all the profile modification is restricted downstream of the static pressure port.

5 Conclusion

In the present work it is shown that the angle-of-attack interface modification (AOA interface) on the original Pitot tube adversely affects (increases) the subsonic Cp in the compensation region. However, this detrimental effect on the compensation characteristics of the original Pitot tube can be overcome by rear-body compensation (RC3) profile adjustment downstream of the static pressure port. The combination of the AOA interface and the rear-body compensation modification (AOA interface and RC3 profile) restores the Pitot tube subsonic compensation characteristics to the desirable original level (without an AOA interface). Therefore, the feasibility of rear-body compensation as a design refinement technique to adjust the subsonic compensation characteristics of a Pitot tube is demonstrated.

Nomenclature

β = side-slip angle
Cp = pressure coefficient $(P-P_\infty)/\frac{1}{2}\rho_\infty V_\infty 2$
M = freestream Mach number
P = static pressure
P_∞ = freestream static pressure
RC1 = rear-body compensation profile No. 1
RC2 = rear-body compensation profile No. 2
RC3 = rear-body compensation profile No. 3
SKE = two-equation standard K-ε turbulence model
V_∞ = freestream velocity
ρ_∞ = freestream density
x = axial coordinate
y = radial coordinate
y^+ = nondimensional length scale associated with the turbulence model

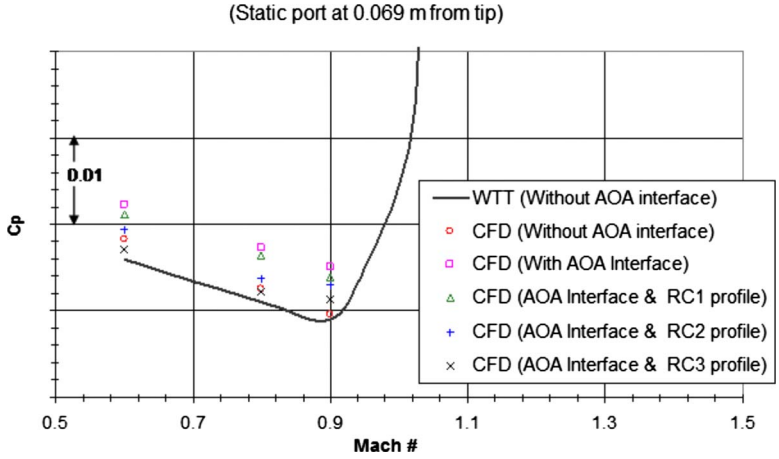

Fig. 9 Computed effect of the three rear-body compensation profiles on design static pressure port in the subsonic regime

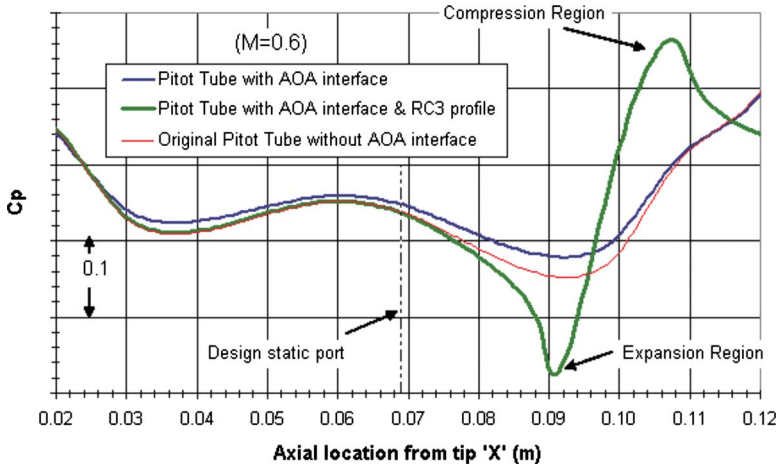

Fig. 10 Effect of the AOA interface and the RC3 profile on Pitot tube surface Cp (subsonic) in the compensation region

References

[1] Garcy, W., 1980, "Measurement of Aircraft Speed and Altitude," NASA Reference Publication No. 1046.

[2] Letko, W., 1947, "Investigation of the Fuselage Interference on a Pitot-Static Tube Extending Forward From the Nose of the Fuselage," NASA, Report No. NACA-TN-1496.

[3] Ritchie, V. S., 1959, "Several Methods for Aerodynamic Reduction of Static-Pressure Sensing Errors for Aircraft at Subsonic, Near-Sonic, and Low Supersonic Speeds," NASA, Technical Report No. TR R-18.

[4] Luo, S., and Bao, Y., 1988, "Computation of Transonic Aerodynamically Compensating Pitot Tube," J. Aircr., **25**(6), pp. 544–547.

[5] Latif, A., Masud, J., Sheikh, S. R., and Parvez, K., 2007, "Robust Design of an Aerodynamic Compensation Pitot-Static Tube for Supersonic Aircraft," J. Aircr., **44**(1), pp. 163–169.

[6] Kim, D.-J., Cheon, Y.-S., Myong, R.-S., Park, C.-W., Cho, T.-H., Park, Y.-M., and Choi, I.-H., 2008, "Design of Pitot-Tube Configuration Using CFD Analysis and Optimization Techniques," Transactions of the Korean Society of Mechanical Engineers B, **32**(5), pp. 392–399.

[7] Schreier, S., 1982, *Compressible Flow*, Wiley, New York, pp. 133–200.

[8] Ames Research Staff, 1953, "Equations, Tables, and Charts for Compressible Flow," NACA, Report No. 1135.

[9] White, F. M., 1991, *Viscous Fluid Flow*, 2nd ed., McGraw-Hill, New York, pp. 500–562.

[10] Masud, J., and Afgan, I., 2009, "Performance Characteristics of Flush Angle-of-Attack Measurement System Integrated on a Pitot Tube," 47th AIAA Aerospace Sciences Meeting and Exhibit, Orlando, FL, Paper No. AIAA-2009–1077.

[11] Sun, Z.-Q., Zhou, J.-M. A., Zhang, H.-J. B., and Hu, J. A., 2007, "On the Influencing Factors in a Pitot Tube Measurement I, Influence of Air Horn and Mounting Angle," Chinese Journal of Sensors and Actuators, **20**(3), pp. 690–693.

[12] Sun, Z.-Q., Zhou, J.-M. A., Zhang, H.-J. B., and Hu, J. A., 2007, "On the Influencing Factors in a Pitot Tube Measurement II, Influence of Total and Static Ports," Chinese Journal of Sensors and Actuators, **20**(4), pp. 941–944.

[13] Leng, X., Zhang, X., Xie, J., and He, F., 2001, "Effects of Pitot Tube on the Measurement of Supersonic Flow," Qinghua Daxue Xuebao/Journal of Tsinghua University, **41**(11), pp. 22–25.

[14] Jennings, G., 2008, "JF-17 Production Commences," Jane's Defense Weekly, **45**(5), p. 14.

[15] ANSYS FLOTRAN, Computational Fluid Dynamics Software Package, ANSYS, Inc., Canonsburg, PA.

[16] ANSYS, Computational Fluid Dynamics Software Package User Guide, ANSYS, Inc., Canonsburg, PA.

[17] Lauder, B. E., and Spalding, D. B., 1972, *Lectures in Mathematical Models of Turbulence*, Academic, London.